Andrada Măicăneanu

Atomistic simulation of oxide materials with catalytic properties

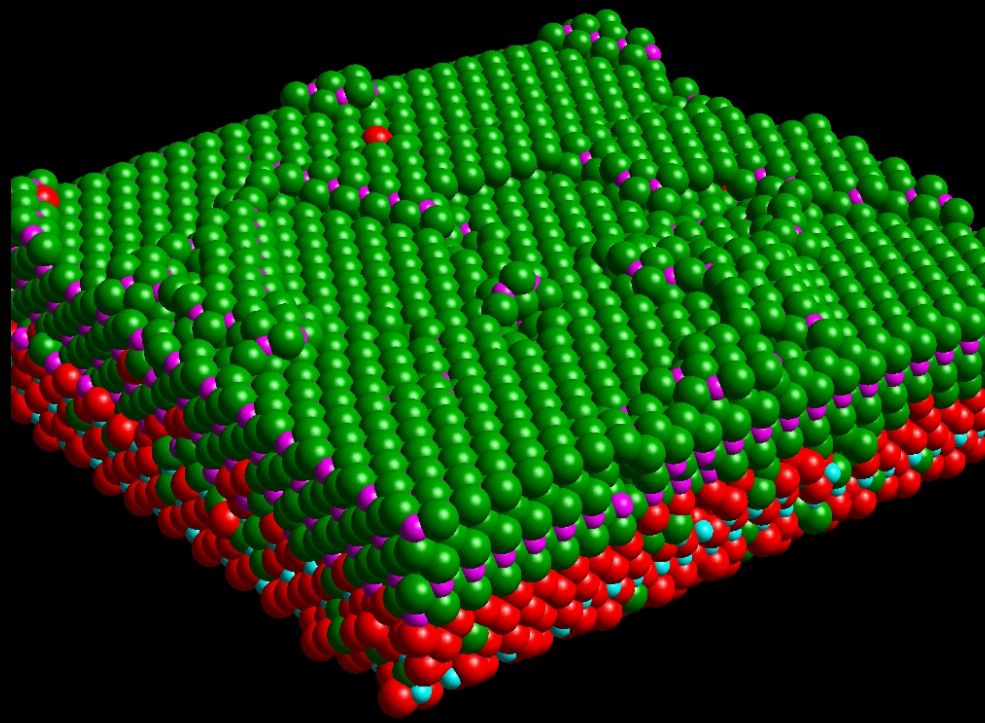

Cranfield
UNIVERSITY

Royal Military College of Science

Department of Environmental and Ordnance Systems

PhD Thesis

Academic Year 2001-2002

S. Andrada Măicăneanu

Atomistic simulation of oxide materials with catalytic properties

Supervisor: **Dean C. Sayle**

October 2001

Andrada Măicăneanu

Atomistic simulation of oxide materials with catalytic properties

Abstract

When supported, thin films demonstrate remarkable structural transformations, with important implications for catalysis, sensors, electrochemistry, semiconductors or superconductors. At present, the tools available to characterize solid-solid systems cannot provide atomic level resolution of, for example mixed screw-edge dislocations. Therefore atomistic simulation can provide an invaluable complement to experiment.

In this work atomistic simulation was employed to generate models of oxide thin films. First an atom deposition methodology was used to create an SrO thin film on a BaO(001) support. The evolution of the thin film from small clusters (submonolayer coverage), to five atomic layers, which includes cracks in its structure, was studied. Specifically, information related to growth and nucleation processes can be explored using this methodology.

Secondly an amorphisation and recrystallisation methodology was developed to explore the more complex system, that of ceria deposited on zirconia and yttrium stabilized zirconia. Simulated amorphisation and recrystallisation involves forcing the thin film to undergo a transformation into an amorphous state prior to recrystallising and therefore the recrystallisation process rather than the (perhaps artificial) initial structure will dictate the final structure. The recrystallisation process enables the evolution of all the important structural modifications as the thin film evolves structurally in response to the support. These include dislocations (pure edge and mixed screw-edge), dislocation networks, grain-boundaries and defects (interstitials, vacancies and substitutionals, including complex defect association) all within a *single* simulation cell.

Acknowledgements

I would like to thank Dr. D. C. Sayle for his help, advice, support and encouragement throughout the course of this work.

Contents

1. Introduction

The revolution that has occurred in computer technology and continuing growth in computer power has led to an increase in the importance of computer simulation. Computational techniques can help to understand and design complex materials and offer an attractive approach in many fields where experimental data are rare and difficult to obtain.

As a result, computational techniques such as energy minimization (EM), molecular dynamics (MD), molecular mechanics (MM), Monte Carlo (MC) and electronic structure techniques are used to fill the informational gap between fundamental materials science and industrial applications.

Using these computational methods, alone or in combination, it is possible to model and predict structures, characterize bonding in solids, model surfaces and interfaces, atomic transport and defect structures, chemical reactions, phase transformations, docking or predict reaction mechanisms (Catlow 1987, 1990, 1994ab, 1997ab, Hafner 2000 and Allan 2000).

1.1. Preparation and characterization methods of solid-solid interfaces

1.1.1. Preparation

Interfaces between materials, e.g. oxide-oxide interfaces, have an important role in supported semiconductors and supported catalysts (thin film on a support). In both cases the presence of an interface can improve the quality of the materials, but in different ways. For superconductors it is desirable to have perfect order between the constituent particles in the thin film and the support to maximize the electrical conductivity. Conversely, for catalysts, imperfections (which may act as active centers for molecular adsorption and may include for example kinks, steps, terraces and point defects, Schwarz 1995) are desirable on the catalyst surface. The type and concentration of such defects can be determined by the mode of preparation or subsequent treatment and the nature of the materials, which generate the interface. Other cases may exist in which neither one of the components

present catalytic activity, but together they have high activity as in case of V_2O_5 on TiO_2 (Sayle D. C. 1996a).

Since the surface imperfections can control the physical and chemical behaviour of solids, it is desirable to control their type and concentration. This goal can be achieved using the preparation mode appropriate for each material, considering the domain where the respective material will be used and what properties are required.

The methods used for interface preparation can be divided in three main categories: vapour deposition, chemical vapour deposition and sputtering (Elliot 1998).

Vapour deposition is perhaps the most straightforward technique, which involves condensation of a vapour onto a cooled substrate, the vapour phase of the starting material being achieved by the heating of a solid or a liquid. To achieve compositional homogeneity and thickness uniformity, the substrate can be rotated about an axis normal to the plane of the substrate. Also, by increasing the substrate temperature, the mobility of the adsorbed vapour species increases allowing structural modifications, with lower free energy, to be explored. Heating of the starting material can be resistive heating, electron-beam heating or laser heating. In the latter case the technique is known as *laser ablation*. Another vapour deposition technique is *molecular beam epitaxy* (MBE), which allows precise compositional control over the deposition and is used widely for interface fabrication (Chambers 2000). The composition of each particular layer is determined by the flux of atoms in each molecular beam (different components), which is controlled by the temperature of the diffusion cell.

Chemical vapour deposition (CVD) is the process whereby reactive precursor vapour phase molecular species react, either homogeneously in the gas phase or heterogeneously at the solid-gas interface at the substrate surface, producing a film with a composition different from that of the starting materials. The precursor molecules can be decomposed using heat (*thermal* CVD), adsorption of UV light (*photo* CVD) or in electrical plasma (*plasma-enhanced chemical vapour deposition* PECVD). When the precursor molecules are gaseous organic species, the technique is named *metal-organic chemical vapour deposition* (MOCVD). A variant of

MOCVD is called *chemical beam epitaxy* (CBE) or *metal-organic molecular beam epitaxy* (MOMBE). The process implies metal-organic precursors as in MOCVD and molecular beams in an ultra high vacuum chamber (UHV) as in case of MBE.

Sputtering is a preparation technique where particles from a target material are physically transported to a substrate. Ejected material from the target, in the form of ionized atoms or clusters of atoms, is passed to a substrate where a film of the target material is deposited. The resultant film should have the same chemical composition as the target, since most elements have similar sputtering rates. One of the sputtering variants is *chemical sputtering* when a compound of the target material and a reactive gas react to form a thin film. Sputtering can be induced if a high negative d.c. voltage is applied to the target called, *d.c. sputtering*, or if a constant magnetic field is places around the target, called *magnetron sputtering*. Radio frequency can be also used, to sputter poorly conducting materials (*r.f. sputtering*).

There are three main modes of growth possible when a material is deposited on a surface: Frank van der Merve or layer-by-layer growth (two-dimensional, 2D), Volmer Weber or island growth (three-dimensional, 3D) and Stranski-Krastanov or layer then island growth (Stoneham 1998, Koinuma 1998 and Chambers 2000). Koinuma (1998) and co-workers also mentioned the spiral growth as a zero-dimensional type of growth.

In table 1.1 a series of surfaces and solid-solid interfaces together with their preparation method and characterization techniques are presented (the table provides a flavour of the various systems and is not exhaustive).

Table 1.1. Methods for preparation of different solid-solid interfaces and characterization methods used.

Interface or surface	Preparation method	Characterization method(s)	Literature source
Iron oxide/MgO(001)	Pulsed laser deposition	TEM, SEM, EBSD	Johnson 1999
NiO/MgO(001) Fe_3O_4/MgO(001) Fe_3O_4/NiO/MgO(001)	Oxygen plasma-assisted (OPA) MBE	RHEED, XRD, SEM	Lind 1992
α-Fe_2O_3/Al_2O_3(0001) α-Fe_2O_3/MgO(001) Fe_3O_4/Al_2O_3(0001) Fe_3O_4/ MgO(001)	OPA – MBE MBE	RHEED, LEED, XPS, XPD, AES	Gao 1997 Kim Y. J. 1997a
Fe_3O_4/Si(100)	Ion beam sputter deposition	XPS, XRD, SEM, TEM	Kim K. J. 2000
SnO_2/glass	CVD	TEM, HVTEM, HREM, EDXS	Park 2000
NiO/MgO(001)	MBE	RHEED, LEED, XRD	James 1999
TiO/MgO(001)	Ti deposition in O_2 atmosphere	RHEED, Li^+ impact-collision ISS	Suzuki 2000
Cu_xO/ZnO(0001) and /ZnO(000$\bar{1}$)	Cu deposition in O_2 atmosphere	LEED, AES	Møller 1999
CuO/MgO(100)	MBE	RHEED, AFM	Brazdeikis 1996
Fe_3O_4/MgO(001)	OPA – MBE	RHEED, XRD, XAS	Chang 2000
SnO_2/ Al_2O_3(0001)	Magnetron sputtering deposition	XRD, TEM, AFM	Rue 1999
TiO_2/Si(100) TiO_2/Al_2O_3(1$\bar{1}$02)	MOCVD	SEM, XRD, XPS	Babelon 1998
Cu_2O/MgO(100)	CVD	TEM, SEM, XRD	Ottosson 1995
RuO_2/TiO_2(110)	OPA – MBE	RHEED, LEED, XPS, XPD	Kim Y. J. 1997b
MgO/$SrTiO_3$(001) MgO, SrO, NiO and Fe_3O_4/MgO(001)	OPA – MBE r.f. OPA – MBE	RHEED	Chern 1997, 1999
$SrZrO_3$/$SrTiO_3$(001)	Metal-organic deposition	TEM, HRTEM, HRSTEM	Ernst 1999

$BaO/SrTiO_3(001)$	Laser MBE	RHEED, AFM, XRD	Ohnishi 1997
$CaTiO_3/SrTiO_3(100)$ $La_{0.7}Sr_{0.3}MnO_3/SrTiO_3$	Laser MBE	RHEED, AFM	Nishikawa 1997
$SrTiO_3/BaTiO_3$	Atomic layer MOCVD	XRD, TEM, SIMS	Wang Z. 2000
SrO, $CaO/SrTiO_3(100)$	Atomic layer MBE	RHEED, AFM	Migita 1996
$LiNbO_3/\alpha\text{-}Al_2O_3(0001)$	Pulsed laser deposition	AFM, RHEED, XPS, XRD	Lee 1998
$SrTiO_3$, $BaTiO_3/SrTiO_3(100)$	Laser MBE	RHEED, AFM	Maeda 1996
$SrTiO_3/LaAlO_3(001)$	r.f. sputtering	AFM, XRD	Wang X. 2000
Cu/Ni(100)	Thermal evaporation of Cu	STM, SPA – LEED	Müller 1998
MgO/Mo(100) MgO/Ag(100) FeO/Pt(111) $Al_2O_3/NiAl(110)$	Oxidation or reactive growth from the metal vapor in O_2 atmosphere	XPS, AES, UPS, RHEED, LEED, SPA - LEED	Wollschläger 1998, 1999
NiO/Ag(100) CoO/Ag(100)	Reactive deposition of Ni or Co in O_2 atmosphere	STM, LEED	Sebastian 1999
Cu/CaO(100)	Electron beam evaporation	AES, EELS, LEED	Waltenburg 1999
Ti/MgO(001)	Electron beam evaporation	TEM, RHEED	Kado 2000
$Pt/SrTiO_3(100)$	MBE	RHEED, AES, XRD, AFM, HRTEM	Polli 2000
$Ni_{100-x}Cu_x/MgO(001)$	d.c. plasma sputtering	TEM	Qiu 2000
$Au/TiO_2(110)$	Vapour deposition	XPS, LEIS	Parker 1999a
Pd, Rh, Co or Ir/Al_2O_3	Vapour deposition	AFM, STM, XPS, LEED	Bäumer 2000
Au/YSZ(100)	Vapour deposition	XPS, XAES	Zafeiratos 1999
Mo/MgO(001)	d.c. magnetron sputtering	LEED, RHEED, STM, XRD	Svedberg 1999
Cu/ZrO_2	Vapour deposition	XPS, XAES	Sotiropoulou 2000
$Ni_{1-x}Fe_x/MgO(001)$	d.c. plasma sputtering	XPS, XRD, RHEED, TEM	Ishino 2000

MgO surfaces	Commercially available	AFM, SEM, TEM, HREED, LEED	Plass 1998, Giese 2000
TiO_2 surfaces	Commercially available	RHEED, STM, AFM	Nörenberg 1999a, 2000
SnO_2	Photo CVD	XRD	Tamura 1999
SnO_2	Ion beam induced CVD	XPS, XRD, SEM, TEM	Jiménez 1999
CeO_2/Si(100)	Magnetron sputtering	TEM, XRD	Kim L. 2000
CeO_2/sapphire	Magnetron sputtering	XRD, TEM, AFM	Španková 2000
CeO_2/α-Al_2O_3	Magnetron sputtering	AFM, XTEM, XRD, HREM	Jacobsen 1999ab
CeO_2/$SrTiO_3$(001) $Ce_{1-x}Zr_xO_2$/$SrTiO_3$(001)	OPA – MBE	RHEED, LEED, XRD, XPS, RBS, AES, AFM, STM	Gao 1999, Kim Y. 1999, Herman1999a
CeO_2/YSZ(100)	MOCVD	XRD, XPS, TEM, SEM, HREM	Liang 1995, Wang A.1999 Pan 1998
CeO_2/Si(100)	Spray pyrolysis	XRD, SEM, AFM	Wang S. 2000
CeO_2	Spray pyrolysis	XRD, SEM, HREM	Vallet-Regi 1997
CeO_2/YSZ(001)	Laser ablation	XRD, X-ray reflectivity	Méchin 1996
CeO_2/Si(001)	Laser ablation	XRD, XPS	Wakiya 2000
CeO_2/Ni(001)	Laser ablation	XRD, Raman spectroscopy	Wang R. –P. 1998
CeO_2	Commercially available	STM, RHEED, LEED, AES	Nörenberg 1999b

1.1.2. Characterization

As can be seen from table 1.1 the main techniques used to characterize solid materials include methods, such as atomic force microscopy (AFM), scanning tunneling microscopy (STM), scanning electron microscopy (SEM), transmission electron microscopy (TEM), diffraction methods such as low-energy electron diffraction (LEED), reflection high-energy electron diffraction (RHEED), X-ray diffraction (XRD), X-ray photoelectron diffraction (XPD) and spectroscopic methods including Auger electron spectroscopy (AES), X-ray photoelectron spectroscopy (XPS) or X-ray adsorption spectroscopy (XAS).

Microscopy techniques can be used to obtain information about surface structure at nanometer scale resolution. All these techniques offer only two-dimensional imaging of a system. However, Koster and co-workers (2000) have developed a new transmission electron microscopy technique that allows three-dimensional imaging of a solid material. The method has been employed to show the three-dimensional mesoporous channels in a zeolite and to locate metal particles also in a zeolite structure.

Diffraction techniques such as RHEED and LEED are used to characterize easily the symmetry of epitaxial films (surface quality and crystallinity). While RHEED can offer information about the structure of the whole thin film; LEED, due to low energy electrons, offers information about the near-surface region. RHEED can be used also in-situ following the growth process from the first atoms deposited until a complete thin film is constructed. LEED and RHEED techniques are used many times just to characterize the substrate on which the deposition will be conducted. XRD, which is usually the first analysis made on a solid material, offers information about the phase content and in-plane orientation of crystalline layers.

Analysis of a solid system can be completed using spectroscopic methods, which can offer information about chemical composition and oxidation state. Therefore the purity and stoichiometry of a material can be elucidated. AES and XPS can be used for example to establish if the substrate on which the deposition will take place is ‘clean’.

A global presentation of the techniques available for surface and interface characterization and information that can be obtained using them is presented by Somorjai (1994) in his book.

To illustrate the information that can be obtained using the various characterization techniques, a few results obtained for growth of different solid-solid interfaces will be presented.

Cu_2O thin films grown by chemical vapour deposition on MgO(100) substrates (Ottoson 1995) were studied using microscopy (HREM, TEM) and diffraction techniques (XRD). It was found that the growth and nucleation of the thin film is strongly dependent on the substrate pre-treatment, several epitaxial orientations being observed: (100), (110) and

(111) at low temperatures, (100) on a defective substrate and only (110) orientation at high temperature. From the TEM investigations various orientational relationships between the Cu_2O islands (Volmer Weber growth) and substrates were determined. For example for films deposited at 700ºC a small in-plane rotation of less than 2º between Cu_2O grains was observed. Upon coalescence, twin boundaries between the (110) oriented grains were generated. In addition X-ray fluorescence spectroscopy was used to measure the thin film thickness.

The evolution of the CuO film deposited on MgO(100) using molecular beam epitaxy (Brazdeikis 1996) was examined using RHEED and AFM. The RHEED patterns indicate that CuO grows in the form of two-dimensional islands with CuO(111) planes parallel to MgO(100). AFM images show that CuO island density increases during growth, forming large grains of about 200 nm in length.

Metal-organic chemical vapour deposition was used to prepare TiO_2 thin films on Si(100) and $Al_2O_3(1\bar{1}02)$, (Babelon 1998). The morphology of the thin film and the presence of impurities on the thin films surfaces were studied using respectively, SEM and XPS. In the case of deposition on Si, the SEM images show that TiO_2 grown layers have a columnar shape with the thin film surface composed of grains the size of which increases with the substrate temperature. For the deposition on Al_2O_3, columnar structures are also observed, but are less regular in accord with grain size distribution, which is less homogeneous than in the case of deposition on Si. Inspection of the XPS spectra shows the presence of Ti^{4+}, characteristic of a stoichiometric surface and carbon contamination from the decomposition of the metal-organic precursor. The chemical composition of an oxide thin film can also be investigated using Li^+ impact-collision ion scattering spectroscopy (Suzuki 2000).

In the case of NiO deposited on MgO(001) using molecular beam epitaxy, RHEED analyses have shown that growth follows a layer-by-layer mode (James 1999). Also, using XRD, the relaxation of the NiO lattice parameter, as a function of film thickness, was followed. Initially, the overlayer lattice grows coherently on the substrate until ca. 600 Å, (critical thickness), after which dislocations evolve to relieve the lattice strain.

Using TEM and electron backscattered diffraction (EBSD), the growth of an iron oxide thin film on MgO(001) was studied (Johnson 1999). It was determined that the phase of iron oxide, which formed was dependent upon the deposition time used to produce the thin film. For shorter deposition times, thinner films with spinel phase iron oxide were formed (magnetite, Fe_3O_4 and maghaetite, γ-Fe_2O_3). Conversely, for longer deposition times, the corundum phase of Fe oxide was obtained (haematite α-Fe_2O_3).

Interconnectivity between spectroscopic, diffraction and microscopy methods to gather information, can give an overall image of an interface. This is exemplified also in the case of an Fe_3O_4 grown on Si(100) substrate by ion beam sputter deposition (Kim K. J. 2000). In-situ XPS was used to follow the stoichiometry of iron oxide during the deposition; XRD was used to study the effect of the substrate temperature and post-annealing on the crystalinity of the thin film, while SEM and TEM offer images of the surface. TEM also confirm the formation of metallic Fe nanocystallites in the Fe_3O_4 thin film.

$SrTiO_3$ thin films grown on $LaAlO_3$(001) using r.f. sputtering were characterized using AFM and XRD to show the influence of growth temperature on composition, orientation and surface morphology (Wang X. 2000). For growth temperatures as low as 350ºC epitaxial growth was observed. Below 350ºC the films are polycrystalline and three different orientations (100), (110) and (111) can be observed with XRD. ATM shows that films deposited at temperatures below 350ºC and above 650ºC are smooth while the surfaces of the films made at intermediate temperatures are rough and faceted.

The growth of various metals, Pd, Rh, Co and Ir, on a thin alumina film using vapour deposition was followed using mainly STM (Bäumer 2000). It was found that all metals prefer a three-dimensional growth mode (island), irrespective to the deposition temperature and the nucleation process is dominated by defects within the Al_2O_3 substrate. For example in the case of Rh and Pd, point defects are primary nucleation centres at 90 K and line defects at 300 K.

During thermal evaporation and deposition of Cu on Ni(100), the evolution of copper islands was determined using STM (Müller 1998). It was demonstrated that copper islands, as they grow in size, undergo a spontaneous shape transition. Below a critical island size of about 500 atoms the islands have a compact shape, while above this size they become branched out. The branched island shape reflects the energy minimum of binding and strain energy.

Wollschläger (1998) in his paper presents the use of some characterization techniques applied to oxide-metal systems to identify a variety of defects that can appear due to the differences that exist between oxide and metal structures. The morphologies of films in the, MgO/Ag(100), MgO/Mo(100), FeO/Pt(111) and Al_2O_3/NiAl(110) systems, are studied by means of STM and high-resolution spot profile analysis of low energy electron diffraction (SPA – LEED). These techniques are dominantly used to characterize extended defects such as line defects (atomic steps, anti-phase boundaries). Point defects such as vacancies, colour centres can also be studied using these techniques, but they are mostly investigated using spectroscopic techniques since they also influence the electronic properties.

In the following section a few applications of computational techniques in materials science, with focus on oxide materials, will be presented.

1.2. Computer modeling in solid state chemistry

A considerable number of studies have used atomistic simulation to characterize solid materials. Here a few studies relevant to the subject of this thesis together with some information of data that can be obtained using this technique as applied to more complex solids (e.g. polymers, polymers and drugs) are summarized.

Clusters. Metallic and ionic clusters either isolated or supported are ideally suited to study using atomistic computer simulation techniques (Catlow 1997c). In case of the isolated clusters, the morphology corresponding to global minimum can be determined for small clusters.

Also using molecular dynamical techniques it is possible to investigate the thermal evolution of an ionic cluster, the melting process and even evaporation (Catlow 1997c).

Cordatos and co-workers (1996a) give another example of possible cluster analysis. They studied the structure and reducibility of ceria clusters. It was found that the smallest clusters do not crystallize into the bulk, fluorite structure; only for the largest cluster (50 cerium ions) the fluorite structure was clearly observed. This cluster also exhibited (111) surface facets, indicating that this is the most stable surface. The reducibility of the clusters is strongly influenced by the cluster size, with larger particles more difficult to reduce.

A further step in the study of clusters is the way in which these are modified by their interactions with support materials. Clusters of metals on oxide supports have considerable technological importance, especially in catalysis. For Ni clusters supported on a SiO_2(110) surface it was found that the clusters are appreciably distorted as a result of their interaction with the support (Catlow 1997c and references therein). It was found that Ni-Ni distances increase and therefore the cluster size also increases owing to its interaction with the surface. For small copper clusters on MgO(100) it was found that Cu-Cu interactions are stronger than cluster-surface interactions, therefore the three-dimensional structures are preferred with respect to two-dimensional ones; with the cluster in an upright position with respect to the surface (Musolino 1999ab). Further studies indicate that the adsorbed clusters diffuse on the surface by ‘rolling’ and ‘twisting’ motions.

Ionic clusters on ionic supports (for example in the case of oxides) can also be studied using simulation techniques. One example of this type of system is given by Shluger (1995ab) and Sayle D. C. (1997a) who studied NaCl deposited on an MgO(100) surface. In the first case, $(NaCl)_n$ (n=1-48) clusters were placed directly on-top of a perfect MgO surface, while in the second case single NaCl species are deposited sequential on a MgO surface that included a monoatomic step or a vacancy on its surface. These studies offer information about cluster geometry, binding energies, interactions with the surface and cluster diffusion on the surface and more important how the

substrate directs the growth of the overlying material according to the defects present on its surface.

Another application includes the study of clusters, metal or organic molecule clusters, formed in microporous materials (Catlow 1997c). Modeling of such systems can help to understand catalytic or separation processes that take place using these types of materials.

Defects. The main defects that can exist in a material are classified as point defects (vacancies, interstitials and substitutionals), linear defects or dislocations (edge and screw dislocations) and two-dimensional defects (grain boundaries), (Van Vlack 1970). All these defects can influence the properties of a solid material therefore it is important to know their distribution and density within a certain material. Simulation techniques can again contribute with useful information to elucidate their structure and how defects in solid materials can influence properties such as conductivity, diffusion or adsorption of different molecules on a given surface.

The calculation of point defect parameters in ionic solids by atomistic simulation is considered by Harding (1990), which presents a review of both static and dynamic methods that can be used. Also the calculation of defect energies and entropies is considered. A large number of calculations can be performed in this area such as defect formation energies, defect activation energies, binding energies for different types of defect cluster (Catlow 1987) with direct application to, for example superconducting (Allan and Mackrodt 1993) and catalytic materials, TiO_2 (Sayle D. C. 1995a) and ZrO_2 (Dwivedi 1990, Balducci 1997, 1998 and Khan 1998). The calculation of solution energies of cation doping can be used to find the most favorable dopants in certain materials where such treatment can improve electronic or structural properties. In the case of ZrO_2, for example, in accord with experimental results, it was shown that yttrium gives the lowest solution energy (Khan 1998).

The next range of defects that can be studied using computer simulation are linear defects, which include edge and screw dislocations. The atomistic and electronic structure of misfit dislocations at InAs/GaAs(110) heterointerfaces were studied using first principle calculations (Oyama 1999), while in the $BaTiO_3/SrTiO_3(001)$ system,

molecular dynamical simulations were performed in order to understand the formation of misfit dislocation when the thin film reaches its critical thickness (Wunderlich 2000).

Screw dislocations were also studied using atomistic simulation in bulk MgO and NiO as well as terminated at the MgO (100) surface (Watson 1999, 2001). In this way it was possible to calculate dislocation formation energies and draw conclusions about the influence of this type of dislocation on the stability of the crystalline system. It was also found that in some cases the presence of point defects (e.g. vacancies) stabilize the screw dislocation (Watson 1999). In the case of the screw dislocation terminated at the MgO surface it was found that if the deposition of MgO species continues, the growth would take place preferentially at the dislocation core (Watson 2001). The study showed that the binding at the dislocation core is energetically favourable, therefore these surface defects, which are low coordination sites, represent the sites of highest activity.

Two-dimensional defects, such as grain boundaries, were studied using computer simulation in MgO and NiO (Watson 1996, Harris 1999 and Harding 1999a), yttrium-stabilized zirconia (Fisher 1998, 1999ab), or ZnO (Domingos 1999). In the case of NiO and MgO the structure and energies of a series of tilt grain boundaries were calculated in order to obtain a relationship between the grain boundary energy and the tilt angle. The calculations also showed a significant change in the structure of the tilt boundaries as pressure increases (Harris 1999). The grain boundaries in yttrium-stabilized zirconia were studied using molecular dynamics in order to establish their influence over the oxygen diffusion in systems where industrial applications are based on this property (see chapter 4.1.1.2). For ZnO, atomistic simulations of the structure and energies of a series of (0001) twist boundaries were studied. It was also found that if cobalt and barium impurities were introduced in the system, they would have the tendency to segregate to the boundary. This behaviour can have a great influence when ZnO ceramics are used as varistors (Domingos 1999).

Surfaces. The techniques used to characterize bulk solids can be used also to model surfaces. Once a surface is created, specific structural features or surface properties can be elucidated. In this paragraph a few

examples of calculations that can be made on oxide surfaces will be presented. Oliver and co-workers investigated the effect of temperature on the {111}, {110} and Ni {111} surfaces of NiO (1995) and the stability of different WO_3 surfaces (1996). The surface energies for the {110} and Ni {111} surfaces decreased with temperature up to 2000 K, while the surface energy for the {100} remained approximately constant. At 2000 K {110} and Ni {111} surfaces were disordered with appreciable amounts of diffusion of both Ni^{2+} and O^{2-} ions at the surface indicating premelting of the surface. In the case of the more densely packed {100} surface no such behaviour was observed. The temperature at which the crystal melts is different for those three surfaces, indicating that crystal melting is governed by the surfaces exposed. In the case of WO_3 considering the fact that {100}, {110} and {111} surfaces all have a dipole, perpendicular to the surface, reconstructions were applied to generate a non-dipolar unit cell. In the case of {100} surfaces five reconstructions were calculated using energy minimization to establish the most stable surface.

Computer modeling was also used to study V_2O_5 surface structures (Sayle D. C. 1996b), steps on the MgO(100) surface (Harding 1999b), $SrTiO_3$ and $BaTiO_3$ (110) surface relaxation (Heifets 2000) and mineral (magnesium silicate and magnesium aluminate) surfaces including stability and growth (Parker 1997).

Interfaces. Atomistic computer simulation techniques, which are now acquiring a truly predictive capability within solid-state chemistry, provide a complementary method for the study and characterization of solid-solid interfaces. Moreover, using sequential deposition it is possible to study the nucleation and growth mechanisms of species, which form the thin film. Also, it is possible to study the influence of the support and support imperfections over the thin film structure.

A new molecular dynamics code was developed to simulate the growth process of ultrafine metal particles on metal oxide surfaces (Kubo 1994, 1995ab, 1997ab) and then extended to the homoepitaxial and heteroepitaxial growth processes of oxide materials on oxide substrate (Kubo 1999). The model system for this MD simulation consists of two parts: a substrate and a source of particles (metal atoms or molecules). The

number of particles deposited over the substrate is increased one by one at regular time intervals with a defined velocity. The substrate temperature, distance between the substrate surface and the source of particles, the emitting rates of particles, the number of deposited particles and the time intervals between successive depositions are variable parameters. This code was used to investigate the formation process of ultrafine gold particles on MgO(100) surface. The effect of deposition rates of Au atoms, the effect of a groove in the MgO(100) plane (Kubo 1994), the effect of temperature of the MgO substrate and the effect of defects (point defects and steps) (Kubo 1995ab) on the deposition mechanism were studied. It was found that decreasing the deposition rates of Au atoms, the number of fixed atoms on a MgO(100) plane was increased. Also the presence of defects on the MgO(100) surface has a great influence over the configuration and location of Au clusters, in agreement with experimental results. The presence of defects on the MgO(100) plane is desirable for realizing the ultrafine dispersion of Au particles, (higher dispersion, better catalytic activity), since the deposition takes place preferentially on these sites. Also, lowering the temperature of the substrate, led to more Au atoms being fixed on the MgO(100) plane.

Adams and co-workers (2000) present a general overview of methods of modeling thin film growth on an atomic scale including molecular dynamics, energy minimization and Monte Carlo methods for Cu thin film growth. While MD helps to investigate diffusion mechanisms, energy minimization helps to search for a local minimum or a transition state (such as when an atom is jumping from one site to another) and Kinetic Lattice Monte Carlo simulate film growth for large scales (up to millions of atoms) for long duration following phenomena like nucleation and facet growth.

Another growth technique, Kinetic Monte Carlo was developed for simulating the growth of polycrystalline thin Cu films on Cu (Wang 2001). The method consists of an impact angle-based multiple-collision method for the deposition of incident atoms from an atomic beam and surface diffusion of the surface atoms, combined with a restriction of growth within identically oriented grains to simulate the surface morphology and porosity

of a polycrystalline material. The effect of the incident angle of the deposited particles on the morphology of the grown film was explored. It was found that low angles of incidence (near normal) produce smooth columnar films, while large (oblique) angles of incidence produce rough dendritic films.

Phillpot and co-workers (1999) present also a methodology for synthesis of polycrystalline thin films, but for ionic materials and using molecular dynamical simulation. The methodology involves two stages. In the first stage, a polycrystalline substrate is grown by introducing small cylindrical, perfect crystaline seeds into a molten bulk. When the temperature in the system is reduced below the melting point, the seeds act as nucleation centres for the growth of the grains to form a dense columnar microstructure. In the second stage, a large volume of melt is placed on top of the polycrystalline substrate and the thin film is grown by reducing the temperature below the melting point such that an approximately layer-by-layer film growth takes place. This method was used to obtain polycrystalline FeO films with grain size of approximately 4.7 nm. The interiors of the grains are almost perfect single crystals with only few vacancies and no interstitials. The grains are delimited by tilt grain boundaries including low-angle grain boundaries, which consists of arrays of dislocations and high-angle grain boundaries, which are relatively narrow and well ordered.

Sayle D. C. (1997a, 1998a) presented another approach for sequential deposition, which includes energy minimization and dynamical simulation. A detailed description of the code, which will be also used in the present work to build the SrO/BaO(001) interface will be presented in chapter 2.2.4. Construction of interfaces can be also realized using near coincidence site lattice theory (NCSL), cube-on-cube or amorphisation and recrystallisation merthodology (see Appendix B and chapter 2).

Oxide-oxide interfaces simulated using computational techniques will be discussed in detail in chapter 3.1.1.

Diffusion. Another important issue that can be addressed using computer simulation is diffusion in solid materials. Oxide materials, which exhibit high ionic conductivity with applications including fuel cells, gas

sensors, membrane materials or catalysts, can all be studied using simulation techniques. For example, oxygen migration in $La_2NiO_{4+\delta}$ (Minervini 2000), ionic transport (oxygen, cation and incorporated proton) in ABO_3 perovskite oxides (Islam 2000) and oxygen diffusion in zirconia solid solutions (Khan 1998) were investigated and the results obtained are in good agreement with experimental data. Migration of defects in oxide materials can also be explored as in the case of NiO(001) where the cation vacancy diffusion is the main diffusion process on this surface (Karakasidis 1999).

Catalysis. Computer simulation techniques have been used also to study fundamental problems in catalysis such as: models of structures at the atomic level of crystalline and amorphous catalysts, elucidation of the local structure of active sites in solids or on their surface or determination of mechanisms of molecular diffusion and adsorption at active sites (Catlow 1997b). Besides the study of these processes, simulation techniques can be used to calculate adsorption energies, adsorption isotherms, heat of adsorption, diffusion coefficients, reaction rates, reactant conversion and product yields and selectivities (Broadbelt 2000).

Using electronic structure techniques, Watari (1995) and Kobayashi (1995) studied the adsorption of CO and NO chemisorption on heavy metal surfaces and respectively CO reaction with MgO surfaces. It was found that CO is adsorbed onto the Mg atom with either C- or O- end, but not to the O atom; adsorption on the O atom being possible only when the adjacent Mg site is occupied by CO. Also the adsorption is stable for five, four and three coordinated sites, and the stabilization increases in this order.

Even if a mechanism cannot be proposed based on atomistic simulation, this technique can also be used as a first approach of an adsorptive phenomenon. Sayle D. C. and co-workers (1996b) studied sorption of ethene molecule on V_2O_5 surfaces. They found that (001), (200) and (301) V_2O_5 surfaces present low-energy adsorption sites for ethane. Also the ethane molecule is observed to approach closer to the exposed ions on the (301) surfaces, which is reflected in the binding energy, which is greater than on the other two surfaces.

Another atomistic simulation study describes the adsorption of water on MgO, CaO, α-Fe_2O_3, Mg_2SiO_4 and $CaCO_3$ (de Leeuw 1996, 1999 and Parker 1999b). The adsorption of water on MgO and CaO surfaces was found to take place on all five, four and three coordinated sites, but it is more advantageous on lower coordinated sites. The dissolution process can also be studied by evaluating the energies of replacing the surface cations with protons. The dissolution energies are highly dependent on cation coordination and the type of cation present, with Ca being energetically more favoured than Mg.

Further models for the adsorption and reaction are reviewed by Catlow (1997b) including: sorption of isomers of butene in silicalite, butanols in ZSM-5, p-xylene in ferrierite, synthesis of $CoAlPO_4$-5 and $CoAlPO_4$-34 in the presence of template molecules, the elucidation of reaction mechanisms for oxidative coupling of methane on Li/MgO catalysts and reactivity of methanol at alumino-silicate Brønsted acide sites showing the great impact of computational methods in heterogeneous catalysis.

Zeolites. Another class of materials that can be studied using computer simulation are zeolites. In this class is included the ZSM-5 zeolite, which presents high catalytic activity coupled with excellent shape selectivity. Computer simulations can help to describe crystal structures and temperature induced phase transition (Yamahara 1995), atomic processes in thermal destruction of zeolites with different structures (Oumi 1995) or to study decomposition mechanism of NO on Cu-ZSM-5 catalyst models (Yokomichi 1995). For copper exchanged ZSM (Cu-ZSM-5) and mordenite (Cu-mordenite) were identified low-energy configurations for copper ions within the system. In case of Cu-ZSM-5 catalyst a model for the active site configuration and its location for NO decomposition was proposed (Sayle D. C. 1997bc, 1998b, Nachtigallová 1999).

Polymers, proteins and drugs. Computer simulation techniques can provide detailed information about polymer structures, sequence distribution in direct relation to the thermodynamic and mechanical properties (Madkour 1997), sorption of gas molecules into a polymer film (Ito 1998) or diffusion of small molecules in amorphous polymers (Li 1997). In the case of

proteins, information about structure, folding in position of global minimum under physiological conditions or aminoacids sequence in protein chain can be obtained with help of simulation techniques. Another application of theoretical studies is in pharmaceuticals where the interaction of new drugs with DNA and enzymes can be established prior to pharmacological testing (Leach 2001).

2. Methodology

2.1. Potential Models

To ensure that the surface and interface calculations reflect the system under study, it is necessary to use an appropriate potential model to describe the interactions in the crystal.

The types of potential model can be divided into two main categories. First are *molecular mechanical forcefields* in which the energy is given as a function of bond lengths, angles, torsional planes and other cross-terms, which are described explicitly for the particular system, and therefore different potential forms exist for each system. The second approach focuses on atoms or ions rather than bonds and is particularly useful for extended solids where bonds are not defined specifically, although the potential contains two-body and if is necessary three-body terms. The *Born model potential for ionic solids* provides an example of this later category.

For the simulation studies performed in this work, the Born model for ionic solids (Born 1954) was employed, with integer charges assigned to each ion corresponding to their formal oxidation state.

The lattice energy is defined as 'the energy of the crystal with respect to component ions at infinity' (Catlow 1987), and is given by:

$$E_L = \sum_{ij} \frac{q_i q_j}{r_{ij}} + \sum_{ij} \Phi_{ij}(r_{ij}) + \sum_{ijk} \Phi_{ijk}(r_{ijk}) + \ldots, \qquad \textbf{(2.1)}$$

where q_i, q_j represent the charges for ions *i* and *j* respectively,

r_{ij} is the distance between ions *i* and *j*,

r_{ijk} include distances between ions *ij*, *ik* and *jk*,

Φ_{ij} refers to all pairs of ions *i* and *j* interactions (two-body term) and

Φ_{ijk} refers to all trios of ions *i*, *j* and *k* interactions (three-body term).

In this equation it is possible to include terms involving a larger number of ions, but in practice it is rare to continue the summation beyond the three-body terms and in most of the studies, including this present work, even this term is omitted. Three-body terms depend upon the deviation of the bond angle from an equilibrium value and are necessary to account for the vibrational properties of ionic materials, but their contribution to the lattice energy is small (Catlow 1987).

Many body potentials become important in systems where covalent bonds are present. Three-body interactions consider bonds between a central ion *i*, and two adjoining ions *j* and *k*, making a bond angle of θ (fig. 2.1), therefore the potential function can be represented by:

$$\Phi_{ijk}\left(r_{ijk}\right) = \frac{1}{2} k_{ijk}\left(\theta - \theta_0\right)^2, \qquad \textbf{(2.2)}$$

where k_{ijk} represents the force constant and

θ_0 the equilibrium bond angle.

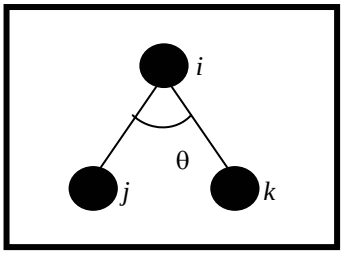

Fig. 2.1. *Bond type considered for three-body calculations.*

Four-body interactions, or torsionals, are used to model systems that have a planar structure due to π bonding. There are two planes defined between the ions *i*, *j* and *k* and between *j*, *k* and *l* separated by torsional angle φ, fig.2.2.

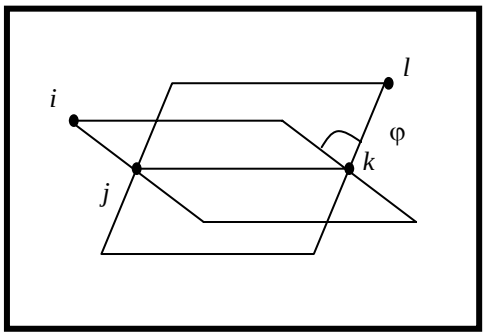

Fig. 2.2. *Quartet of ions and torsional angle in a four-body potential.*

The potential energy will be proportional to twice the angle between the planes, with a minimum when the angle is 0 or π radians according to equation:

$$\Phi_{ijkl}\left(r_{ijkl}\right) = k_{ijkl}\left(1-\cos n\varphi\right), \qquad \textbf{(2.3)}$$

where r_{ijkl} includes the distances between ions *i*, *j*, *k* and *l*

k_{ijkl} is the force constant and

φ the torsional angle between the two planes

n integer.

Three- and four-body interactions have been used to model successfully systems such as SiO_2, zeolites, $MgSiO_4$, $CaCO_3$, $BaSO_4$, benzene and proteins (Watson 1994 and references therein).

2.1.1. Coulombic term, $\sum_{ij}\frac{q_i q_j}{r_{ij}}$

The first term of equation 2.1, is the Coulombic term, which corresponds to the electrostatic interactions between pairs of ions *i* and *j* with charges q_i and q_j separated by a distance r_{ij}.

This term gives computational problems due to the long-range nature of Coulombic interactions, which converge very slowly, (as $1/r_{ij}$), in real

space. In the codes we used for our calculations the method developed by Ewald (1921) is employed to circumvent the slow convergence. The Ewald technique sums the electrostatic interactions in both real and reciprocal space, which leads to much more rapid convergence than by direct real space summation (see Appendix B). For all the calculations performed, a precision for the Ewald summation has to be established. In this thesis, by trialing each system investigated, it was established that a precision of 10^{-3} for the beginning of the simulation (dynamical simulation) and 10^{-4}, 10^{-6} for the end of the simulation (energy minimisation) was sufficient to obtain good structural and energetic results in concordance with the experiment. A precision of 10^{-6}, used throughout each simulation, would be prohibitive computationally for the systems considered in this work.

2.1.2. Short-range terms

The contribution from three-body terms to the lattice energy for the systems considered here is negligible. Consequently only two-body terms are included.

The two-body short range potential for ionic solids can be described by either Lennard-Jones or Buckingham forms. The Lennard-Jones potential is characterised by an attractive part dependent on r^{-6} and repulsive part dependent on r^{-12}, according to the equation:

$$\Phi_{ij}\left(r_{ij}\right) = \frac{A}{r_{ij}^{12}} - \frac{C}{r_{ij}^{6}} \qquad \textbf{(2.4)}$$

The potential employed in this thesis, which describes better non-bonding interactions in an ionic material is the Buckingham potential, in which the r^{-12} term of the Lennard-Jones potential is replaced by an exponential repulsive term (eq. 2.5). The Buckingham potential, includes both Pauli repulsion between neighbours due to the overlap of the electronic clouds, $A\exp\left(-r_{ij}/\rho\right)$, and van der Waals dispersive and covalent interactions, C/r_{ij}^{6}:

$$\Phi_{ij}(r_{ij}) = A\exp\left(-\frac{r_{ij}}{\rho}\right) - \frac{C}{r_{ij}^{\,6}} \qquad \textbf{(2.5)}$$

In equations 2.4 and 2.5, r_{ij} is the distance between ions *i* and *j* and A, ρ, C are parameters that can be derived for each material.

To reduce the computational expense the $C/r_{ij}^{\,6}$ term can be omitted with an adequate adjustment for the A parameter. In this case the potential function is known as Born-Mayer potential. The dependence between energy and distance in a crystal lattice is shown in figure 2.3.

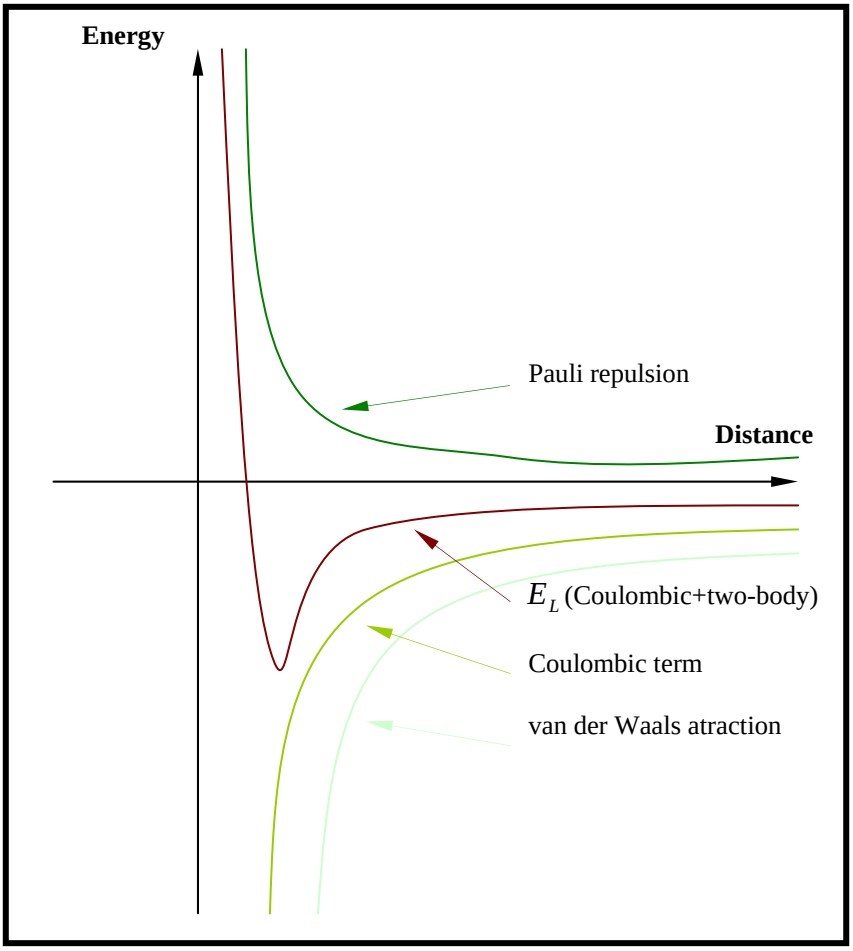

Fig. 2.3. *Energy-distance dependence.*

2.1.3. Ionic polarisability

When modelling defects, the electronic polarisation of the surrounding lattice cannot be neglected. One solution to this problem is to employ the shell model, developed by Dick and Overhauser (1958). This model makes a connection between the short-range interactions and ionic polarisation, and it is used when electronic polarisability of the free ion is significant.

The model considers that each ion has two components: a core with charge X in which the mass is concentrated, and a massless shell with charge Y, the two being connected by a harmonic spring. The formal charge of the ion is given by the sum between core and shell charges, X+Y. Figure 2.4 shows a schematic representation of the shell model.

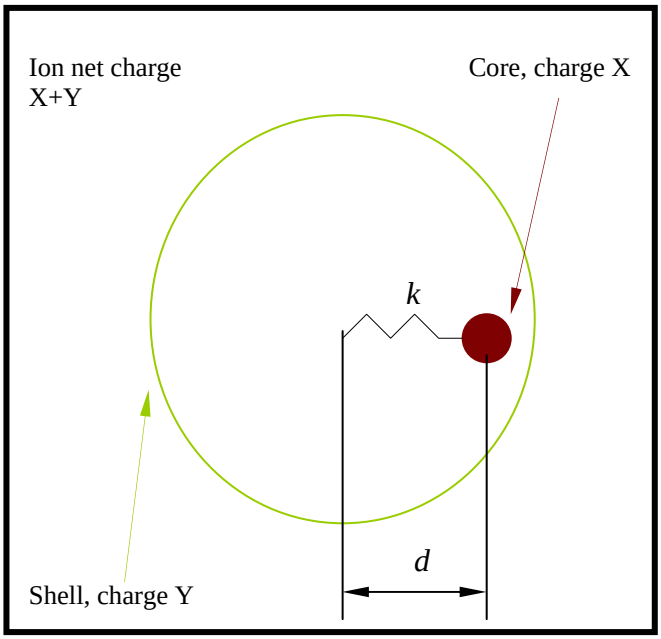

Fig. 2.4. *Schematic representation of the shell model.*

The core-shell energy is given by:

$$E_{core-shell} = \frac{1}{2} k d^2 , \qquad \textbf{(2.6)}$$

where k is harmonic spring constant and

d is the relative displacement of the core and shell.

The polarisability of the free ion is:

$$\alpha = \frac{Y^2}{K}, \qquad \textbf{(2.7)}$$

where $K = k + d$.

The parameters Y and k are obtained by empirical fitting to dielectric constants, elastic constants or phonon dispersion curves.

A disadvantage of using the shell model is that the calculations became considerably computational more expensive since the number of species effectively doubles.

During the amorphisation of an oxide thin film, defects that are likely to influence the structure are created. Since the available computational resources do not allow us, at present, to include shell model in our calculations, future studies will have to address this problem by including the electronic polarisability in the model.

2.1.4. Potential parameters

The potential parameters, A, ρ and C from the Buckingham equation and the shell charges, Y and spring constant k from the shell-core model of ionic polarisability can be derived principally using two methods. Since potential derivation is not one of the goals of this study, the methods used to calculate them are presented briefly.

- ***Empirical fitting***. Here the potentials are derived using a least squares fitting procedure to experimental data (adjusted iteratively until best agreement between experimental and calculated crystal properties) is reached. The experimental data may include for example, lattice constants, lattice energy, elastic constants, dielectric constants, piezoelectric constants and phonon frequencies. Derivation of these parameters is described in great detail in the literature (Catlow and Mackrodt 1982) with applications for ionic

materials (Lewis 1985, Lewis and Catlow 1985, Bush 1994, Gale 1996 and Telfer 1997). The potentials used in this work (for anion-anion and anion-cation interactions) were all fitted empirically and are presented for each system studied, with their sources, in chapters 3 and 4. Since cations are generally smaller than anions and anion-anion interactions are very small at equilibrium lattice spacing, cation-cation interactions are assumed to be purely coulombic. As more experimentally determined material properties become available, the accuracy of the calculated potential parameters increases, since there is more data with to fit. Specifically, for nucleation sites on the surface (e. g. edges, kinks and corners) bond distances will be different from bulk values. Therefore it would be appropriate to consider in future, potentials, which reflect lower coordinative saturation of such surface species.

- ***Non-empirical fitting*** with two approaches: *electron-gas method* and *ab-initio calculation*. The first one is based on methods developed by Wedepohl (1967) and applied by Gordon and Kim (1972) and considers electrons in an atom or ion as a degenerate Fermi gas. This method considers the electron density of a lattice of ions to be the sum of the electron densities of the individual isolated ions and interaction energy of pairs of ions as sum of four terms: Coulomb energy, electron kinetic energy, exchange energy and correlation energy, each of them being dependent upon the electron densities (Harding 1990 and Catlow 1987). This method has the advantage that it is computationally inexpensive. The second method uses a quantum-mechanical approach to calculate interatomic potentials (Elliott 1998). The advantage of these methods is that potential parameters can be calculated for systems where there is insufficient or unavailable experimental data. For example it might be used to derive potentials, which describe interatomic potentials during a growth process where there is unlikely to be any experimental data.

2.2. Theoretical Models

2.2.1. Energy minimisation

For almost all molecules with the exception of very simple ones, the potential energy is a very complex function depending on the coordinates. The way in which the energy varies with the coordinates is called the *potential energy surface* or *hypersurface* (Leach 1996), fig. 2.5.

During a simulation study we are interested in finding arrangements of ions, which correspond, to a stable state for the system, which is where an energy minimum is reached; any movement away from a minimum gives a configuration with higher energy. For every surface there will be a large number of minima. The minimum with the lowest energy is known as a *global minimum*, while all the others are called *local minima* (fig. 2.5). The minimisation of the energy for an ionic structure is a very important part of the simulation work.

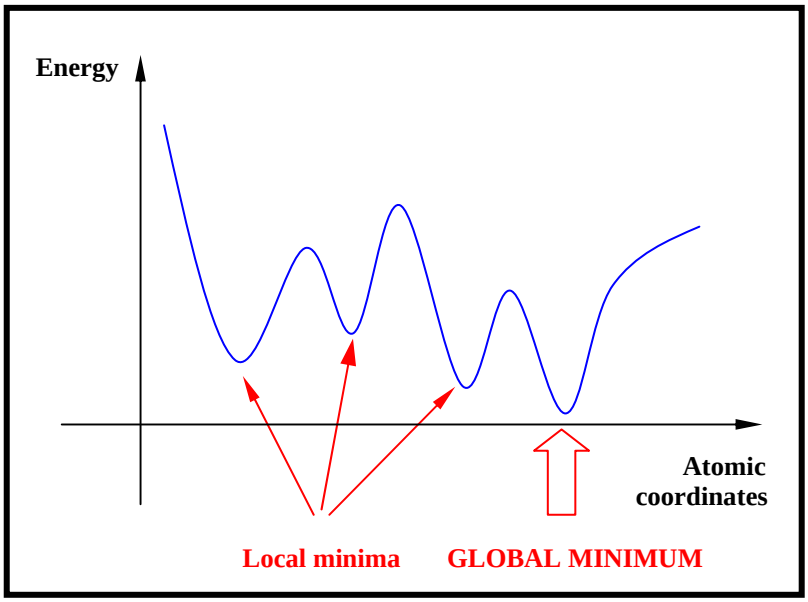

Fig. 2.5. *Schematic representation of a simple one-dimensional energy surface with local and global energy minima.*

During the energy minimisation the ion positions are adjusted until a minimum energy configuration is reached at zero Kelvin to obtain a more

stable structure. This means that is necessary to find a point for each ion where the force acting upon it is zero:

$$\frac{\partial E_L}{\partial r_i} = 0\,, \qquad \textbf{(2.8)}$$

where E_L is total energy of the system (potential energy)

r_i is coordinate system.

The commonly used procedures for energy minimisation are optimisation at constant volume, where the unit cell remains frozen (no variations in cell dimensions) and optimisation at constant pressure, in which both cell variables and ions coordinates are adjusted to remove forces on both the ions and the unit cell as a whole (Watson 1997).

For equation 2.8, iterative numerical methods are used to search for a minimum. There are many methods available, such as first-order minimisation methods including *steepest descent*, *conjugate gradients* and second derivative methods such as *Newton-Raphson* (Leach 1996 and Jensen 1999).

Steepest Descent: in this method, the gradient vector ($\vec{g}$) points in the direction where the function increases most, therefore the function value can be always lowered by stepping in the opposite direction along a search direction defined as $\vec{d} = -\vec{g}$. The starting point for each iteration is the molecular configuration obtained from the previous step, so the vector of variables x whose value is x_{k+1} for the $(k+1)^{th}$ iteration are directly related to the previous values determined for the $(k)^{th}$ iteration.

$$\vec{x}_{(k+1)} = \vec{x}_{(k)} - \alpha_{(k)} \left(\frac{\partial E}{\partial x} \right)_{(k)}\,, \qquad \textbf{(2.9)}$$

where $\alpha_{(k)}$ is a numerical constant chosen for each iteration in order to increase the efficiency of the procedure.

Conjugate Gradient method improves the steepest descent method by performing each line search not along the current gradient, but along a line which is constructed so that is 'conjugate' to the previous search directions (while in the steepest descent method both the gradients and the directions of successive steps are orthogonal, in conjugate gradients method, the gradients at each point are orthogonal but the directions are conjugated). The first step is equivalent to a steepest descent step, but subsequent steps are performed along a line, which is a mixture of the current negative gradient and the previous search direction:

$$\vec{d}_{(k)} = -\vec{g}_{(k)} + \beta_{(k)}\vec{d}_{(k-1)}, \qquad \textbf{(2.10)}$$

where β can be chosen from different mathematical expressions depending upon the gradient vector (Jensen 1999).

Newton-Raphson method employs the second derivatives to direct the minimisation ensuring a more rapid convergence. The minimisation proceeds according to the expression:

$$\vec{x}_{(k+1)} = \vec{x}_{(k)} - \vec{H}_{(k)}\vec{g}_{(k)}, \qquad \textbf{(2.11)}$$

where $\vec{g}_{(k)}$ is the gradient vector and

$\vec{H}_{(k)}$ is the inverse of the second derivative matrix, $W_{ij} = \dfrac{\partial^2 E}{\partial x_i \partial x_j}$.

According to this method, the $\vec{H}_{(k)}$ matrix is not recalculated every iteration, but instead is updated using algorithms such as Broyden-Fletcher-Goldfarb-Shanno and Davidon-Fletcher-Powell (Gay 1995 and Gale 1997), to reduce computational cost. The $\vec{H}_{(k)}$ is explicitly recalculated only after a defined number of iterations or if the minimiser has a sharp change in direction on the energy hypersurface.

The computer simulation codes used in this thesis take into consideration a combination of minimisation methods depending on the complexity of the system (Gay 1995 and Gale 1997). For our particular system, SrO/BaO(001), energy minimisation was performed using the MARVIN code, which employs a *quasi-Newton* technique.

2.2.2. Molecular dynamics

Molecular dynamics is used to explore more efficiently the potential *hypersurface* of a structure. Through this method it is possible to overcome potential barriers and explore many local minima. Some of them may reflect configurations, which are more stable than can be explored using energy minimisation alone. For example, during the energy minimisation an ion can became 'trapped' on a flat region of the surface (local minimum). During the molecular dynamics the ion can migrate on an edge (lower coordinated region), which corresponds to a more stable state.

In molecular dynamics, the equations of motion are solved iteratively for all particles to give the time evolution of a system using interatomic potentials to represent the forces within the system.

The force F on an atom can be evaluated directly from the first derivative of the potential energy, E, with respect of the coordinates, r, and can be implemented in Newton's second law of motion (2.12).

$$F = ma, \qquad \textbf{(2.12)}$$

which becomes:

$$-\frac{\partial E}{\partial r} = m\frac{\partial^2 r}{\partial t^2} \qquad \textbf{(2.13)}$$

There are many algorithms for integrating the equations of motion, such as Verlet, Verlet leap-frog, velocity Verlet, Beeman or Gear predictor-corrector algorithms, (Leach 1996). It has been shown that for short time steps the predictor-corrector method may be more accurate, but for longer time steps the Verlet algorithm may be better (Leach 1996). A few considerations about Verlet leap-frog algorithm will be presented since the

molecular dynamics calculations in DL_POLY code are all based on this integration method (Smith 1999).

All the algorithms assume that the position and dynamical properties (e. g. velocity, acceleration) for each atom can be approximated as Taylor series expansions:

$$r(t+\partial t) = r(t) + v(t)\partial t + a(t)\frac{\partial t^2}{2}... \quad \textbf{(2.14)}$$

$$v(t+\partial t) = v(t) + a(t)\partial t + ... \quad \textbf{(2.15)}$$

Moreover, in the leap-frog algorithm it is assumed that the velocity, $v(t)$, is changing linearly during ∂t, therefore it can be calculated as an instantaneous velocity at $\frac{\partial t}{2}$. The following relationships are used:

$$r(t+\partial t) = r(t) + v(t+\frac{\partial t}{2})\partial t\,, \quad \textbf{(2.16)}$$

where

$$v(t+\frac{\partial t}{2}) = v(t-\frac{\partial t}{2}) + a(t)\partial t\,, \quad \textbf{(2.17)}$$

and the velocities at time *t* can be calculated from:

$$v(t) = \frac{1}{2}\left[v(t+\frac{\partial t}{2}) + v(t-\frac{\partial t}{2}) \right] \quad \textbf{(2.18)}$$

With velocities calculated using these relationships and the acceleration deduced from Newton's law of motion (eq. 2.12 and 2.13) the new atom coordinates can be calculated and updated.

Before the iterative process can be started, it is necessary to assign initial velocities to each atom. This can be done by random selection from a Maxwell-Boltzmann distribution at the temperature of interest:

$$P(v)\partial v = \left(\frac{m}{2\pi kT}\right)^{3/2} \exp\left(\frac{-mv^2}{2kT}\right) 4\pi v^2 \partial v, \qquad \textbf{(2.19)}$$

where $P(v)$ is the probability of velocity v

m is mass of particle

v is velocity of particle

T temperature and

K is Boltzmann constant.

Since the system is in motion, the temperature is directly related to the kinetic energy, so an expression for temperature in terms of velocity can de derived:

$$K = \frac{3}{2}kT \qquad \textbf{(2.20)}$$

$$T = \frac{mv^2}{3k} \qquad \textbf{(2.21)}$$

The total energy of the system can be represented as the sum of the kinetic energy and potential energy. With the kinetic energies defined in term of velocities, the total energy of a system with a given set of positions and velocities is given by:

$$E_{total} = \sum_{i=1}^{N} \frac{1}{2} m_i v_i^{\,2} + E(r) \qquad \textbf{(2.22)}$$

In dynamical calculations the choice of a time step in accord with the type of system and motion present is critical. The time step should be approximately one order of magnitude smaller than the fastest process in the system (Leach 1996 and Jensen 1999). Molecular motions, rotations and vibrations, typically occur with frequencies in the range 10^{11}-10^{14} s^{-1}, and

time steps of the order of ca. 10^{-15} seconds are required to model such motions with sufficient accuracy. If the time-step is too large, lattice vibrations will occur within the time step leading to big errors, while if the time step is too small the simulation will exceed the available computer time before the ions have moved a significant distance. In this study a time step of 5×10^{-3} ps was used in all calculations, which means that after each iteration, 5×10^{-3} ps, the coordinates, velocities, accelerations and energies are recalculated.

In this work we employ NVE microcanonical ensemble: constant number of particles N, volume V and energy E.

Molecular dynamics simulation is a powerful tool in materials science. It can be used to study time dependent properties such as diffusion (Fisher 1998, Suzuki 1998ab, Khan 1998 and Karakasidis 1999) phase stability, melting, defects (Jacobs 1997 and references therein) and to elucidate structural evolution of a thin film grown by atom deposition (Sayle D. C. 1999ab and 2000a) or evolution from an amorphous structure to a crystalline one with structural modifications that arise (Sayle D. C. 2000c, 2001a and Maicaneanu 2001ab). The latter is a new simulation methodology, which has been developed in this present work for fluorite structured systems.

2.2.3. Surfaces and interfaces simulation

To investigate the behaviour of ions in the bulk, and at surfaces and interfaces the **GULP** - **G**eneral **U**tility **L**attice **P**rogram (Gale 1997), **MARVIN** - **M**inimisation **A**nd **R**elaxation of **V**acancies and **I**nterstitials **N**ear Surfaces Program (Gay 1995) and **DL_POLY** (Smith 1999) codes were used.

GULP is a code used to simulate three-dimensional periodic systems (bulk crystal structures), to calculate materials properties and conversely to derive empirical potential parameters through least-square fitting. The code can be used also for structure optimisation through energy minimisation and to study defect structures in solid solutions (Balducci 1997). In this thesis the GULP code was used to calculate lattice parameters for SrO, BaO,

CeO_2, ZrO_2 and YSZ, based on values of potentials available in the literature and to calculate hybrid potentials (see chapters 3 and 4).

MARVIN is a computer code designed specifically for simulations of surfaces and interfaces employing two-dimensional periodic boundary conditions (PBC), fig. 2.6. PBC enable a simulation to be performed using a relatively small number of particles in such a way that the particles from the edges experience forces as if they were in the bulk. PBC describe periodicity in solids modelling and ensures the removal of the problems associated with edge effects. The simulation box containing the particles under study (blue and red balls in fig. 2.6) is replicated periodically through space to give an infinite 'lattice'.

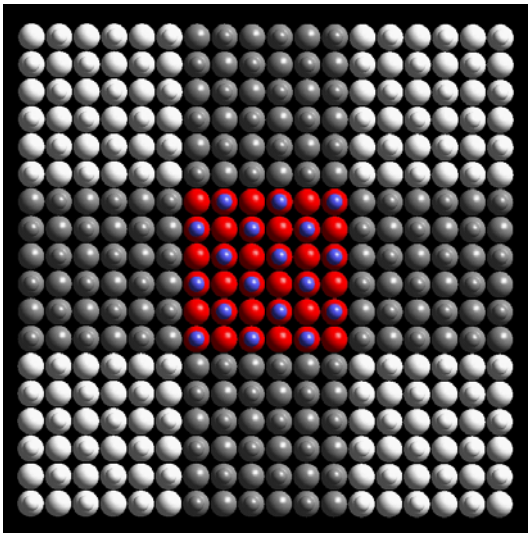

Fig. 2.6. *Representation of two-dimensional periodic boundary conditions employed in simulations performed with MARVIN code.*

If a particle is moving in the simulation box during the simulation under the action of interatomic forces, its image in all other boxes moves in exactly the same way. The size of the simulation cell must be chosen in such a way, to minimise the computational expenses whilst excluding the possibility for the apparition of any artificial strain in the lattice.

The simulation cell used, fig. 2.7, consists of one block for surface simulations and two blocks A and B for interface simulations, where block

B contains the supported thin film. Each block is divided in two regions: ions from region 1 are allowed to move under dynamics, or to relax under energy minimisation, whilst those from region 2 are held fixed relative to one another, but allowed to move as a whole in response to region 1. Ions included in region 2 ensure the correct crystalline environment for the lower ions in region 1.

MARVIN can perform both energy minimisation and dynamical simulations.

DL_POLY is a code designed to perform molecular dynamics simulations of macromolecules and biological systems, polymers, ionic systems, simple atomic systems and solutions on distributed memory parallel computers. The code was written to accommodate three-dimensional periodic boundary conditions, cubic, orthorhombic, parallelepiped, truncated octahedral, rhombic dodecahedral, slab and hexagonal prism. For interfaces studied using this code, cubic periodic boundary conditions (fig. 2.8) were employed. To represent the free surface within the three-dimensional periodic boundary condition regime, a void normal to the surface (ca. 55 to 75 Å in size) was introduced.

All DL_POLY molecular dynamical simulations were performed within the **NVE** ensemble with instantaneous velocity scaling to the simulation temperature used throughout.

Simulations were performed on a Silicon Graphics O2 Workstation with a R10000 processor for the calculations using the GULP code and on a Silicon Graphics Origin 2000 with 26 R12000 processors and 13 Gb of RAM memory, for MARVIN and DL_POLY codes. The simulations were performed using all 26 processors of the Origin, enabling very large systems to be considered. For the CeO_2/YSZ(111) system, the whole simulation procedure takes around three weeks (on 26 processors) to complete. The graphical analysis of the interfaces was made using MSI molecular graphics package (Cerius^2).

Fig. 2.7. *Representation of regional approach for surface and interface calculations in an ionic crystal.*

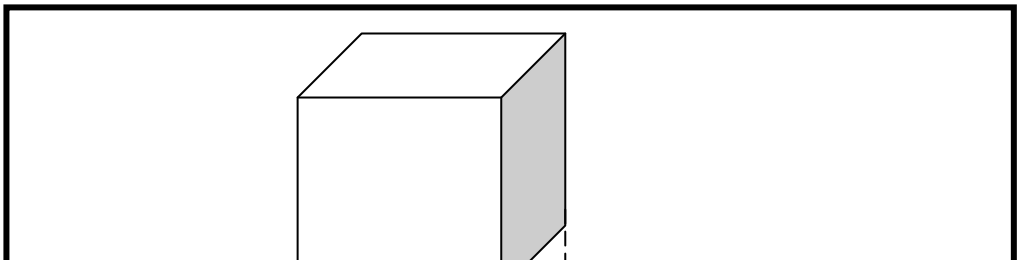

Fig. 2.8. *Schematic representation of three-dimensional cubic periodic boundary conditions employed for molecular dynamical simulation with DL_POLY code. Blue surface represents the surface under study.*

The stability of surfaces and interfaces considered in this study are characterized via the surface energy. For interfaces, the surface energy is given by:

$$\gamma = [E_{total}(hkl) - nE_{substrate}(hkl) - mE_{film}] / A(hkl), \quad \textbf{(2.23)}$$

where E_{total} is the total energy of the interface, [eV]

$E_{substrate}$ is the energy of the support, [eV]

E_{film} is the energy of the thin film, [eV]

A is the simulation cell area, [Å^2]

n, m represents the number of primitive unit cells within support and thin film respectively and

(hkl) Miller indices defining the particular plane of the support.

2.2.4. Interface construction

The thin film interfaces can be constructed in three ways: atom deposition, layer-by-layer epitaxial growth and cube-on-cube construction. Each methodology is now discussed in turn:

Atom deposition. In this case the interface is generated via the sequential deposition of individual ions onto the surface of the support until a thin film of required thickness is achieved (fig.2.9). An additional programme (Sayle D. C. 1998a) for the deposition was written to work in conjunction with the MARVIN code, which performed the minimisation and dynamical simulation. The programme introduces the ions that will form the thin film at random positions above the support surface and moves them vertically towards the surface until they are within 2.5 Å from the surface or any previously deposited species. Energy minimisation and/or dynamical simulation is then applied to the whole system. The process is repeated until the required thickness for the thin film is reached. A disadvantage of this method is that it is computationally expensive since the dynamical simulation is applied after each deposition step and therefore it cannot be use for large simulation cells or to create thin films of significant thickness. Conversely, using this method it is possible to obtain information about epitaxial growth mechanism, nucleation sites and to generate clusters at sub-monolayer deposition levels.

Layer-by-layer epitaxial growth. Here, the interface is created by sequential deposition of monolayers onto the support until the required thickness for the thin film is reached (fig 2.10). A monolayer is placed on top of the support and then dynamical simulation and energy minimisation are applied to the system. The cycle is repeated until the desired film thickness is reached (Sayle D. C. 2000a). Since the dynamical simulation is applied after the addition of each monolayer and not after each ion as in case of atom deposition, the procedure is less computationally expensive and therefore larger cells and thicker films may be simulated.

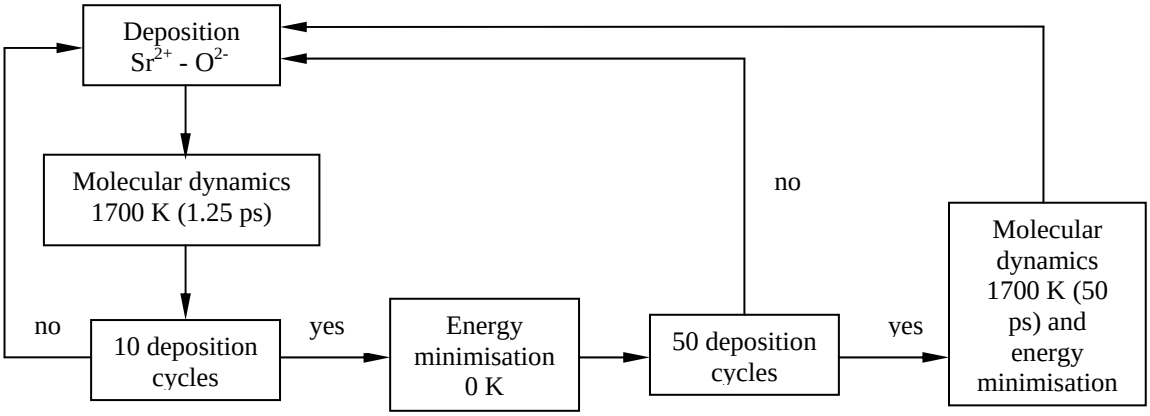

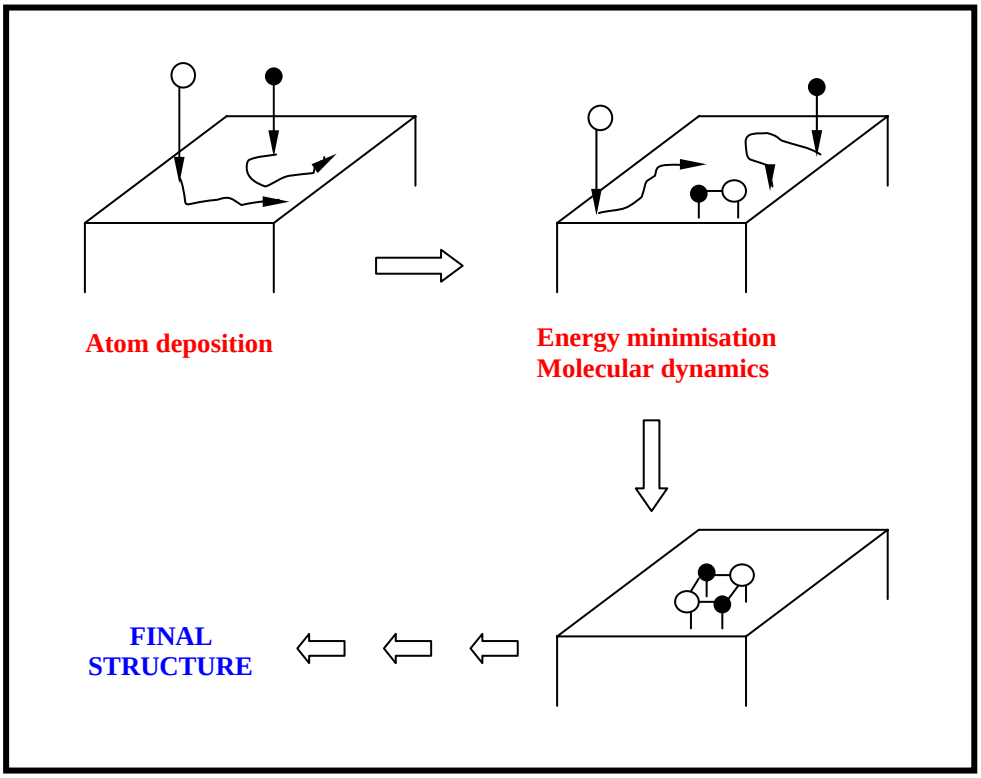

Fig. 2.9. *Representation of the atom deposition process for the SrO/BaO(001) system.*

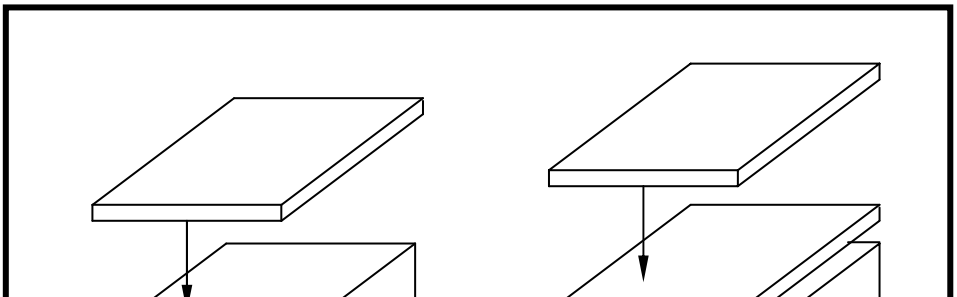

Fig. 2.10. *Representation of layer-by-layer methodology for interface building.*

Cube-on-cube construction. Here the interface is created by placing the whole thin film directly onto the support followed by dynamical simulation and energy minimisation (fig. 2.11). Since only a single dynamical simulation is performed, a much larger simulation cell may be used, allowing the formation and evolution of many misfit induced defects, such as dislocations, lattice slip and twist boundaries. Since the simulation cell used in atom deposition or layer-by-layer growth is to small to accommodate such defects, the cube-on-cube methodology offers a viable approach for elucidating their structure (Sayle D. C. 2000a).

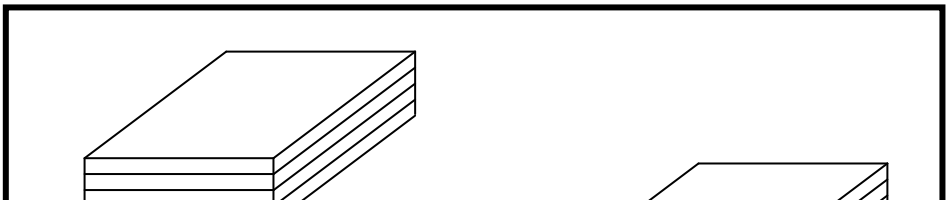

Fig. 2.11. *Schematic representation of cube-on-cube methodology for interface construction.*

In this work two systems are investigated: SrO/BaO(001) (negative misfit) using atom deposition and cube-on-cube methodologies and CeO_2/zirconia based materials (positive misfit) using a cube-on-cube methodology, which enables a much larger simulation cell to be considered.

Epitaxial considerations. To model an interface, the epitaxial relationship between the lattice parameters for the thin film and underlying support must be addressed. Here the thin film is constrained to accommodate the entire lattice misfit associated with the system. For example, the thin film may be placed directly on top of the support with cations and anions in the thin film constrained to lie directly above their respective counterions in the underlying support, which corresponds to a *coherent* structure (see Appendix C). For a ceria thin film deposited on yttrium-stabilized zirconia (YSZ), the support will maintain its natural lattice parameter (5.1 Å), whilst the ceria must be compressed from 5.4 to

5.1 Å to ensure coherence. The misfit associated with this configuration is +6.1%. To obtain coherence the thin film (ceria) needs to be compressed by 5.9%.

An alternative construction is to generate a *commensurate* structure. In our example, the incommensurate relationship between the ceria thin film and the YSZ support can be improved by placing, for example, a 13×13 ceria thin film on top of a 14×14 YSZ support, resulting in a lattice misfit of –1.3%. To accommodate the misfit, the ceria thin film must be compressed by –1.3%.

A variety of commensurate configurations with different lattice misfits can be constructed in this way. Near coincidence site lattice theory (NCSL) (Sutton 1987, Sayle T. X. T. 1993) can also be used to generate alternative configurations with a range of low associated misfits including rotations of the thin film with respect to the support or various (hkl)/(h'k'l') combinations.

Once the initial configuration has been generated, the system can then be simulated using static or dynamical methods.

We now describe a new simulation methodology, 'simulated amorphisation and recrystallisation', which eliminates the need for starting structures.

2.2.5. Amorphisation and recrystallisation methodology

Simulated amorphisation and recrystallisation is based upon the cube-on-cube methodology described above, with the thin film strained under considerable compressive or tensile stress (fig. 2.12).

To generate models of supported oxide thin films that are more realistic, various structural features, including epitaxial relationships and various defects must be introduced within the model. The defects, which evolve in response to misfit accommodation, may include dislocations arrays, vacancies, substitutions and interstitials including clustering of such defects. All these type of defects will evolve and act to reduce the lattice misfit thereby stabilizing the thin film. For catalytic systems, these defects will, in part, be responsible for the catalytic properties of these materials. However, simulations based upon the initial configurations generated by

some particular NCSL are very unlikely, under dynamical simulation, to surmount the energy barriers required to facilitate the formation of these defects. This is because the energy barriers to evolve for example a dislocation within a crystalline material are likely to be very high and therefore the duration of the dynamical simulation required to obtain such a structure would be prohibitively large. Consequently, this approach becomes untenable in generating a realistic model for a catalytic system like CeO_2/YSZ or indeed any supported thin film.

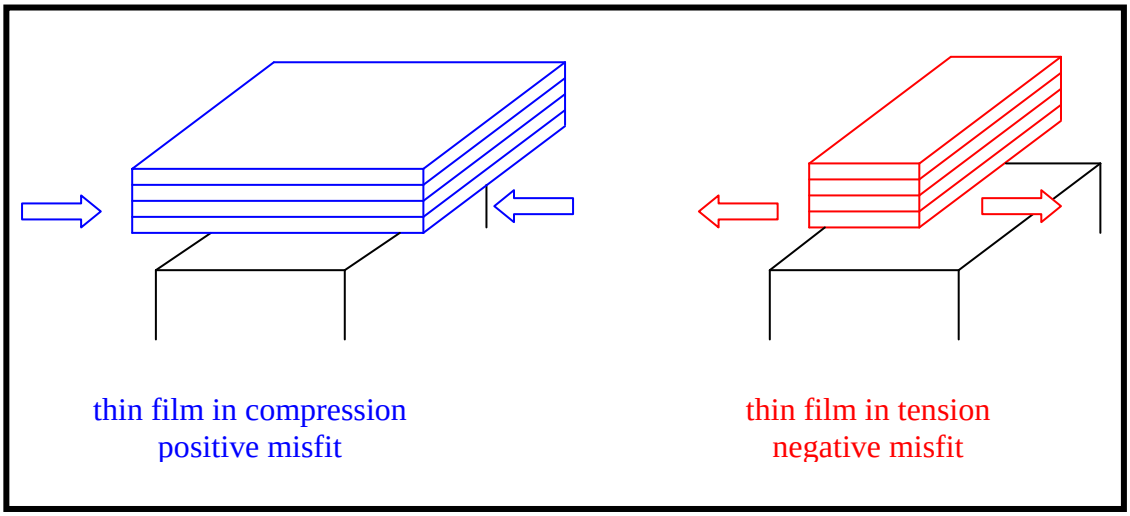

Fig. 2.12. *Schematic representation of positive and negative misfit between thin film and support.*

To address this problem one might consider introducing each of the structural features 'by hand' and than simulating this 'trial system' using energy minimisation or dynamical methods. However, such an approach is no longer appropriate since, for example, the nature, location and concentration of the dislocation arrays and associated defects presents a prohibitively large number of permutations to consider. In addition, the inclusion of a dislocation will influence the structure of neighbouring dislocations. The model must therefore also include the synergy of interaction of each of the structural features present in the system and the effect such synergistic interactions have on each of the structural features

present within the system. Therefore, we require an approach whereby the simulation, will allow a natural evolution of all structural features that would exist within a real system. Moreover two additional factors that arise when simulating interfaces at the atomic level must be satisfied. First, the simulation cell must be sufficiently large to accommodate the incommensurate nature of the system (Schnitker 1998) and second, the final structure should not be influenced by the starting structure. For example, if the initial configuration were erroneous, any final structure, which reflects structurally the preparatory configuration, would also be suspect. Accordingly, 'amorphisation and recrystallisation methodology' was developed (Sayle D. C. 1999c and 2001a) to solve the problems discussed above.

Simulated amorphisation and recrystallisation involves forcing the thin film to undergo a transformation into an amorphous state prior to recrystallising and therefore the recrystallisation process rather than the initial structure will dictate the final structure. In addition, the recrystallisation process is controlled by the interaction between the amorphous thin film and the substrate, which does not undergo an amorphous transition. Central to this methodology is that the dynamical simulation, as applied to amorphous structures, allows a more comprehensive exploration of the configurational space due to the high-energy amorphous starting point and the conformational freedom this gives rise to. In particular, the initial strain under which the thin film is constrained is critical in generating the desired high-energy amorphous transition. If the strain is too low, the system may not go amorphous and therefore no structural modifications will evolve. Alternatively, for greater but still inadequate initial strain the system will go amorphous, although the amorphous structure may have insufficient energy to allow complete exploration of the potential hypersurface. Here the procedure may result in certain regions, which remain amorphous (Sayle D. C. 2001c). Conversely, if the initial amorphous inducing strain is too large, the velocities of the ions will be so high such that the thin film will loose all integrity and the simulation will fail catastrophically.

Preliminary calculations, using various trial starting structures have to be performed for each system since it was observed that the initial strain required to induce adequate amorphisation is system dependent. For simple binary oxides the tolerances are high and a wide range of strains are valid, while for systems with fluorite structures, it was found that the tolerances are narrow.

Since the amorphous solid can explore its flatter potential energy surface more readily than starting from a crystalline solid, the dynamical simulation is capable of surmounting energy barriers to enable the thin film to accommodate appropriate (energetically favourable) structures. These include the epitaxial relationships with respect to the underlying support together with a range of defects, such as dislocations, grain-boundaries, vacancies, interstitials, and reduced interfacial ion densities including intermixing of ions across the interface, which evolve to lower the energy (Sayle D. C. 2000bc).

In the following chapter the SrO/BaO(001) system is considered. The interface was generated using atom deposition and cube-on-cube methodologies. Characterisation of the interfaces obtained using both methods was performed using graphical techniques.

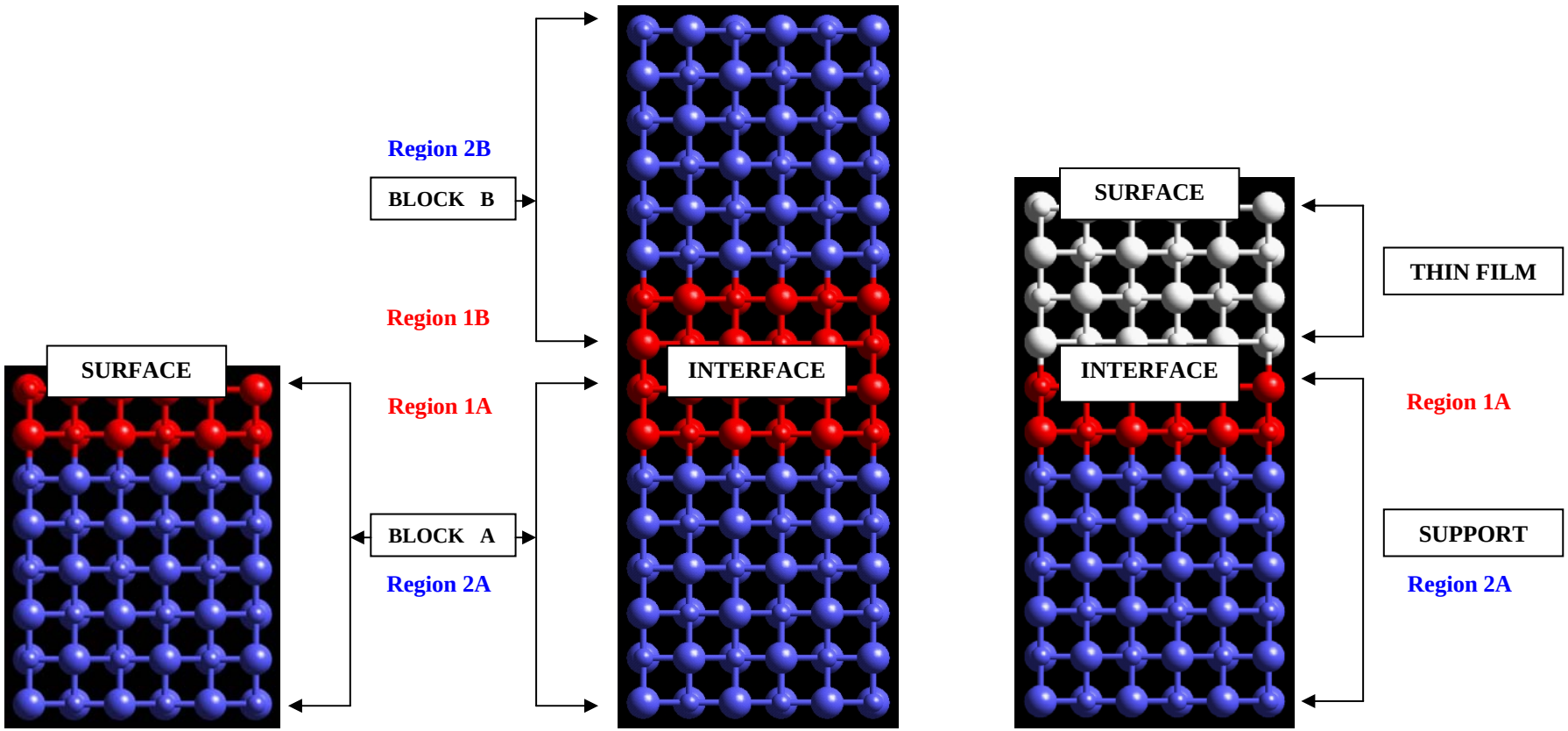

Fig. 2.7. *Representation of regional approach for surface and interface calculations in an ionic crystal.*

3. SrO/BaO(001) interface

3.1. Introduction

The aim of this chapter is to investigate the growth and structure of the SrO/BaO(001) system obtained using atom deposition and cube-on-cube construction.

3.1.1. Lattice simulation of oxide-oxide interfaces

The construction of well-defined oxide-oxide interfaces are of great importance in many technological areas including electronic, magnetic, optical and catalysis. Computer simulation techniques can provide useful structural information at the atomistic level of these types of interfaces. Such information can help explain experimental results or provide new structural insights regarding, for example the interactions at an interface between two oxide materials.

Various simulation methods have been employed to generate oxide-oxide interface these include atom deposition, NCSL, amorphisation and recrystallisation and are presented with a few examples in the following section.

Atom deposition methodologies. The molecular dynamics code, developed by Kubo (1994), see chapter 1.2, and used initially to simulate the growth process of ultrafine metal particles on metal oxide surfaces was used also to simulate the homoepitaxial and heteroepitaxial growth of oxide materials on oxide substrates such as MgO/MgO(001), (Kubo 1997c), $SrTiO_3$/$SrTiO_3$(001), (Kubo 1998a), ZnO/ZnO(0001), (Kubo 2000) and SrO and BaO/$SrTiO_3$(001), (Kubo 1997d, 1998b).

In this earlier work, Kubo and co-workers studied the homoepitaxial growth of MgO on MgO(001), realised at 300 K and 1000 K. At 300 K, where the surface diffusivity is low, molecules remain at the position where they hit the surface and clusters are formed on the surface. During the MgO deposition, molecules retain the rocksalt type structure and the (001) plane remains exposed at the surface, although some defects were observed.

Increasing the temperature, a smooth and flat MgO thin film was formed and layer-by-layer homoepitaxial growth was observed.

In the case of SrO and BaO deposition on $SrTiO_3$ the molecular dynamical simulation was performed in order to predict an appropriate buffer layer for the $YBa_2Cu_3O_{7-x}/SrTiO_3$ heterojunction. Two-dimensional and epitaxial growth of the SrO thin film was observed on the $SrTiO_3$(001) surface whilst maintaining the perovskite type structure and (001) oriented configuration. Some defects can be formed in the thin film at 300 K, while at 713 K a monoatomically flat and smooth layer, without any defects was formed. Conversely, BaO deposition on the $SrTiO_3$(001) attached directly to the TiO_2 atomic plane, led to the formation of films with high stress. If the SrO layer is introduced first, a smooth BaO/SrO/$SrTiO_3$(001) system can be fabricated with no interfacial stress, suggesting that the BaO/SrO layer is an appropriate buffer layer for the $YBa_2Cu_3O_{7-x}/SrTiO_3$ system.

In the case of ZnO(0001) homoepitaxial growth it was found that at 700 K on a smooth surface, adsorbed ZnO molecules, are quickly evaporated, suggesting that ZnO thin films rarely grow from the smooth ZnO(0001) surface. On a surface containing a step, the first ZnO molecule is bonded at the step, while the second attaches such that a new step is formed (step flow mechanism). The process continues in the same manner until the step is lost.

Another approach for sequential deposition was developed by Sayle D. C. (1997a, 1998a), and was used to simulate the growth of NaCl clusters on MgO(001) substrates (Sayle D. C. 1997a), CaO/SrO interfaces (Sayle D. C.1998a, 1999a), homoepitaxial growth of SrO, BaO/SrO(001) (Sayle D. C. 1999a), CaO/MgO(100), MgO/SrO(100), SrO/MgO(100), BaO/MgO(100), SrO/CaO/MgO(100) and $Ba_{0.5}Ca_{0.5}O$/SrO/(100) systems (Sayle D. C. 1999b) and to examine the influence of the misfit on the structure and stability of epitaxial thin films. It was shown that deposited materials form clusters on the support, reproducing the structure of the underlying substrate. It was also observed that perfect monolayer coverage does not occur; rather a second layer starts to evolve before the previous one is complete for both negative and positive misfits. Misfit accommodation is realised via crack formation, for negative misfit and dislocations in the case

of a positive misfit. The surface of the support exposed, on which the deposition process is conducted, plays a significant role in determining the growth of the thin film (Sayle D. C. 1998a, 1999a). In the case of CaO deposited on SrO, the flat SrO(001) surface yields the most coherent films, consistent with the rocksalt structure, while SrO surfaces, exposing a high concentrations of steps or surface roughness, perturb the CaO growth leading to poorer quality films (Sayle D. C. 1998a).

Another way to compensate for the misfit is via a rotation of the thin film with respect to the support as in the case of BaO/MgO(100), +27% misfit, and CaO/MgO(100), +13% misfit, where rotations and dislocations were observed (Sayle D. C. 1999b). The influence of the lattice misfit over the structure of the thin film can be controlled with implications for final properties of the thin film. If a buffer layer of CaO is included in the SrO/MgO(100) system a coherent SrO thin film structure can be obtained in contrast to the amorphous structure observed without a buffer. Also, pseudomorhic growth can be realised. For example calcium and barium deposited in equal portions onto the SrO(100) support, the lattice parameter was modified sufficiently to ensure a perfect growth in contrast with dislocations observed for the undoped BaO/SrO(100) system.

The disadvantage of the deposition method is that it is computationally expensive and therefore cannot be used for large simulation cells or to create thin film of significant thickness. A method that enables the use of larger simulation cells, where misfit induced defects such as dislocations, lattice slips or grain boundaries can evolve, is the deposition of a layer until a thin film is formed (Sayle D. C. 2000a) or deposition of a whole thin film on top of a support. The thin film-support matching can be realised using near-coincidence site lattice theory, NCSL, or by fitting using compression or expansion (see Appendix B).

NCSL methodology. NCSL theory was used to generate BaO/MgO(100), MgO/MgO(100), CeO_2/Al_2O_3(0001), (Sayle T. X. T. 1993, Sayle D. C. 1995b), V_2O_5/TiO_2 (Sayle D. C. 1996a) interfaces to elucidate the interfacial stability and interfacial configurations. It was found that for the BaO/MgO(100) and CeO_2/Al_2O_3(0001) systems, the stability of the interfaces is strongly dependent opon the mismatch and the misorientational

angles of the two incommensurate lattice structures as well as on the initial orientations of the ions and their relaxation at the surface (Sayle T. X. T. 1993). For the V_2O_5/TiO_2 system, it was found that V_2O_5 thin films exhibit remarkable structural modifications compared with the unsupported V_2O_5, with important implications for catalysis (sorption properties and oxygen storage capacity). One important modification consists of changes in the surface vanadyl O-O bond distances, which the authors suggested were dependent upon the thickness of the supported thin film.

Amorphisation and recrystallisation methodology. In the case of SrO deposited on MgO(100), the SrO thin film is forced to accommodate a +20% misfit (Sayle 1999c, 2000a). The thin film, initially constrained under compresion due to the misfit, undergoes an amorphous transition and then recrystallises (see chapter 2) back to its natural lattice parameter. During the recrystallisation process, structural modifications including mixed screw-edge dislocations, lattice slip and low angle rotations of particular crystalline regions within the supported thin film were evolving and were identified in the system.

The same method (amorphisation and recrystallisation) was used to simulate MgO/BaO(001) system. Here the MgO thin film is forced to accommodate a -27% misfit, (MgO lattice parameter is smaller than BaO), (Sayle D. C. 2000b) and amorphisation is tension induced. In this case the major structural features observed were the presence of misoriented nanocrystallites separated by grain boundaries and rotated, with respect to the underlying support, by various angles; dislocations and vacancies were also observed. CaO/MgO(001), SrO/MgO(001) and BaO/MgO(001) systems were also studied using the same method (Sayle D. C. 2000c, 2001a). It was found that a larger system allowed many structural modifications to be presented within a single simulation cell: screw-edge and pure edge dislocations, vacancies, interstitials and substitutions, lattice slip, coherent domains, commensurate regions and low angle rotated domains.

The study was extended to include the oxide-perovskite systems. Specifically, $MgO/SrTiO_3$ and $BaO/SrTiO_3$(001) interfaces were investigated (Sayle D. C. 2001b). Again the thin film is forced to undergo a

controlled amorphous transition prior to recrystallising. It was found that different structural characteristics evolve in each system due to the difference in lattice parameter. In the $MgO/SrTiO_3(001)$ system, +7.4% misfit, the MgO thin film is oriented at 0º with respect to the underlying $SrTiO_3$, while BaO undergoes a rotation of 45º. For the $BaO/SrTiO_3$ system, the lattice misfit is reduced from +34% to –0.3%. Also the structural characteristics of the thin film are critically dependent upon the plane exposed at the interface by the $SrTiO_3$ support (either SrO or TiO_2). For the $MgO/SrTiO_3(001)$, SrO terminated, the lattice misfit is accommodated by the presence of dislocations, while in the case of TiO_2 terminated $SrTiO_3$, some regions of MgO accommodate a 'pseudohexagonal' type structure. For the $BaO/SrTiO_3(001)$ system, the BaO thin film comprises a high concentration of dislocations when supported on TiO_2 terminated $SrTiO_3$, while for the SrO terminated $SrTiO_3$ no dislocations are present in the thin film.

All these remarkable results, which are, in part, supported by experiment (Jia 2001) show how simulation can offer a powerful complementary technique to experiment.

3.2. Simulation study of the SrO/BaO(001) interface

The calculations presented in this chapter are based on the Born model for ionic solids, as was described previously, using a rigid ion model to reduce the computational expense. The potential parameters employed in this study to model the SrO thin film and underlying BaO support were taken from Lewis and Catlow (1985) and are presented in table 3.1. For all the surface simulations undertaken in this section, the MARVIN code was used to construct the BaO(001) surface, SrO/BaO(001) interface and to perform both the energy minimisations and molecular dynamical calculations.

BaO and SrO are both ionic solids, which adopt a rocksalt type structure. Full cell parameters, calculated using the GULP code, based on potentials presented above, and experimental data are listed in table 3.2. Calculated lattice parameters are therefore in good agreement with the

experimental data. The lattice for both oxides is face-centred cubic, with each M^{2+} cation surrounded by six O^{2-} anions in a regular octahedral arrangement. The misfit between the two materials calculated using equation B.1 (Appendix C) is –6.7 %. The misfit between the two materials that form the interface is critical, and give rise to many structural modifications. Clearly, high accuracy of the lattice parameters is essential to ensure that the misfit is correct.

Construction of the SrO/BaO interface was achieved using two methods: atom deposition and cube-on-cube construction as described in chapter 2. For cube-on-cube construction, the SrO thin film was placed directly on top of the support (*coherent* structure), therefore to accommodate the misfit, the SrO thin film must be compressed by –6.9%, (eq. C.2 Appendix C).

Considering the two-region approach used in the MARVIN code, for our system, block A will contain BaO and region 1 of block B will contain the SrO thin film, figure 3.1.

Table 3.1. Short-range potential parameters used in the simulation study (Lewis and Catlow 1985).

Ionic pair	**A [eV]**	**ρ [Å]**	**C [eV·Å^{-6}]**
Ba^{2+} - O^{2-}	931.70	0.3945	0.00
Sr^{2+} – O^{2-}	1400.00	0.3500	0.00
O^{2-} – O^{2-}	22764.30	0.1490	27.89

Table 3.2. Full cell parameters for SrO and BaO (Bever 1986).

	a = b = c	
	Exp.	**Sim.**
BaO	5.5393	5.52
SrO	5.1602	5.16
	α = β = γ	
BaO	90°	
SrO	90°	

Fig. 3.1. *Representation of the 10×10 simulation cell. Barium is coloured orange, strontium is blue, oxygen (BaO) is red and oxygen (SrO) is green.*

3.2.1. The structure and characterisation of the SrO/BaO(001) interface generated via atom deposition

To explore the growth of a SrO thin film, strontium and oxygen ions were deposited in accord with the procedure described previously on two simulation cells of different sizes. Considering the PBC approach used in MARVIN code, if the simulation cell is too small the interactions between neighbouring cells (images) will influence artificially the thin film structure. Conversely if the simulation cell is too big, the numbers of species becomes prohibitively large and therefore computationally too expensive. Therefore, in this work, the deposition was performed on a 10×10 BaO(001) surface, and on a 14×14 BaO(001) surface, in order to observe how the simulation cell size might influence the growth process. The 10×10 and 14×14 refer to the size of the simulation cell. For example, the 10×10 corresponds to ten ions or five BaO units, for each side of the simulation cell. For the 10×10 simulation cell, each lattice plane comprises 100 ions (50 barium and 50 oxygen ions), whereas the 14×14 simulation cell has 196 ions per layer (98 barium and 98 oxygen ions). The surface areas of the simulation cells are 760 $Å^2$ and 1489 $Å^2$, respectively.

After the deposition of each Sr^{2+}-O^{2-} pair, (fig.2.9), dynamical simulation at 1700 K with a time step of 5×10^{-15} s (250 equilibration steps) was applied to the whole system, (which includes both the support and deposited species) to direct the deposited ions into low energy configurations. After each 10 deposition steps (10 SrO species) energy minimisation was performed until 200 SrO species were deposited, the process was then continued with energy minimisation performed every cycle. The process was repeated until a thin film, five layers thick was formed on the support for the 10×10 simulation cell. Conversely an equivalent of only two monolayers was deposited on the support for the 14×14 simulation cell, due to the much higher computational cost of this simulation.

As was mentioned before, dynamical simulation was performed for 250 steps after each deposition cycle (one SrO species). Although 250 dynamical simulation iterations are insufficient to enable adequate mobility

of ions after each deposition, its cumulative effect after depositing, for example 250 SrO species, 62500 iterations, might be sufficient to lead the system to a lower energy configuration. This methodology could be improved if: (a) – dynamical simulation is performed at a higher temperature for the same number of iterations (250) when ionic mobility is increased, allowing the structure to overcome certain energy barriers, or (b) – some structures obtained during the deposition process are subjected to long term dynamical simulation until energy convergence and then the deposition process is restarted.

The deposition programme was run twice for both simulation cell sizes, to explore structurally any differences that might appear owing to the random nature of the deposition process. Two sets of structures named 10×10.1, 10×10.2 and 14×14.1, 14×14.2 were thus obtained. Clearly, many more runs would improve the statistical sample. However, the high computational cost of generating such a sample is, at present, prohibitive.

For different coverages*, the structures obtained during the deposition cycles were subjected separately to long term dynamical simulation at 1700 K and energy minimisation to ensure convergence. The structures were chosen in such a way to follow the growth of the thin film. For the 10×10 simulation cell, structures were obtained after the deposition of 21, 50 or 49 for the 10×10.2 system, 100, 150, 200, 225 and 250 SrO species. For the 14×14 simulation cell, structures obtained after the deposition of 19(18 for 14×14.2 set), 50, 87, 100, 150, 196 (198 for 14×14.2 set) were considered.

When a larger simulation cell is used, many simulations at low coverages can be performed. For example if there are 18 SrO species deposited on a 14×14 support, only 9.18% of the surface is covered, while on a 10×10 support 18% of the surface will be covered, therefore on a larger simulation cell deposition process can be continued for longer at submonolayer level. In this way more information about evolution and

* Coverage is defined as the ratio between the number of Sr^{2+}-O^{2-} pairs deposited and the number of Ba^{2+}-O^{2-} pairs comprising a single layer of the support within the simulation cell (table 3.3).

structure for a wide variety of clusters can be obtained. Also energy terms arising from artificial cluster-cluster interactions across the periodic boundary will be reduced for larger cells.

The surface energies for the final structures were calculated using equation (2.23), (table 3.3) and the structures obtained were analysed using graphical techniques (Cerius^2) and radial distribution functions (RDF).

Table 3.3. Thin film energies as a function of coverage.

SrO species deposited 10×10 cell	**Coverage**	**γ, [J/m^2] 10×10.1**	**γ, [J/m^2] 10×10.2**
21	0.42	1.00	1.01
49	0.98	-	1.22
50	1.00	1.23	-
100	2.00	1.37	1.49
150	3.00	1.64	1.80
200	4.00	1.79	2.01
225	4.50	1.88	1.94
250	5.00	1.83	1.87
SrO species deposited 14×14 cell	**Coverage**	**γ, [J/m^2] 14×14.1**	**γ, [J/m^2] 14×14.2**
18	0.18	-	0.72
19	0.19	0.73	-
50	0.51	0.92	0.97
87	0.89	1.11	1.18
100	1.02	1.17	1.19
150	1.53	1.35	1.36
196	2.00	2.12	-
198	2.02	-	1.56

3.2.1.1. SrO/10×10BaO(001)

As was described above, for the 10×10 simulation cell, the growth process was performed twice until an equivalent of five monolayers had been deposited. 'Snapshots' of the evolving SrO thin film for the 10×10.1, are presented in figure 3.2 (each picture comprises nine simulation cells).

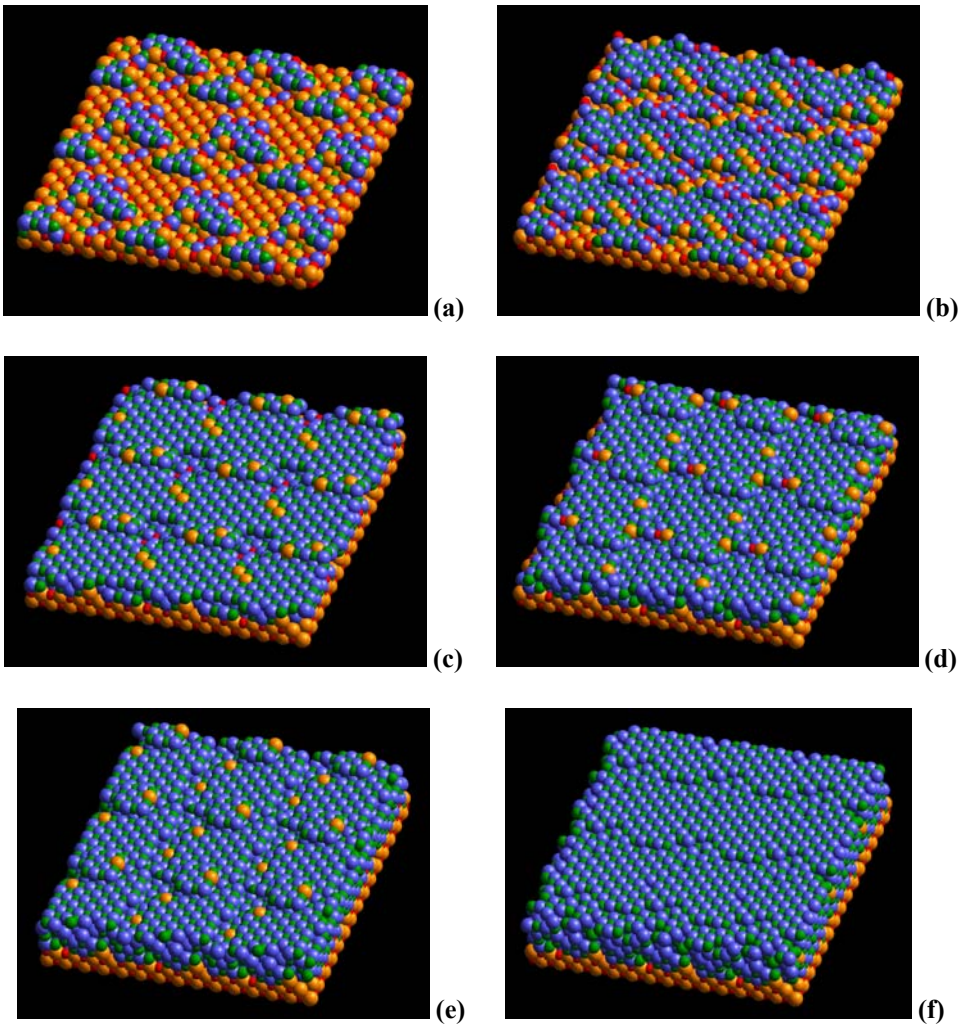

Fig. 3.2. *Representation of the SrO/BaO(001) system after the deposition of (a) 0.42, (b) 1.0, (c) 2.0, (d) 3.0, (e) 4.0 and (f) 5.0 equivalent SrO monolayers onto a 10×10 BaO(001) support. Notation as in figure 3.1. To preserve clarity only two planes from the support are represented.*

21 SrO. After the deposition of 21 SrO species, figure 3.2a and 3.3, the SrO was observed to form clusters on the BaO surface, with the Sr and O species lying almost directly above their respective counter-ions in the support. Accordingly, the SrO clusters accommodate a rocksalt type structure and exhibit the (001) plane at the surface. Growth of small clusters on the surface, as opposed to the formation of isolated and dispersed Sr and O species, suggests that the clusters provide energetically favourable nucleation sites for the adsorption of Sr and O species compared with a 'clean' BaO surface in accord with previous studies (Shluger 1995ab). Also the shape of the clusters (bridged clusters) was observed to be similar for both simulations performed (figure 3.3), suggesting that the random nature of the deposition process does not influence significantly the resulting structures. Two trials are therefore representative considering that molecular dynamics and energy minimisation are sufficient to drive the system in low energy configurations, when higher energy local minima are overcome.

A closer inspection of the system comprising 21 SrO species deposited on a 10×10BaO(001) support reveals that a number of barium ions from the support exchange for strontium ions from the clusters. The same behaviour can be observed for oxygen ions, which are also migrating across the interface (oxygen from the BaO support is labelled O and oxygen from SrO thin film is labelled O1). To illustrate this, the ion distribution as a function of lattice plane is presented in table 3.4. The importance of ions interchanges between thin film and support will be discussed later.

Calculated SrO bond distances range from 2.30 Å, at the cluster edge, to 2.57 Å at its centre with an interfacial separation varying between 2.35 and 2.57 Å. The natural SrO bond distance is 2.58 Å. The shorter bond distances on the edge of the clusters reflect the low coordinative saturation of ions from these regions. BaO bond distances, layer 1(BaO) and layer 2(BaO), are calculated to range from 2.65 to 3.35 Å in regions covered by SrO clusters, and ca. 2.76 Å in uncovered ('clean') regions. Clearly, the clusters perturb considerably the underlying support; the natural (bulk) BaO bond distance is 2.76 Å.

Thin film energies were calculated to be 1.00 J/m^2 and 1.01 J/m^2 for the 10×10.1 and 10×10.2 systems, respectively. This small difference in

energy values can be associated with a difference in ions positions in the cluster (fig. 3.3).

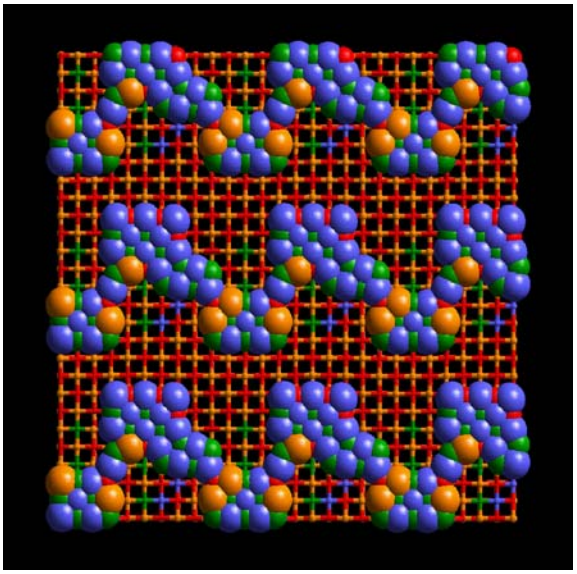

10×10.1

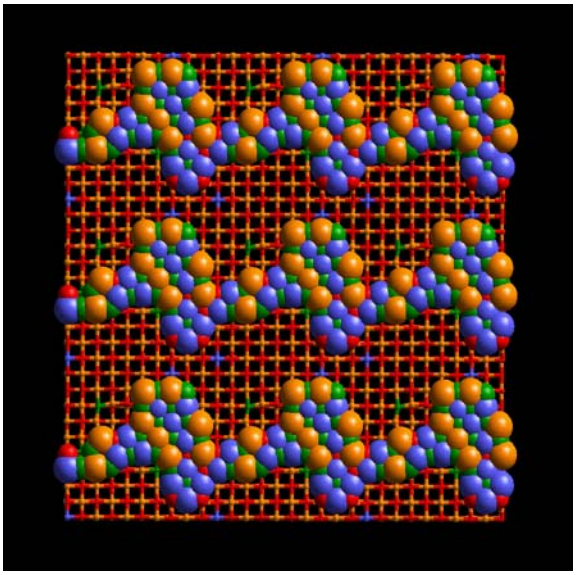

10×10.2

Fig. 3.3. *Representation of SrO/BaO(001) system after the deposition of 21 SrO species. In each picture nine simulation cells are represented for a better analysis of the cluster structure. Notation as in figure 3.1.*

Table 3.4. Ions per layer in the 10×10 simulation cell for 21 SrO species deposited. (oxygen from the support is labelled O and oxygen from thin film is labelled O1).

	Layer no.*	Number of			
		O	**O1**	**Sr**	**Ba**
10×10.1	L1(BaO)	50	-	-	50
	L2(BaO)	44	6	4	46
	L1(SrO)	6	15	17	4
	TOTAL	**100**	**21**	**21**	**100**
10×10.2	L1(BaO)	50	-	-	50
	L2(BaO)	44	5	8	41
	L1(SrO)	6	16	13	9
	TOTAL	**100**	**21**	**21**	**100**

* according to figure 3.1

50 (49) SrO. After the deposition of 50 SrO species and 49 species onto the BaO support for systems 10×10.1 and 10×10.2 respectively, SrO forms bilayered clusters on the BaO surface; the second layer starts to form rather than cover the entire surface with a monoatomic layer. Since the natural (bulk) SrO bond distance, (2.58 Å), is smaller than that for BaO, (2.76 Å), it can be suggested that in an attempt to reduce strain arising from SrO bond expansion, a new layer starts to form rather than fill the space between the clusters (figure 3.2b and figure 3.4a).

Sr-O bond distances in the cluster range from 2.24-2.40 Å in the top layer (low coordinated region) to 2.57-2.70 Å in the interfacial layer. In the support, bond distances between barium and oxygen ions have an average of 2.76 Å in accord with bulk values.

Surfaces energies in these two cases are 1.23 J/m^2 for the structure with 50 SrO species deposited and 1.22 J/m^2 for the structure with 49 SrO species deposited. A bigger value in the first case appears as a result to the presence of one extra SrO species on the surface in the 10×10.1 system.

After 50 species deposited, the deposition process will continue in the same way with the next layer starting to form before the last one to be complete

(behaviour observed for CaO/SrO also, Sayle D. C. 1999a) until an equivalent of five monolayers is reached (figure 3.2).

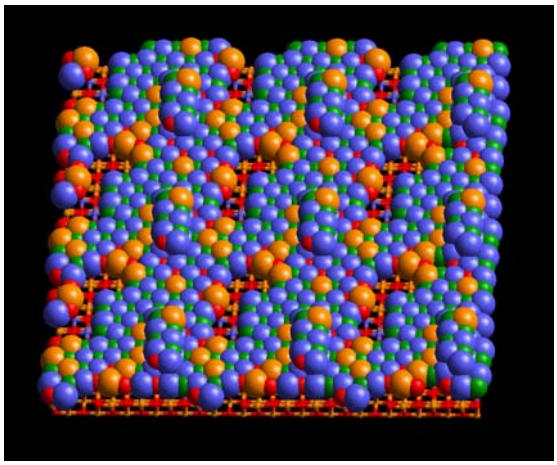

(a) – 1700 K

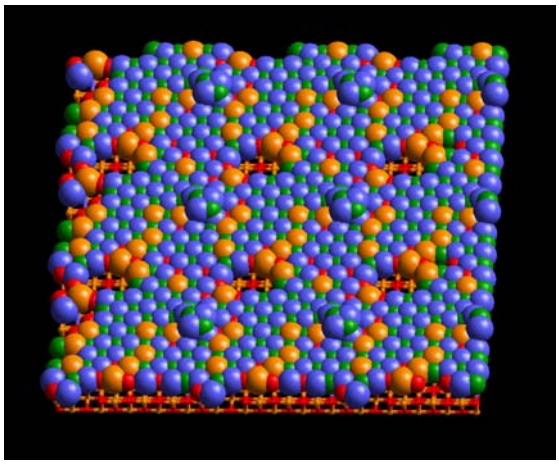

(b) – 2200 K

Fig. 3.4. *Representation of the SrO/BaO(001) system after the deposition of 49 SrO species and dynamical simulation performed at 1700 K and 2200 K. Notation as in figure 3.1. Each picture comprises nine simulation cells.*

250 SrO. The deposition was continued until five equivalent monolayers of SrO were deposited on the 10×10 BaO(001) support. We obtained two structures (for the two runs of the deposition code), with slightly different configurations, figure 3.5 and 3.6 (each picture comprises

nine simulation cells). For the first structure, figure 3.5, the thin film comprises five layers of SrO with cracks formed during the growth. The surface energy of this structure is 1.83 J/m^2. In the second case, figure 3.6, we have almost the same structure in the first four layers. However the fifth layer is incomplete; six ions are present on the surface starting a sixth layer. Moreover the surface energy is higher (less stable) than for the first structure, 1.87 J/m^2. In both cases cracks starts to form from the third layer of the thin film through the surface, but for the second structure in the fifth layer we have holes created due to the deposition of the rest of the ions in the sixth layer (ions from the sixth layer are shown in a white box, figure 3.6). It can be suggested that if holes (or isolated clusters on the surface) are formed during the growth process the final surface will be less stable.

If the 10×10.1 SrO/BaO(001) interface is studied layer-by-layer it is easy to observe that in the first and second layer of the thin film, the SrO maintains 'on-top' configuration with respect to the BaO support with the Sr and O species lying directly above their respective counter-ions. Consequently SrO bond distances calculated using radial distribution function (RDF) have values close to the BaO bond distance (table 3.5). Further from the interface, SrO bond distances decrease until the top layer (surface) where the value of 2.58 Å is reached, which suggest that SrO relaxes back to its natural lattice parameter further from the interface resulting in the formation of cracks (table 3.5). The relative sizes of the cracks per layer are presented in table 3.6. In the SrO interfacial plane the strain energy associated with the 'on-top' configuration is, in part, compensated by energetically favourable cation-anion interactions across the interface. Conversely, the energy cannot be recovered for SrO planes further from the interface, and therefore the SrO relaxes back to its natural lattice parameter leading to the formation of surface cracks.

Table 3.5. Calculated SrO and BaO bond distances (from RDF) for the 10×10.1 SrO/BaO(001) system obtained through deposition, and the 14×14 SrO/BaO system obtained through cube-on-cube construction.

Layer number*	**RDF bond distance 10×10.1 [Å]**	**RDF bond distance 14×14 [Å]**	**Bulk bond distance [Å]**
L1(BaO)	2.76	2.75 (BaO)	2.76 (BaO)
L2(BaO)	2.76	2.76 (BaO)	
L1(SrO)	2.76	2.76 (SrO)	
L2(SrO)	2.75	2.74 (SrO)	
L3(SrO)	2.71	2.72 (SrO)	
L4(SrO)	2.66	2.66 (SrO)	
L5(SrO)	2.58	-	2.58 (SrO)

* according to figure 3.1

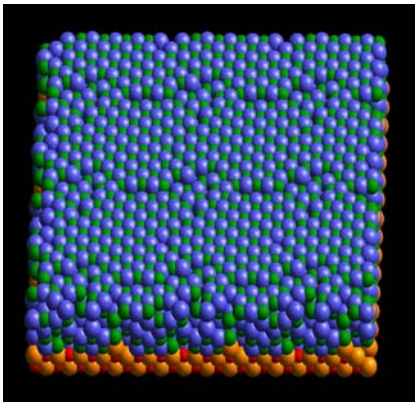

10×10.1 SrO/BaO(001) interface

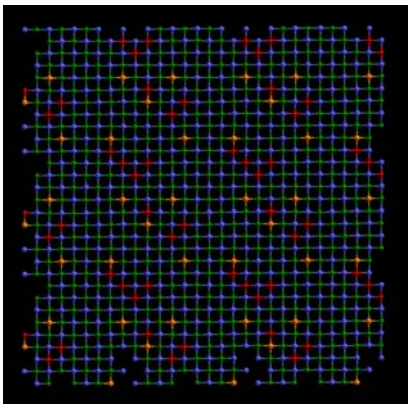

layer 1(SrO)

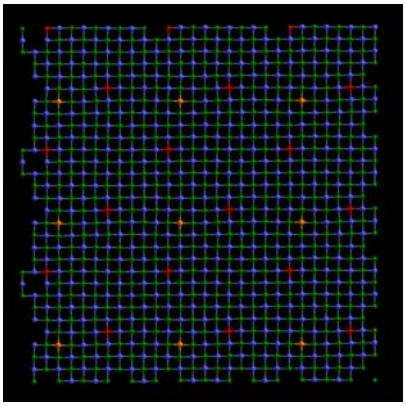

layer 2(SrO)

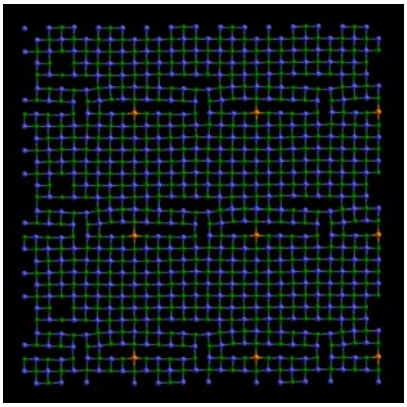

layer 3(SrO)

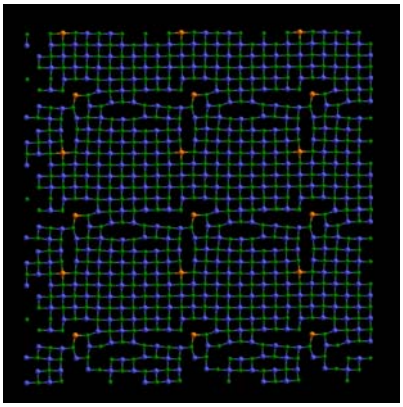

layer 4(SrO)

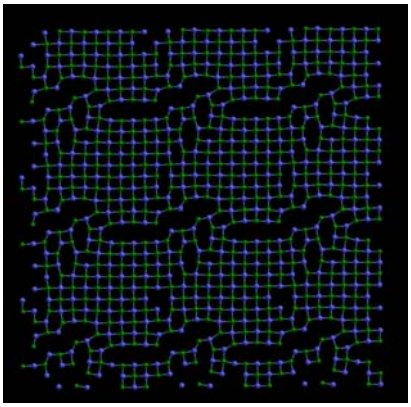

layer 5(SrO)

Fig. 3.5. *Layer-by-layer representation of the SrO/BaO(001) system after the deposition of 5.0 equivalent monolayers onto a 10×10 BaO(001) surface; 10×10.1.*

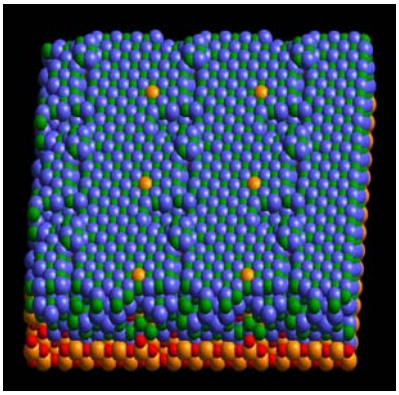

10×10.2 SrO/BaO(001) interface

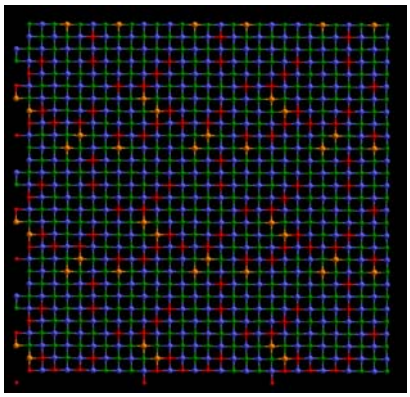

layer 1(SrO)

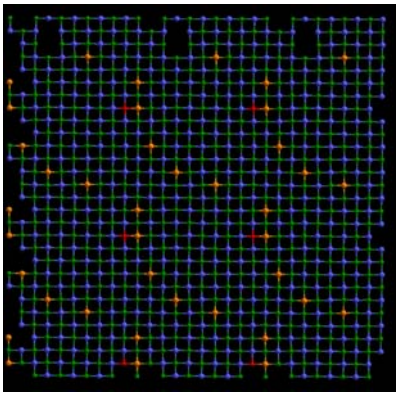

layer 2(SrO)

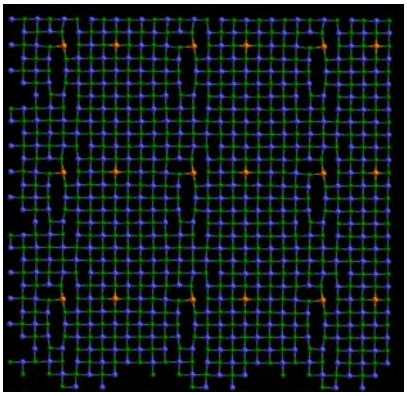

layer 3(SrO)

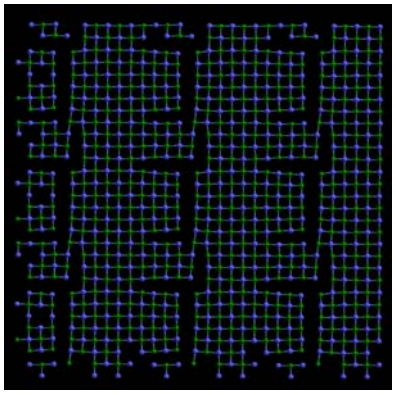

layer 4(SrO)

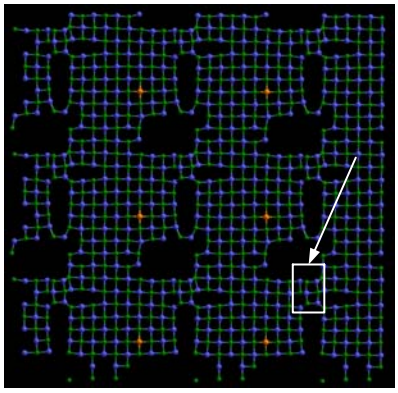

layer 5(SrO)

Fig. 3.6. *Layer-by-layer representation of the SrO/BaO(001) system after the deposition of 5.0 equivalent monolayers onto a 10×10 BaO(001) surface; 10×10.2.*

Table 3.6. Size of the cracks opening for thin films obtained through: (a) – atom deposition and (b) – cube-on-cube construction.

Layer number*	(a) [Å]	(b) [Å]
L3(SrO)	3.13-3.45	3.12-3.73
L4(SrO)	3.49-4.12	3.10-4.47
L5(SrO)	3.80-5.04	-

* according to figure 3.1

Next step is to investigate a larger simulation cell, 14×14, to explore the evolution of the thin film at lower deposition levels.

3.2.1.2. SrO/14×14BaO(001)

For the BaO(001) 14×14 system, due to computational constraints, the deposition was performed until an equivalent of two monolayers was reached. Again the deposition programme was repeated (system 14×14.1 and 14×14.2). In figure 3.7, the structures obtained after the deposition of 18-19, 100 and 198-196 SrO species are presented. For these systems dynamical simulation at 1700 K followed by energy minimisation was performed to ensure structural and energy convergence.

For low coverage, (fig. 3.7a and b), the clusters have similar structures as those for the smaller (10×10) simulation cell. As the coverage increases, a second SrO layer starts to form prior to the formation of a complete monolayer, (fig. 3.7c and d). Eventually pyramidal type clusters are formed on the surface (fig 3.7e and f).

Bond distances in the 14×14 SrO/BaO(001) interface have average values ranging from 2.75 Å for the BaO support to 2.27-2.64 Å for the SrO in the thin film. The smallest value, 2.27 Å, was calculated for ions from the top layer of the pyramidal clusters (figure 3.7e and f).

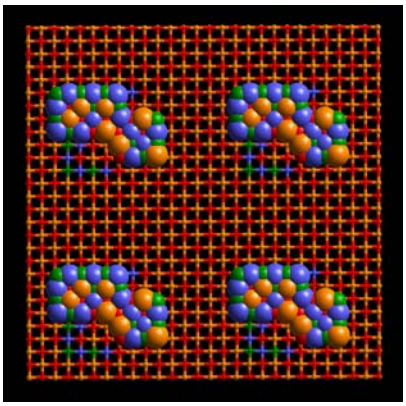

(a) - 14×14.1/coverage 0.19

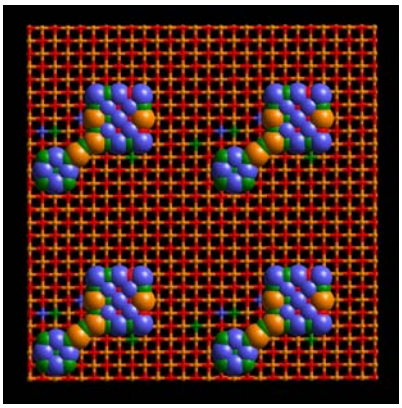

(b) - 14×14.2/coverage 0.18

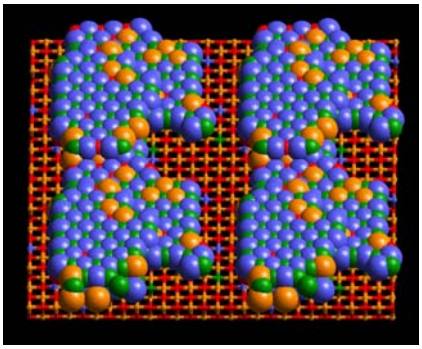

(c) - 14×14.1/coverage 1.02

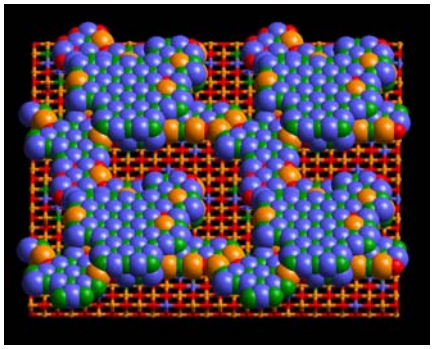

(d) - 14×14.2/coverage 1.02

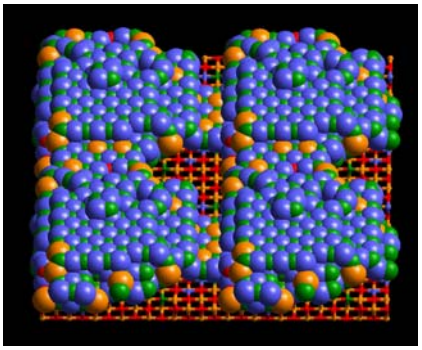

(e) - 14×14.1/coverage 2.00

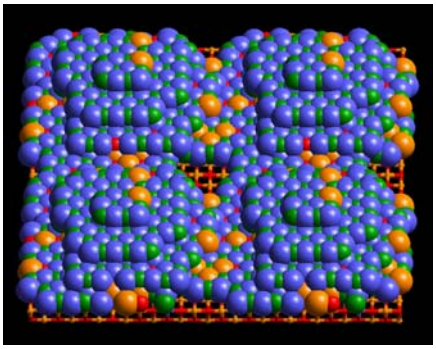

(f) - 14×14.2/coverage 2.02

Fig. 3.7. *Representation of the SrO/BaO(001) system after the deposition of (a) 0.18, (b) 0.19, (c) 1.02, (d) 1.02, (e) 2.02 and (f) 2.00 equivalent SrO monolayers on a 14×14 BaO(001) surface in two cases. Notation as in figure 3.1. Each picture comprises four simulation cells.*

3.2.2. The structure and characterisation of the SrO/BaO(001) interface obtained by cube-on-cube construction

Because the deposition method is computationally very expensive, an alternative methodology was employed to create thicker thin films. Here the interface was constructed by placing four SrO(001) layers directly above an 14×14 BaO(001) support (*coherent* structure). The interface obtained in this way was then subjected to long-term dynamical simulation at 2200 K followed by energy minimisation. The structure and surface energy are then compared with those obtained in the deposition process.

A closer study of the thin film, figure 3.8, reveals that cracks are formed from the third layer of the thin film, as in case of the deposition process.

The final energy for four layers thin film obtained through cube-on-cube construction is 1.69 J/m^2 comparable with 1.65 J/m^2, which is the energy of the four layers thin film obtained through atom deposition. The latter value was calculated for an interface comprising a four layer thin film obtained from the final 10×10.1 structure (deposition of an equivalent of five monolayers) after removal of the top layer (fifth) as described in fig. 3.9. This calculation was made considering that the four-layer SrO thin film obtained using atom deposition it was not atomically flat, the fifth layer starts to form and the thin film contains holes, (see chapter 3.2.5), which gives a certain instability to this structure. Therefore the energy value in this case cannot be directly compared with the value in case of four-layer thin film obtained using cube-on-cube construction.

As the deposition process continues, the stresses that appear in the upper layers force filling of holes present in lower layers, therefore an atomically flat thin film will be obtained. As a result, if the top layer (fifth) is cut and energy recalculated a more stable structure (200 SrO species – four layers) is obtained with an energy value that can be directly compared with that for the structure obtained using cube-on-cube method (200 SrO species – four layers).

The difference between thin film energies for the interfaces obtained using the two construction methods is attributed to ion interchange observed for the interfaces obtained using atom deposition (see chapter 3.2.4).

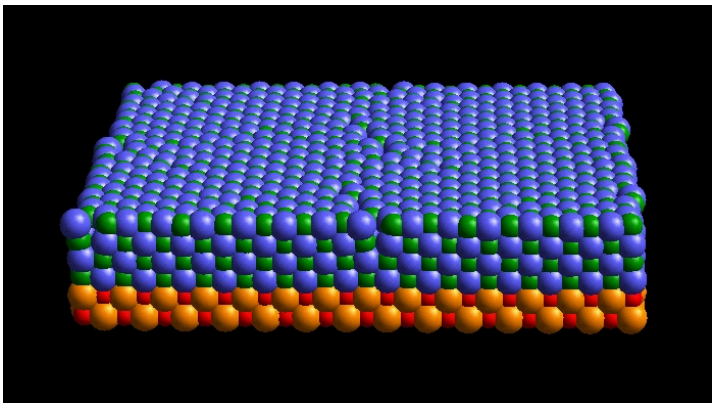

SrO/BaO(001) interface - 'on-top' fitting

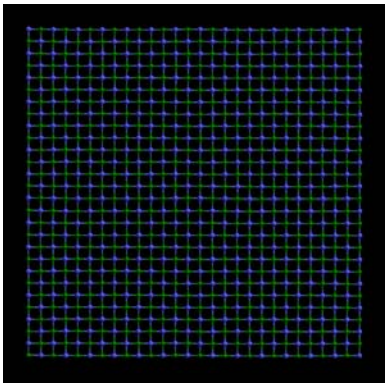

layer 1(SrO)

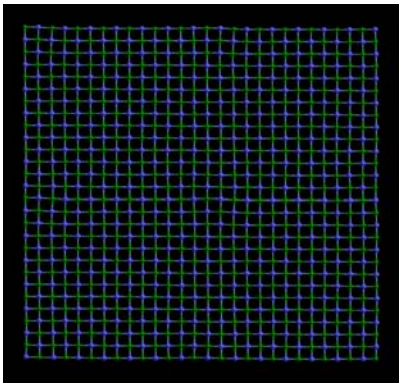

layer 2(SrO)

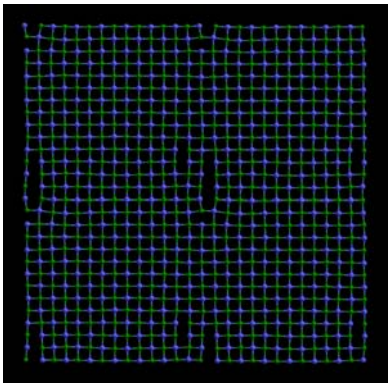

layer 3(SrO)

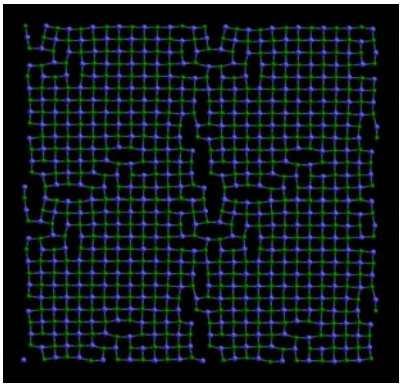

layer 4(SrO)

Fig. 3.8. *Representation of the SrO/BaO(001) system after placing of four SrO(001) layers 'on-top' of the 14×14 BaO(001) support. Notation as in figure 3.1.*

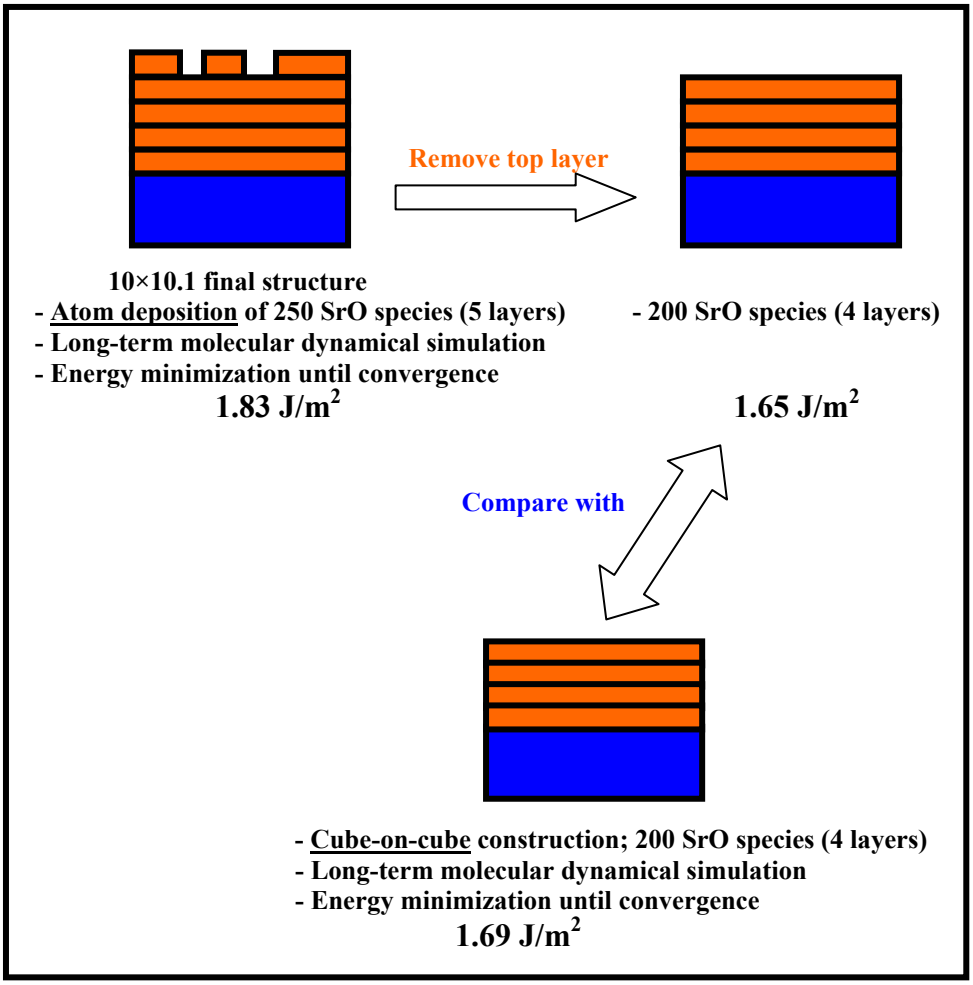

Fig. 3.9. *Schematic representation of the steps involved in the calculation of surface energy in case of the SrO/BaO(001) system obtained using cube-on-cube construction.*

Bond distances in the support and thin film, and crack openings are presented in tables 3.5 and 3.6, respectively through comparison with those obtained for the deposited thin film.

Considering that after dynamical simulation and energy minimisation the interfacial structures, energy and bond distances (SrO and BaO) values are very close for atom deposition and cube-on-cube

construction, we can conclude that both methods can be used in conjunction to model oxide-oxide interfaces.

3.2.3. Thin film energy

Inspection of the interfacial energies of the SrO/BaO(001) system reveals that the energy increases with film thickness, therefore the interface becomes less stable (table 3.3, fig. 3.10 and 3.11). To maintain an on-top configuration will require each layer of the thin film to be strained and therefore such configuration cannot be sustained for thick films. Clearly, such strain energy terms will be additive for each additional layer. Accordingly, at a particular 'critical thickness' (Frank 1949 and Dong 1998), the strain energy will destabilise the interface system such that it becomes energetically favourable for the system to facilitate the evolution of structural modifications such as dislocations, which reduce the misfit. For improved models, dislocations and other type of defects have to be included also. To allow evolution of such structural modifications, larger systems are required (min. 20×20). Using the power of a parallel computer, which permit simulation of system comprising thousands of atoms, in the next section a 40×40 system will be considered.

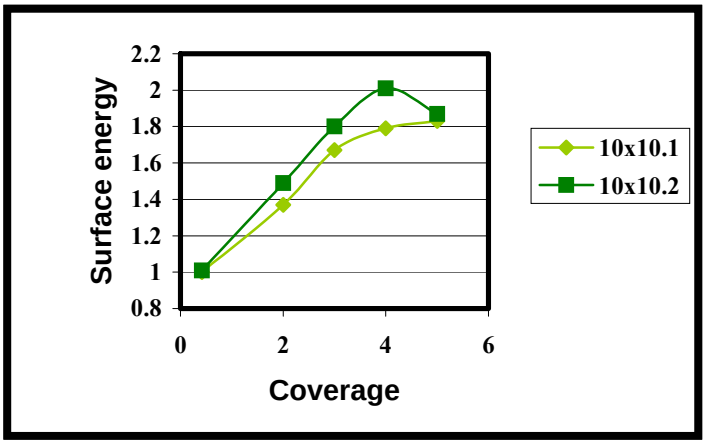

Fig. 3.10. *Surface energy, [J/m^2] as a function of coverage for 10×10 simulation cells.*

A closer study of the energy values and associated structures revealed that for different runs of the deposition code, with a difference in the thin film structure a difference in the energy value would also appear. For example in the case of 10×10.2 structure, which includes large voids in the fifth layer of the thin film and a partially occupied sixth layer (fig. 3.6), the energy is 1.87 J/m^2, while for 10×10.1 structure where the SrO planes comprising the thin film occupied fully (fig. 3.5), the energy is only 1.83 J/m^2. This suggests that the presence of voids is energetically unfavourable for the SrO/BaO(001) system.

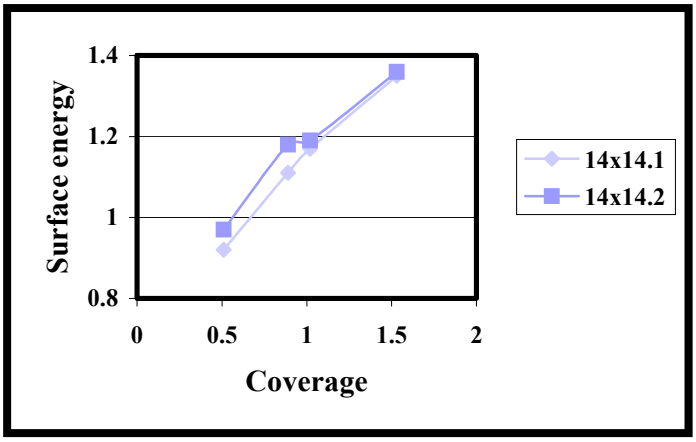

Fig. 3.11. *Surface energy, [J/m^2] as a function of coverage for 14×14 simulation cells.*

3.2.4. Ionic migration

As was mentioned before, a closer inspection of the interface reveals that during the deposition process barium and oxygen (labelled O) ions migrate out of the support to fill lattice positions within the SrO thin film (fig. 3.2 to 3.7, table 3.7 and 3.8). 18% of the barium ions from the interfacial layer migrate across the interface as far as the forth layer of the thin film during the deposition. The resulting vacancies within the support are subsequently filled by the strontium and oxygen (labelled O1) species deposited.

An additional calculation was performed in which all the Ba and Sr ions that had migrated (into the SrO thin film and BaO support,

respectively) were ‘exchanged’. The total energy of the system (for both size of the simulation cell) was found to be higher (less stable) for all deposition levels considered (fig. 3.12 and fig. 3.13).

This behaviour suggests that the interdiffusion of the Ba and Sr species, within SrO thin film and BaO support, respectively, helps to accommodate the lattice misfit thereby stabilising the system. Moreover, since the barium ion is larger compared with strontium (Weast 1982), the SrO lattice parameter will be increased when a proportion of the Sr lattice sites are filled with Ba. Conversely, a decrease in the BaO lattice parameter will be observed when Sr occupies Ba lattice sites. The simulation therefore suggests that, for this system, a smooth transition from one lattice parameter (BaO) to another (SrO) is energetically favourable compared with a sharp transition. This observation can have implications for the design of the buffer layers within incommensurate interface systems.

A study by Lind et al. on the growth of Fe_3O_4/NiO thin films using oxygen-plasma-assisted molecular beam epitaxy reported diffusion across the interface, ‘of the order of 1 or 2 atomic layers’ (Lind 1992). Another experimental study on the growth of RuO_2 on TiO_2 by molecular beam epitaxy uses a high temperature to create at the interface a solid solution of Ru and Ti to ‘keep the edge dislocation density to a minimum’ (Kim Y. J. 1997b). The temperature is then decreased gradually during the deposition and the lattice parameters are reduced from those of TiO_2 to those of RuO_2 avoiding in this way defects evolution.

Table 3.7. Ions per layer for the 10×10.1 simulation cell.*

No. of SrO pairs deposited	Layer No.	Number of			
		O	**O1**	**Sr**	**Ba**
50	L1(BaO)	50	-	-	50
	L2(BaO)	41	9	7	43
	L1(SrO)	5	34	33	7
	L2(SrO)	4	7	10	-
	TOTAL	**100**	**50**	**50**	**100**
100	L1(BaO)	50	-	-	50
	L2(BaO)	41	9	9	41
	L1(SrO)	8	42	45	5
	L2(SrO)	1	44	43	2
	L3(SrO)	-	5	3	2
	TOTAL	**100**	**100**	**100**	**100**
150	L1(BaO)	50	-	-	50
	L2(BaO)	41	9	9	41
	L1(SrO)	8	42	45	5
	L2(SrO)	-	50	49	1
	L3(SrO)	1	41	39	3
	L4(SrO)	-	8	8	-
	TOTAL	**100**	**150**	**150**	**100**
200	L1(BaO)	50	-	-	50
	L2(BaO)	41	9	9	41
	L1(SrO)	8	42	45	5
	L2(SrO)	1	49	49	1
	L3(SrO)	-	50	49	1
	L4(SrO)	-	42	41	1
	L5(SrO)	-	8	7	1
	TOTAL	**100**	**200**	**200**	**100**
250	L1(BaO)	50	-	-	50
	L2(BaO)	41	9	9	41
	L1(SrO)	7	43	45	5
	L2(SrO)	2	48	49	1
	L3(SrO)	-	50	49	1
	L4(SrO)	-	50	48	2
	L5(SrO)	-	50	50	-
	TOTAL	**100**	**250**	**250**	**100**

Table 3.8. Ions per layer for the 14×14.2 simulation cell.*

No. of SrO pairs deposited	Layer No.	Number of			
		O	**O1**	**Sr**	**Ba**
18	L1(BaO)	98	-	-	98
	L2(BaO)	93	5	4	94
	L1(SrO)	5	13	14	4
	TOTAL	**196**	**18**	**18**	**196**
50	L1(BaO)	98	-	-	98
	L2(BaO)	87	10	14	83
	L1(SrO)	11	40	36	15
	TOTAL	**196**	**50**	**50**	**196**
100	L1(BaO)	97	1	-	98
	L2(BaO)	81	17	19	79
	L1(SrO)	16	48	48	16
	L2(SrO)	2	34	33	3
	TOTAL	**196**	**100**	**100**	**196**
198	L1(BaO)	97	1	-	98
	L2(BaO)	76	22	21	77
	L1(SrO)	19	73	75	17
	L2(SrO)	4	57	59	2
	L3(SrO)	-	39	38	1
	L4(SrO)	-	6	5	1
	TOTAL	**196**	**198**	**198**	**196**

* oxygen from the support is labelled O and oxygen from thin film is labelled O1 (table 3.7 and 3.8)

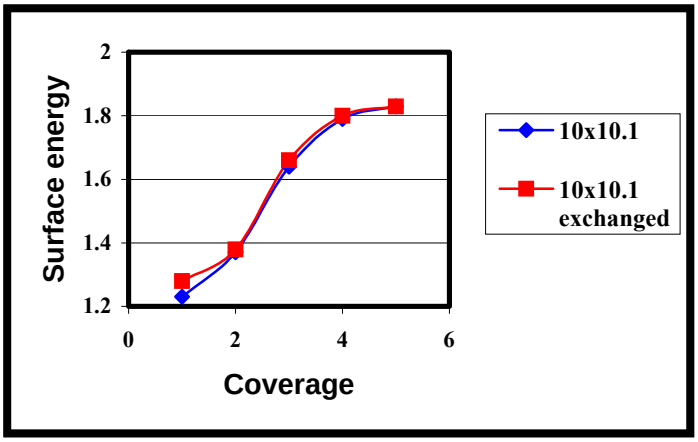

Fig. 3.12. *Surface energy, [J/m^2] as a function of coverage for the 10×10.1 simulation cell for structures obtained through deposition and structures obtained through changes of ions places.*

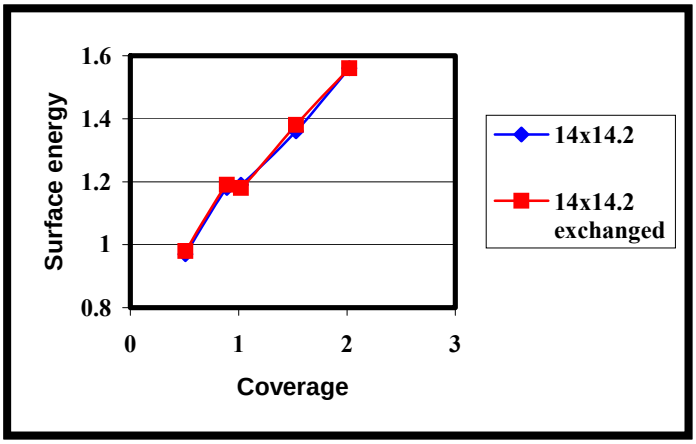

Fig. 3.13. *Surface energy, [J/m^2] as a function of coverage for the 14×14.2 simulation cell for structures obtained through deposition and structures obtained through changes of ions places.*

3.2.5. Dynamics temperature influence

Using the same temperature for dynamical simulation during the growth process for all the calculations, it is easy to see that surface energies have bigger values for one set of structures irrespective of the size of simulation cell (fig. 3.10 and 3.11). Therefore from the energetic point of

view those structures are not so stable as the other; consequently the probability for those surfaces to exist is smaller. The temperature at which dynamical simulation is run (i.e. higher temperature) is likely to influence the thin film structure, which might have a positive impact on the energetic of these systems.

Using a higher temperature for dynamical simulation, the system will be more perturbed, while ionic mobility is increased, allowing the structure to potentially overcome certain energy barriers. Therefore it is likely that lower energy structures will be obtained.

The trial was made at 2200 K for two structures, with low and high coverage, from the 10×10.2 set of structures. The final structures (including molecular dynamics at 1700 K and energy minimisation) obtained after deposition of 49 SrO species (0.98 coverage) and 200 SrO species (4.0 coverage) are subjected to dynamical simulation at 2200 K and energy minimisation.

In the case of low coverage, ions from the top layer are partially displaced to the interfacial layer (figure 3.4b). In the case of high coverage only a slight rearrangement of the ions in the thin film was observed by comparison with the starting structure (fig. 3.14 and 3.15), suggesting that the temperature is not high enough to enable the migration of ions from the top layer to fill holes present in the thin film.

Although the structural modifications are not very important, during the dynamical simulation at 2200 K, the surface energies decrease; therefore more stable surfaces are obtained (table 3.9). It can be suggested that a dynamical simulation at a higher temperature allows the system to find a minimum with a lower energy.

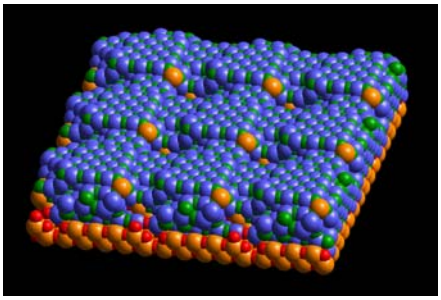

SrO/BaO(001) interface

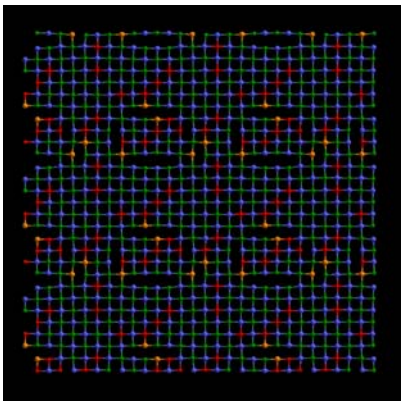

layer 1(SrO)

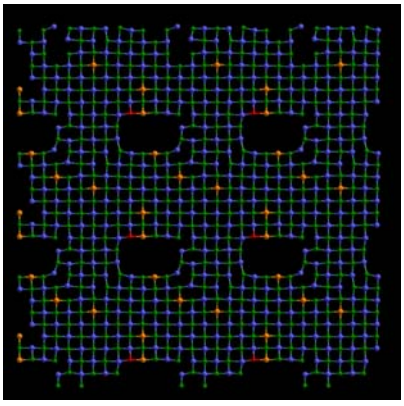

layer 2(SrO)

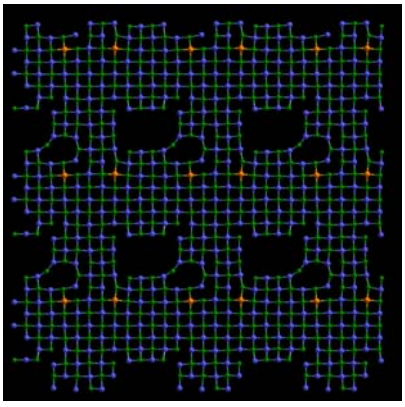

layer 3(SrO)

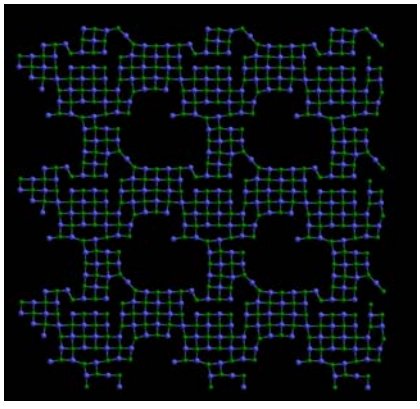

layer 4(SrO)

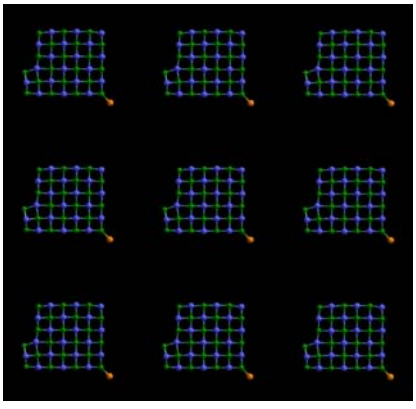

layer 5(SrO)

Fig. 3.14. *Layer-by-layer representations of the SrO/BaO(001) system after the deposition of 4.0 equivalent monolayers on 10×10 BaO(001) surface and 1700 K dynamical simulation. Notation as in figure 3.1.*

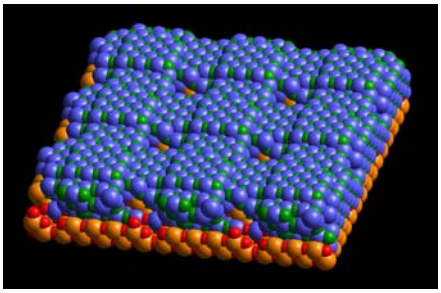

SrO/BaO(001) interface

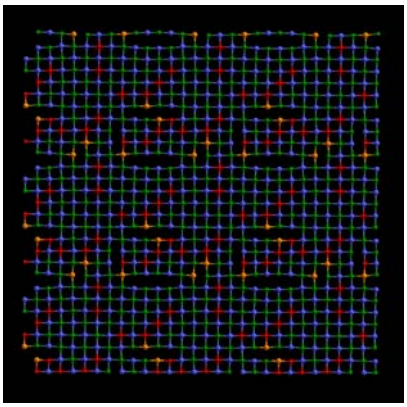

layer 1(SrO)

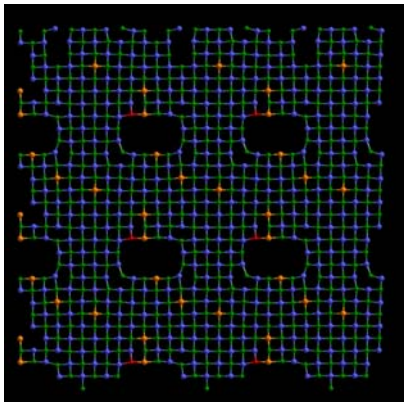

layer 2(SrO)

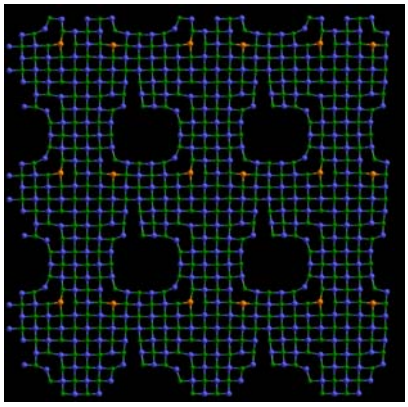

layer 3(SrO)

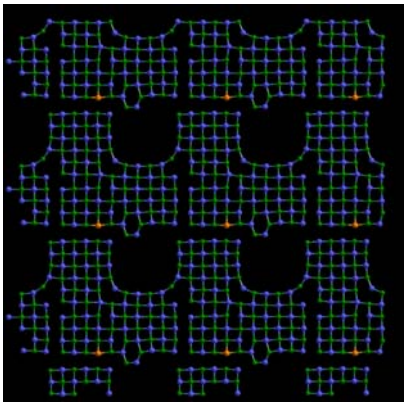

layer 4(SrO)

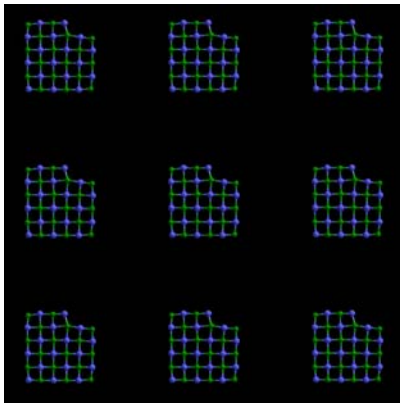

layer5(SrO)

Fig. 3.15. *Layer-by-layer representations of the SrO/BaO(001) system after the deposition of 4.0 equivalent monolayers on 10×10 BaO(001) surface and 2200 K dynamical simulation. Notation as in figure 3.1.*

Table 3.9. Influence of the MD simulation temperature on the surface energy.

Number of SrO species deposited	γ [J/m^2]	
	10×10.2	
	1700 K	2200 K
49	1.22	1.12
200	2.01	1.91

The results presented in this section suggest that the deposition procedure can be improved if the long term dynamical simulation is performed using a higher temperature, perhaps just below the melting point, for each deposition level considered (table 3.3). Moreover, if a structure subjected to long term dynamical simulation is then used to continue the deposition, lower energy configurations can be obtained during the growth process.

3.3. Summary

In this chapter, the SrO/BaO(001) system was constructed using two methodologies: atom deposition and cube-on-cube construction.

The first method involves a sequential deposition of strontium and oxygen ions onto the surface of the BaO support, followed by long-term dynamics and energy minimisation to find low energy configuration.

At low coverage, the SrO forms clusters on the surface as opposed to isolated and dispersed Sr and O species, which reproduce the rock-salt structure of the support and provide nucleation centres for further, deposited species. For theoretical monolayer coverage, a second layer starts to form prior to complete monolayer coverage. As the deposition continues, the evolution of the thin film was observed to be similar; the next layer starts to form before the last one to be complete until an equivalent of five monolayers is reached.

The final structure obtained, with five layers thin film (10×10.1), comprises cracks that are formed from the third layer of the thin film, suggesting that SrO cannot sustain an 'on-top' configuration further from the interface and relaxes back to its natural parameters. Moreover, a migration of a few barium ions from the support to the thin film and strontium ions from the thin film to the support was observed. As the calculated (strontium and barium ions 'exchanged' to their places in the thin film and support, respectively) thin film energies showed, the SrO/BaO(001) system it proved to be more stable with barium ions occupying lattice sites in the thin film and strontium ions in the support.

The influence of temperature on the final structure of the thin film was also considered. Using a higher temperature for the dynamical simulation, at low coverage (0.98) spaces in the interfacial layer of the thin film are partially filled with ions, which migrate from the second layer and deposition can then be restarted from a better interfacial configuration (lower energy). For high coverage (4.0), slight structural modifications after dynamics at higher temperature together with a decrease in surface energy were observed.

The second method used to create the thin film consist of placing four SrO layers directly above on 14×14 BaO support, when SrO is constrained to occupy 'on-top' positions over the support. After dynamical simulation at 2200 K and energy minimisation the final structure has the same structural characteristics as that obtained through sequential deposition (including cracks from the third layer of the thin film) with exception of migration across the interface, which is not appearing in this case.

It can be concluded that the deposition process for the SrO/BaO(001) system follows the same path irrespective of the size of the simulation cell: formation of clusters rather than a clean monolayer; clusters with similar structure; similar evolution during the growth with a new layer that starts to form before the previous one has completed; and ionic migration. If a larger size for the simulation cell is used, additional information about structure of the thin film at submonolayer level can be obtained. Also, using two different methods to build the interface, atom deposition and cube-on-cube construction, similar structures for the

SrO/BaO(001) system were obtained. An atom deposition method is preferential when information about epitaxial growth mechanism are requested on small simulation cells due to computational constrains, while a cube-on-cube construction can be use on much larger systems.

In the following chapter, systems comprising ceria deposited on zirconia-based materials (pure zirconia and yttrium stabilised zirconia) are considered. The interface was generated using ‘amorphisation and recrystallisation’ methodology.

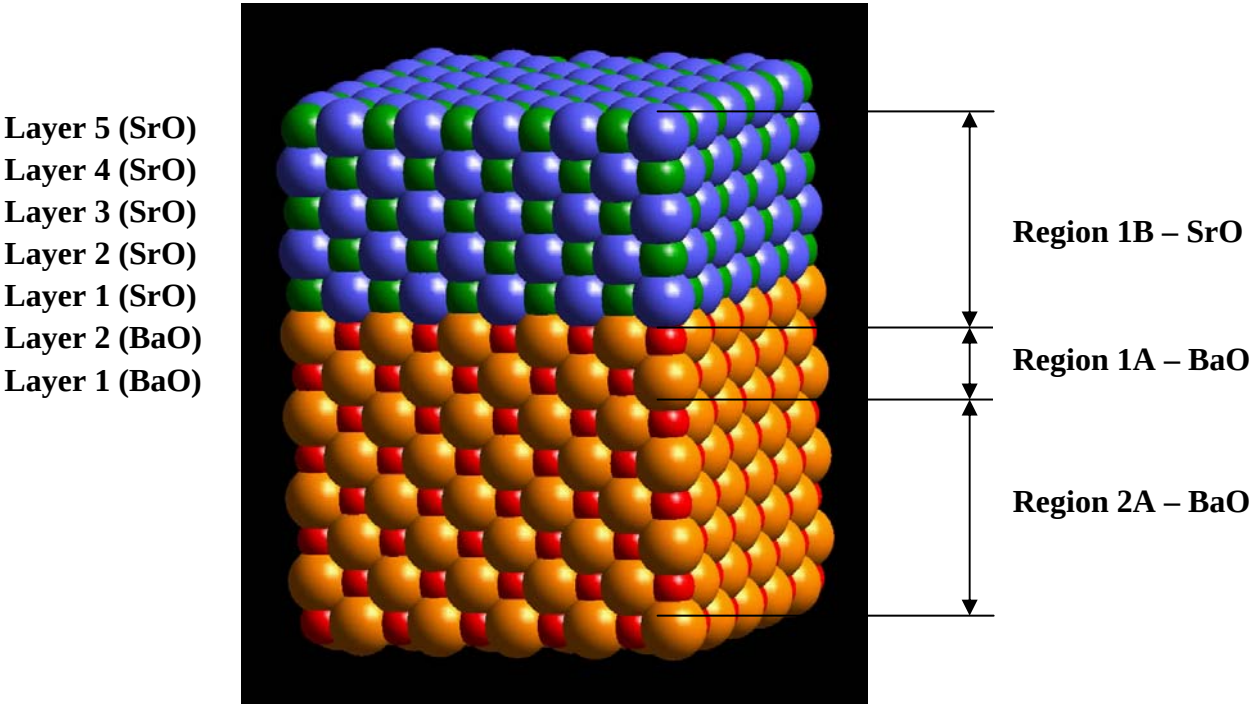

Fig. 3.1. *Representation of the 10×10 simulation cell. Barium is coloured orange, strontium is blue, oxygen (BaO) is red and oxygen (SrO) is green.*

4. CeO_2 thin films supported on zirconia and zirconia based substrates

4.1. Introduction

In this chapter, atomistic computer simulation will be used to generate and characterize thin ceria films supported on zirconia and yttrium-stabilized zirconia, which play an important role in catalytic processes. Such systems, on which a noble metal (Pt, Rh) is also deposited, comprise a major component of three-way-catalysts used for the removal of NO_x, CO and hydrocarbons from exhaust gases (Trovarelli 1996). When deposited, it is likely that both the structure and associated properties of the system will be altered. While chemical and physical properties can be relatively easily determined experimentally, the structure at the atomic level cannot be elucidated exactly. Accordingly, atomistic simulation techniques are employed to explore the structure of the supported CeO_2 thin films.

4.1.1. Zirconia (ZrO_2)

4.1.1.1. General considerations

Zirconia is an important technological material with a wide range of applications, from heterogeneous catalysis to neoceramic tools (Cerrato 1997ab), due to its polymorphism. Zirconia can be used in oxygen sensors and generators, electrolytes in solid fuel cells, refractory materials in metallurgy, thermal barrier coatings in engines, catalysts and catalysts supports and as a component in glasses, composites, pigments and piezoelectric ceramics (Wagner 1992, Stefanovich 1994, Khan 1998, Leoni 1998, Mekhemer 2000, Pasel 2000, Matsumoto 2000, Zorn 1999, Nakatsuji 2000, Liu 1996, Wang Y. 1997, Wang D. 1999 and Štefanić 1998ac).

Zirconia has three structural modifications, which have different physical and thermomechanical properties. At low temperatures, 0-1273 K, ZrO_2 has a monoclinic (*m*) structure. At temperatures between 1273 K and 1473 K the transition to a tetragonal (*t*) phase occurs, and at 2643 K (*c*) fluorite starts to form. The cubic structure is maintained until 2953 K, which is the point of transition to a liquid phase (Bever 1986 and Stefanovich

1994). The cubic fluorite structure of ZrO_2 is not stable at lower temperatures because the radius of the zirconium cation is too small to sustain 8-fold cubic coordination and hence the lower symmetry distortions occur (oxygen anions are packed more closely around the zirconium cation). The cell parameters for all structural modifications and values for cubic form obtained in this work are presented in table 4.1.

Partially stabilized tetragonal zirconia and fully stabilized cubic zirconia can be obtained from amorphous precursors at room temperature if (a) divalent, trivalent or tetravalent cations are introduced into the ZrO_2 lattice (e.g. Ca^{2+}, Mg^{2+}, Y^{3+}, Cr^{3+}, Ga^{3+}, Ce^{4+}, Ge^{4+}), (Dwivedi 1989, 1990, Stefanovich 1994, Li P. 1994abc, Dai 1996, Khan 1998, Štefanić 1998c, Wang D. 1999 and Zacate 2000); (b) the crystallization of the amorphous precursors occurs in the presence of surface-adsorbed anionic species (e.g. sulfates), (Štefanić 1998b) or in the presence of increasing concentrations of basic mineralizers, LiOH, NaOH, KOH or $(CH_3)_4N$, (Dell'Agli 2000); (c) the crystallites are generated under controlled chemical/physical conditions (e.g. pH, calcination temperature), and/or their average size remains below ca. 300 Å (Cerrato 1997a and references therein, Garvie 1965 and 1978). The hypothesis, advanced by Garvie that the tetragonal and monoclinic phases are in equilibrium at 300 ºC when the crystallite size is about 300 Å was invalidated by the results obtained by Srinivisan (1992 and 1993) who obtained monoclinic particles of ca. 100 Å in size.

Cerrato and co-workers (1997ab) have shown that precipitated amorphous zirconia, sintered at high temperatures, becomes 'virtually pure *m*-ZrO_2' with crystallites terminated predominantly along the (111) plane. Zirconia can be also prepared through reactive electron beam evaporation, electron beam evaporation, sputtering, ion-assisted deposition, pulse laser deposition, sol-gel processing and metal organic chemical vapour deposition (Gao 2000 and Jones 1999). Through reactive sputtering, *m*-ZrO_2, with a small fraction of *t*-ZrO_2 is obtained (Koski 1999 and Gao 2000). High quality epitaxial thin films (used as buffer layers between silicon and thin films with perovskite like structure) of *t*-ZrO_2 exposing the (001) plane can be fabricated on Si(100) wafers via sol-gel processing (Bae 2000). If the sol-

gel method is associated with supercritical drying it is possible to obtain *c*-ZrO_2 (Wang Y. 1997).

Table 4.1. The cell parameters for structural modifications in zirconia (ZrO_2), [Å].

Lattice param. /bond type	Stefanovich 1994 and references therein		Li P. 1994a	Bever 1986	Khan 1998 and references therein		This work (potentials from Dwivedi and Cormack 1990)
	Expt.	**GULP**	**Expt.**	**Expt.**	**Expt.**	**GULP**	**GULP**
				(*m*) – ZrO_2			
a	5.151	5.241	5.148	5.1454	-	-	-
b	5.212	4.898	5.200	5.2075	-	-	-
c	5.317	5.578	5.322	5.3107	-	-	-
angle	99.23(γ)	90.00(γ)	99.20(β)	99.14(β)	-	-	-
				(*t*) – ZrO_2			
a	5.050	5.074	-	3.640	-	-	-
b	5.182	5.216	-	5.270	-	-	-
angle	90.00	90.00	-	90.00	-	-	-
				(*c*) – ZrO_2			
A	5.090	5.075	-	5.065	-	5.076	5.07
angle	90.00	90.00	-	90.00	-	90.00	90.00
Zr – O	-	-	-	-	2.204	2.176	2.19
O – O	-	-	-	-	2.563	2.538	2.53
Zr - Zr	-	-	-	-	3.589	3.620	3.59

As was mentioned before, one way to stabilize the cubic fluorite structure of ZrO_2 is to incorporate divalent, trivalent or tetravalent cations in zirconia structure. When stabilizing agents such as CaO, MgO, Fe_2O_3, Y_2O_3, CeO_2, GeO_2 are added to ZrO_2, the dopant cation substitutes for zirconium and oxygen vacancies are created to maintain charge continuity. The best way to stabilize cubic zirconia is to use Y^{3+} as a dopant (Khan 1998). As the

yttrium content increases, the thin film converts from a mixture of monoclinic and cubic phase to a single cubic phase (Boulouz 1999).

Yttrium-stabilized zirconia (YSZ) is a material used on a large scale in different areas due to its properties: high ionic conductivity, low thermal conductivity, resistance to thermal shock for columnar microstructures, chemical inertness and good mechanical properties (Dubourdieu 1999). The ionic conductivity of YSZ thick films and coatings can be exploited in solid-oxide fuel cells and oxygen sensors, while its chemical inertness and thermal properties are used in the development of thermal barrier coatings for engines. YSZ thin films are used as buffer layers for the deposition of high temperature superconductors (Xiong 1998ab), as a support for MgO that is also a buffer layer for superconducting and ferroelectric films (Stampe 1998) and as a support for catalytic materials such as platinum (Luerβen 2000) or oxide materials including ceria (Dmowski 1996, 1998).

YSZ thin films and coatings can be grown on different substrates using electron-beam physical vapour deposition, sputtering, laser deposition, chemical vapour deposition, plasma-enhanced chemical vapour deposition, molecular organic chemical vapour deposition and aerosol-assisted chemical vapour deposition (Dubourdieu 1999 and references therein, Holzschuh 1991, Garcia G. 1997 and 2000, Wang H. B. 2000, and Vasco 2000). By varying the proportion of each precursor, the growth rate and temperature, it is possible to control precisely the composition and structure of the YSZ thin film obtained through these methods. For example, in the case of YSZ deposition on Si(001), when the deposition temperature increases, the preferred orientation of the YSZ with respect to underlying support during the crystallization changes from (001) to (111) (Garcia 1997). The cell parameters for cubic YSZ, literature data and values obtained in this work, are presented in table 4.2.

4.1.1.2. Lattice simulation

Computer simulation techniques can also be used to study zirconia and stabilized zirconia solid solutions. Dwivedi and Cormack (1990) examined the CaO-ZrO_2 system using atomistic simulation. They calculated defect association energies, binding energies for various types of defect

cluster and migration energies for oxygen ions. It was found that the defect energy of a vacancy is lower in *c*-ZrO_2 than in *t*-ZrO_2, suggesting therefore that the presence of vacancies stabilises the *c* phase. Defect association energy calculations for an anion vacancy and a dopant calcium ion show that the preferential sitting of oxygen vacancies is in the next-nearest-neighbour (NNN) position with respect to the dopant cation, at low dopant coordination. Negative association energies of various clusters indicate that defect association and cluster formation will occur in the CaO-ZrO_2 system. The probability of cluster formation and cluster size increases with dopant concentration. Values calculated using computer simulation techniques are in accord with experimental results giving confidence in the potentials when applied to more complex systems such as those under study in this work.

Stefanovich and co-workers (1994) extended the study of zirconia, stabilized with divalent cations, to the ZrO_2-MgO system. They confirm results obtained by Dwivedi and Cormack and identify factors that contribute to the mechanism of stabilization of cubic zirconia by impurities, such as lattice distortion around vacancies, a smaller dielectric constant in the cubic phase and impurity-stimulated increase of ionicity (smaller ionicity or higher covalency favours structures with lower coordination number).

Khan (1998) investigated, using computer simulation techniques, the defect and transport properties of zirconia doped with different cations including alkaline-earth, rare-earth and other divalent and trivalent dopants. CaO, MnO, Y_2O_3, Gd_2O_3 and Sc_2O_3 are calculated to be the most favourable dopants enhancing oxygen diffusivity in their solid solutions with zirconia. It was confirmed that cation dopants with a larger ionic radii than Zr^{4+} prefer the charge-compensating oxygen vacancies to be at a next-nearest-neighbour (NNN) site, leaving them in 8-fold coordination. Conversely, undersized dopants prefer the vacancy to be situated at nearest-neighbour (NN) positions. Zacate and co-workers (2000) extended the research over a new group of M_2O_3-doped cubic ZrO_2 solutions, with the same conclusion for the position of oxygen vacancies. They also predicted lattice parameters, as a function of dopant concentration, to be in good agreement with experimental data.

Table 4.2. Lattice parameters of cubic yttrium stabilized zirconia, [Å].

Reference	8 mol. % Y_2O_3 in YSZ		10 mol. % Y_2O_3 in YSZ	
Ingel 1986 in Dubourdieu 1999	5.125 bulk		5.130 Bulk	
Holzschuh 1991	5.110 thin film		5.115 thin film	
Miller 1993 in Dubourdieu 1999	5.140 thin film		5.145 thin film	
Li P. 1994a	-		5.1486 bulk	
			Zr – O	2.15
			Zr - cation	3.58
			Y – O	2.33 (2.28 pure Y_2O_3)
			Y - cation	3.62
Dubourdieu 1999	5.142 thin film		5.145 thin film	
Putna 1999	5.129		-	
Dmovski 1996, 1998	-		5.23** surface 5.131** bulk	
Stampe 1998	-		5.139***	
This work (potentials from Dwivedi and Cormack 1990 and Lewis and Catlow 1985)	5.106*		-	
	Zr – O	2.15		
	Zr – Y	3.60		
	Zr – Zr	3.60		
	Y – Y	3.60		
	Y – O	2.34		
	O – O	2.55		

* Atomistic computer simulation. All other values are experimental.

** Values for 9.5 mol. % Y_2O_3.

*** Cubic YSZ; mol. % Y_2O_3 is not mentioned.

Computer simulation in conjunction with molecular dynamics simulation was also used to investigate grain-boundaries (Zhilyaev 1997) and oxygen diffusion along grain-boundaries (Fisher 1997, 1998, 1999ab and Li H. 1998) in cubic zirconia. It was shown that the activation energy for diffusion decreases (oxygen diffusion increases) as the grain-boundary tilt angle increases, reaching a minimum value at tilt angles equal to ca. 40-50º (Li H. 1998). Although the symmetrical tilt grain-boundaries are able to

support intrinsic oxygen diffusion, they impede the overall conductivity in systems of 8% Y_2O_3 in zirconia (Yttrium Stabilized Zirconia-YSZ). Diffusion of oxygen ion vacancies along the boundary is less rapid than that in the bulk, with maximum oxide ion conductivity in the bulk observed at around 8-10 mol % Y_2O_3 (cubic phase), (Fisher 1999a) and confirmed through molecular dynamics simulation studies (Brinkman 1995 and Yamamura 1999). Segregation of dopants ions to the symmetrical tilt grain-boundary further decreases the overall conductivity by trapping vacancies in the grain-boundary regions. The twist boundary, in contrast, enables rapid diffusion across the boundary plane (Fisher 1999a, 1999b). It was reported that for ultrafine-grained YSZ (average grain size 10nm), maximum ionic conductivity is reached at 3 mol % YSZ in the tetragonal phase both in grains and grain boundaries and is higher than that of the fully stabilized cubic zirconia (Ramamoorthy 1999).

4.1.2. Ceria (CeO_2)

4.1.2.1. Structure and properties

Ceria is a binary solid oxide of cerium, which presents the fluorite (CaF_2) structure with each Ce^{4+} cation surrounded by eight equivalent nearest O^{2-} anions forming corners of a cube and each O^{2-} anion surrounded by a tetrahedron of four cerium ions. In a reducing atmosphere at elevated temperatures, CeO_2 is known to form an oxygen-deficient, nonstoichiometric oxide CeO_{2-x} (with $0 < x \leq 0.5$). The most important characteristic of ceria is that, even after loss of considerable amounts of oxygen from its lattice and formation of large number of oxygen vacancies, CeO_2 remains in its fluorite crystal structure, and these suboxides are reoxidized to CeO_2 in an oxidizing environment (Trovarelli 1996). The ability of ceria to shift from Ce^{4+} to Ce^{3+} in reducing atmosphere and from Ce^{3+} to Ce^{4+} under oxidizing conditions, with charge compensation facilitated via oxygen vacancies, is called *oxygen storage capacity* (OSC), (eq. 1).

$$CeO_2 \rightleftharpoons CeO_{2-x} + \tfrac{1}{2}xO_2 \qquad \textbf{(1)}$$

Recent studies have suggested that the properties of CeO_2 can be improved by introducing foreign cations into its cubic lattice, through the preparation of solid solutions. Enhancing the catalytic, textural, redox and oxygen storage properties and decreasing the reduction temperature of ceria, can increase the overall performance of cerium-based catalyst. The solid solution usually promotes the formation of oxygen vacancies and increases the oxygen mobility leading to a higher OSC (Trovarelli 1997, Masui 2000). Ceria doped with ZrO_2 and/or PrO_x, Y_2O_3, La_2O_3, CuO, TbO_2 (Trovarelli 1996, Trovarelli 1997, Rao 1994, Vidmar 1997, Markaryan 1999, Kašpar 1999, Terribile 1999 and Vidal 2000); SiO_2 (Rocchini 2000); MnO_x (Machida 2001); Hf^{4+} (Zamar 1995); codoping with Sm_2O_3, Gd_2O_3 and Tb_2O_3 (O'Connell 2000) can all be used to improve CeO_2 properties. Among the different cations investigated, those with ionic radii smaller than that of Ce^{4+} effectively stabilize the CeO_2 against sintering (Kašpar 1999).

Computer simulation studies have also shown that the OSC and ionic conductivity of CeO_2 can be increased if Ca^{2+} (de Carolis 1999), Zr^{4+}, Hf^{4+}, Th^{4+} (Balducci 1997, 2000), Gd^{3+}, La^{3+}or Y^{3+} are introduced into the ceria lattice (Minervini 1999, Inaba 1999 and Hayashi 2000).

The reducibility of CeO_2 can also be improved by supporting on Al_2O_3, ZrO_2, or YSZ. A theoretical study of Sayle D. C. (1995b) suggest that $CeO_2(111)$ when supported on $Al_2O_3(001)$ exhibits lower oxygen vacancy formation energy compared with the unsupported CeO_2. Experimental studies have identified weakly bound surface oxygen species on ceria films deposited on Al_2O_3, which are not present on the unsupported $CeO_2(111)$, (Putna 1996, 1997). A comparison between the properties of ceria thin film vapour deposited onto polycrystalline zirconia and zirconia based substrates such as YSZ, showed that these materials are more efficient than α-Al_2O_3 in promoting ceria reducibility (Putna 1999 and Ferrizz 2000).

The properties of the ceria-based catalytic systems can be enhanced further via the addition of precious metals such as Pt, Pd, Rh (Pfau 1995, Golunski 1995, Trovarelli 1996, Trovarelli 1999, Fornasiero 1999 and Ozawa 1999). Precious metals promote the OSC of ceria, which can help the transfer of the oxygen from the bulk to the surface, while CeO_2 stabilizes the dispersion of the precious metal.

4.1.2.2. Ceria as catalyst and catalyst promoter

As a catalyst and catalyst promoter, ceria and ceria containing materials are used in many processes such as: removal of sulphurous oxides from flue gases (Trovarelli 1999 and Wang J.-A. 1998, 1999), removal of organics from wastewaters (Trovarelli 1999 and Matatov-Meytal 1998) and as a component in many catalysts for a wide group of reactions (e.g. annonoxidation, oxidation, dehydrogenation), (Trovarelli 1996 and references therein, Zhu 1996, Groppi 1999, Siokou 1999, Pantu 2000, Larsson 2000, Luo 1999, Chen 1998 and Imamura 2000). However, perhaps, the most important application of ceria containing materials is as a component in three-way-catalysts (TWC) for the treatment of automobile exhaust gases (Ozawa 1998, Farrauto 1999 and Trovarelli 1999). In an engine, fuel rich conditions (reducing atmosphere) alternate with lean conditions (oxidizing atmosphere) around the stoichiometric composition and ceria has the ability to work in both cases owing to the OSC. Therefore, ceria can transform at the same time carbon monoxide, nitrogen oxides and hydrocarbons into non-toxic products.

Although the main role of ceria is to supply and substract oxygen, several other useful properties are attributed to this material (Trovarelli 1996, 1999 and Kašpar 1999):

- Promote noble metal dispersion
- Promote the water gas shift and steam reforming reactions
- Increase the thermal stability of the support
- Promote noble metal reduction and oxidation
- Store and release hydrogen and sulphur
- Form surface and bulk vacancies, and
- Form intermetalic M – Ce compounds, which act as active sites and promote simultaneously the oxidation of CO and the reduction of NO.

Although ceria and ceria-based materials are used in many catalytic reactions, other processes also benefit from the use of cerium and its derivatives. For example, organometallic-soluble compounds of cerium are used as fuel additives for diesel engines and industrial boilers to reduce carbon deposits after combustion (Lahaye 1996 and Trovarelli 1997). Ceria

is also used in fuel cell technology (Sahibzada 1997 and Hartmanova 1999ab), multilayer coatings for optical devices (Kanakaraju 1997), buffer layers together with YSZ for YBCO high temperature superconductors (Mechin 1996, Aguiar 1998, Wang A. 1999, Jacobsen 1999b and Gnanarajan 1999), corrosion resistant coatings, dielectric layer structures in integrated circuits and gas sensors (Konstantinov 2000).

4.1.2.3. Ceria thin films and surfaces; experiment and simulation

Ceria thin and thick films can be deposited on many substrates, for example: sapphire, silicon, YSZ, MgO, $SrTiO_3$, $LaAlO_3$, $LiNbO_3$, silica glass, indium tin oxide glass, zirconia ceramics and various metals and alloys (Konstantinov 2000). Physical methods for preparation include techniques such as: laser ablation, r.f. magnetron sputtering, d.c. sputtering, electron beam evaporation, molecular beam epitaxy, molecular organic chemical vapour deposition and spray pyrolysis.

If prepared using magnetron sputtering at deposition temperatures above 600°C, a CeO_2 polycrystalline thin film with a preferred (001) orientation could be deposited on Si(001) (Kim 2000). Using the same method, but for deposition on sapphire, a (001) oriented CeO_2 thin film was obtained. Deposited layers display small size mosaicity (~200 Å) separated by rectangular boundaries. The mosaic blocks are twisted with respect to each other by angles of ca. 6-7º (Španková 2000). Jacobsen and co-workers (1999ab), observed extremely sharp microfacetting on the surface of thin CeO_2 thin films grown on α-Al_2O_3. They found trapezoidal and pyramidal shaped grains oriented at 90º with respect to each other. The growth orientation normal to the surface is (001), with (111) and (001) planes exposed at the grain surfaces.

Using oxygen-plasma-assisted molecular beam epitaxy, CeO_2(001) (Kim 1999) and $Ce_{1-x}Zr_xO_2$(001) (Gao 1999) mixed oxide thin films were grown epitaxially on $SrTiO_3$(001). The surface of the CeO_2 thin film consists of small islands, which coalesce with increasing substrate temperatures improving thin film quality, (Kim 1999). In the case of ceria-zirconia mixed oxide, the film grows layer-by-layer for a few monolayers, followed by island formation (Gao 1999). Herman (1999ab), determined

experimentally that the CeO_2(001) surface grown on $SrTiO_3$(001) substrate is terminated with 0.5 monolayers of oxygen resulting in a stable surface with a zero dipole moment (see Appendix C).

Metal-organic chemical vapour deposition (MOCVD) is another method that can be used to grow epitaxial CeO_2 thin films on different substrates. Liang and co-workers (1995), using a special source evaporator, have shown that CeO_2(100) films are grown on YSZ(100), while on a sapphire $(1\ \bar{1}\ 0\ 2)$ substrate, both (111) and (100) oriented CeO_2 are presented depending on substrate temperature. A closer study of CeO_2 growth on a sapphire substrate showed that the mismatch, which exists between the two materials, is mostly accommodated within the first one or two atomic planes of the CeO_2 layer (Zandbergen 2000). The periodicity of misfit dislocations is ~40 Å and correlates well with the misfit between the ceria and sapphire lattice parameters for a CeO_2 thin film perfectly (001) oriented. Using a different precursor, Pan (1998) obtained polycrystalline ceria thin films on YSZ(100), polycrystalline YSZ and α-Al_2O_3, which shows an oriented growth behaviour in both [111] and [100] directions. Low temperature growth of CeO_2 on YSZ(001) by MOCVD resulted in smooth and epitaxial (001) oriented thin films, which exhibit a columnar microstructure (Wang A. 1999). Owing to the lattice mismatch, the interfacial area between the CeO_2 and YSZ substrates, contains atomic stacking dislocations with a periodicity of ~44 Å.

Spray pyrolysis is a well-known method for the synthesis of oxides, in the shape of powders or films (Vallet-Regi 1997). Generally, oxides obtained in this way present a morphology characterized by spherical particles constituted from small crystallites. Using this method, CeO_2 particles with grain sizes calculated to be ca. 49 Å, were obtained. Each particle contains a large number of very small CeO_2 crystallites with (111) and (100) orientations, randomly distributed. When deposited on Si(100) (Wang S. 2000), glass (Elidrissi 2000) or silica substrates (Konstantinov 2000), ceria films have a polycrystalline cubic structure with surface texture (grain size) depending on the source solution and spraying temperature. Moreover, crystallite orientations can be predominantly (111) and/or (100)

depending on preparative conditions. The structural characteristics of CeO_2 obtained by this method make it adequate for use in catalysis.

Laser ablation is another technique used to grow CeO_2 thin films. If deposited on YSZ(001), Si(001) the thin film will have an (001) orientation and a 'cube-on-cube' alignment with the substrate (Méchin 1996, Aguiar 1998 and Wakiya 2000). If deposited on Ni(001), ceria presents a (111) or (001) orientation depending on deposition temperature or if the process is ion beam assisted (Wang R.-P. 1998).

Table 4.3. Lattice parameters of ceria (CeO_2).

References	Lattice parameters, [Å]		
	Expt.	Sim.	
Dmowski 1998 **Putna 1999**	5.385 thin film on YSZ 5.411 bulk	-	
de Carolis 1999	-	5.42	
Mogensen 2000	5.4113 room temp.	-	
This work (potentials from Sayle T. X. T. 1994a)	-	5.42	
		Ce – O	2.35
		O – O	2.71
		Ce – Ce	3.83

Nörenberg and Briggs (1997, 1998 and 1999b) studied defect structure and surface morphologies of nonstoichiometric CeO_2(111) surfaces created by annealing at 1000ºC under ultra high vacuum conditions (UHV). They found that the nonstoichiometric surface appears well ordered and atomically flat with regions containing triangular defects. The authors proposed that the triangular defects consist of three oxygen vacancies. If the annealing is continued for a longer period and/or at higher temperature, line defects will appear on the surface. After repeated annealing in UHV (extreme case of oxygen lean conditions), the line defects are replaced with hexagonal arrays of triangular defects. These results are in agreement with theoretical predictions made by Sayle T. X. T. (1992 and 1994a) and Conesa (1995) through atomistic computer simulation.

Sayle T. X. T. (1992, 1994a and 1994b) investigated different surfaces of ceria, their structure, relative stability, the role of oxygen vacancies on ceria surfaces in the oxidation of CO and the influence of noble metals ions on catalytic activity of ceria. It was found that the stability of ceria surfaces increases in the order (310), (110) and (111). In addition, the formation of oxygen vacancies on the (110) and (310) surfaces is easier and CO oxidation on these surfaces is more energetically favourable. It was also found that vacancies are more stable at the surface than in the bulk of the crystal and that Rh^{3+}, Pd^{2+} and Pt^{2+} segregate, together with oxygen vacancies, at the surface, influencing the catalytic activity of ceria.

In agreement with previous works, Conesa (1995) reported that the (111) surface is the most stable one, followed by (110), and (100). Other surfaces such as (210) and (310) are much less stable, suggesting that these surfaces suffer important reconstructions and/or faceting. For the (111) surface, it was found that anion vacancies have a tendency to associate in paired structures on (111) surface.

A theoretical study on growth of ceria clusters (Cordatos 1996a) also showed that these clusters exhibit (111) surface facets, indicating that this is the most stable.

Another extensive work on CeO_2 was performed by Vyas and coworkers (1998). Different ceria surfaces were predicted using four different inter-atomic potentials. It was found that the surface energy change as a function of surface orientation is maintained for all potentials. In accord with previous results it was also found that the (111) surface is the most stable, irrespective of the potential used.

Baudin and co-workers (2000) showed in a recent study, using molecular dynamical simulation on CeO_2 slabs, that interplanar relaxation is largest for the (001) cation-terminated surface, decreasing for (011) and (111) surfaces with mean square displacements (MSD) for oxygen and cerium ions following the same trend. They confirmed again that (111) surface is the most stable.

Based upon careful consideration of the literature this study will specifically focus on CeO_2/ZrO_2(111), CeO_2/YSZ(111) and CeO_2/YSZ(110) systems. The cubic ZrO_2 was chosen as a model system for the support,

which will be extended to cubic YSZ. Considering that the ceria (110) surface is a surface with lower stability compared with the (111), (Sayle T. X. T. 1992, 1994ab and Balducci 1998), the resulting (110) system may present improved catalytic properties. Reconstruction of the thin film in response to the support is expected to take place, which might include different structural modifications that can help for example to increase oxygen mobility across the interface and in the thin film leading to a better catalytic material.

4.2. Methodology

The calculations presented in this chapter are based on the Born model for ionic solids, as was described previously, using a rigid ion model to reduce the computational expense. The potential parameters employed in this study to model the CeO_2 thin film and underlying ZrO_2 and YSZ supports were taken from Lewis and Catlow (1985) for Y^{3+}, Dwivedi and Cormack (1990) for Zr^{4+} and O^{2-} and Sayle T. X. T. (1994a) for Ce^{4+} (table 4.4). These potentials have been used to model lattice parameters (Balducci 2000), thermal expansivities (Khan 1998), conductivity and diffusion properties (Khan 1998) for CeO_2-ZrO_2, ZrO_2-M_xO_y and CeO_2-M_xO_y solid solutions, in accord with experiment. In addition, a mean field strategy (Morris 1993) was employed to represent the fixed ions comprising the yttrium-stabilized zirconia support, considering the standard two-region methodology (Gay 1995).

A mean field strategy was chosen to represent the ions included in region 2 of the YSZ support rather then create a 'real' yttrium-stabilized zirconia environment, which would necessitate the introduction of specific defects (oxygen vacancies to compensate for the introduction of randomly distributed Y^{3+} ions that replace Zr^{4+}). These types of defects can be inhomogeneous, owing to the random distribution, giving perhaps artificial results for anything other than huge systems. Therefore by using a mean field strategy 'hybrid' ions can be created with assigned potentials obtained by averaging the real potentials over the average occupancy of Zr/Y.

The basic mean field strategy employed in this study is now discussed. $Zr_xY_{1-x}O_{2-x/2}$, is assumed to contain a single, 'hybrid' cationic species, between Zr^{4+} and Y^{3+}. Considering that 10% (x=0.1), which corresponds to 9.24 mol. % Y_2O_3 (the value was chosen to be consistent with experimental and theoretical data, which confirm that maximum oxide ion conductivity in bulk YSZ was observed at around 8-10 mol % Y_2O_3), of the zirconium ions are replaced with yttrium, and oxygen vacancies are created to preserve electroneutrality of the system, the new 'hybrid' charges will be +(4-x) and –(2-x/2) for the 'hybrid' M(Zr/Y) and O species, respectively. Accordingly, the short-range parameters describing 'hybrid' – 'hybrid' interactions and 'hybrid' – ion interactions can be calculated (table 4.4) by scaling the short range repulsive interactions to give a value based upon average occupancy, using the following equations:

$$\Phi_{M^{3.9+}-O^{2-}} = (1-x)\Phi_{Zr^{4+}-O^{2-}} + x\Phi_{Y^{3+}-O^{2-}} \quad \textbf{(4.1)}$$

$$\Phi_{M^{3.9+}-O^{1.95-}} = (1-x/4)\Phi_{M^{3.9+}-O^{2-}} \quad \textbf{(4.2)}$$

$$\Phi_{O^{1.95-}-O^{1.95-}} = (1-x/4)(1-x/4)\Phi_{O^{2-}-O^{2-}} \quad \textbf{(4.3)}$$

New lattice parameters for yttrium-stabilized zirconia were then calculated using the GULP code, based upon these 'hybrid' potentials.

The materials explored in this study, CeO_2 and YSZ (10% of the Zr^{4+} ions replaced with Y^{3+}, which corresponds to 9.24 mol. % Y_2O_3) are both ionic solids with fluorite type structure (Mogensen 2000 and Li P. 1994a). ZrO_2 was also assumed to have a fluorite type structure in spite of its polymorphism (see chapter 4.1.1.1). This assumption was made considering that the cubic and tetragonal phase can be stabilized at room temperature if the crystallites are obtained in appropriate conditions. Also the potentials available for modelling monoclinic zirconia give poor values for lattice parameters; the differences between experimental and theoretical data are smaller for cubic fluorite structure compared with monoclinic (Stefanovich 1994). Therefore considering that for our complex systems a

very good representation of the lattice parameters is essential for interfacial matching, potential parameters for the cubic structure were chosen.

Table 4.4. Potentials parameters of the form $\Phi = A\exp(-r/\rho) - Cr^{-6}$ employed in this study; $M^{3.9+}$ represents the 'hybrid' yttrium/zirconium species; cut off = 10 Å.

Short-range potential parameters			
Ionic pair	**A [eV]**	**ρ [Å]**	**C [eV·Å^{-6}]**
Ce^{4+} - O^{2-}	1986.83	0.3511	20.40
Zr^{4+} - O^{2-}	985.87	0.3760	0.00
Y^{3+} – O^{2-}	1345.10	0.3491	0.00
O^{2-} – O^{2-}	22764.30	0.1490	27.89
Short-range potential parameters using mean field approach			
$M^{3.9+}$ - O^{2-}	1021.79	0.3733	0.00
$M^{3.9+}$ - $O^{1.95-}$	996.25	0.3733	0.00
Ce^{4+} - $O^{1.95-}$	1937.16	0.3511	19.89
Zr^{4+} - $O^{1.95-}$	961.22	0.3760	0.00
Y^{3+} - $O^{1.95-}$	1311.47	0.3491	0.00
O^{2-} - $O^{1.95-}$	22195.20	0.1490	27.19
$O^{1.95-}$ - $O^{1.95-}$	21626.10	0.1490	26.50

The first system considered, $CeO_2/ZrO_2(111)$ is used as a model representative of the more complex CeO_2/YSZ(111) system.

Lattice parameters, calculated using the GULP code, based on potentials presented above, and experimental data are listed in table 4.1-4.3 for ZrO_2, YSZ and CeO_2, respectively. The calculated lattice parameters are in good agreement with experimental data, therefore they are suitable for interfacial simulations on complex systems. The misfit based upon calculated lattice parameters between CeO_2 and ZrO_2, CeO_2 and YSZ, calculated using equation B.1 (Appendix B), are +6.7% and +6.1%, respectively.

The construction of the CeO_2/ZrO_2 and CeO_2/YSZ interfaces was achieved using 'cube-on-cube' methodology and explored using a simulated amorphisation and recrystallisation methodology as described in chapter 2. The ceria thin film is constrained initially under considerable pressure and placed on top of the support. The thin film responds, under dynamical simulation, to this huge initial pressure and relieves it via a transition of the thin film from a crystalline to an amorphous structure. Prolonged dynamical simulation results in the recrystallisation of the thin film together with the evolution of structural modifications as the system responds to the lattice misfit and interaction potential of the support. The construction for each particular system will be described later.

The dynamical simulations, which employ three-dimensional periodicity, were performed using the DL_POLY code (Smith 1999), and therefore a void, 55 – 75 Å in size depending on the thin film thickness, normal to the surface was introduced to represent the free surface. The distance is sufficient to ensure that interactions between the system and its periodic images normal to the interface are negligible. The simulation cell contains ions distributed in two regions: region 1 comprises the thin film and the first six repeat units of the support and ions within this region are allowed to move under the dynamical simulation, while region 2 comprises ions (four repeat units of the support) that are kept fixed to ensure a correct crystalline environment (fig. 2.7 and 2.8).

All simulations were performed within **NVE** ensemble: constant **N**umber of particles, constant **V**olume and constant **E**nergy with instantaneous velocity scaling to the simulation temperature used throughout. This prevents the rapid and large build up of excess kinetic energy as the thin film evolves from the highly strained initial configuration, via an amorphous transition, to a crystalline phase with reduce strain and a range of defects.

The evolution of the amorphisation and recrystallisation process was monitored using radial distribution functions (RDF) and mean square displacements (MSD) of the ions during the dynamical simulation.

4.3. $CeO_2/ZrO_2(111)$ interfaces

First, the stable type 1 $ZrO_2(111)$ surface (see Appendix C) is considered as a substrate for supporting CeO_2 thin films.

To generate the $CeO_2/ZrO_2(111)$ system, two $CeO_2(111)$ repeat units (thick) were placed on a 40×40 $ZrO_2(111)$ substrate (ca. 144 Å for each side of the simulation cell), giving an interfacial area of 17,849 $Å^2$. The 40×40 refers to the size of the simulation cell, which comprises 40 ions or 20 ZrO_2 units for each side of the simulation cell. Amorphisation was induced by constraining the CeO_2 thin film under compression (following equation B.2 Appendix B) in two cases: (a) 15%; (b) 31%. These two cases of initial setup for the $CeO_2/ZrO_2(111)$ system, were chosen in order to explore the possibility of amorphisation induced by either 'medium' or 'high-strain' and to investigate whether this has any influence on the final structure.

4.3.1. 15% compression

The $CeO_2/ZrO_2(111)$ system was created by placing a 44×44 CeO_2 thin film directly above a 40×40 $ZrO_2(111)$ support, (two repeat units included in region 1 and four repeat units included in region 2), giving a simulation cell containing 40,416 ions. The CeO_2 was then compressed by 15% to ensure the thin film fitted exactly within the simulation cell.

Dynamical simulation, with a time-step of 5×10^{-3} ps, was then applied to the system for 140 ps at 2000 K, 450 ps at 1000 K and 130 ps at 0 K; the latter acts effectively as an energy minimisation and was performed until the energy converged. For each temperature, the dynamical simulation was performed for sufficient a duration to ensure that the system was no longer evolving structurally nor energetically.

4.3.1.1. Amorphisation and recrystallisation

The MSD of cerium and oxygen ions during the dynamical simulation is presented in fig. 4.1. It can be seen that for cerium, the MSD increase rapidly at the beginning of the simulation, during the amorphisation process, while after ca. 50 ps it plateaus indicating much reduced diffusion as the recrystallisation nears completion. For the oxygen ions the same

behaviour was observed at the beginning of the amorphisation, while at the end, the gradient of the curve remains positive indicating high mobility of the oxide ions. The shape of the MSD curves suggests that the thin film does not melt (Sayle D. C. 2001a).

The calculated Ce-O RDF within the CeO_2 thin film are shown for the initial configuration (fig. 4.2a), after 0.25 ps (fig. 4.2b), after 25 ps (fig. 4.2c) and at the end of the simulation (final structure, fig. 4.2d). Inspection of the figures reveals that after 0.25 ps, the CeO_2 thin film loses partially the long-range order, suggesting an amorphous transition without melting. At 25 ps, the ceria thin film starts to regain long-range order, indicating recrystallisation of the CeO_2 thin film. The RDF graph for the final structure depicts broad peaks indicating poor crystallinity. In addition, inspection of the atom positions for the final structure, fig. 4.3, reveals the presence of large crystalline regions separated by amorphous regions.

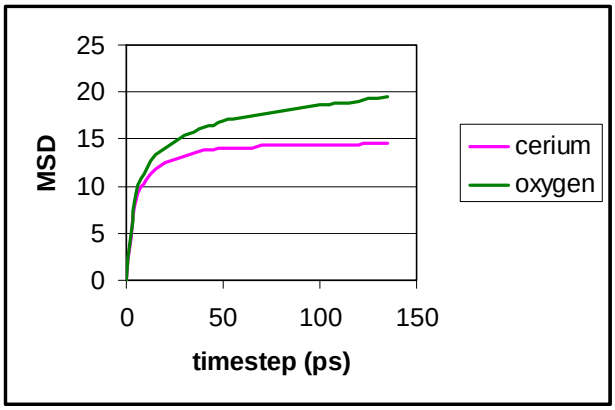

Fig. 4.1. *Calculated cerium and oxygen mean square displacements (MSD) measured in $Å^2$ within the $CeO_2/ZrO_2(111)$ system during dynamical simulation performed at 2000 K.*

Since under 15% compression the thin film remains partially amorphous, it can be suggested tentatively that the methodology has led to an artificial structure. This might be due to the amorphous starting point having insufficient energy (not enough compression) to explore the configurational space. The next system considered will contain the thin film under a higher compression (+31%).

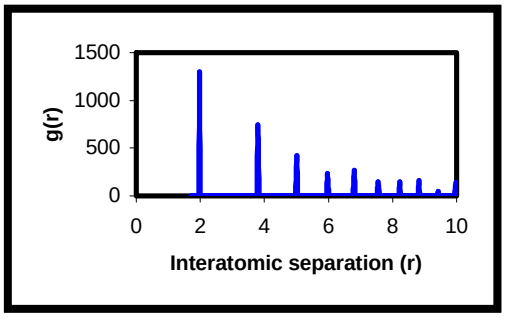

(a)

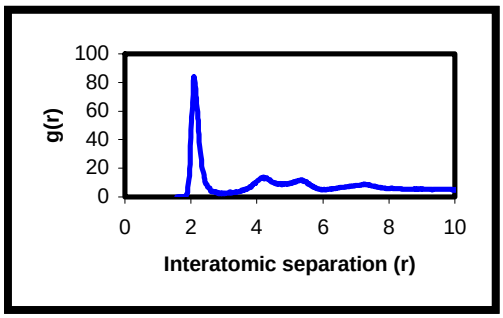

(b)

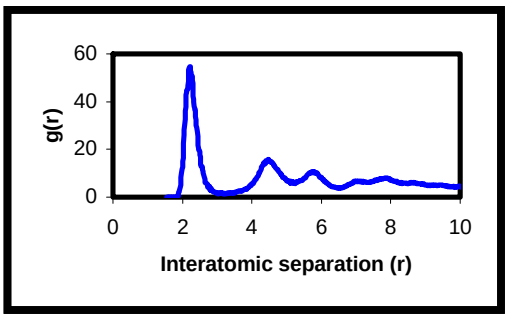

(c)

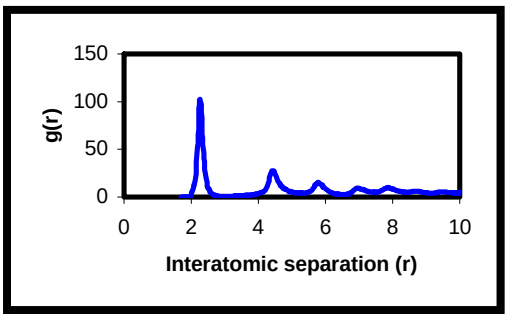

(d)

Fig. 4.2. *Calculated Ce-O radial distribution functions within the CeO_2 thin film during dynamical simulation performed at 2000 K: (a) initial; (b) after 0.25 ps; (c) after 25 ps and (d) at the end of simulation. Interatomic separations are measured in Å.*

Fig. 4.3. *Plan view of the $CeO_2/ZrO_2(111)$ system. Only two units of the support are presented for clarity. Zirconium is coloured light blue, cerium is magenta, oxygen (ZrO_2) is red and oxygen (CeO_2) is green.*

4.3.2. 31% compression

The $CeO_2/ZrO_2(111)$ system, was created by placing a 54×54 CeO_2 thin film directly above a 40×40 $ZrO_2(111)$ support, (six repeat units included in region 1 and four repeat units included in region 2), giving an interfacial area of 17,849 $Å^2$ and 65,496 ions within the simulation cell. The CeO_2 was then compressed by 31% to ensure that the thin film fitted exactly within the simulation cell. A trial simulation (dynamical simulation at 2000 K for 125 ps) with only two ZrO_2 repeat units included in region 1 revealed complete recrystallisation of the CeO_2 thin film. Accordingly, the thickness of the support included in region 1 was increased to six ZrO_2 repeat units to ensure adequate representation of the support within the model.

Dynamical simulation, with a time step of 5×10^{-3} ps, was then applied to the system for 115 ps at 3400 K, 55 ps at 2500 K, 5 ps at 2000, 1500 and 1000 K, 40 ps at 500 K, 10 ps at 100 K and 20 ps at 0 K; the latter acts effectively as an energy minimisation and was performed until the energy converged. For each temperature, the dynamical simulation was performed until the system was no longer evolving structurally nor energetically.

4.3.2.1. Amorphisation and recrystallisation

Structural characterisation and evolution of the amorphisation and recrystallisation, induced via a 31% compression of the CeO_2 thin film, is presented in figures 4.4a-c for the initial structure, after 0.25 ps and final structure, respectively.

Fig. 4.4a depicts the initial structure with the ceria thin film constrained under considerable pressure together with the calculated Ce-O RDF. As the dynamical simulation progresses, the thin film expands along the surface normal in an attempt to eliminate the considerable strain present in the initial structure and causes the thin film to amorphise. After 0.25 ps, fig. 4.4b, the corresponding Ce-O RDF demonstrates almost no long-range order indicating the amorphous transition. After prolonged dynamical simulation, the ceria thin film starts to recrystallise realising, at the end of the simulation, a cubic fluorite structure, fig. 4.4c. However, the RDF graph exhibits here sharp peaks, in contrast with the final structure for the case of

15% compression (fig. 4.2d) suggesting that for 31% compression a structure with higher crystallinity is obtained.

The success of the simulated amorphisation and recrystallisation methodology in generating the CeO_2 structure from an amorphous solid suggests that the methodology is applicable to study supported fluorite structured systems in addition to the supported rocksalt-structured systems considered previously (Sayle D. C. 1999c, 2001a).

4.3.2.2. Structural characterization

Inspection of the final structure of the $CeO_2/ZrO_2(111)$ system, fig. 4.4c, reveals that the thin film has recrystallised completely into the fluorite structure, with the CeO_2 exposing the (111) plane at both the interface and CeO_2 surface. The thin film comprises ca. five CeO_2 repeat units with partial (ca. 25%) occupancy of the surface layer (layer five, fig. 4.5a), which comprises small clusters ranging from Ce_2O_4 and Ce_4O_8, to large clusters with surface areas up to ca. 2000 $Å^2$. A layer-by-layer representation of the cerium thin film sublattice is presented in fig. 4.5a-e. The white atoms in fig. 4.5a represent the few cerium ions, which have started to populate the sixth layer.

The underlying $ZrO_2(111)$ support, which comprises six layers in region 1, include significant structural modifications such as dislocations and vacancies only in the first two layers from the interface, fig. 4.6a-b, with the remaining four layers maintaining a perfect cubic fluorite structure.

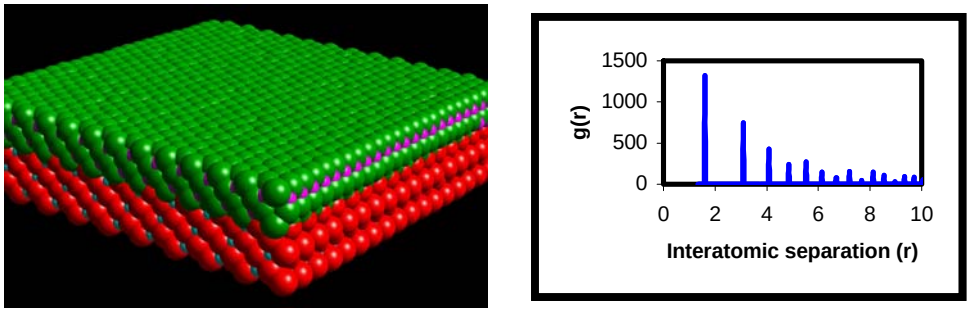

(a)

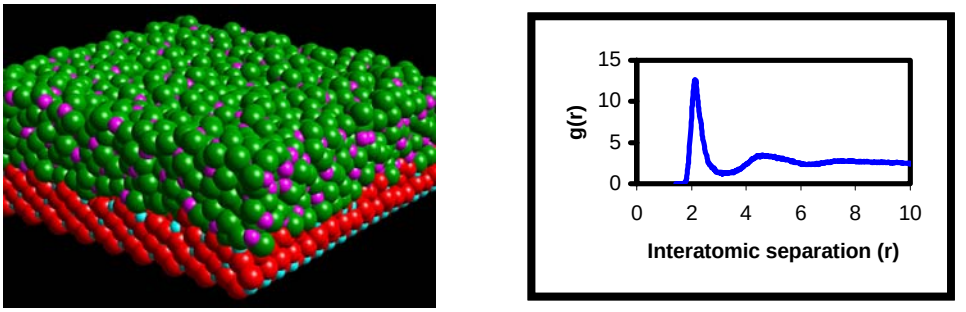

(b)

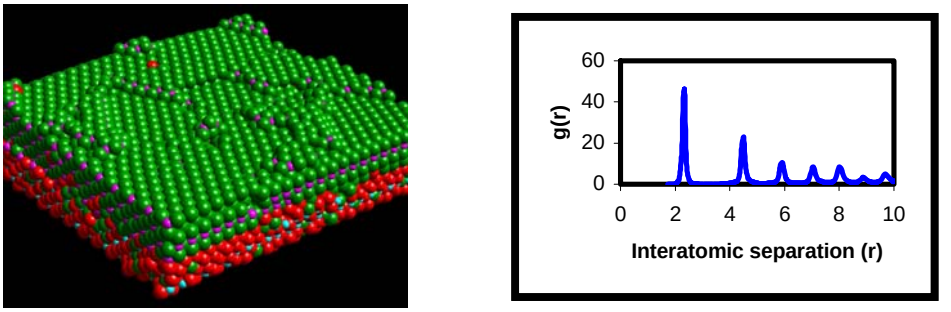

(c)

Fig. 4.4. *Sphere model representation of the $CeO_2/ZrO_2(111)$ interface during dynamical simulation performed at 3400 K: (a) starting structure; (b) after 0.25 ps and (c) final structure. For reason of clarity, only part of the full simulation cell and three planes of the support are depicted. Zirconium is coloured light blue, cerium is magenta, oxygen (ZrO_2) is red and oxygen (CeO_2) is green. To the right of each figure the corresponding Ce-O RDF is presented. Interatomic separations are measured in Å.*

Epitaxial relationships

The CeO_2 thin film lies almost coherent with the underlying ZrO_2 support, with the CeO_2 accommodating a 38×38 CeO_2(111)/40×40 ZrO_2(111) pattern with no rotation of the CeO_2 with respect to the underlying ZrO_2. The lattice misfit associated with such a configuration is therefore reduced from +6.7%, which is the bulk misfit between ceria and zirconia, to ca. +1.6% based upon the final interfacial structure; 38×38 CeO_2(111)/40×40 ZrO_2(111) or 19 CeO_2 units matched with 20 ZrO_2 units (see Appendix C). To maintain such a configuration, the CeO_2 thin lattice must be compressed by 1.6% to accommodate the misfit, which corresponds theoretically to a 'lattice parameter' of 5.34 Å. The matching between the interfacial cerium (layer 1) and zirconium (layer 6) sublattices is presented in fig. 4.7. The 'calculated' strain of +1.6% is not homogeneously distributed across the interface owing to the presence of the dislocations; rather it is expected that around the dislocation the local strain will be higher. Future studies will address this problem by visualising the strain gradient using colour contours.

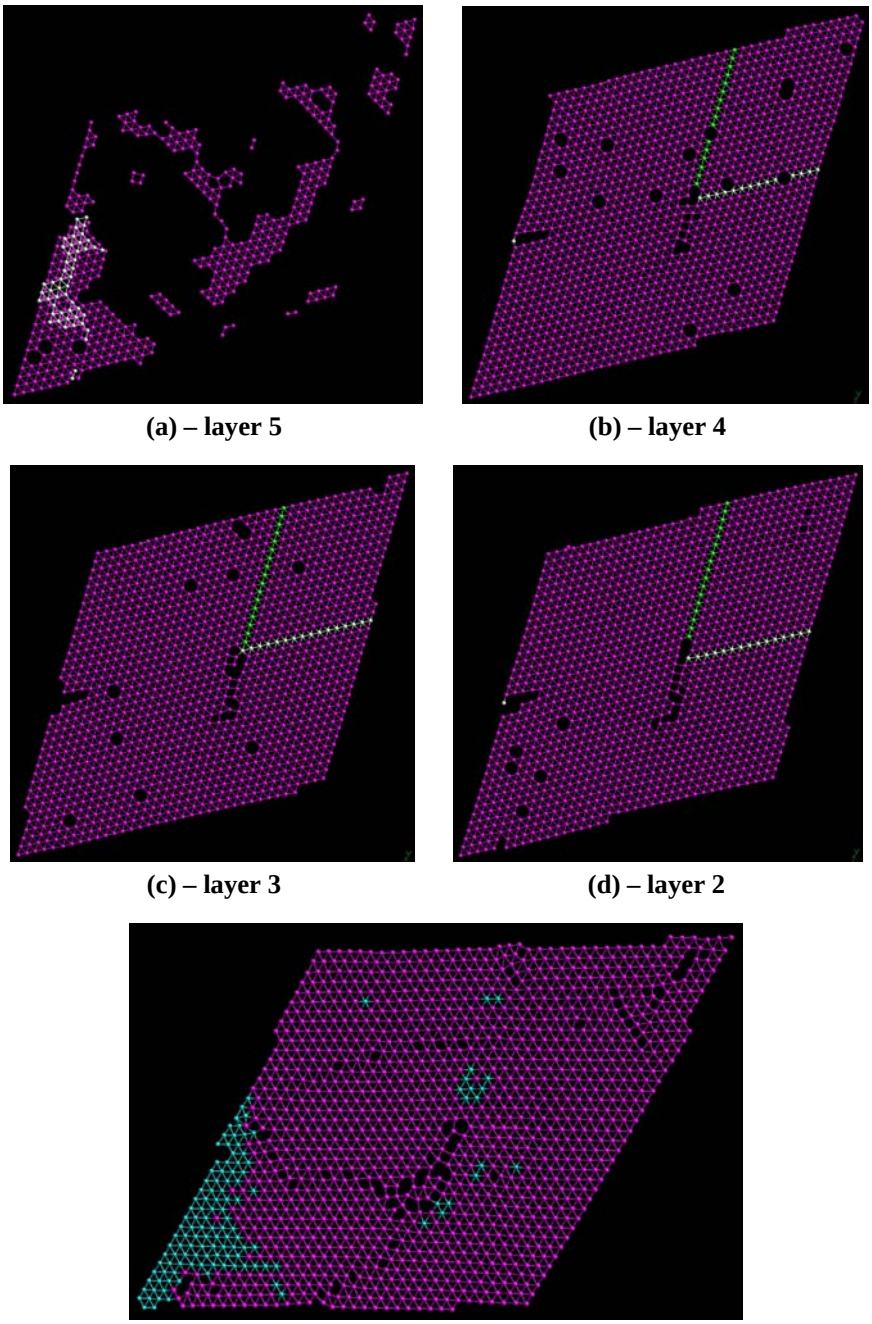

(a) – layer 5 **(b) – layer 4**

(c) – layer 3 **(d) – layer 2**

(e) – layer 1 (interfacial)

Fig. 4.5. *Layer-by-layer representation of the CeO_2 thin film. Only the cerium sublattice is shown for clarity. Cerium is coloured magenta and zirconium light blue.*

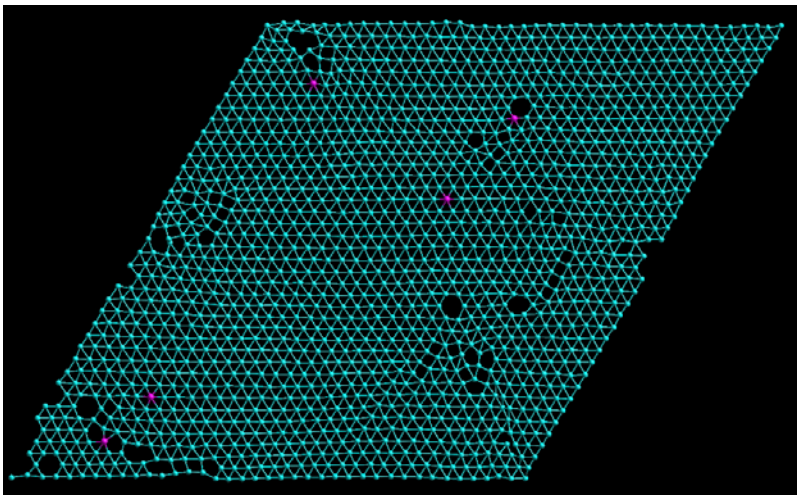

(a) – layer 6 (interfacial)

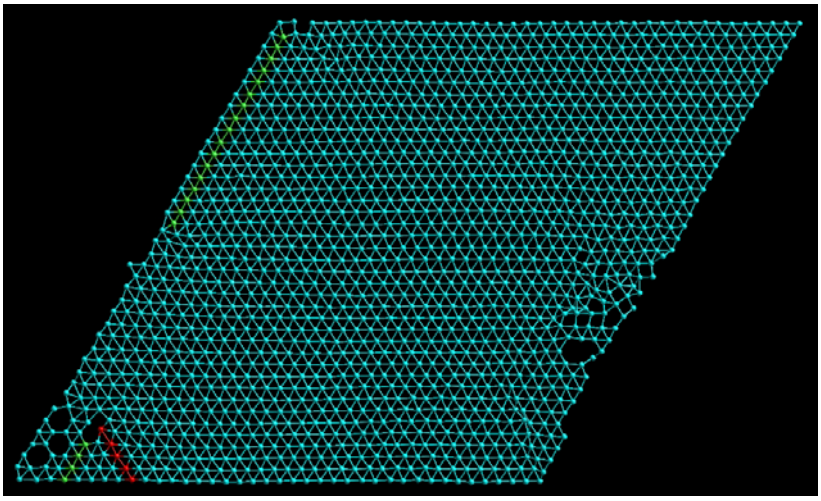

(b) – layer 5

Fig. 4.6. *Representation of the sixth (interfacial) and fifth $ZrO_2(111)$ underlying layers. For reasons of clarity only the zirconium sublattice is shown. Cerium is coloured magenta and zirconium light blue.*

Fig. 4.7. *Representation of the interfacial matching between CeO_2 thin film (layer 1) and underlying ZrO_2 support (layer 6). Only the cation sublattice is shown for clarity. Cerium is coloured magenta and zirconium light blue.*

Defects

A detailed analysis of the system, using graphical techniques, revealed that the system comprises cerium (ca. 0.8% for the whole thin film) and zirconium vacancies (ca. 0.3% for the first two layers near the interface) charge compensated by associated oxygen vacancies. Moreover, the density of vacancies within CeO_2 thin film increases within planes further from the interface (fig 4.5).

Analysis of the ceria and zirconia interfacial layers indicates interdiffusion between zirconium and cerium ions across the interfacial plane. Zirconium ions are observed to migrate up into the ceria interfacial layer and are visible as clusters and isolated ions (fig. 4.5e). Conversely only five cerium ions are present in the zirconia interfacial layer as individual ions (fig. 4.6a). Surprisingly it was observed that the number of cerium and zirconium cations that migrate across the interface is not equal. Considering the presence of other defects in this region such as vacancies and dislocations, and the unbalanced migration across the interface for cerium and zirconium ions it can be suggested that the distribution of all these defects facilitates some kind of strain gradient. Further work is needed to understant more fully this phenomenon.

The RDF, calculated layer-by-layer, in the thin film and support were determined and are presented as relative distances* in fig. 4.8.

For the underlying ZrO_2 support, Zr-O bond distances decrease towards the interface (from the bulk value of 2.19 to 2.04 Å), while O-O bond distances increase (from the bulk value of 2.53 to 2.82 Å). The Zr-Zr bond distances remain approximately in accord with the parent oxide.

Again such unusual structural modifications can be attributed to the system minimising interfacial strain.

For the CeO_2 thin film, the Ce-O, Ce-Ce and O-O bond distances show little deviation compared with the parent CeO_2. However, in the fifth and sixth layers owing to the low coordination of the ions in the surface region, which exist as clusters, the bond distances are much reduced. Calculated RDF for the whole thin film are: 2.35 Å for Ce-O, 3.85 Å for

* Relative distances were calculated as the difference between the M-O, M-M, and O-O bond distances and the corresponding values for the parent oxides (M=Ce, Zr).

Ce-Ce and 2.72 Å for O-O, in good agreement with bulk values 2.35, 3.83 and 2.71 Å, respectively (table 4.3).

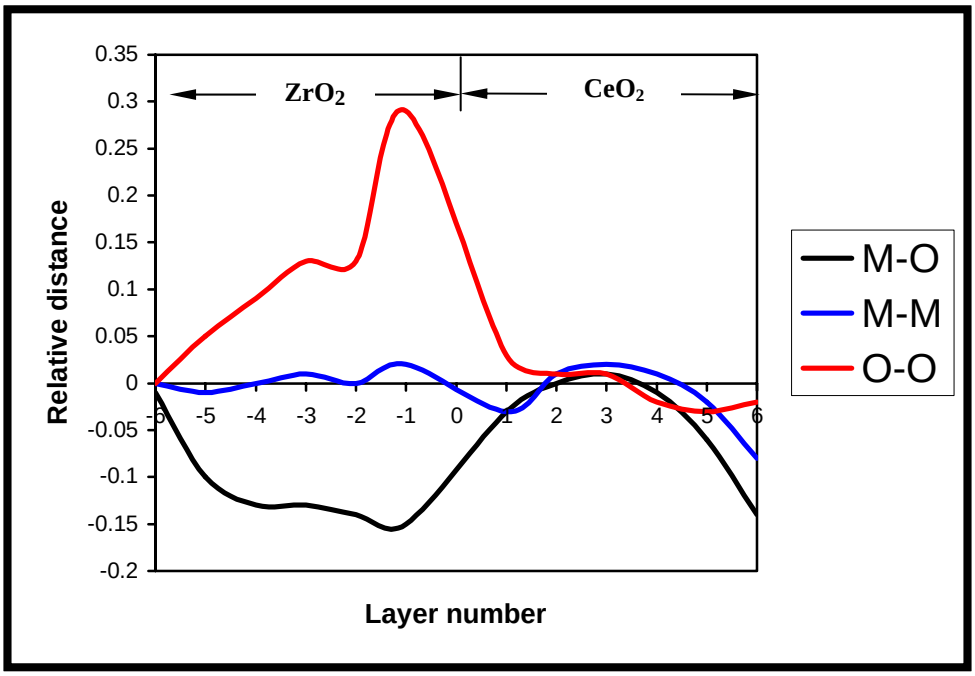

Fig. 4.8. *Representation of the relative distances, in Å, calculated between bulk values and determined values as a function of layer number in the $CeO_2/ZrO_2(111)$ system. A layer number of '0' represents the interface. (M=Ce, Zr)*

Dislocations

Careful inspection of the structure revealed complex dislocation networks including pure edge and mixed screw-edge dislocation, which have evolved within the system.

The screw-edge dislocation, as depicted in fig. 4.9a-b, traverses the entire thickness of the CeO_2 thin film and moreover, extends into the first layer of the ZrO_2 support, resulting in considerable perturbation of the underlying ZrO_2 support. In response, zirconium and oxygen ions migrate from the support to form a large associate defect cluster ca. 1500 Å in size,

which emanates from the base of dislocation core. Fig. 4.10 depicts more clearly the edge component of this screw-edge dislocation.

At present the tools available to analyse experimentally solid-solid systems cannot provide structural characterisation with atomic level resolution of these types of mixed screw-edge dislocations. Therefore atomistic simulation can provide an invaluable complement to experiment. Moreover, there have been no studies, which have focused on elucidating possible screw-edge type dislocations within CeO_2. Accordingly this is the first time a mixed screw-edge dislocation has been identified to evolve within a supported fluorite system. Indeed, the simulation methodology employed in this study has enabled the *evolution* of such defects.

Pure edge dislocations were observed in both the CeO_2 thin film and the ZrO_2 support. Inspection of the interfacial ZrO_2 and CeO_2 layers (fig. 4.11 and fig 4.12) revealed the presence of a network of edge dislocations, which lie parallel to the interfacial plane. It is notable that the concentration of dislocation is higher within the ZrO_2 interfacial layer compared with the overlying CeO_2. In case of the CeO_2 thin film, considering that the recrystallisation process takes place via an amorphous phase and the thin film can expand in a direction normal to the interface, the strain can be reduced not only through edge dislocation insertion but also through expansion; therefore the number of edge dislocation in the interfacial ceria layer will be smaller.

The second ZrO_2 layer from the interface (layer 5, fig. 4.6b) also contains structural modifications including dislocations. It is clear that the overlying thin film impose structurally a strong influence on the underlying ZrO_2 support.

In interfacial layers (both CeO_2 and ZrO_2), groups or single ions that appear as interstitials (indicated using arrows in fig. 4.11 and fig. 4.12) were also observed.

Further analysis revealed edge dislocations that evolve in the thin film, from the interfacial plane to as far as the fourth layer (depicted as white and light green lines in fig. 4.5b-d and fig. 4.13).

Misfit edge dislocations were also identified upon viewing cross-sections of the interface (fig. 4.14). Fig. 4.14a depicts a side view of the

simulation cell, which shows the presence of a regular array of dislocations with calculated inter-dislocation separations of ca. 65 Å, 82 Å, 50 Å and 75 Å, with a periodicity of ca. 68 Å. Misfit edge dislocations are evolving until the interfacial plane or until the layer under, in the ZrO_2 support. To illustrate more clearly the atomistic structure of the core region, fig. 4.14b, presents an enlarged segment of one of the dislocations.

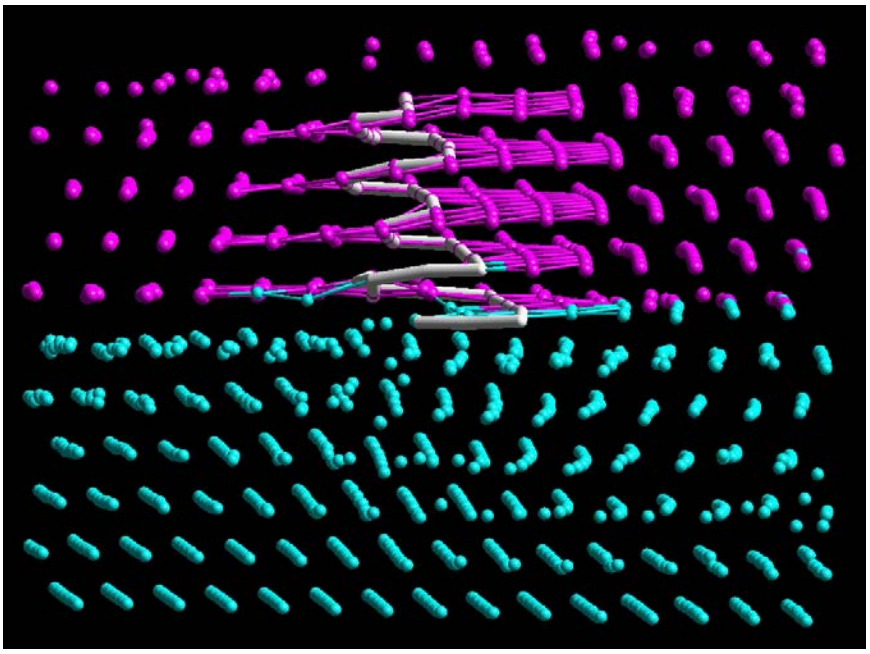

(a)

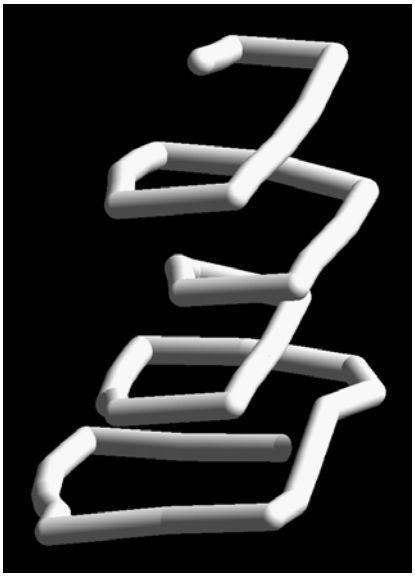

(b)

Fig. 4.9. *Stick model representation of the screw-edge dislocation (core structure) within the supported CeO_2 thin film: (a) in the surrounding cation sublattice and (b) as spiral of cerium ions. Only the cation sublattice is shown for clarity. Cerium is coloured magenta and zirconium light blue.*

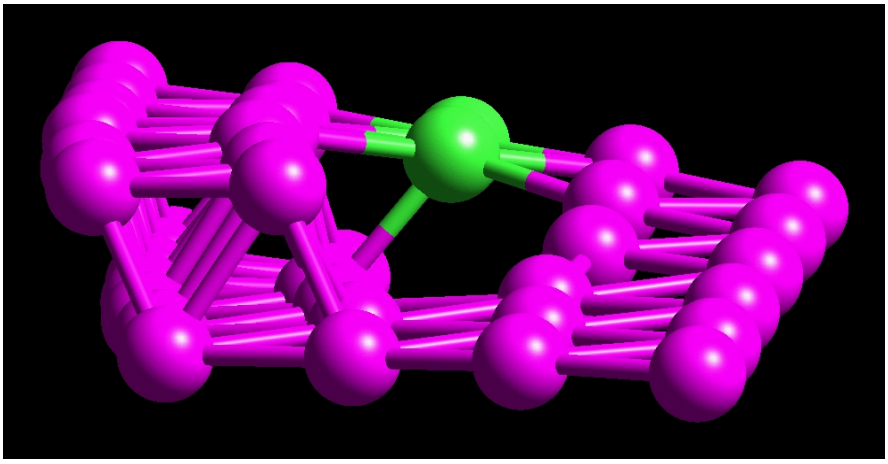

Fig. 4.10. *Ball and stick model representation illustrating more clearly the edge component (light green spheres) of the mixed screw-edge dislocation. Only the cerium sublattice is shown for clarity.*

Fig. 4.11. *Ball and stick representation of the interfacial zirconium sublattice, showing the complex dislocation network.*

Fig. 4.12. *Ball and stick representation of the interfacial cerium sublattice depicting the dislocation network within the layer.*

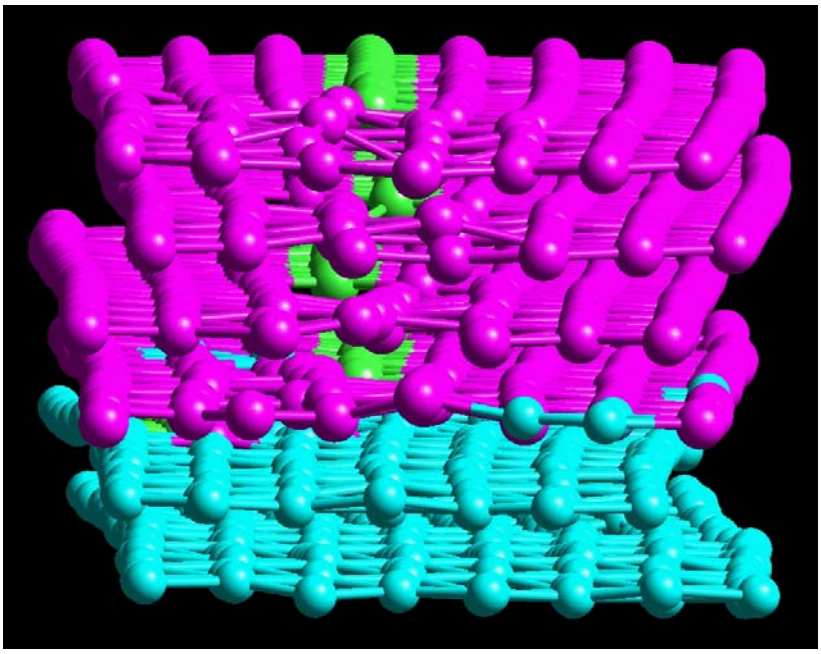

(a)

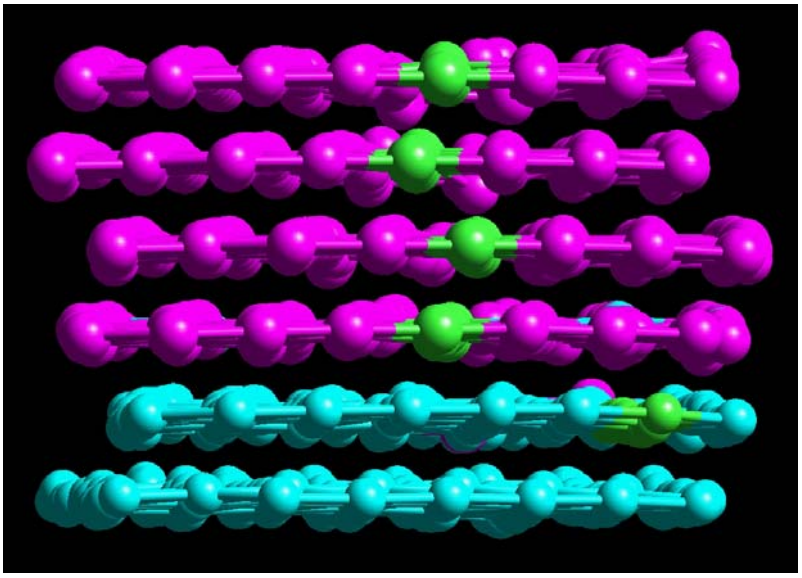

(b)

Fig. 4.13. *Representation of pure edge dislocations evolving in the first four layers of the CeO_2 thin film and interfacial ZrO_2 layer: (a) back view (perspective) and (b) front view. Green balls represent the edge dislocations. Cerium is coloured magenta and zirconium light blue.*

Fig. 4.14. *(a) Ball and stick representation of a cross-section of the $CeO_2(111)/ZrO_2(111)$ interface depicting the regular array of dislocations (red); (b) enlarged segment depicting more clearly, the core structure. For reasons of clarity only the cation sublattice is shown. Cerium ions are magenta and zirconium ions are light blue. Black horizontal arrows represent the interfacial plane.*

4.4. CeO_2/YSZ interfaces

Since the methodology was successful in generating a crystalline structure, for the $CeO_2/ZrO_2(111)$ model system, which also included a range of defects, the study was extended to examine the more complex system that of CeO_2/YSZ.

Two terminations of the underlying YSZ are considered, first the CeO_2 thin film was deposited on YSZ(111), and then on YSZ(110). Taking into account the fact that CeO_2 thin films were found to grow epitaxialy on (111) and (110) YSZ with the CeO_2 lying in the same direction as the underlying support (Putna 1999 and references therein) and considering that the ceria (110) surface has been identified as more unstable and potentially more reactive compared with the (111), one might expect a greater perturbation of the CeO_2 thin film and underlying YSZ(110) support compared with the CeO_2/YSZ(111). Consequently, the catalytic properties of the CeO_2/YSZ(110) system may be improved compared with the CeO_2/YSZ(111) system.

4.4.1. CeO_2/YSZ(111) interface

To generate the CeO_2/YSZ(111) interface three steps were followed (fig. 4.15). First, a $CeO_2/ZrO_2(111)$ system was constructed by placing two $CeO_2(111)$ repeat units (thick) directly on top of ten repeat units of $ZrO_2(111)$ support, (six repeat units included in region 1 and four repeat units included in region 2), using a 'cube-on-cube' methodology. In particular, a 54×54 (which corresponds to 54 cerium atoms or 27 CeO_2 units for each side of the simulation cell) CeO_2 thin film was placed directly above a 40×40 $ZrO_2(111)$ support, giving an interfacial area of 17,849 $Å^2$ and 65,496 ions within the simulation cell. To ensure the CeO_2 fits exactly within the simulation cell, the thin film was compressed by 31%.

Simulation trials on the $CeO_2/ZrO_2(111)$ system where the thin film was compressed by only 15% (see chapter 4.3.1 and Sayle D. C. 2001c), revealed that the initial pressure was not enough to generate an appropriate amorphous structure. Consequently, the energy of the system was insufficient to facilitate adequate recrystallisation of the thin film and the

final structure contained regions, which remained amorphous. Accordingly, a 31% compression was used to induce amorphisation.

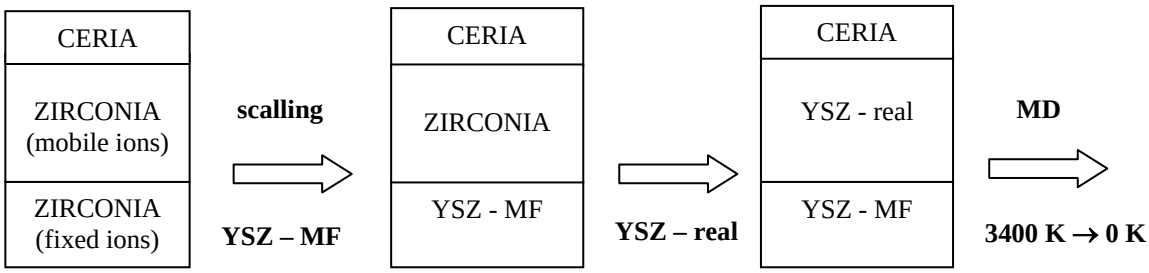

Fig. 4.15. *Schematic representation of the three stages involved in constructing the thin film interface.*

The second step was to introduce the mean field 'hybrid' ions into region 2 of the support and to scale the entire simulation cell from 5.075 Å, corresponding to cubic ZrO_2, to 5.106 Å corresponding to YSZ – MF. Accordingly, the interfacial area increased to 18,064 $Å^2$.

Finally, yttrium species were introduced into region 1 by replacing 10% of the Zr^{4+} ions with Y^{3+} (960 yttrium ions), corresponding to 9.24 mol. % Y_2O_3. 480 oxygen ions were then removed to maintain charge neutrality of the system. To facilitate such a procedure, an additional programme was used (Maicaneanu 2001b) to introduce yttrium ions and oxygen vacancies, at random, into the zirconia lattice. The whole simulation cell comprises finally 65,016 ions.

Dynamical simulation, with a time step of 5×10^{-3} ps, was applied to the system for 150 ps at 3400 K, 40 ps at 2500 K, 25 ps at 2000 K, 5 ps at 1500 K, 15 ps at 1000 K, 5 ps at 500 K and 85 ps at 0 K; the later acts effectively as an energy minimisation and was performed until the energy converged. For each temperature, the dynamical simulation was performed until the system was no longer evolving structurally nor energetically.

4.4.1.1. Amorphisation and recrystallisation

The MSD of cerium and oxygen ions for dynamical simulation at 3400 K is presented in fig. 4.16. It can be seen that for cerium, the MSD

increase rapidly at the beginning of the simulation during the amorphisation process reflecting high mobility of the cerium ions. Conversely, after ca. 50 ps the MSD plateaus, indicating little diffusion once recrystallisation nears completion. For the oxygen ions similar behaviour is observed at the beginning of the amorphisation, whilst towards the end, the curve maintains a positive gradient indicating that the oxygen species retain significant mobility even after recrystallisation. This is to be expected due to the high mobility of oxygen within CeO_2 at high temperature.

We note that even if 3400 K is higher than the melting point of CeO_2 (2750 K, Mogensen 2000) it was found that CeO_2 did not melt at this temperature since scaled dynamics was imposed throughout the simulation. This strategy was used since the amorphisation and recrystallisation requires a considerable amount of computer time. Clearly, the higher the temperature the faster the ionic migration and hence recrystallisation. Accordingly, the most efficient use of computational resources is achieved by maximizing the simulation temperature without melting the system.

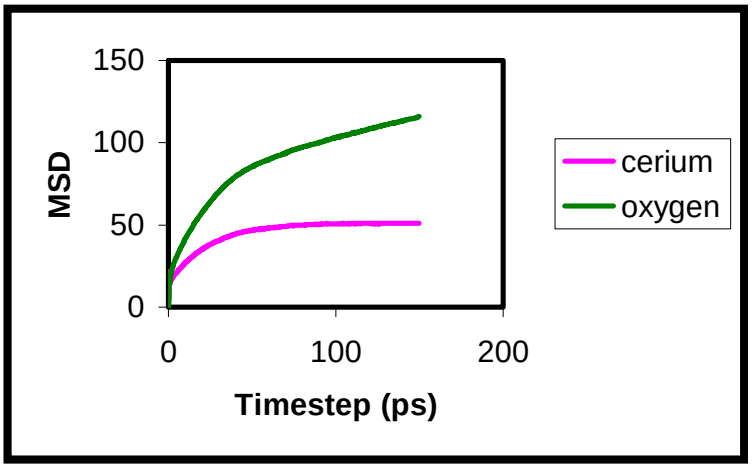

Fig. 4.16. *Calculated cerium and oxygen mean square displacements (MSD) measured in $Å^2$ within the CeO_2/YSZ(111) system as a function of time during dynamical simulation performed at 3400 K.*

The calculated Ce-O RDF within the CeO_2 thin film during dynamical simulation performed at 3400 K are shown in figs. 4.17a-e after

0.005, 0.25, 25, 150 ps and at the end of the simulation (final structure), respectively. Initially, the RDF peaks are sharp (fig. 4.17a) reflecting the high crystallinity of the initial structure. After 0.25 ps, fig 4.17b, the CeO_2 thin film loses long-range order, indicating an amorphous transition. At 25 ps, fig. 4.17c, the ceria thin film starts to regain long-range order, indicating recrystallisation of the CeO_2 thin film. At the end of the first stage of dynamical simulation (3400 K), after 150 ps, the thin film regains much of its crystallinity as depicted in fig. 4.17d. However, it is clear that the structure has rearranged significantly as shown by a shift of the RDF peaks from 1.9, 3.2 and 4.1 Å to 2.2. 4.3 and 6.0 Å respectively. Specifically the lattice parameter increases from 3.78 Å, associated with a 31% strain, to a value commensurate with the parent oxide, 5.42 Å. The RDF for the final structure, fig. 4.17e, shows sharp peaks indicating a highly crystalline structure obtained after cooling the system to 0 K.

For a visual link to the thin film structure, we show, in figs. 4.18a-c, part of the simulation cell comprising the thin film and three layers of the support. Fig. 4.18a represents the initial structure with the ceria thin film constrained under considerable pressure. As the dynamical simulation progress, the thin film expands along the surface normal in attempt to eliminate the huge strain present in the initial structure and causes the CeO_2 thin film to go amorphous after about 0.25 ps, fig. 4.18b. After prolonged dynamical simulation, the ceria thin film starts to recrystallise realising, at the end of the simulation, a cubic fluorite structure, fig. 4.18c.

Inspection of the MSD, RDF and structures for our system and comparison with those obtained by Sayle and Watson (2001a) for the SrO/MgO(001) system suggests that the thin film proceeds from a highly strained but crystalline initial structure, through an amorphous (solid) transition and then a final crystalline form. We find no evidence that at any stage does the CeO_2 become molten.

The next step is to identify and characterize all the structural modifications that evolve during the recrystallisation process in the thin film and the support in the final structure of the CeO_2/YSZ(111) system.

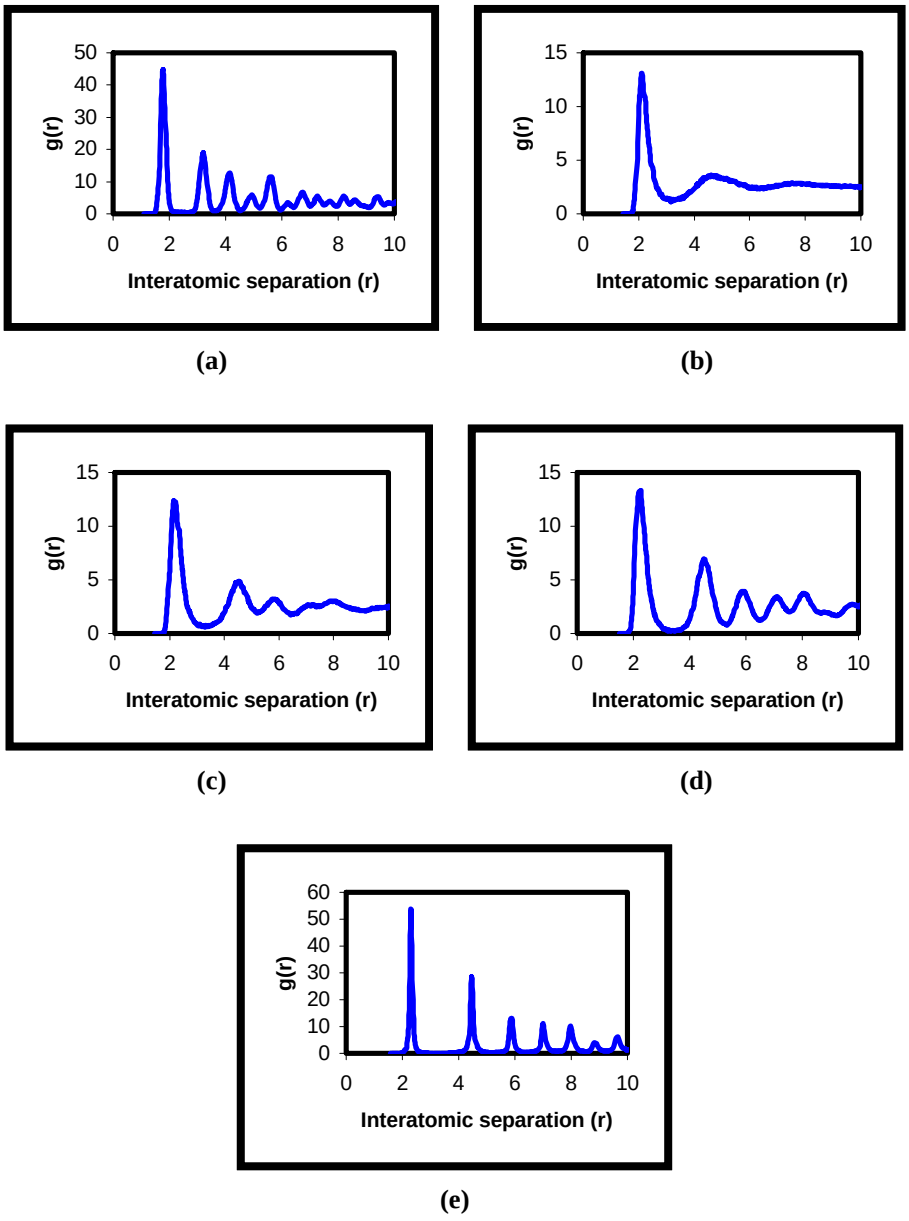

Fig. 4.17. *Calculated Ce-O radial distribution functions within the CeO_2 thin film during dynamical simulation performed at 3400 K after: (a) 0.005 ps; (b) 0.25 ps; (c) 25 ps; (d) 150 ps and (e) at the end of the simulation. Interatomic separations are measured in Å.*

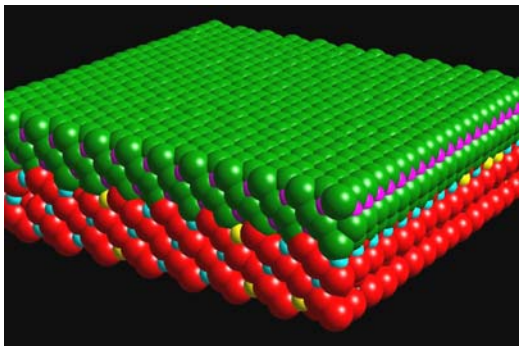

(a)

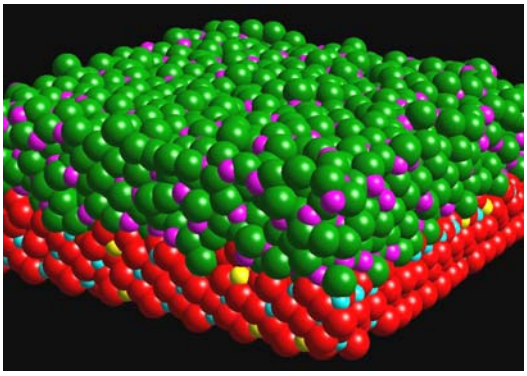

(b)

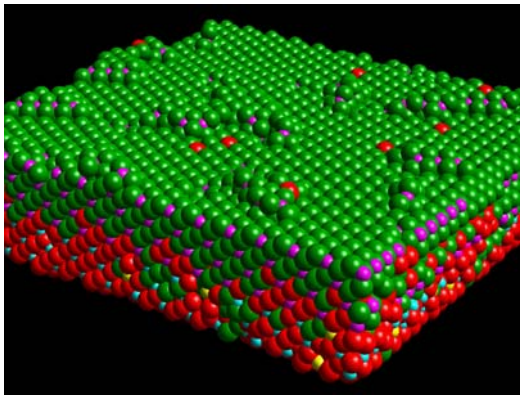

(c)

Fig. 4.18. *Representation of the CeO_2/YSZ(111) interface during dynamical simulation performed at 3400 K: (a) starting structure; (b) after 0.25 ps of dynamical simulation and (c) final structure. Zirconium is coloured light blue, cerium is magenta, yttrium is yellow, oxygen (YSZ) is red and oxygen (CeO_2) is green. To preserve clarity of the figure only a small part of the full simulation cell is shown together with three unit cells of the underlying support.*

4.4.1.2. Structural characterization

The final CeO_2 thin film, which is approximately 20 Å thick, exposes the (111) plane at both the interface and the surface and comprises ca. five CeO_2 repeat units with an incomplete surface layer. The surface layer (layer five) has an occupancy of about 25% and comprises small clusters ranging from, for example, Ce_2O_4 and Ce_4O_8, to larger clusters up to ca. 600 $Å^2$ in surface area (fig. 4.19 and 4.20a). The structure of each cerium layer is presented in figs. 4.20a-e.

The underlying YSZ support includes many structural modifications in the interfacial layer and few modifications in the next two layers from the interface, figs. 4.21a-c, while the other three layers maintain an unmodified cubic fluorite structure, (fig 4.21d).

Epitaxial relationships

Inspection of the epitaxial relationships that exist between the CeO_2 thin film and the YSZ support, reveals that the thin film lies almost coherent (fig. 4.22) with the underlying YSZ support with the CeO_2 accommodating a 37×38 pattern with no rotation of the thin film with respect to the support. The 37×38 refers to 37 atoms along the $[\bar{1}\ 1\ 0]$ and 38 along the $[\bar{1}\ 0\ 1]$, which are along the surface lattice vectors defining the simulation cell (fig. 4.23). The lattice misfit (based upon a 40×40 lattice for the underlying YSZ) associated with such a configuration is therefore reduced from +6.1% (bulk misfit) to -1.7% along the $[\bar{1}\ 1\ 0]$ and +1.0% along $[\bar{1}\ 0\ 1]$. We suggest that the misfit is reduced further (via relaxation of the lattice) by the CeO_2 being constrained under compression along the $[\bar{1}\ 0\ 1]$ in conjunction with tension along the $[\bar{1}\ 1\ 0]$. Surprisingly, the *interfacial YSZ* layer of the support also changes and presents a 39×39 pattern in contrast to the initial 40×40 configuration of the preparatory configuration; the remaining YSZ below retains the original 40×40 configuration.

Experimentally, Putna et al. (1999), who explored the structure and reducibility of ceria deposited on YSZ by vapour deposition, found that deposition on the YSZ(111) surface, resulted in the formation of semicoherent, epitaxial CeO_2 films oriented in the direction of the support.

In addition, Dmowski and co-workers (1998) found, for the same system (a 20 Å CeO_2 thin film deposited on yttrium stabilized zirconia), that the YSZ lattice parameter was 5.23 Å. This is larger than the value obtained for bulk diffraction (5.13 Å) of YSZ with yttrium doping levels of ca. 9.5%. Moreover, the authors suggest that there is some inhomogeneity in the YSZ crystal, which results in a change in lattice parameter as a function of depth. In this present study, the calculated lattice parameter for the 39×39 YSZ interfacial layer is ca. 5.24 Å in accord with the experimental results of Dmowski and co-workers.

The values assigned to the misfit have been based purely upon geometrical considerations. However, the presence of defects in the system together with ionic relaxation helps to reduce further any residual strain in the system.

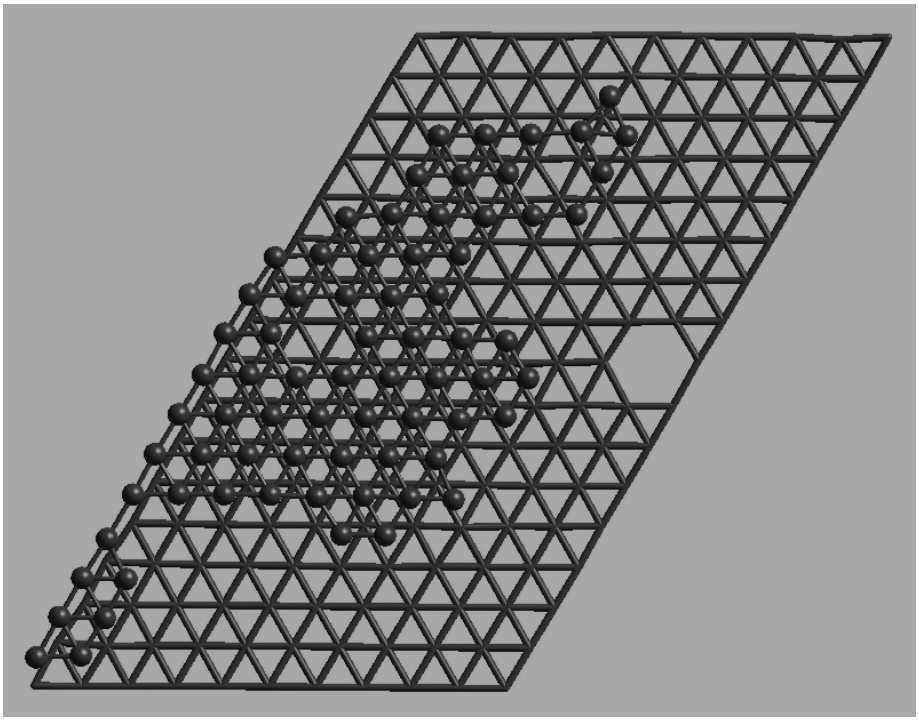

Fig. 4.19. *Ball and stick representation of one particular cluster from the CeO_2 surface layer (fifth layer from the interface). In addition, part of the underlying CeO_2 layer (fourth from the interface) is included as stick model. Only cerium sublattice is shown for reasons of clarity.*

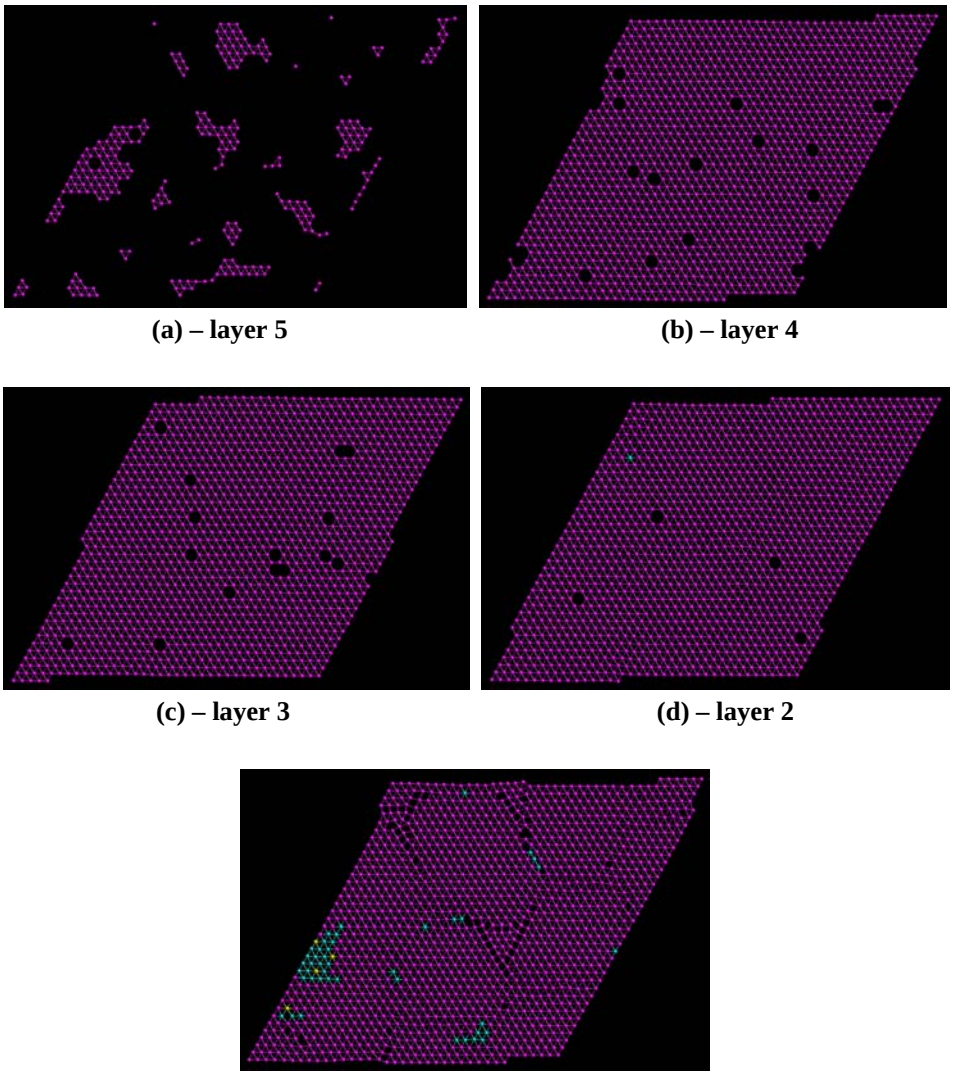

(a) – layer 5 **(b) – layer 4**

(c) – layer 3 **(d) – layer 2**

(e) – layer 1 (interfacial)

Fig. 4.20. *Layer-by-layer representation of the CeO_2 thin film. Only the cerium sublattice is shown for clarity. Cerium is coloured magenta, zirconium light blue and yttrium yellow.*

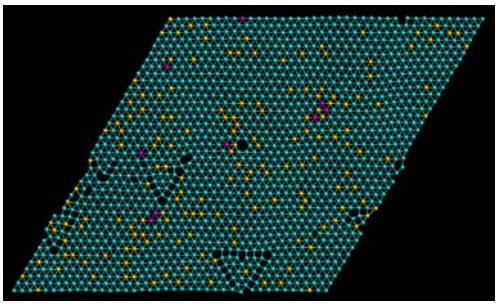

(a) – layer 6 (interfacial)

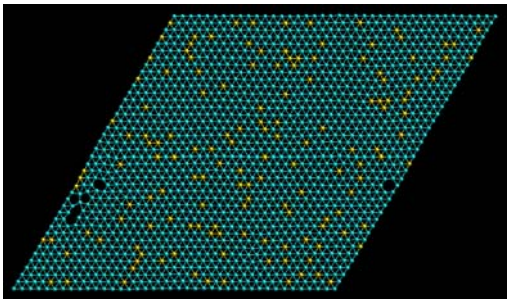

(b) – layer 5

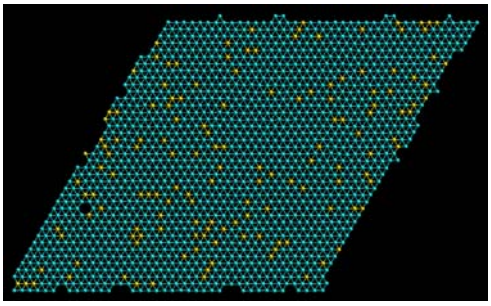

(c) – layer 4

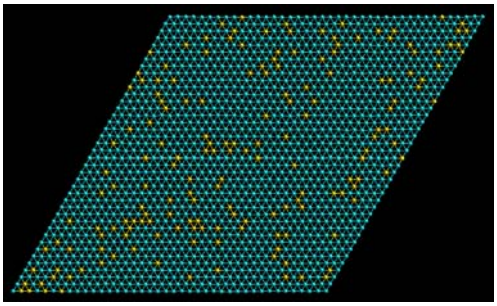

(d) – layer 3

Fig. 4.21. *Ball and stick representation of the first four ZrO_2(111) layers below the interfacial plane. For reasons of clarity only the zirconium sublattice is shown. Zirconium is coloured light blue, yttrium yellow and cerium magenta.*

Fig. 4.22. *Representation of the interfacial CeO_2 and YSZ planes, illustrating the epitaxy between the two materials at the interface. Only the cation sublattices and yttrium dopants are shown for clarity. Colour notation as fig. 4.18.*

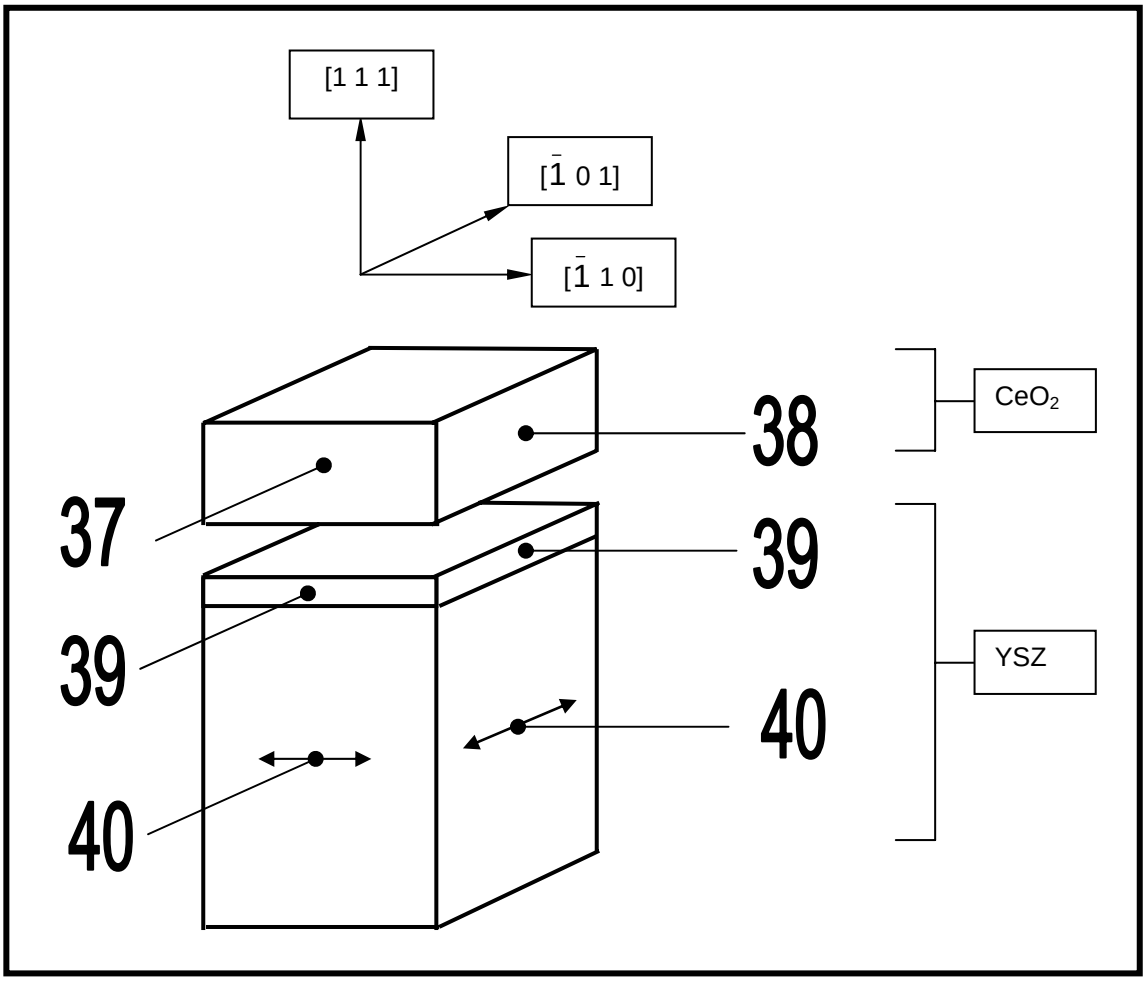

Fig. 4.23. *Schematic representation of the final structure of the CeO_2/YSZ(111) interface, highlighting the epitaxial relationships at the interfacial region.*

Defects

A layer-by-layer analysis of the system, using graphical techniques, revealed that the CeO_2 comprises ca. 0.8% cerium vacancies. However, no cerium vacancies were observed in the interfacial layer. For example, within the third CeO_2 plane from the interface, fig. 4.20c, 16 cerium vacancies are present. For the underlying YSZ support, 0.2% zirconium vacancies were identified within the first three layers from the interfacial

YSZ plane, figs. 4.21a-c. Clearly, the evolution of cerium and zirconium vacancies within the system disrupts the charge neutrality. Accordingly, oxygen vacancies are also present to restore charge balance. In addition, careful inspection of each layer revealed that the density of cerium vacancies within the CeO_2 thin film increases within planes further from the interface.

Analysis of the system also revealed interdiffusion of cerium, zirconium and yttrium across the interfacial planes. Cerium ions were observed to occupy zirconium lattice sites within the YSZ support and zirconium and yttrium occupying both cerium lattice sites and interstitial positions within the CeO_2 thin film. The interdiffusion is modest; ca. 3% of the interfacial cerium ions are displaced. Defect association as dimeric and trimeric cerium clusters was also observed. However, one particular cluster as shown in fig. 4.24, comprises, surprisingly, 23 zirconium and 3 yttrium ions, which may have evolved to help relieve locally the high strain within this particular region. In addition, the interdiffusion was observed to occur across only the interfacial CeO_2 and YSZ layers, which is in line with the experimental work of Lind et al (1992).

RDF analysis allowed a comprehensive study of bond distances for both CeO_2 thin film and underlying YSZ support (fig. 4.25). For the YSZ support the same behaviour was observed as in the case of the ZrO_2 support. Specifically, Zr-O bond distances decrease toward the interface (average value Zr-O 2.11 Å), while O-O bond distances increase in the same direction (average value 2.60 Å) and cation-cation and Y-O bond distances remain approximately constant at 3.60 Å for Zr-Zr and Zr-Y, 3.61 Å for Y-Y, and 2.35 Å for Y-O. These values are in good agreement with YSZ bulk values (table 4.2).

For CeO_2, the bond distances are commensurate with the parent oxide (table 4.3) suggesting little bulk strain within the system. Reduced bond distances in the fifth layer of the thin film can be attributed to the low coordination of ions within this layer, owing to the presence of small clusters, fig. 4.19 and 4.20a.

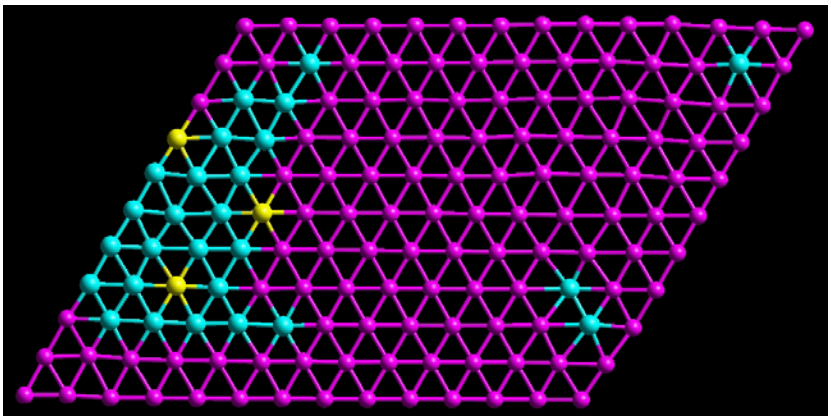

Fig. 4.24. *Representation of a small segment of the cerium interfacial layer illustrating the nature of the interdiffused cluster of zirconium ions and yttrium dopants. Oxygen ions have been omitted to preserve clarity. Colour notation as in figure 4.18.*

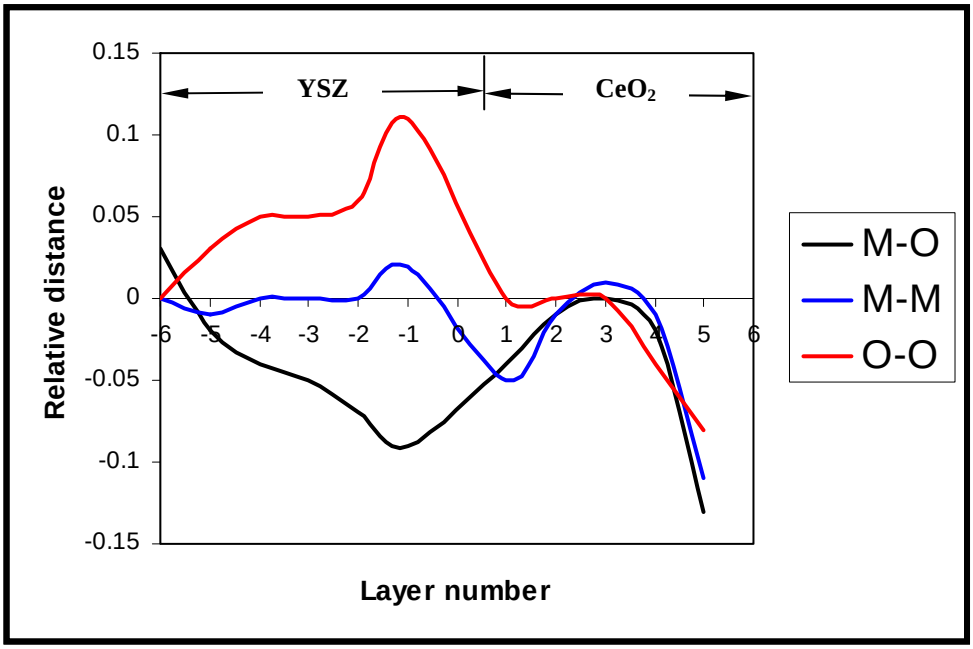

Fig. 4.25. *Representation of the relative distances, in Å, calculated between bulk values and determined values as function of layer number in the CeO_2/YSZ(111) system. A layer number of '0' represents the interface. To ensure the clarity of the picture only zirconium bond distances in the support were considered. (M=Ce, Zr)*

Dislocations

Inspection of the interfacial YSZ and CeO_2 layers (fig. 4.26 and fig. 4.27 respectively) revealed the presence of a network of edge dislocations, which lie parallel to the interfacial plane. The figures also demonstrate a higher concentration of dislocations within the underlying YSZ support compared with the overlying CeO_2. In figs 4.28a-c an enlarged segment of two neighboring dislocations is depicted, showing more clearly their core structure. Similar dislocation networks were observed, using transmission electron microscopy (TEM), in the GaAs/InP system; in GaSb/GaAs system, a square network of dislocations was found (Rocher 1999), fig. 4.29.

Associated interstitial ions were also observed. In the interfacial CeO_2 layer, six groups of interstitial ions comprising between 1 and 3 ions are observed, fig. 4.27 (white arrows), while in the YSZ interfacial layer, fig. 4.26 (white arrows), two groups, comprising 3 and 33 ions as interstitials, are identified.

Further inspection of the CeO_2 and YSZ layers revealed the presence of a pair of pure edge dislocations in the second YSZ layer from the interface, fig. 4.30 and 4.21b, while all the others are free of dislocations.

Fig. 4.31 depicts a side view of the simulation cell, which shows the presence of a regular array of dislocations with calculated inter-dislocation separations of ca. 61 Å, 50 Å, 47 Å, 65 Å and 54 Å with an average periodicity of ca. 55 Å. An enlarged segment of one such dislocation is shown in Fig. 4.31b to illustrate more clearly the atomistic structure of the core region. In contrast to the dislocations identified above, the lines of the dislocations identified here do not lie parallel to the interfacial plane. The figure also demonstrates that the dislocation cores reside in regions of poor match, halfway between the regions of good match (or coherent regions). A plan view of the simulation cell (fig. 4.22) reiterates this argument. An investigation of the atomistic structure of the $SrZrO_3/SrTiO_3$ interface, fabricated using metal-organic deposition of $SrZrO_3$ layers on $SrTiO_3$ single crystal substrates, showed that the dislocation core resides in regions of poor match (Ernst 1999). In addition, Wang A. et al. (1999) who explored the structure of the CeO_2/YSZ(001) system using metal-organic vapour

deposition observed dislocation arrays with a periodicity of ca. 44 Å in accord with the results presented in this study. It can be suggested that regions of poor match that exist across the interfacial plane help to maximize the interaction across the majority of the interfacial area in accord with experimental findings (Ernst 1999). A regular array of misfit dislocations were also identified in thin films of the perovskite manganites solid solutions (e.g. $La_{0.35}Pr_{0.35}Ca_{0.3}MnO_3$) deposited on YSZ, fig. 4.32.

In a previous study, on the $CeO_2/ZrO_2(111)$ system (Maicaneanu 2001a), both pure edge and mixed screw-edge dislocations were identified to have evolved within the supported CeO_2 thin-film. However, after careful analysis, we found no evidence of mixed screw-edge dislocations within either the supported CeO_2 or the underlying YSZ support for this present system.

The epitaxial relationship that evolves between the CeO_2 and underlying YSZ, enables the bulk lattice misfit and therefore the strain energy, associated with the system, to be reduced (based upon geometrical criterion) from ca. 6% to –1.7% along the [$\bar{1}$ 1 0] and +1.0% along [$\bar{1}$ 0 1]. However, this lattice misfit remains significant since the strain energy terms are additive for each layer comprising the thin film. At some particular (critical) thickness (Dong 1998), the strain energy terms will outweigh the energy associated with interfacial interaction and structural modifications, as we have identified above, will evolve.

Fig. 4.26. *Ball and stick representation of the interfacial YSZ layer, showing the complex dislocation network. To preserve clarity of the figure only the cation sublattice of the YSZ interfacial plane is depicted.*

Fig. 4.27. *Ball and stick representation of the interfacial cerium sublattice depicting the dislocation network within the layer.*

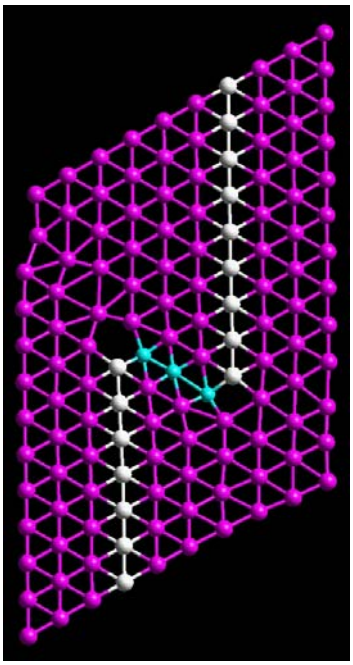

(a)

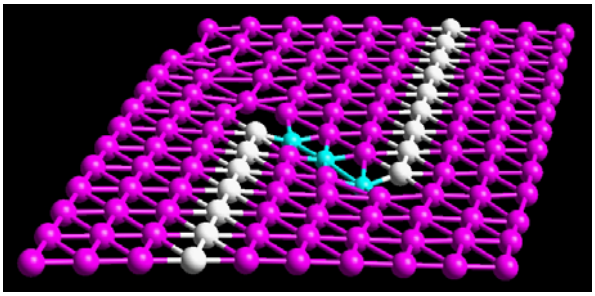

(b)

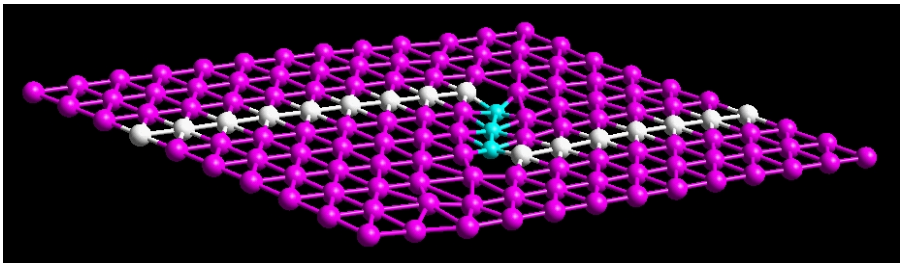

(c)

Fig. 4.28. *Enlarged view of two neighbouring dislocations depicting more clearly their core structure: (a) plan view; (b) and (c) are side views. Only the cerium sublattice is shown for clarity. Cerium is coloured magenta and white (dislocation) and zirconium, light blue.*

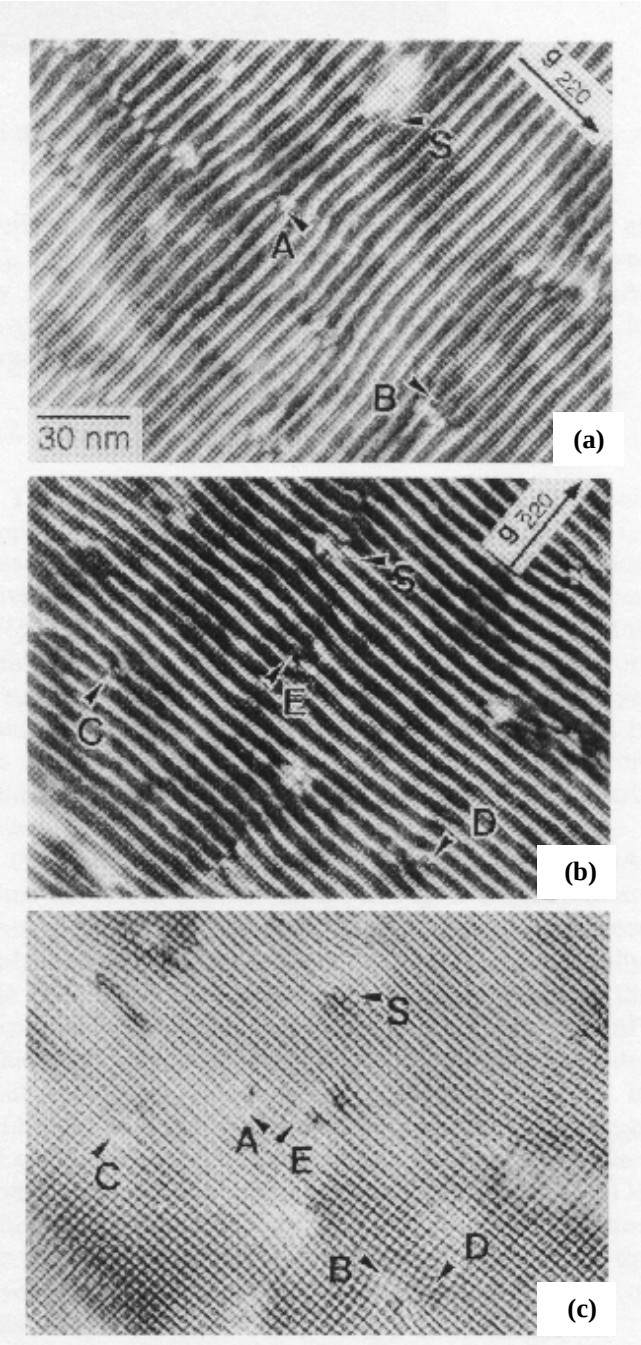

Fig. 4.29. *Plan view of the GaSb/GaAs heterostructure: (a) and (b) Lomer dislocations arrays, (c) regular Moiré pattern showing a well-relaxed layer and threading dislocations (A, … E), (Rocher 1999).*

Fig. 4.30. *Ball and stick representation of the second YSZ layer from the interface (layer five fig. 4.21b) showing a pair of edge dislocation. Only the cation sublattice is shown to preserve clarity.*

Fig. 4.31. *Cross-section of the CeO_2(111)/YSZ(111) interface: (a) across the entire simulation cell; (b) enlarged view of the dislocation far left in fig. 4.29a depicting more clearly the core structure. Cerium ions are magenta, zirconium ions are light blue and red (dislocation) and yttrium, yellow. The interfacial plane is marked with white horizontal arrows.*

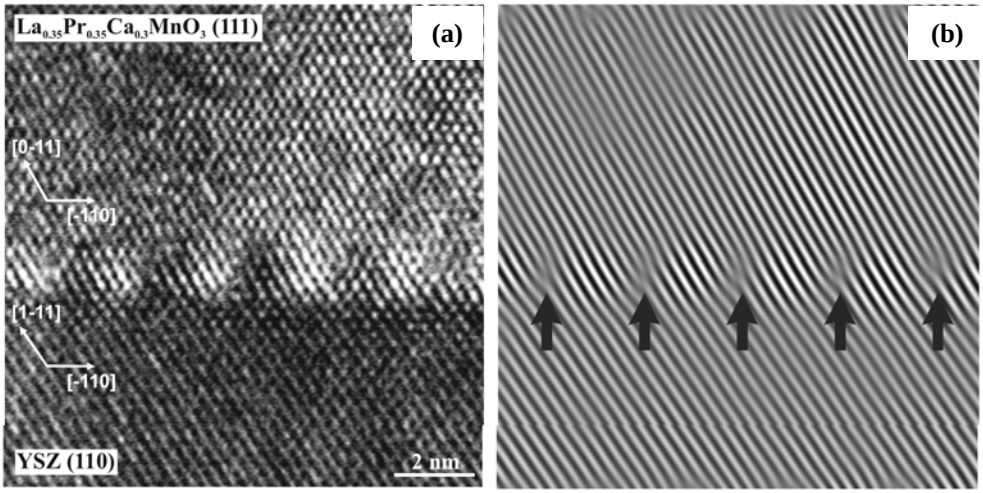

Fig. 4.32. *Semicoherent interface of the perovskite manganite with YSZ substrate. Black arrows demonstrate the regular sequence of the misfit dislocations at the interface in the Fourier transformed image (b), (Gorbenko 2000).*

4.4.2. CeO_2/YSZ(110) interfaces

Construction of the CeO_2/YSZ(110) interface follows the same steps that were described in previous chapter to generate CeO_2/YSZ(111) system, fig. 4.15:

- Placing of (*i*) two and (*ii*) four CeO_2(110) repeat units (thick) on top of ten repeat units of ZrO_2(110) support, (six repeat units included in region 1 and four repeat units included in region 2). Considering the rectangular shape of the (110) surface, a 54×27 CeO_2 thin film was placed directly above a 40×20 ZrO_2(110) support, giving an interfacial area of 14,573 $Å^2$ and comprising 32,748 ions in case (*i*) and 41,496 ions in case (*ii*). Each arrangement corresponds to a compression of ca. 31% for the overlying CeO_2 thin film.
- Introduction of the mean field 'hybrid' ions into region 2 of the support and scaling the entire simulation cell to the YSZ – MF lattice parameters. Accordingly, the interfacial area increased to 14,749 $Å^2$.

- Introduction of yttrium species into region 1 of the support by replacing 10% of the Zr^{4+} ions with Y^{3+} (480 yttrium ions), corresponding to 9.24 mol. % Y_2O_3. 240 oxygen ions were then removed to maintain charge neutrality of the system. The whole simulation cell will contain finally (*i*) 32,508 and respectively, (*ii*) 41,256 ions.

4.4.2.1. Initial thin film thickness = 2 CeO_2 units

Here, dynamical simulation, with a time step of 5×10^{-3} ps, was applied to the system in three cases: (a) 3400 K, (b) 2500 K and (c) 1000 K to explore the amorphisation of the thin film.

(a) At 3400 K, the thin film lost integrity and the simulation failed catastrophically ('blew-up'). Considering that the (110) surface is less stable than the (111), (Sayle T. X. T. 1994a), (where the same temperature for dynamical simulation resulted in a perfect crystallized thin film), at 3400 K the velocities of ions that form the thin film are so high that the thin film looses integrity.

(b) At 2500 K, the system evolves as expected via an amorphous transition without melting. Dynamical simulation was run for 325 ps at 2500 K, 115 ps at 2000 K, 15 ps at 1500 and 1000 K, 65 ps at 500 K and 110 ps at 0 K (energy minimization). For each temperature, the dynamical simulation was performed until the system was no longer evolving structurally or energetically. The final thin film structure was observed to be ca. 95% amorphous with only ca. 5% crystalline. The final energy of the system is –957230 eV.

(c) At 1000 K, the system evolves again without melting (50 ps at 1000 K and 130 ps at 0 K), but the final structure of the thin film is almost completely amorphous (ca. 99%). The final energy of the system is –956842 eV, which indicates that this system is less stable than the previous system, (ca. 5% crystalline regions), suggesting that a higher crystallinity confers a higher stability of the system.

2500 K

The calculated Ce-O RDF within the CeO_2 thin film during dynamical simulation performed at 2500 K are shown in figs. 4.33a-e after 0.005 ps, 0.25 ps, 25 ps, 325 ps and at the end of the simulation, respectively. After one step, fig. 4.33a, the RDF show dense peaks, which corresponds to a high compressed crystalline structure. After 0.25 ps, the CeO_2 thin film loses the long-range order, indicating an amorphous transition, fig. 4.33b. At 25 ps, the ceria thin film has regained some long-range order; two additional peaks have started to evolve at ca. 5.5 and ca. 8 Å, fig. 4.33c. After 325 ps, fig. 4.33d, the RDF shows increased peak definition.

The RDF for the final structure, fig. 4.33e, depicts broad peaks with an incomplete regaining of the long-range order, suggesting poor crystalinity within the final structure compared with previous RDF for CeO_2/YSZ(111) system, fig. 4.17e.

The MSD of cerium and oxygen ions during dynamical simulation at 2500 K is presented in fig. 4.34. The graph shows that for cerium, the MSD increases rapidly at the beginning of the simulation, during the amorphisation process, while after ca. 25 ps it plateaus indicating much reduced diffusion. For the oxygen ions, the MSD increase rapidly at the beginning and maintain a large positive gradient indicating high mobility of oxygen ions. By comparison with the previous two systems (fig. 4.1 and 4.16) it is easy to observe that the gradient associated with the oxygen MSD curve is much higher.

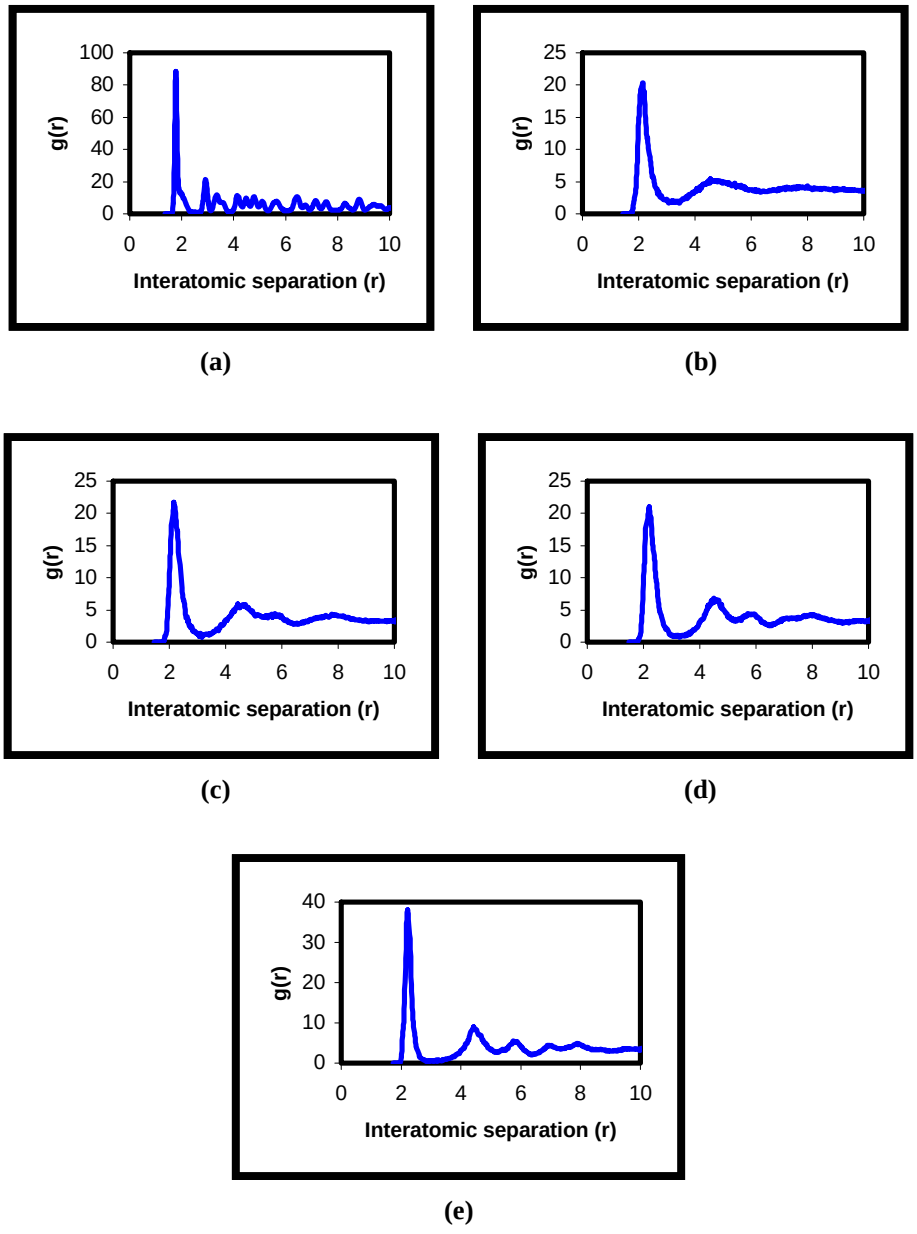

Fig. 4.33. *Calculated Ce-O radial distribution functions (RDF) within the CeO_2 thin film during dynamical simulation performed at 2500 K after: (a) 0.005 ps; (b) 0.25 ps; (c) 25 ps; (d) 325 ps and (e) at the end of the simulation. Interatomic separations are measured in Å.*

The highly strained starting structure and the amorphous structure obtained after 0.25 ps of dynamical simulation at 2500 K are presented in fig. 4.35ab.

Inspection of the final structure, fig. 4.36, reveals presence of very small crystalline areas interdispersed with large amorphous regions (ca. 95%).

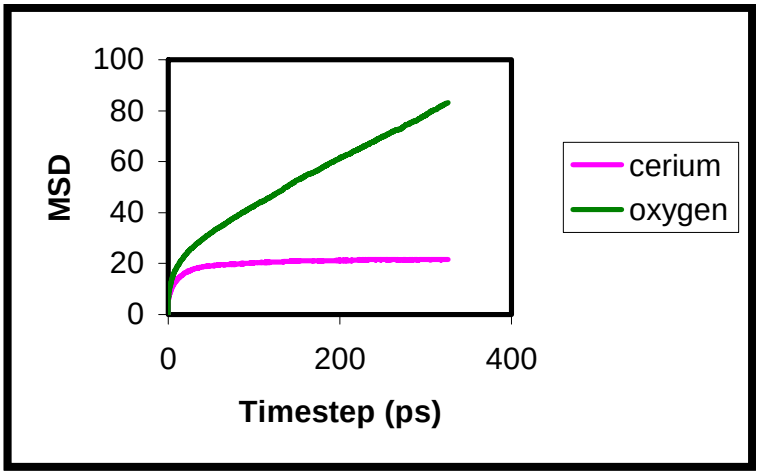

Fig. 4.34. *Calculated cerium and oxygen mean square displacements (MSD) measured in Å^2 within the CeO_2/YSZ(110) system during dynamical simulation at 2500 K.*

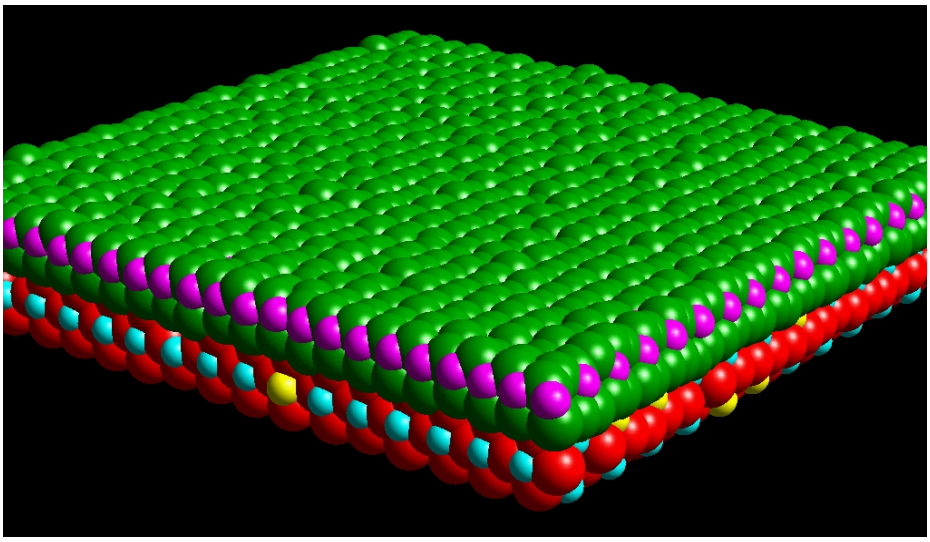

(a)

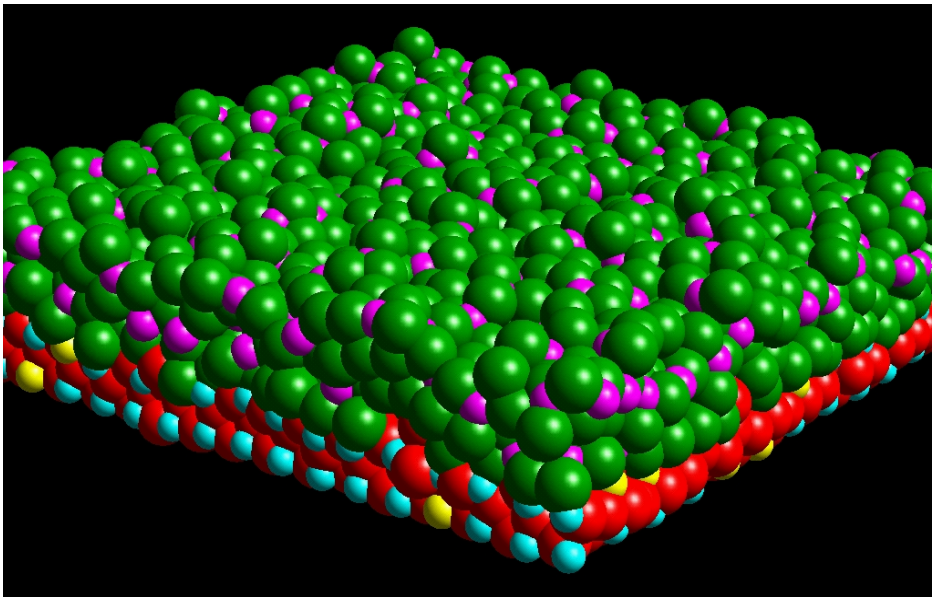

(b)

Fig. 4.35. *Representation of the CeO_2/YSZ(110) interface during dynamical simulation performed at 2500 K: (a) starting structure and (b) after 0.25 ps of dynamical simulation. Zirconium is coloured light blue, cerium magenta, yttrium yellow, oxygen (YSZ) is red and oxygen (CeO_2) green. To preserve clarity of the figure, only a small part of the simulation cell is shown together with three unit cells of the underlying support.*

Fig. 4.36. *Top view of the final structure of the CeO_2/YSZ(110) system, (thin film and three unit cells of the underlying support). Colour notation as in fig. 4.35.*

1000 K

Considering that a simulation temperature of 2500 K might be too high may be one reason why the final structure remains amorphous, in the next trial, dynamical simulation will be performed at 1000 K for 50 ps and 130 ps at 0 K to minimize the energy of the system.

Calculated Ce-O RDF within CeO_2 thin film during dynamical simulation at 1000 K, are shown in fig. 4.37a-c. The initial structure is analogous with the first presented for the 2500 K dynamical simulation. After 0.25 ps, fig. 4.37b, the CeO_2 thin film loses long-range order, indicating an amorphous transition. At the end of the simulation, the RDF indicates that the thin film did not regain long-range order, suggesting that the thin ceria film remains amorphous.

By comparison with the RDF presented for dynamical simulation performed at 2500 K it is clear that this system presents even poorer crystallinity (amorphous phase estimated at 99%). Moreover, this system is calculated to also be less stable energetically.

The following section considers a thicker CeO_2 film supported on YSZ(110).

4.4.2.2. Initial thin film thickness = 4 CeO_2 units

Considering that the recrystallization of the CeO_2 thin film for the previous case was better for dynamical simulation performed at 2500 K, the procedure was repeated for the system that contains initially four repeat units of ceria supported on YSZ(110).

Dynamical simulation, with a time step of 5×10^{-3} ps, was applied to the system for 325 ps at 2500 K, 155 ps at 2000 K, 85 ps at 1500 K, 20 ps at 1000 K, 85 ps at 500 K and 260 ps at 0 K; the later acts effectively as an energy minimization and was performed until the energy converged. For each temperature, the dynamical simulation was performed until the system was no longer evolving structurally or energetically.

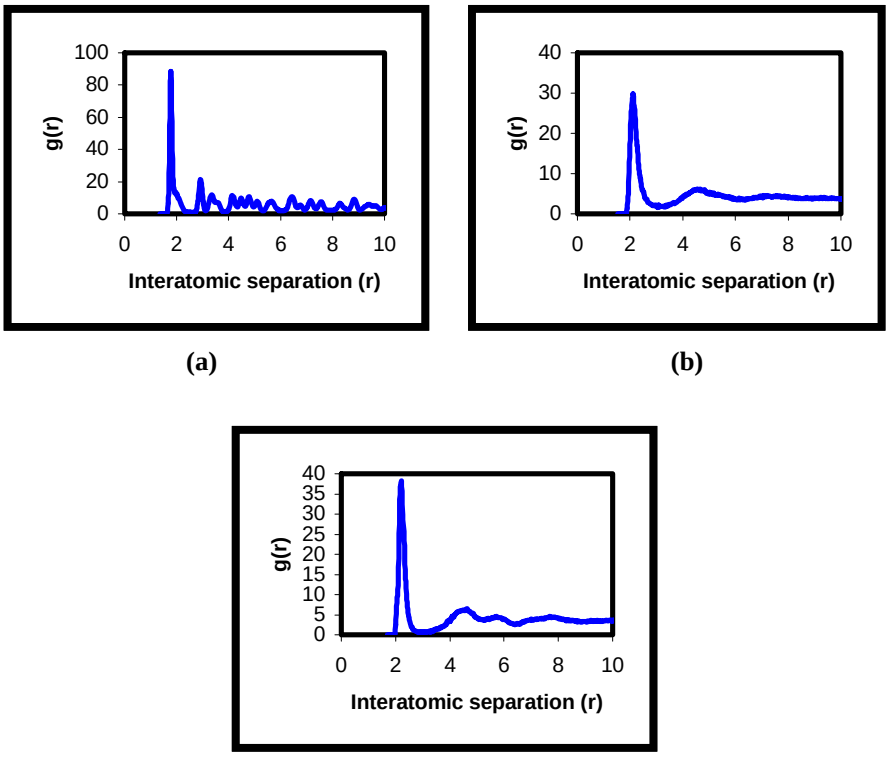

Fig. 4.37. *Calculated Ce-O radial distribution functions (RDF) within the CeO_2 thin film during dynamical simulation performed at 1000 K after: (a) 0.005 ps; (b) 0.25 ps; (c) at the end of the simulation. Interatomic separations are measured in Å.*

Amorphisation and recrystallisation

The MSD of cerium and oxygen ions for dynamical simulation performed at 2500 K is presented in fig. 4.38. The MSD of cerium increases rapidly at the beginning of the simulation during the amorphisation process reflecting the high mobility of the cerium ions. Conversely at ca. 100 ps, the MSD plateaus, indicating little diffusion. For the oxygen ions a similar behaviour is observed at the beginning of the amorphisation, whilst towards the end, the curve maintains a positive gradient indicating that oxygen species retain significant mobility even after recrystallisation.

The gradient of the oxygen MSD is also about 7 degrees lower compared with the MSD for two CeO_2 layers, suggesting a lower mobility of oxygen ions in this present system.

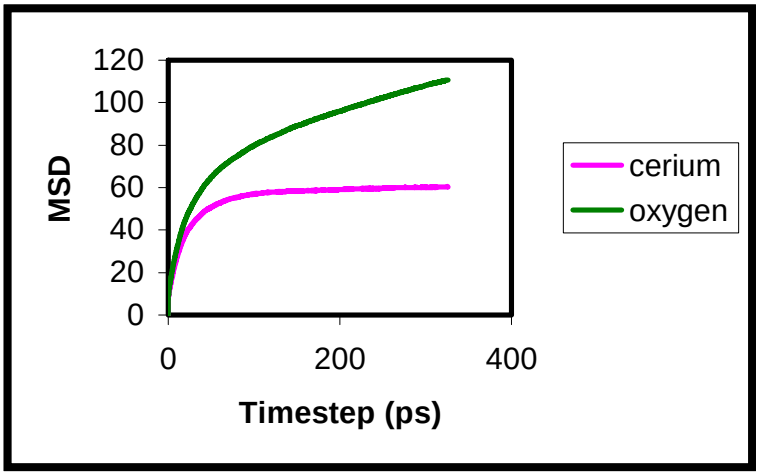

Fig. 4.38. *Calculated cerium and oxygen mean square displacements (MSD) measured in $Å^2$ within the CeO_2/YSZ(110) system during dynamical simulation at 2500 K. Starting structure contains four CeO_2 units deposited on the YSZ support.*

Calculated Ce-O RDF within the CeO_2 thin film during dynamical simulation performed at 2500 K are shown in figs. 4.39a-f after 0.005 ps, 0.25 ps, 50 ps, 150 ps, 325 ps and at the end of simulation (final structure). After 0.005 ps, the RDF shows peaks at 1.9, 3.2 and 4.2 Å, which correspond to the parent CeO_2, (thin film), under 31% compression. After 0.25 ps the CeO_2 thin film loses long-range order, indicating the amorphous transition. At 50 ps the thin film still maintains an amorphous structure although long-range ordering is starting to establish. After 150 ps, the CeO_2 thin film starts to regain long-range order, indicating that recrystallisation of the thin film begins. The RDF peaks are sharpening during dynamical simulation, (325 ps), suggesting that the recrystallisation process continues. At the end of the simulation the RDF exhibits sharp peaks indicating a crystalline structure.

In comparison with the RDF of the final structure for the CeO_2/YSZ(111) system, fig. 4.17e, the peaks are broader suggesting that the thin film is not perfectly (completely) recrystallised. For the (111) system, the first peak, for example, is at 2.35 Å (range 2.25 to 2.45 Å), while for the (110) system the analogous peak is at 2.35 Å (range 2.15 to 2.55 Å).

In fig. 4.40 the initial CeO_2/YSZ(110) structure is presented, (fig.4.40a), which comprises a CeO_2 thin film, four layers thick, and the amorphous structure (fig. 4.40b) obtained after 0.25 ps of dynamical simulation at 2500 K. During the amorphisation process, the thin film expands along the surface normal when the thickness almost doubles (fig. 4.40b). Inspection of the final structure, fig. 4.41 shows that the thin film contains crystalline regions separated by amorphous regions, supporting data obtained from the Ce-O RDF, fig. 4.39f.

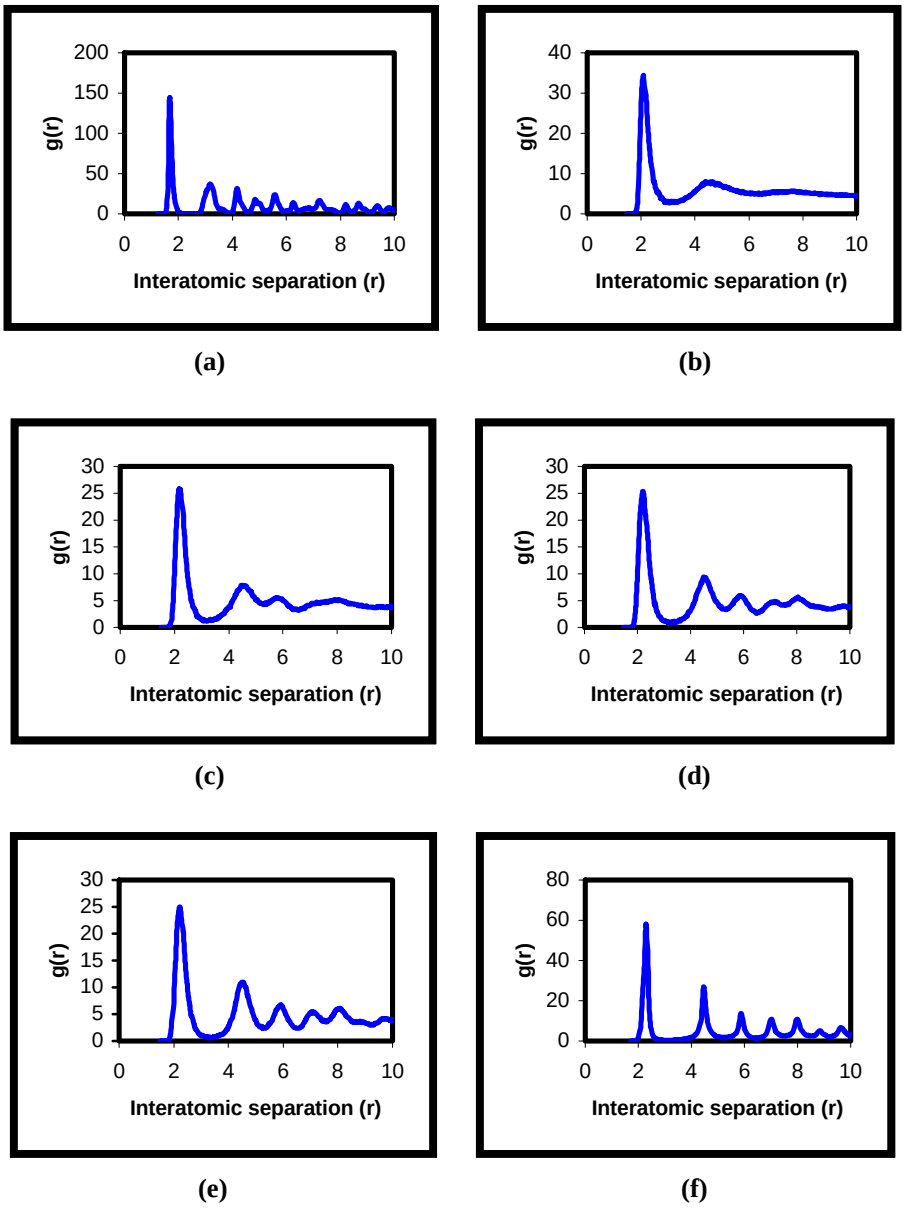

Fig. 4.39. *Calculated Ce-O radial distribution functions (RDF) within the CeO_2 thin film during dynamical simulation performed at 2500 K after: (a) 0.005 ps; (b) 0.25 ps; (c) 50 ps; (d) 150 ps; (e) 325 ps and (f) at the end of the simulation. Interatomic separations are measured in Å.*

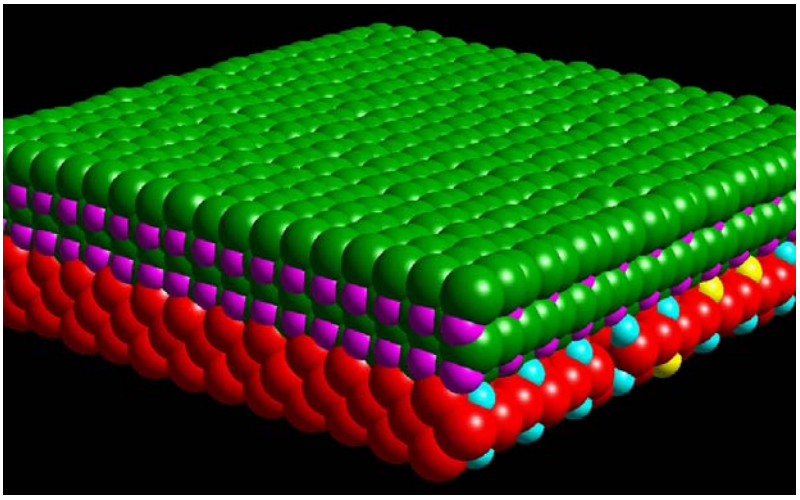

(a)

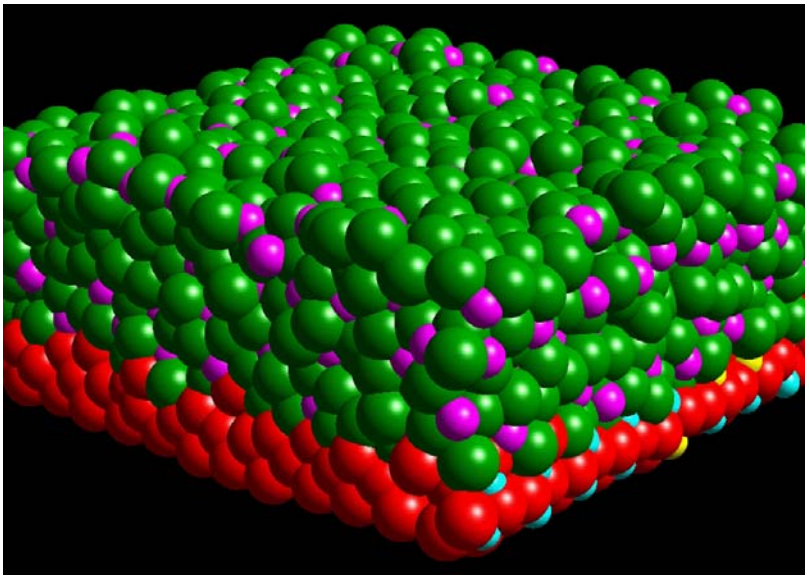

(b)

Fig. 4.40. *Representation of the CeO_2/YSZ(110) interface during dynamical simulation performed at 2500 K: (a) starting structure and (b) after 0.25 ps of dynamical simulation. Zirconium is coloured light blue, cerium magenta, yttrium yellow, oxygen (YSZ) is red and oxygen (CeO_2) green. To preserve clarity of the figure, only a small part of the simulation cell is shown together with three unit cells of the underlying support.*

Fig. 4.41. *Representation of the final structure of the CeO_2/YSZ(110) interface. Zirconium is coloured light blue, cerium magenta, yttrium yellow, oxygen (YSZ) is red and oxygen (CeO_2) green. To preserve clarity of the figure, only a small part of the simulation cell is shown together with three unit cells of the underlying support.*

Structural characterization

Surprisingly the final CeO_2 thin film has a polycrystalline structure and comprises ten CeO_2 repeat units with an incomplete surface layer and a final thickness of approximately 40 Å. The surface layer (layer ten) and layer nine are incomplete and comprise clusters and isolated CeO_2 groups.

A layer-by-layer analysis of cerium and zirconium sublattices allows an easier identification of regions with different crystalline orientations of the CeO_2 thin film with respect to the underlying YSZ(110) support. Specifically, CeO_2(111), CeO_2(110) and CeO_2(100) (dipolar surface – Appendix D) can all be identified (fig. 4.42 and 4.43). The (100), (110) and (111) surfaces of CeO_2 are presented in fig. 4.44 to aid structural interpretation. Moreover, the YSZ support was also strongly perturbed by the overlying ceria thin film. The apparition of regions with (110) and (100) orientations in the first two layers from the interface was observed, fig. 4.45. It was observed also that some crystallites are rotated by ca. 4-5º and 10º.

In fig. 4.46 a plan view of the CeO_2/YSZ(110) system is presented showing the crystallite distribution within the system.

Experimental studies of CeO_2, obtained by spray pyrolysis (Vallet-Regi 1997) and r. f. sputtering (Španková 2000), showed the presence of polycrystalline ceria particles and surfaces. With spray pyrolysis, each particle contains crystallites randomly distributed, exposing the (111) and (100) surfaces, fig. 4.47. For ceria deposition on a sapphire substrate, as-deposited CeO_2 layers consist of small mosaic blocks (ca. 200 Å in size), fig. 4.48. The CeO_2 mosaic blocks are twisted with respect with each other by an angle of 6-7º. (111) and (001) oriented grains can be obtained at 640-680ºC.

The size of the crystallites in the CeO_2/YSZ(110) system, presented in fig. 4.46, range from ca. 50 $Å^2$ (7) to ca. 3500 $Å^2$ (8) and comprise about 60% of the total area of the system.

Defects

Close inspection of the CeO_2 thin film and YSZ support indicates the presence of vacancies (the majority existing as clusters of vacancies) and intermixing across the interfacial plane of cerium, zirconium and yttrium

ions. The underlying YSZ support presents modifications in the first five layers from the interface. Conversely, for the CeO_2/YSZ(111) system only two layers demonstrate significant modifications, suggesting that the CeO_2 thin film perturbs the underlying YSZ more strongly within the CeO_2/YSZ(110) system.

A layer-by-layer analysis of the system, revealed that the YSZ support comprises vacancies, ca. 3.7%, identified in the first five layers from the interfacial plane, fig. 4.45. In the CeO_2 thin film, vacancies are present predominantly as clusters; at least 10% of the lattice sites within the CeO_2 planes are vacant.

Interdiffusion of cerium, zirconium and yttrium ions across the interfacial plane were also observed. Cerium ions occupy zirconium and/or yttrium lattice sites within the YSZ support and zirconium and yttrium occupy cerium lattice sites within the CeO_2 thin film. Interdiffusion takes place across the interface in the first two YSZ layers and in the first four CeO_2 layers. In the thin film ca. 11.7% of cerium ions are replaced with zirconium and yttrium, while in the YSZ support substitution is ca. 6.8%. Interdiffused ions are present either as clusters, mainly in the interfacial layers (both YSZ and CeO_2) or dispersed in the next layers from the interface. A cluster of ca. 100 $Å^2$ containing yttrium and zirconium ions was identified in the interfacial ceria layer.

It is well known that (100) surface has a lower stability (Sayle T. X. T. 1994a) and is categorised as a dipolar type 3 surface (see Appendix D). It was found experimentally, for CeO_2(100) supported on $SrTiO_3$, that this surface can exist and is terminated with 0.5 monolayers of oxygen (Herman 1999ab), which facilitates quenching of the dipole. Therefore a highly defective top layer helps stabilize this type of surface. Here the presence of vacancies clusters and two incomplete surface layers can create an alternation of charges in successive planes that enable the surface dipole to be quenched in regions where (100) crystallites are present.

By comparison with the CeO_2/YSZ(111) system, where vacancies were present in the proportion of ca. 0.2% in the YSZ support and 0.8% in the CeO_2 thin film and interdiffusion is modest (ca. 3%), it can be concluded

that modifications that appear in case of CeO_2/YSZ(110) system are much more intense. This can be due to the lower stability of the (110) surface.

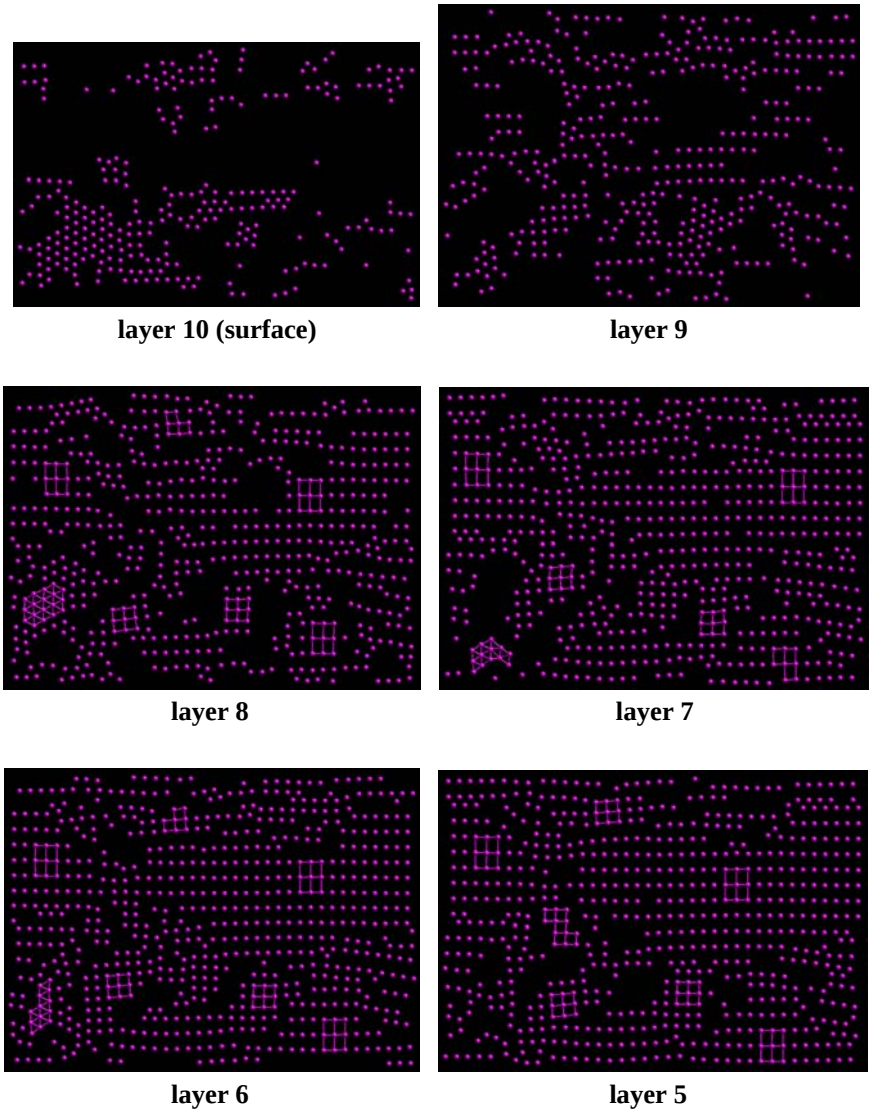

Fig. 4.42. *Layer-by-layer representation of six (top) layers of the CeO_2 thin film. Only the cerium sublattice is shown to preserve clarity.*

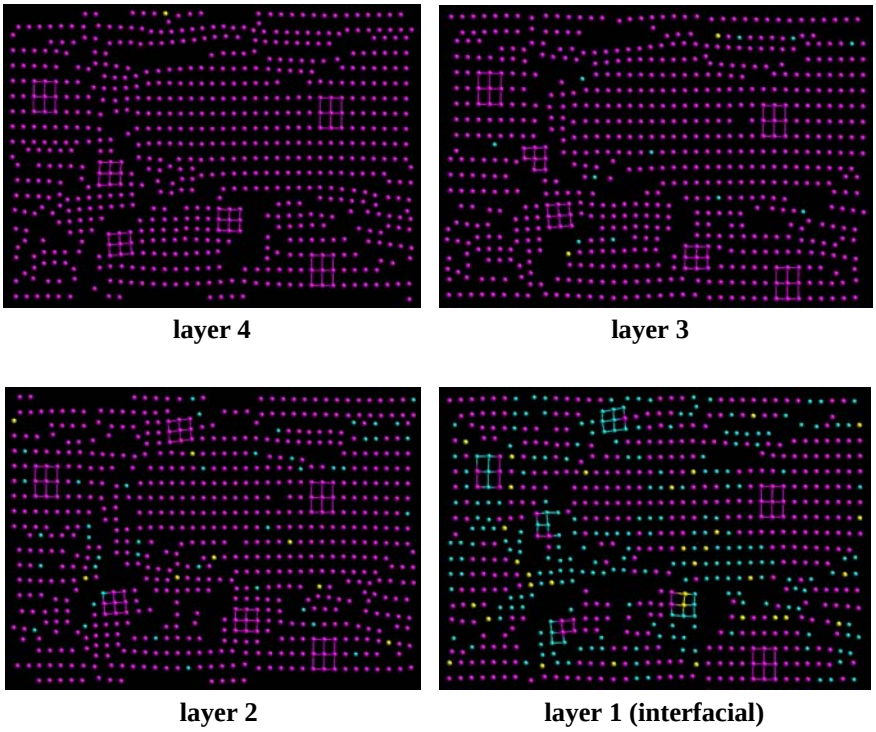

Fig. 4.43. *Representation of the first four layers of the CeO_2 thin film. To preserve clarity only the cerium sublattice is shown. Cerium is coloured magenta, zirconium light blue and yttrium yellow.*

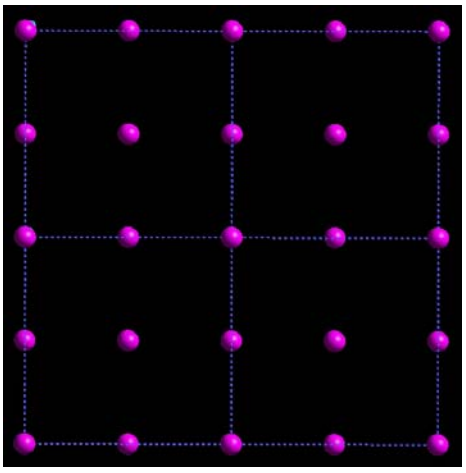

(100)

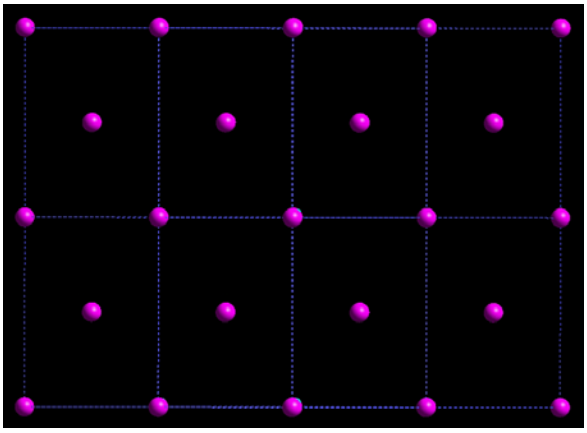

(110)

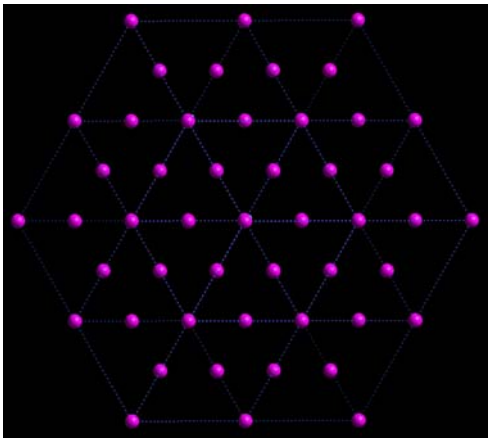

(111)

Fig. 4.44. *Representations of (100), (110) and (111) surfaces.*

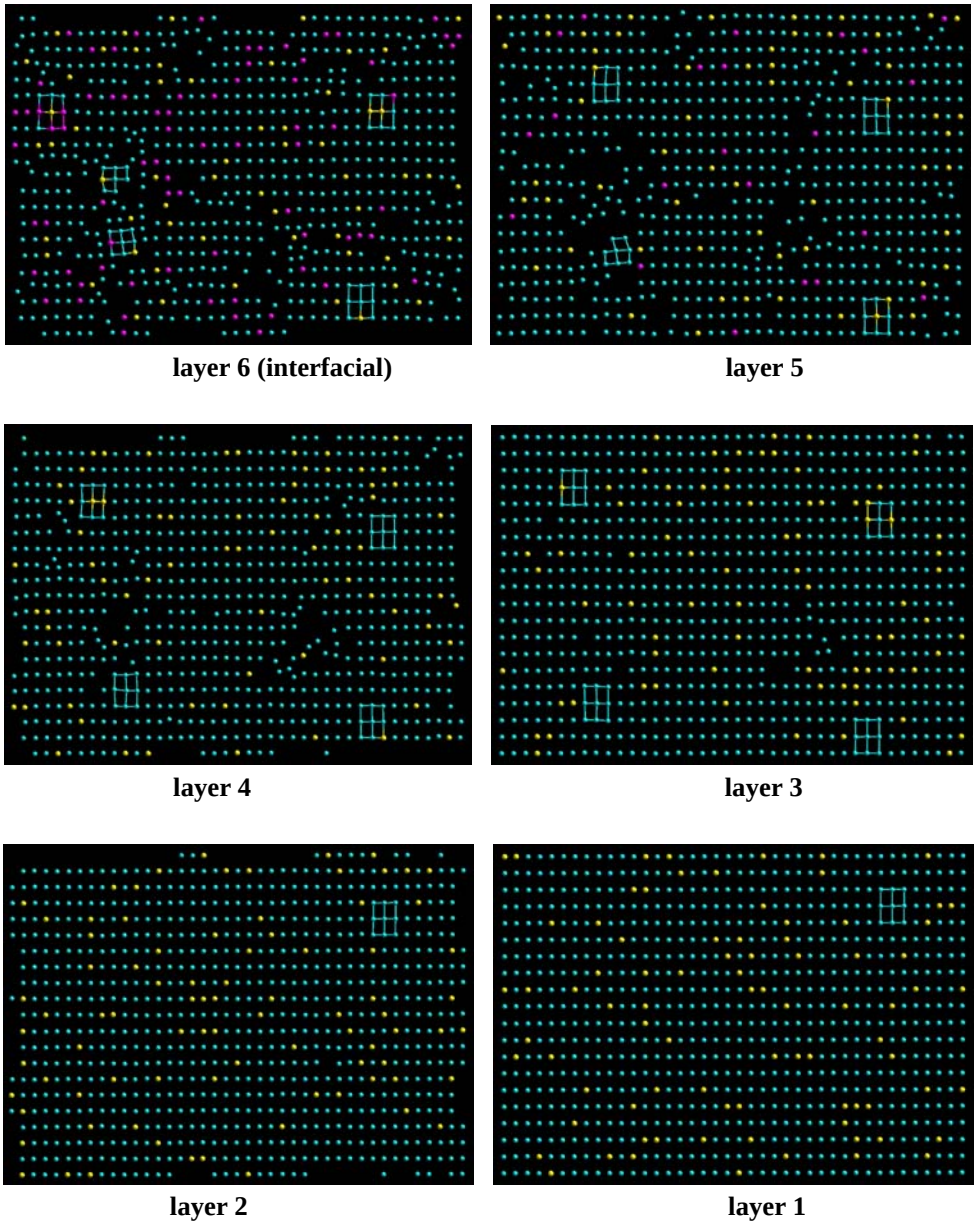

Fig. 4.45. *Layer-by-layer representation of the YSZ layers of the support. Only the cation sublattice is shown. Zirconium is coloured light blue and yttrium yellow.*

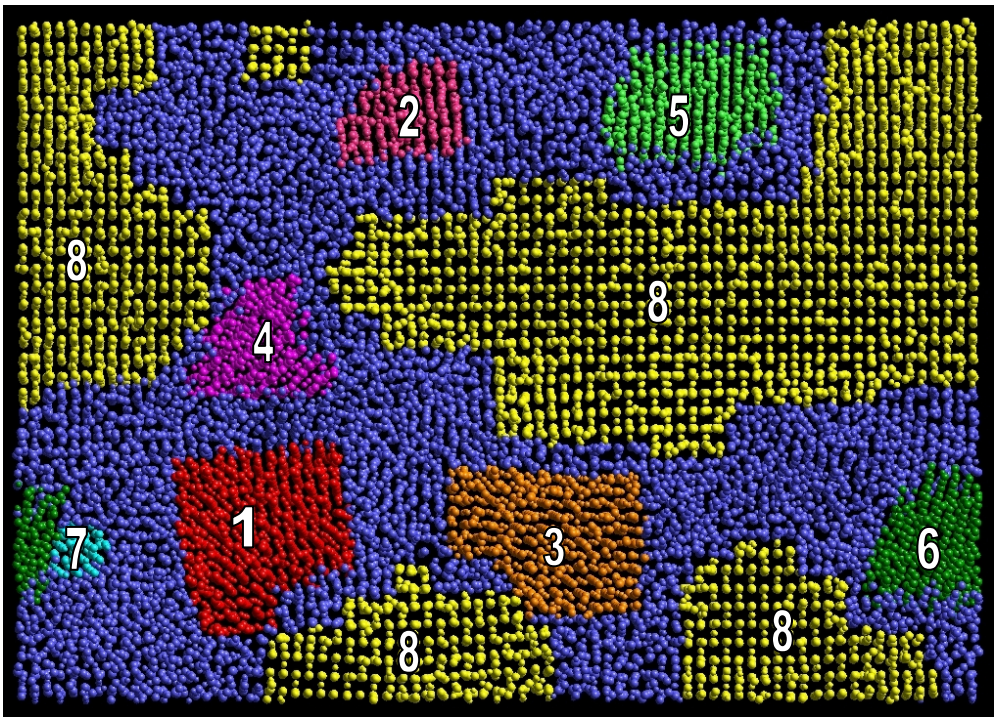
2
5
8
8
4
1
7
3
6
8
8

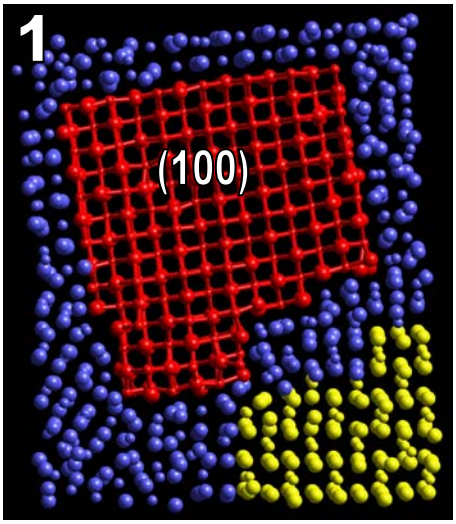
1
(100)

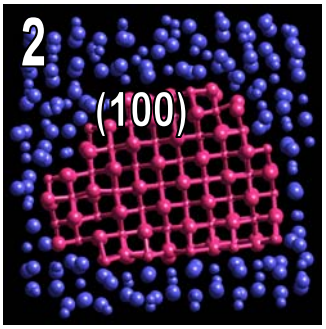
2
(100)

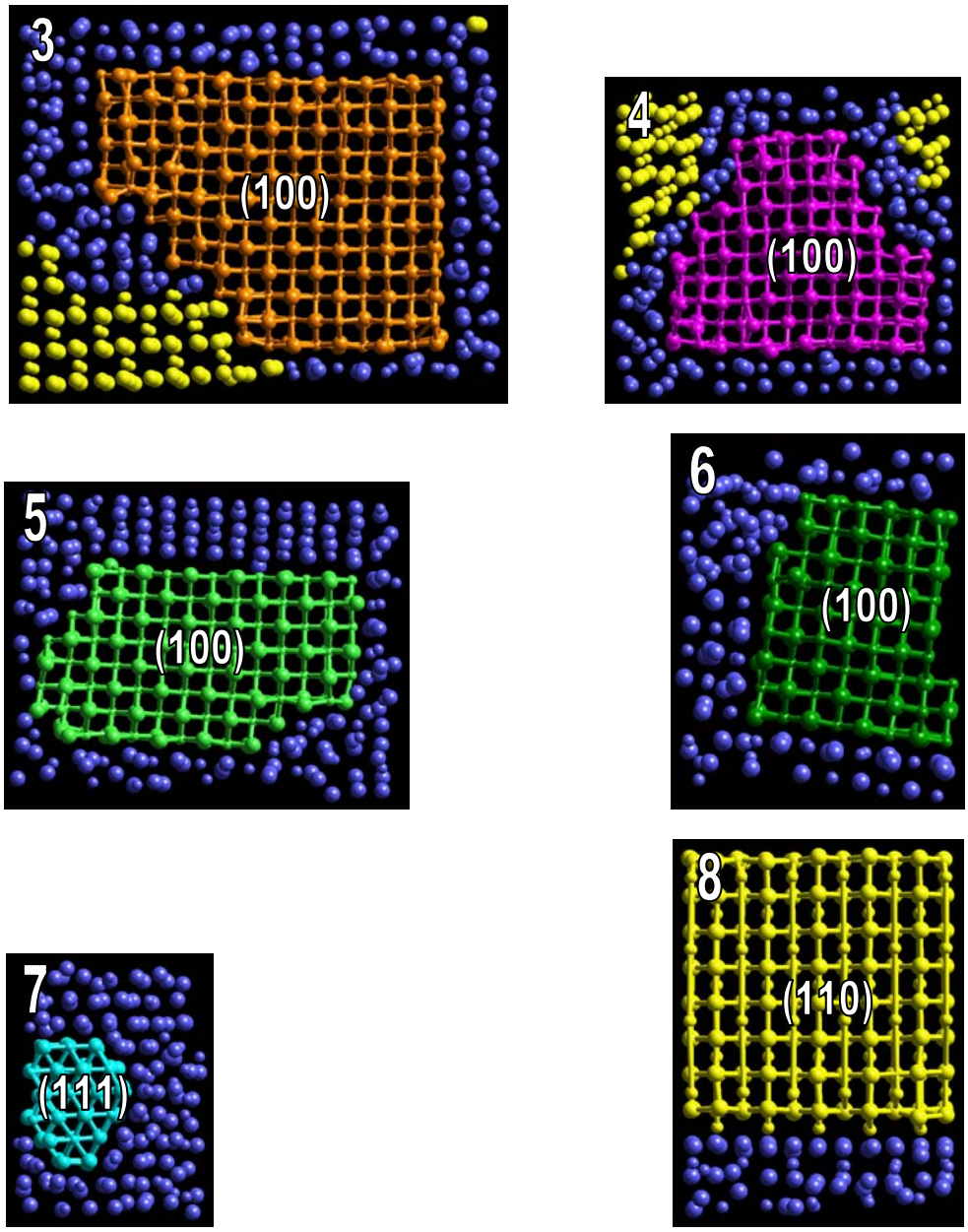

Fig. 4.46. *Plan view representation of the CeO_2/YSZ(110) system (previous page). Coloured regions represent crystallites (1-8) within the thin film with different orientations. Oxygen ions are represented as large spheres and cations as small spheres.*

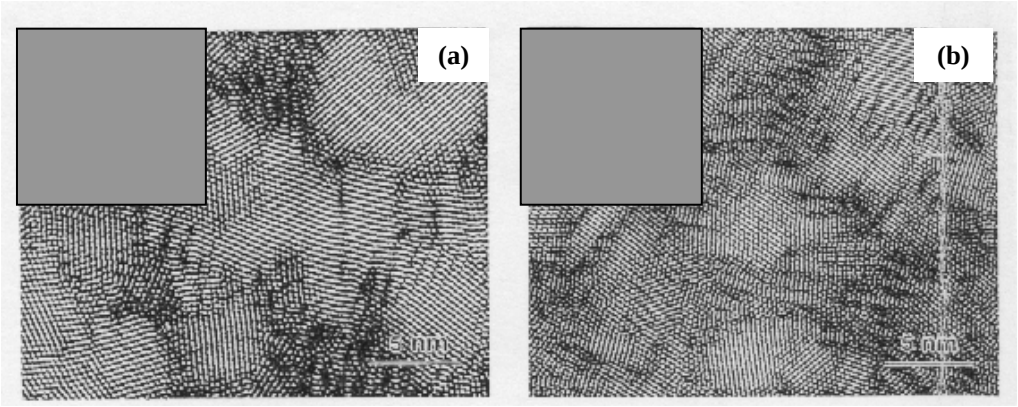

Fig. 4.47. (a), (b). *Fourier transformed images showing the shape and distribution of CeO_2 crystallites containing (111) and (200) planes, (Vallet-Regi 1997).*

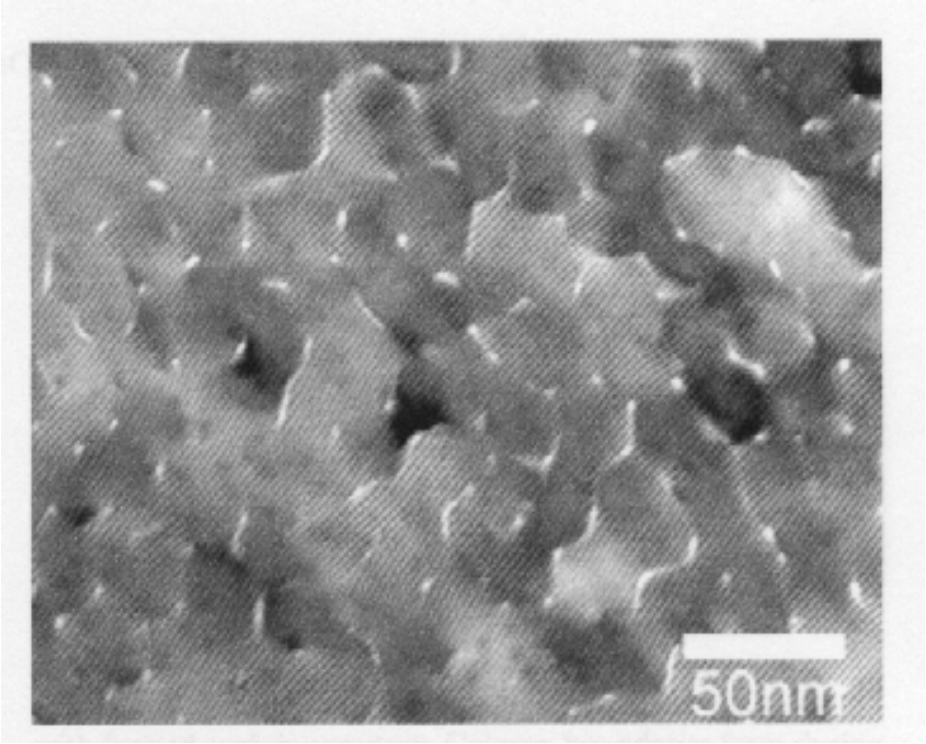

Fig. 4.48. *Transmission electron microscopy micrograph of the epitaxial CeO_2 layer deposited on Al_2O_3. The layer consists of misoriented mosaic blocks (~20 nm) separated by voids in some cases (Španková 2000).*

Analysis of the bond distances, calculated in the CeO_2/YSZ(110) system, fig. 4.49, shows that their evolution follows a similar path as for the CeO_2/YSZ(111) system, fig. 4.25. For the underlying YSZ support, the Zr-O bond distances decrease towards the interface, while O-O bond distances increase in the same direction. For Y-O and cation-cation, bond distance remains constant at approximately 2.34 Å and 3.61 Å, respectively. It was also observed that in the YSZ interfacial plane, bond distances have increased values, 3.75 Å for Zr-Zr and Zr-Y and 3.81 Å for Y-Y, by comparison with bulk values (table 4.2). Considering also the structural modifications that appear in the interfacial YSZ plane (fig. 4.45) and the fact that Ce-Ce bond distances in the CeO_2 interfacial plane are 3.81 Å (average value) it can be suggested that the underlying YSZ support relaxes significantly to improve the interaction across the interface and also to help minimise the strain gradient.

For the supported CeO_2 thin film, the average bond distances are in good agreement with bulk values: 2.72 Å for O-O, 2.31 Å for Ce-O and 3.83 Å for Ce-Ce bond distances. Smaller values in layer nine and ten compared with bulk values (table 4.3), confirm low coordination of these layers, which are incomplete.

The presence of many regions comprising low coordinated ions in conjunction with regions (crystallites) exposing both the (100) and (110) surfaces, which have lower stability compared with the (111), are likely to be important with respect to the catalytic properties of the material.

Epitaxial relationships

Inspection of the epitaxial relationships that exist between the CeO_2 thin film and the YSZ support revealed that the thin film lies almost coherent with the underlying support, with the CeO_2 accommodating a 37×20 pattern with no rotation of the thin film with respect to the support. The 37×20 refers to 37 atoms along the [$\bar{1}$ 1 0] and 20 along the [0 0 1], which lie along the surface lattice vectors defining the simulation cell, fig. 4.50. The lattice misfit (based upon a 40×20 lattice for the underlying YSZ) associated with such a configuration is therefore reduced from +6.1% (bulk misfit) to –1.7% along the [$\bar{1}$ 1 0].

Considering that no dislocations were observed in the system it could be suggested that the polycrystalline structure facilitates increased relaxational freedom at grain boundaries and grain junctions. Therefore the –1.7% residual stress can be reduced further via localised ionic relaxation in regions localised at grain boundaries and the interconnecting amorphous regions.

The interfacial YSZ layer and the layer immediately underneath, also change configuration and present a 38×20 pattern in contrast to the initial 40×20; the remaining YSZ below maintains a 40×20 configuration.

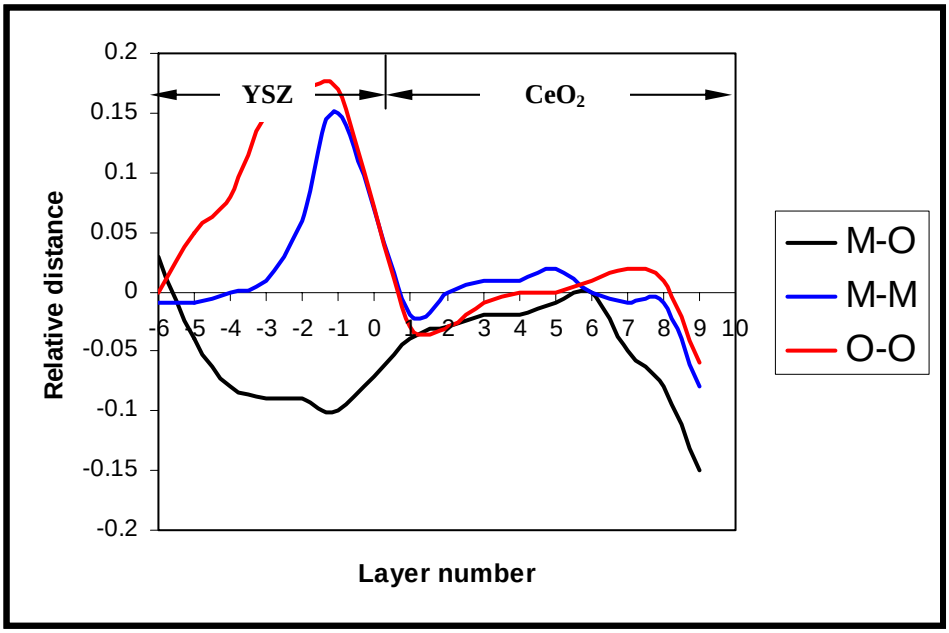

Fig. 4.49. *Representation of the relative distances, in Å, calculated between bulk values and determined values as function of layer number in the CeO_2/YSZ(110) system. A layer number of '0' represents the interface. To ensure the clarity of the picture only zirconium bond distances in the support were considered. (M=Ce, Zr)*

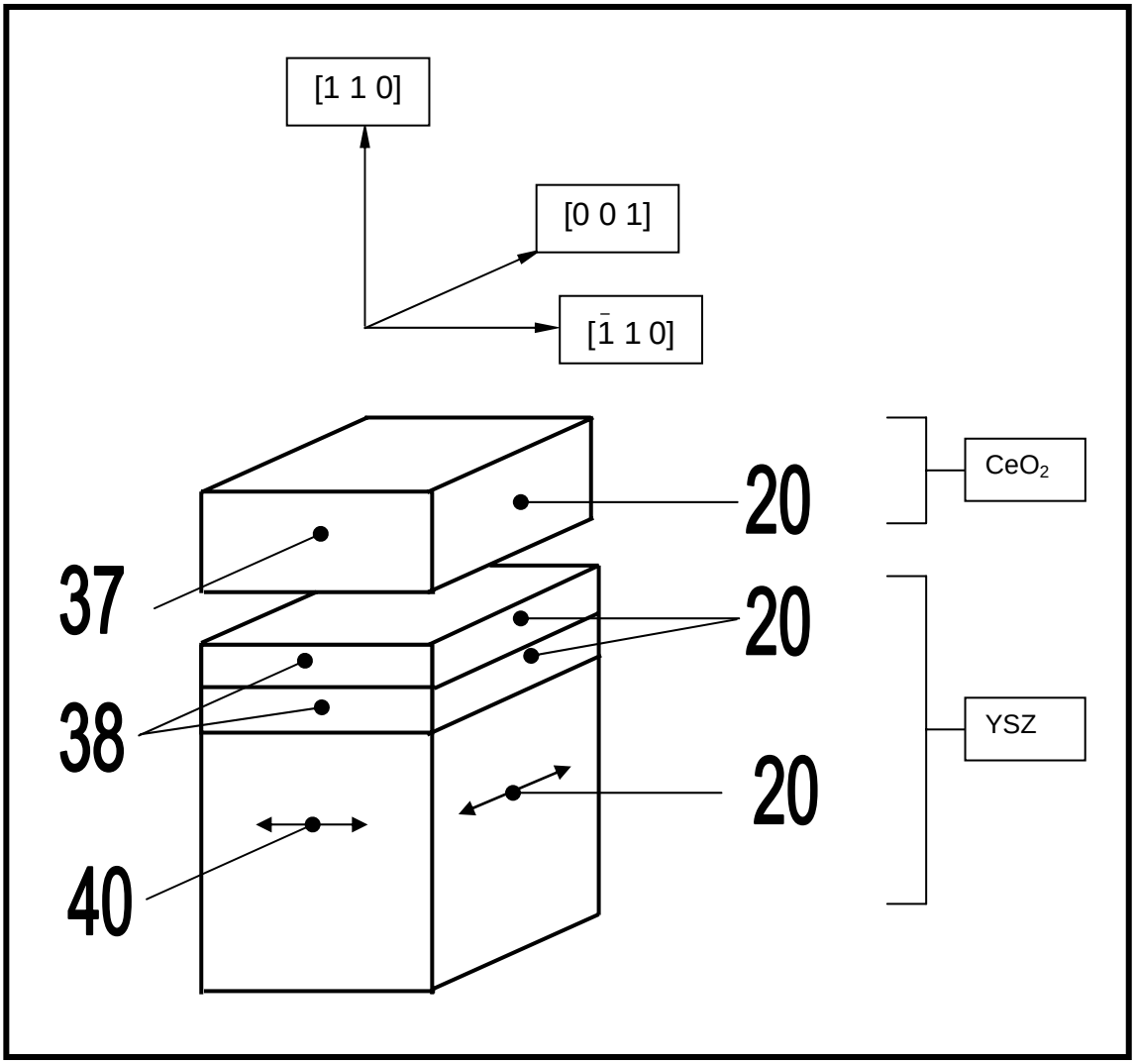

Fig. 4.50. *Schematic representation of the final structure of the CeO_2/YSZ(110) interface, highlighting the epitaxial relationships at the interfacial region.*

4.5. Summary

In this chapter, the CeO_2/ZrO_2(111), CeO_2/YSZ(111) and CeO_2/YSZ(110) systems were considered and generated using a cube-on-

cube methodology and explored using a simulated amorphisation and recrystallisation methodology.

The first interface considered was the model $CeO_2/ZrO_2(111)$ system. In this case amorphisation was induced by constraining the CeO_2 thin film under compression in two cases, +15% and +31%, to explore amorphisation induced via medium and high strain and to investigate whether this has any influence on the final structure of the thin film.

The structural evolution of the amorphisation and recrystallisation processes was monitored using RDF and MSD of the ions during dynamical simulation. Molecular graphical techniques aided structural identification and defect analysis.

In the first case, when the thin film was constrained under +15% compression, it was observed that the thin film recrystallised only partially. Inspection of the final structure reveals the presence of large crystalline regions separated by amorphous regions.

In the second case, +31% compression, the final structure revealed that the thin film has completely recrystallised into the fluorite structure, with the CeO_2 exposing the (111) plane at both interface and surface layers. Structural modifications and defects, which include pure edge dislocations, a mixed screw-edge dislocation, cerium, zirconium and oxygen vacancies and interdiffused ions across the interfacial plane were identified in the system. This is the first time a mixed screw-edge dislocation has been identified to evolve within a supported fluorite system. Indeed the simulation methodology employed in this study has enabled the *evolution* of such defects.

As the $CeO_2/ZrO_2(111)$ model system with the ceria thin film under +31% compression was shown to generate a high-energy amorphous solid, which lead to improved thin film crystallinity, the study was extended towards the examination of the CeO_2/YSZ(111) system with amorphisation again induced via a +31% compression of the overlying CeO_2 lattice.

After prolonged dynamical simulation, the CeO_2 recrystallises into a cubic fluorite structure. The final CeO_2 thin film exposes the (111) plane at both interface and surface and has a final thickness of ca. 20 Å. Structural modifications that arise in this system comprise pure edge dislocations and

defects including vacancies, interstitial ions and interdiffused ions. The influence of the thin film over the underlying YSZ support extends over the first two layers (ca. 4 Å into the support).

Considering that the (110) surface of CeO_2 and ZrO_2 is unstable compared with the (111) surface and potentially more reactive (more important catalytically), the next step of this work was to create a CeO_2/YSZ(110) system. Two thicknesses of the thin film were considered, specifically two and four CeO_2 units.

For the thin film, which comprises two CeO_2 units, after dynamical simulation performed at different temperatures (2500 K and 1000K), the final structure of the thin film remained amorphous. For the simulation performed at 3400 K, the thin film looses integrity and the simulation failed.

In the second case, when four CeO_2 units were deposited, a remarkable polycrystalline structure was generated. The thin film comprises crystallites with various orientations with respect to each other and exposing the (110), (100) and (111) planes at the surface. In this case the influence of the thin film over the support extends ca. 15 Å into the YSZ support. The presence of polycrystalline ceria, with crystallites randomly distributed exposing the (111) and (100) surfaces were observed experimentally in case of ceria obtained using spray pyrolysis (Vallet-Regi 1997).

Experimental studies identified that the (100) CeO_2 surface, (dipolar surface), can exist if is terminated with 0.5 monolayers of oxygen (Herman 1999ab), which facilitate quenching the dipole. Therefore a highly defective top layer helps stabilize this type of surface. Here the presence of vacancies clusters and two incomplete surface layers can create an alternation of charges in successive planes that enable the surface dipole to be quenched in regions where (100) crystallites are present. However, further studies are required to generate more definitive models of how such a dipole associated with this system is quenched.

Clearly, the thin film and support have a considerable influence over one another, resulting in profound structural modifications. Such modifications are likely to influence the catalytic properties of the material. For example low coordinative saturation of surface species may provide models for active centres. Moreover the dislocations are expected to

influence the mobility of oxygen ions within the system influencing the OSC of the material.

Further studies are necessary to explore oxygen mobility at different temperatures and how the presence of different type of defects can influence it. One must also consider the influence of Ce^{3+} and associated oxygen vacancies required to maintain charge neutrality. Accordingly, polarization of the lattice will influence the migration therefore the model can be improved via the introduction of the shell model into further studies. Strain distribution across the interface and in the interfacial planes can be also addressed by visualising the strain gradient.

Conclusions

This study is structured in four chapters. In the first chapter, experimental methods used to prepare and characterize oxide materials and interfaces are discussed. In addition, theoretical calculations that have been performed on solids from clusters to solid-solid interfaces are reviewed.

In the second chapter, the methodology and computer codes used to study oxide-oxide interfaces are presented.

The third chapter contains a study of the SrO/BaO(001) model system constructed using two methodologies: atom deposition and cube-on-cube construction. The first method allows the study of the growth and nucleation of the thin film by sequential deposition of strontium and oxygen ions onto a BaO(001) support. Evolution of the thin film from small clusters, at submonolayer level, to a thin film five layers thick, which includes cracks in its structure, was studied. To perform a comparison between the thin film structures, the thin film was also constructed using cube-on-cube method. Here, the thin film exhibited similar structural characteristics (cracks). Conversely, this method does not allow study of the growth process, but offers a less computational expensive way to obtain the final structure of an interface.

In the fourth chapter, CeO_2, a material used on a large scale in catalysis (various chemical processes, catalysts and major component of the automobile exhaust catalyst) due to its oxygen storage capacity, was for the first time modelled supported on zirconia and yttrium stabilized zirconia.

An amorphisation and recrystallisation methodology, a powerful new simulation technique was developed to create the oxide-oxide interfaces. Moreover in contrast to almost all previous studies, which start by defining the basic structure of the system, here the thin film is allowed to evolve naturally in response to the support. The methodology enables a variety of structural features to *evolve* within the system. Structural modifications observed in these systems include dislocations, dislocation networks, grain-boundaries and defects (interstitial, vacancies and substitutionals), all within a single simulation cell.

Our calculations suggests that the ceria thin film demonstrates remarkable structural changes including mixed screw-edge dislocations, pure edge dislocations, intermixing across the interfacial plane, different crystalline orientations and hence grain-boundaries and grain junctions, which may help explain its remarkable catalytic properties, and were for the first time identified to evolve within a supported fluorite system.

At present the tools available to analyse experimentally solid-solid systems cannot provide structural characterization with atomic level resolution of for example, mixed screw-edge dislocations. Therefore atomistic simulation can provide an invaluable complement to experiment.

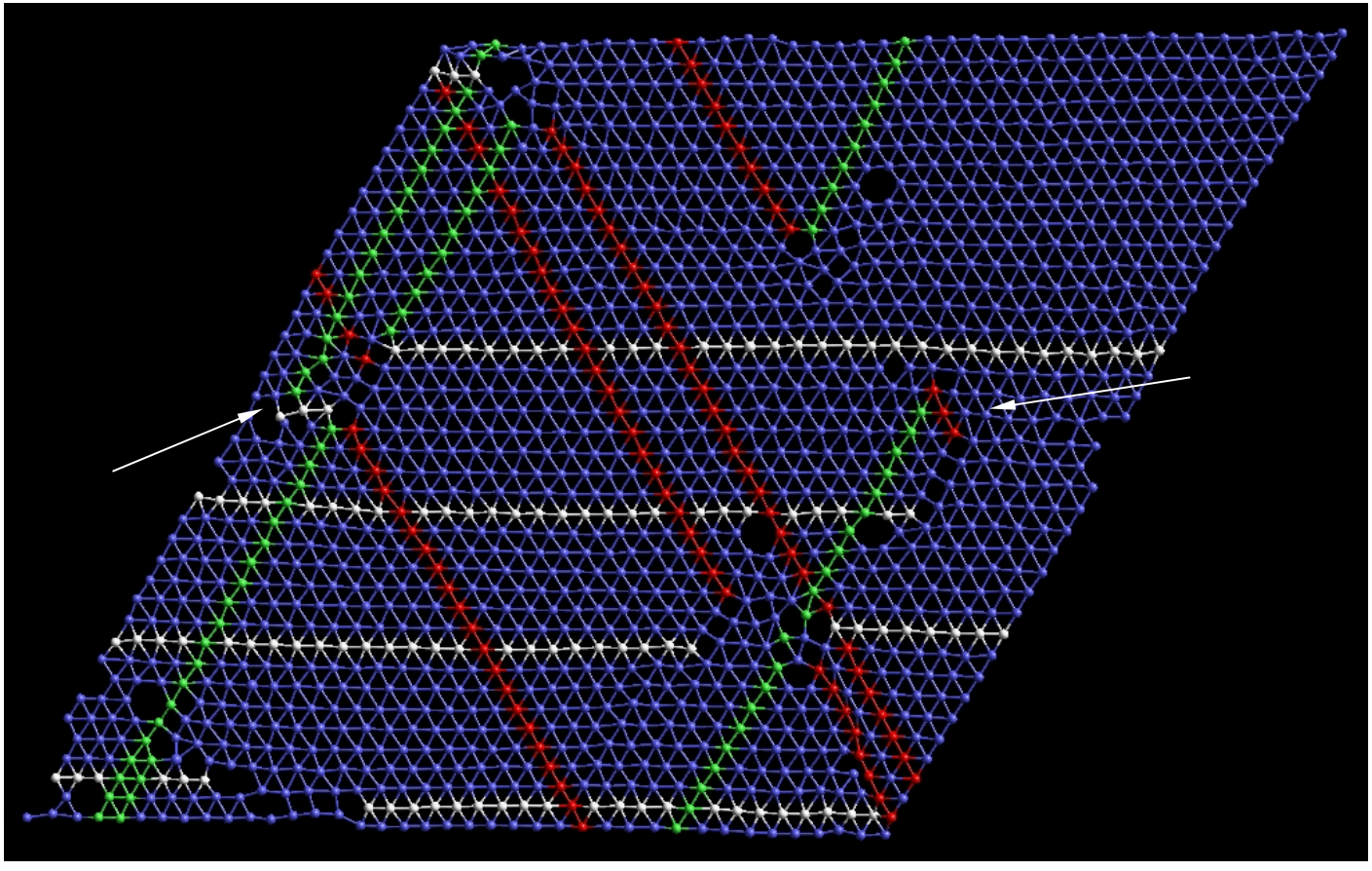

Fig. 4.11. *Ball and stick representation of the interfacial zirconium sublattice, showing the complex dislocation network.*

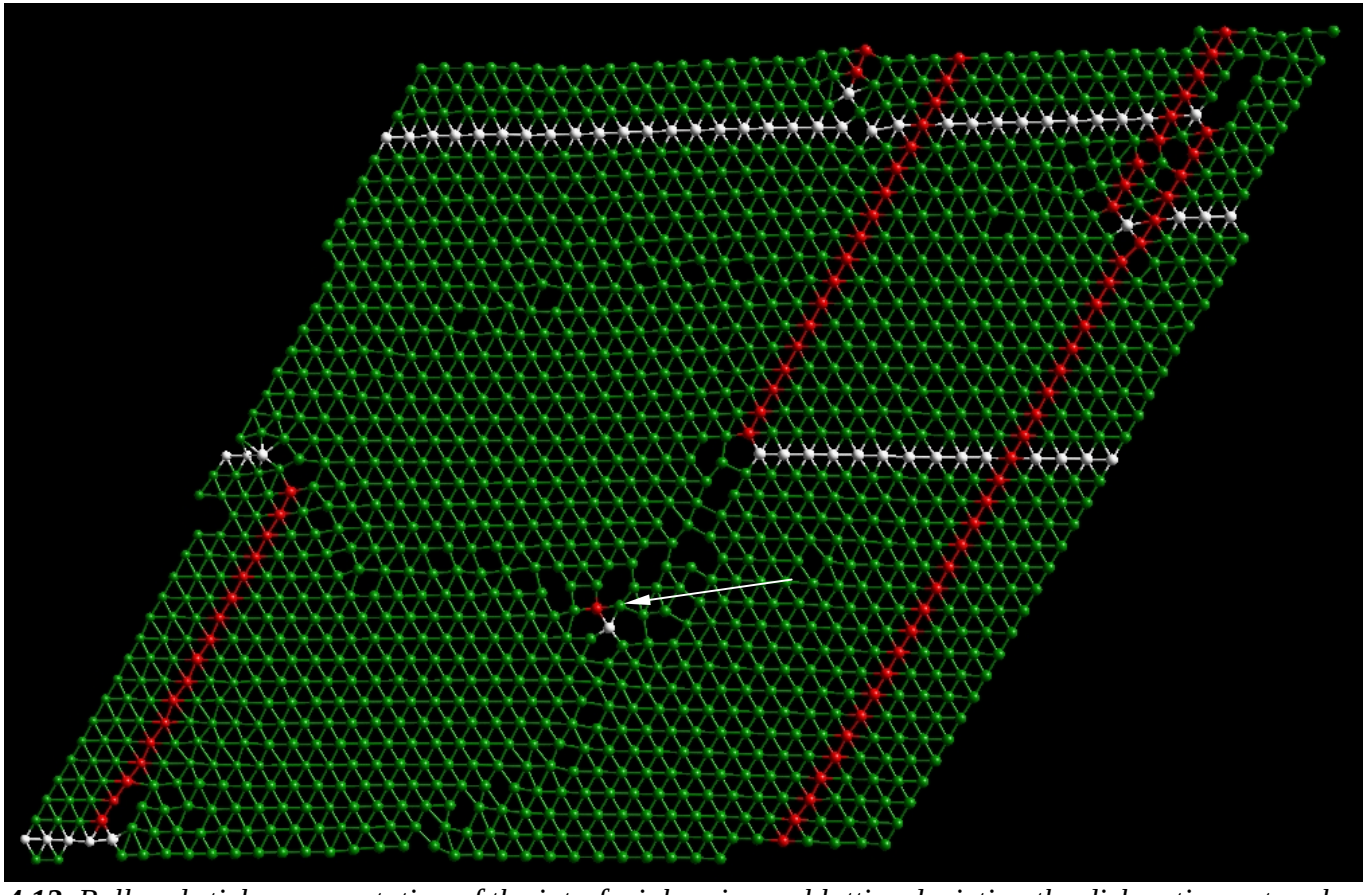

Fig. 4.12. *Ball and stick representation of the interfacial cerium sublattice depicting the dislocation network within the layer.*

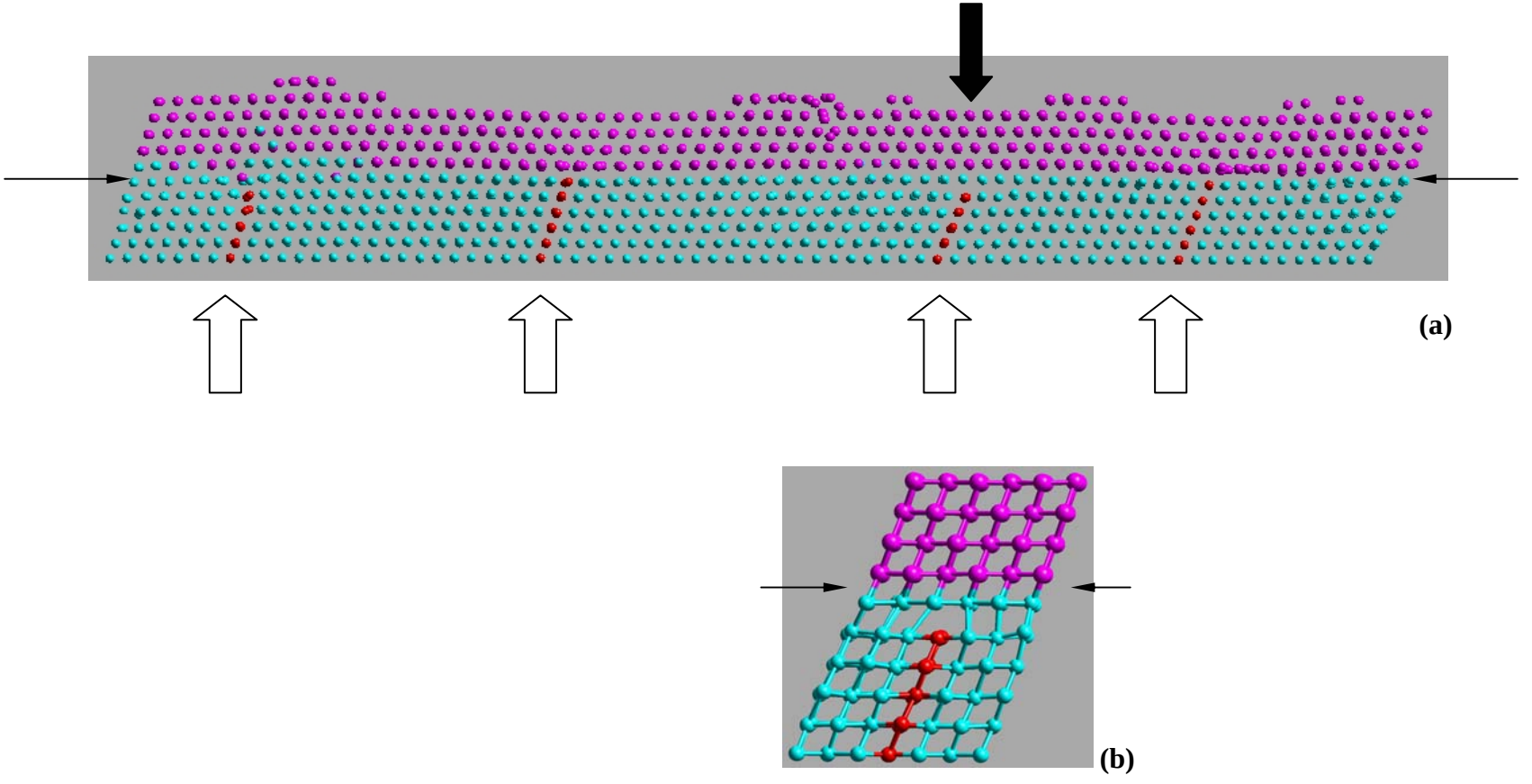

Fig. 4.14. *(a) Ball and stick representation of a cross-section of the $CeO_2(111)/ZrO_2(111)$ interface depicting the regular array of dislocations (red); (b) enlarged segment depicting more clearly, the core structure. For reasons of clarity only the cation sublattice is shown. Cerium ions are magenta and zirconium ions are light blue. Black horizontal arrows represent the interfacial plane.*

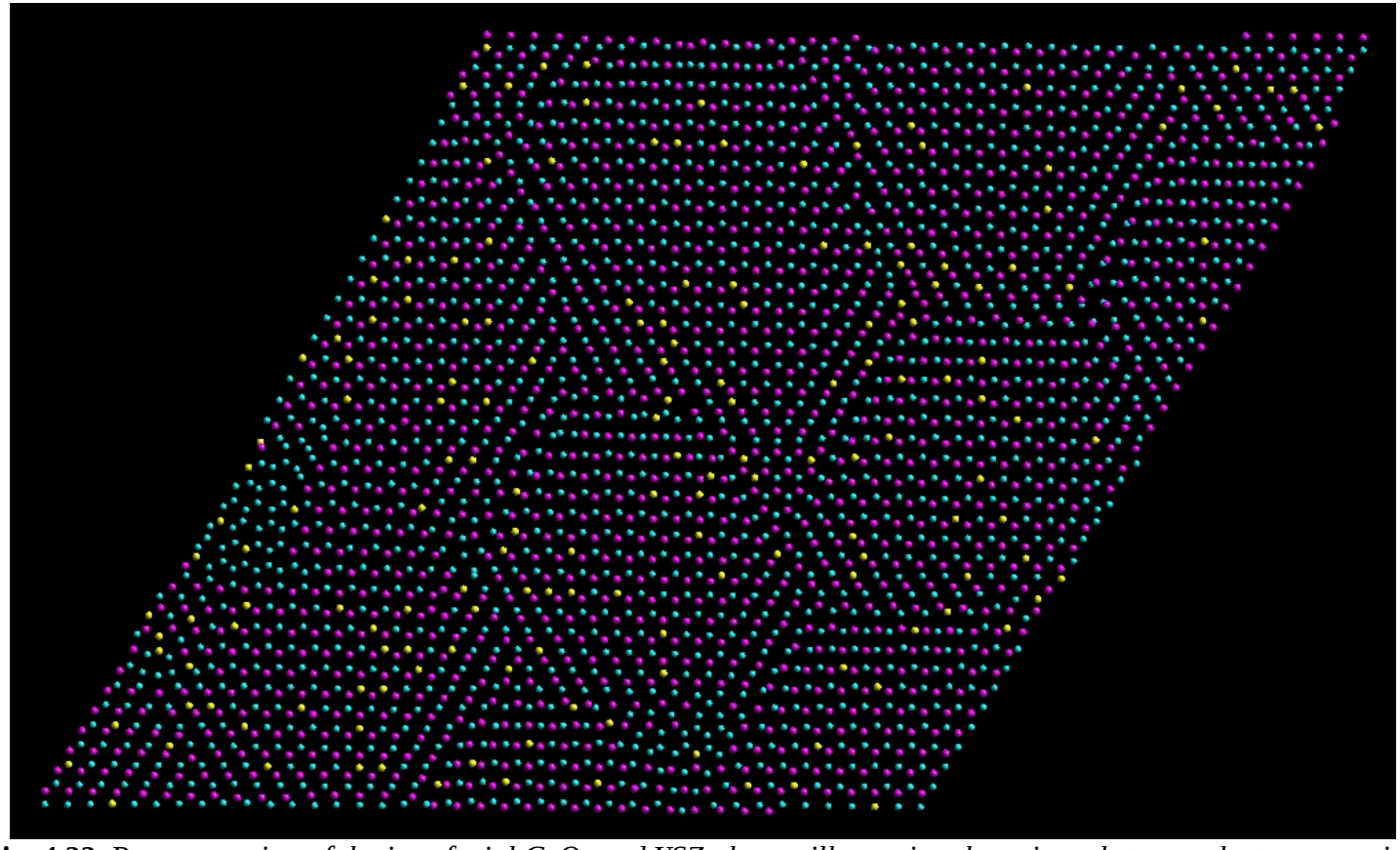

Fig. 4.22. *Representation of the interfacial CeO_2 and YSZ planes, illustrating the epitaxy between the two materials at the interface. Only the cation sublattices and yttrium dopants are shown for clarity. Colour notation as fig. 4.18.*

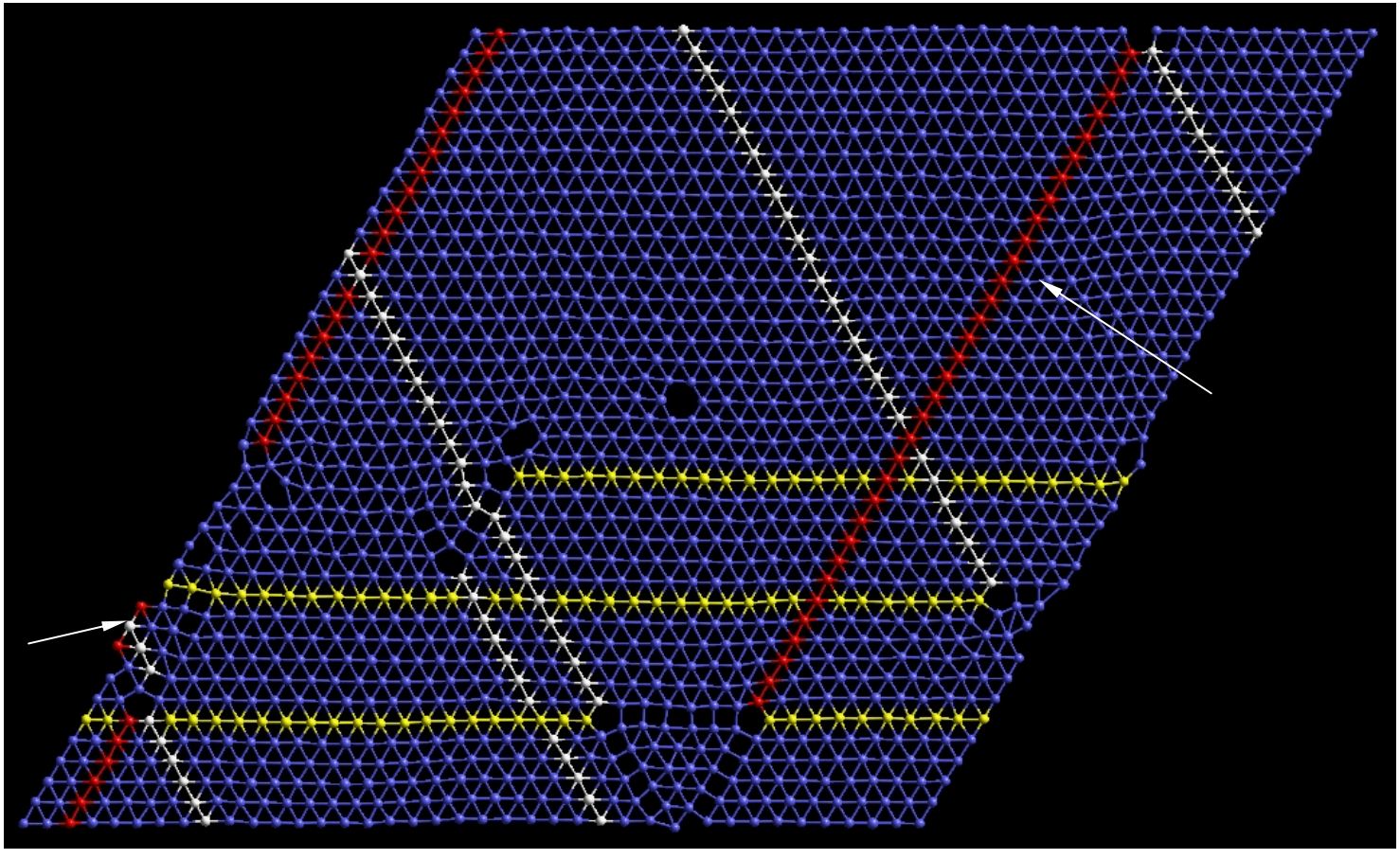

Fig. 4.26. *Ball and stick representation of the interfacial YSZ layer, showing the complex dislocation network. To preserve clarity of the figure only the cation sublattice of the YSZ interfacial plane is depicted.*

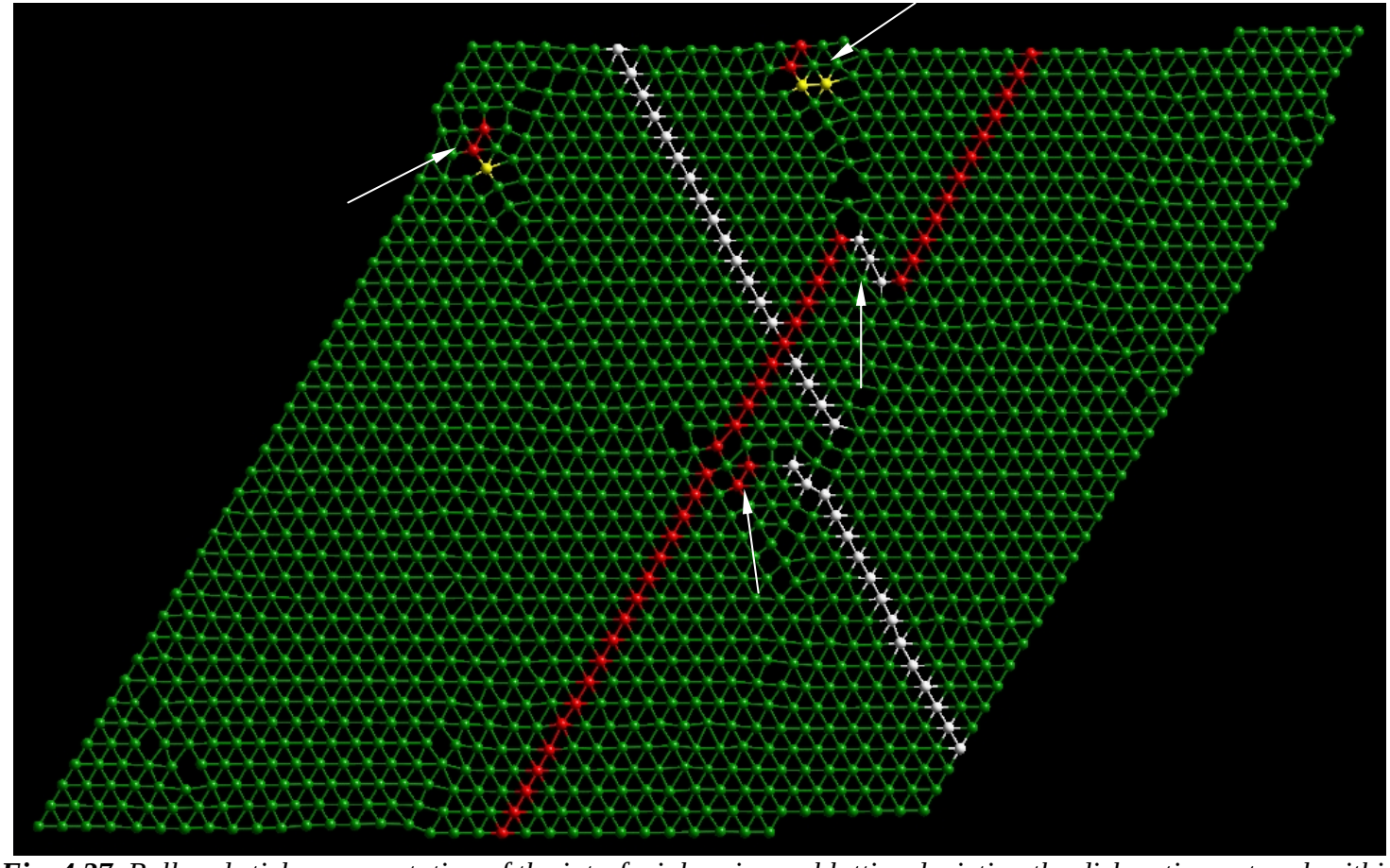

Fig. 4.27. *Ball and stick representation of the interfacial cerium sublattice depicting the dislocation network within the layer.*

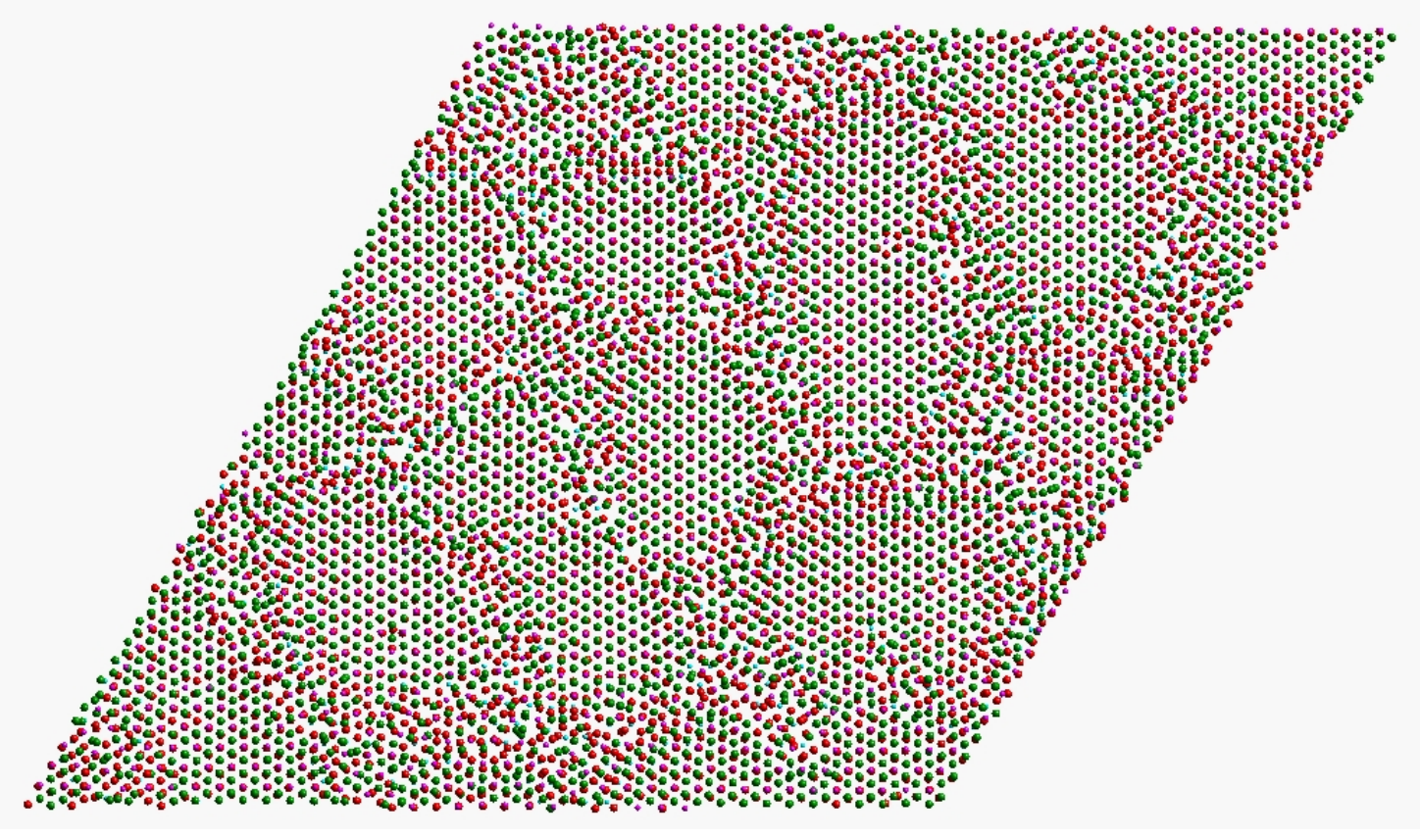

Fig. 4.3. *Plan view of the $CeO_2/ZrO_2(111)$ system. Only two units of the support are presented for clarity. Zirconium is coloured light blue, cerium is magenta, oxygen (ZrO_2) is red and oxygen (CeO_2) is green.*

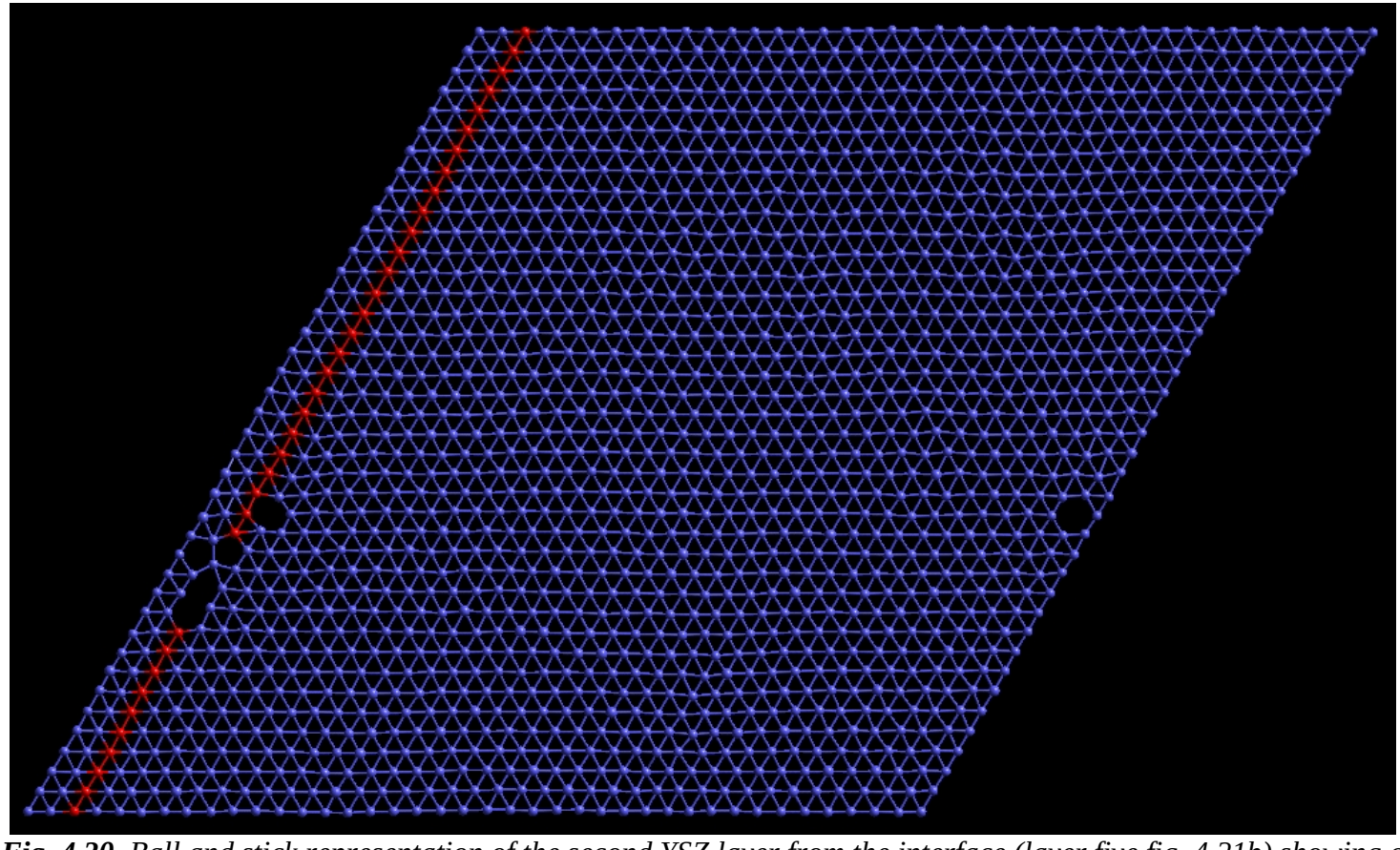

Fig. 4.30. *Ball and stick representation of the second YSZ layer from the interface (layer five fig. 4.21b) showing a pair of edge dislocation. Only the cation sublattice is shown to preserve clarity.*

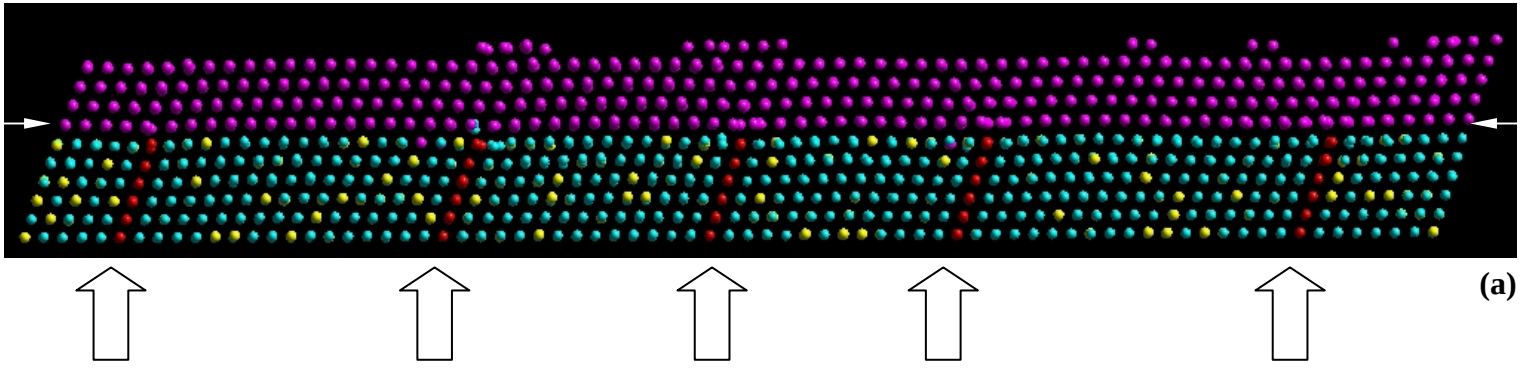

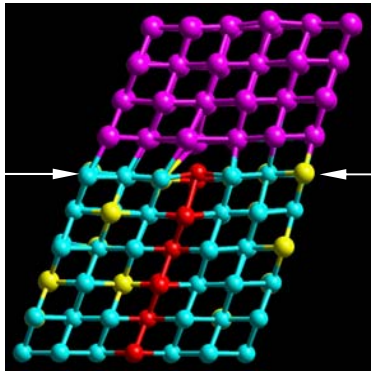

Fig. 4.31. *Cross-section of the CeO_2(111)/YSZ(111) interface: (a) across the entire simulation cell; (b) enlarged view of the dislocation far left in fig. 4.29a depicting more clearly the core structure. Cerium ions are magenta, zirconium ions are light blue and red (dislocation) and yttrium, yellow. The interfacial plane is marked with white horizontal arrows.*

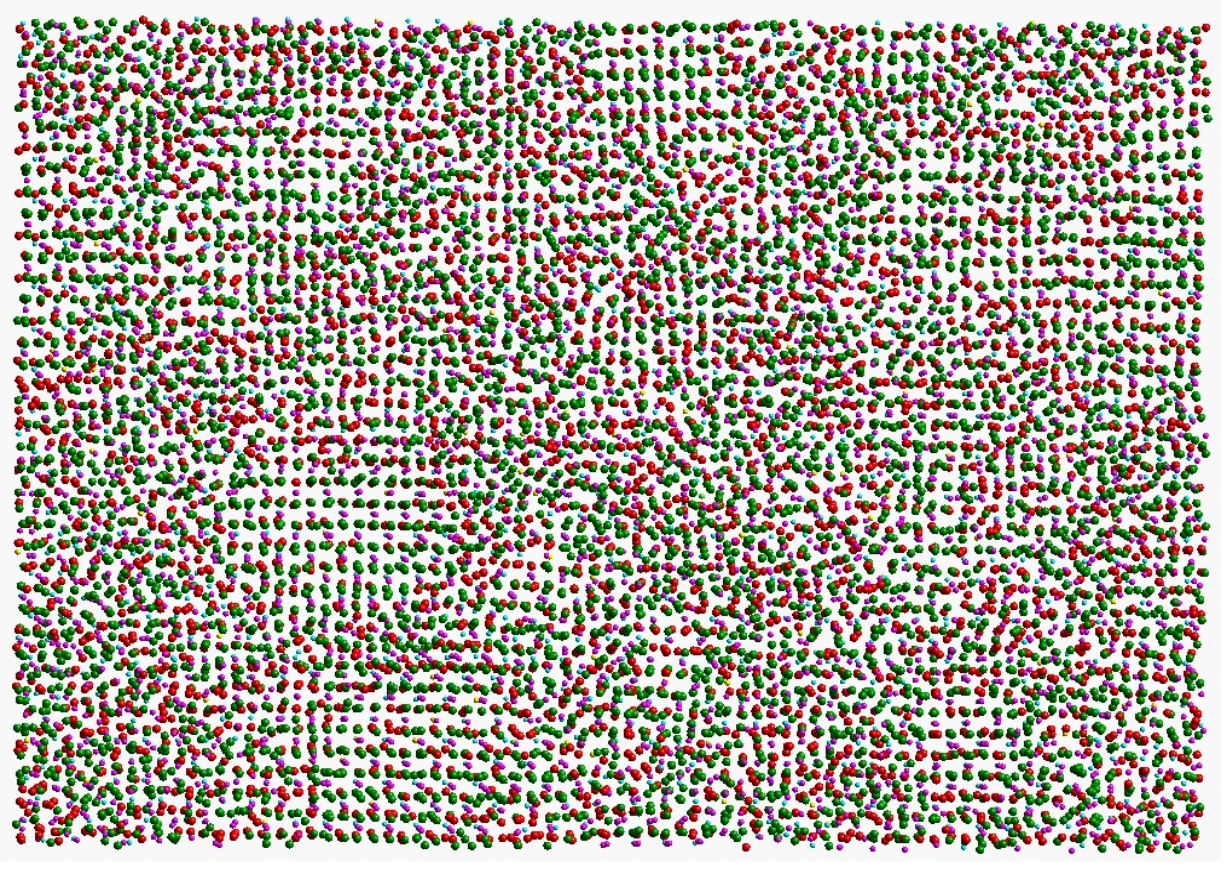

Fig. 4.36. *Top view of the final structure of the CeO_2/YSZ(110) system, (thin film and three unit cells of the underlying support). Colour notation as in fig. 4.35.*

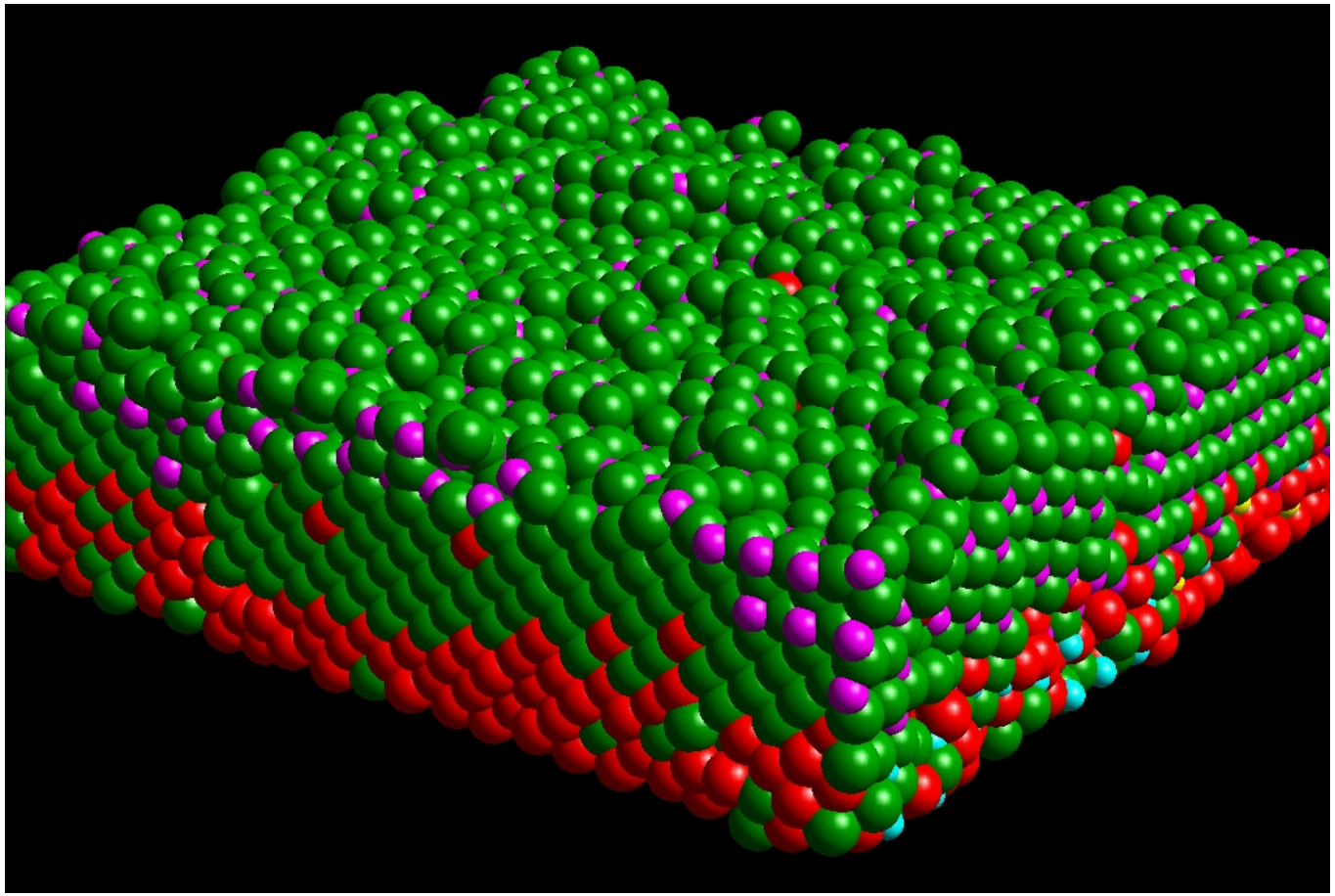

Fig. 4.41. *Representation of the final structure of the CeO_2/YSZ(110) interface. Zirconium is coloured light blue, cerium magenta, yttrium yellow, oxygen (YSZ) is red and oxygen (CeO_2) green. To preserve clarity of the figure, only a small part of the simulation cell is shown together with three unit cells of the underlying support.*

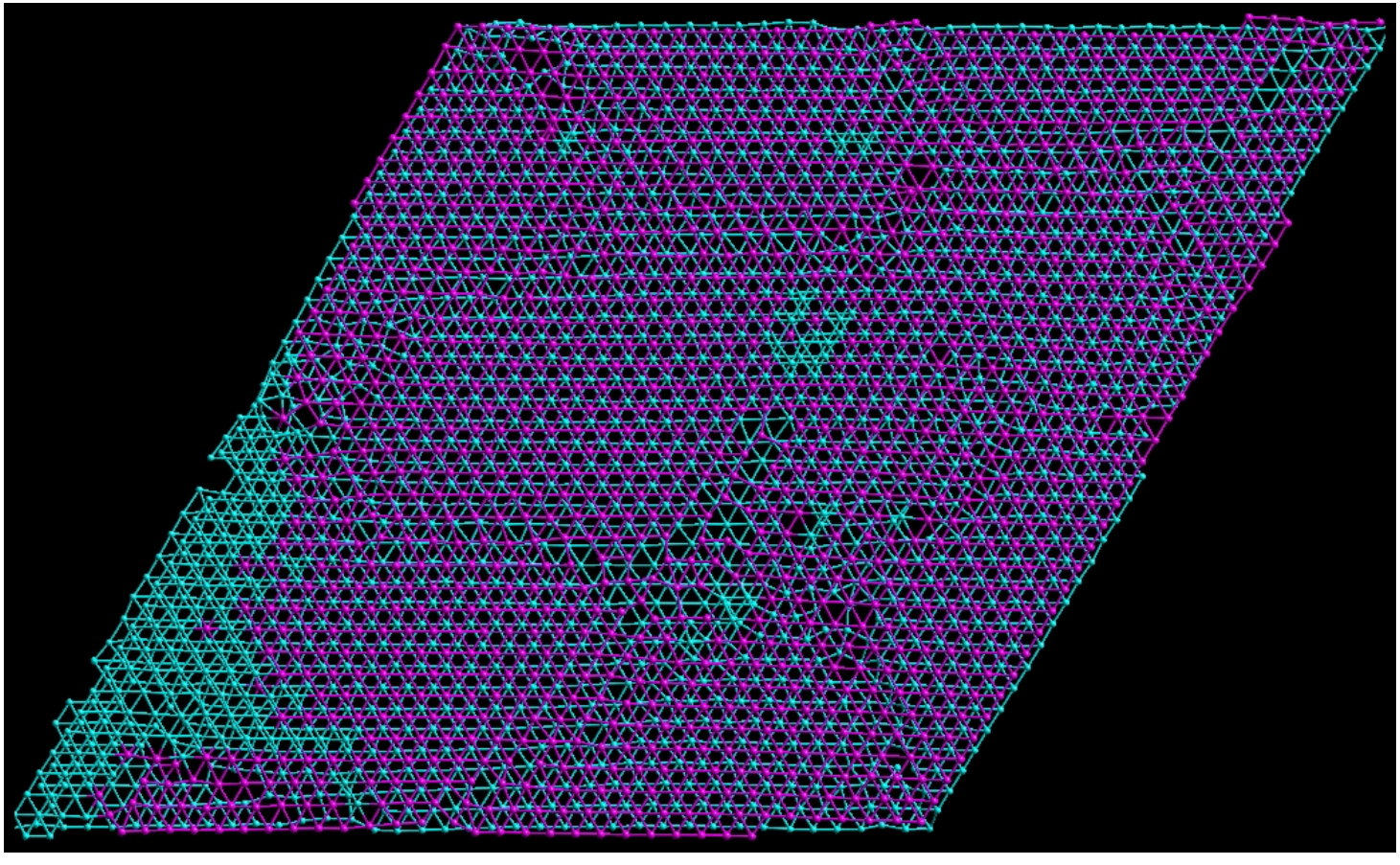

Fig. 4.7. *Representation of the interfacial matching between CeO_2 thin film (layer 1) and underlying ZrO_2 support (layer 6). Only the cation sublattice is shown for clarity. Cerium is coloured magenta and zirconium light blue.*

Appendix A

Characterization methods used to analyse solid-solid interfaces – acronyms

AES – Auger electron spectroscopy
AFM – Atomic force microscopy
EBSB – Electron backscattered diffraction
EDXS – Energy dispersive X-ray spectrometry
EELS – Electron energy loss spectroscopy
HREM – High-resolution electron microscopy
HRSTEM – High-resolution scanning transmission electron microscopy
HRTEM – High-resolution transmission electron microscopy
HVTEM – High-voltage transmission electron microscopy
LEED – Low-energy electron diffraction
LEIS – Low energy ion scattering
Li^+ impact collision ISS – Li^+ impact collision ion scattering spectroscopy
Raman spectroscopy
RBS – Rutherford backscattering spectroscopy
RHEED – Refection high-energy electron diffraction
SEM – Scanning electron microscopy
SIMS – Secondary ion mass spectrometry
SPA – LEED – Spot profile analysis of low energy electron diffraction
STM – Scanning tunnelling microscopy
TEM – Transmission electron microscopy
UPS – Ultraviolet photoelectron spectroscopy
XAES – X-ray induced Auger electron spectroscopy
XAS – X-ray adsorption spectroscopy
XPD – X-ray photoelectron diffraction
XPS – X-ray photoelectron spectroscopy
X-ray reflectivity
XRD – X-ray diffraction
XTEM – Cross-sectional transmission electron microscopy

Appendix B

Ewald summation technique

The first term in the lattice energy equation (chapter 2, eq. 2.1) is represented by the long range Coulombic interaction, which accounts for about 80% of the lattice energy. This term gives computational problems due to the long-range nature of Coulombic interactions, which converge very slowly, as 1/r, in real space. The summation of these terms can however be evaluated to circumvent the slow convergence using the Ewald summation technique (Ewald 1921). This technique is now described.

1/r can be expressed in integral form as:

$$\frac{1}{r} = \frac{2}{\pi^{1/2}} \int_0^{\infty} \exp(-r^2 t^2) dt \,, \qquad \textbf{(B.1)}$$

where *t* is a variable.

This identity can be separated into two terms by splitting the integral at a point η:

$$\frac{1}{r} = \frac{2}{\pi^{1/2}} \int_0^{\eta} \exp(-r^2 t^2) dt + \frac{2}{\pi^{1/2}} \int_{\eta}^{\infty} \exp(-r^2 t^2) dt \,, \qquad \textbf{(B.2)}$$

where η is a variable parameter, chosen to optimise the speed of convergence of the system.

The first term (I_1) of the equation B.2 can be transformed into reciprocal space by Fourier analysis:

$$I_1 = \frac{2}{\pi^{1/2}} \int_0^{\eta} \exp(-r^2 t^2) dt = \frac{4\pi}{V} \sum_{\underline{G}} \frac{1}{G^2} \exp(-G^2/4\eta) \cdot \exp(-i\underline{G} \cdot \underline{r}) \,, \quad \textbf{(B.3)}$$

where $\underline{G}$ is the reciprocal lattice vector and

V the volume of the unit cell.

The second term in the equation B.2 can be evaluated in real space:

$$I_2 = \frac{2}{\pi^{1/2}} \int_{\eta}^{\infty} \exp(-r^2 t^2) dt = \frac{1}{r} erfc(\eta r), \qquad \textbf{(B.4)}$$

where $erfc(\eta r)$ is the complementary error function and is related to the standard error function by:

$$erfc(\underline{r}) = 1 - erf(\underline{r}) \qquad \textbf{(B.5)}$$

The total Coulombic contribution to the lattice energy therefore becomes:

$$\sum_{ij} \frac{q_i q_j}{r_{ij}} = \frac{4\pi}{V} \sum_{\underline{G}} \frac{\exp(-G^2/4\eta)}{G^2} \cdot \sum_{ij} q_i q_j \exp(-i\underline{G} \cdot \underline{r}_{ij}) + \sum_{ij} q_i q_j \frac{erfc(r_{ij}\eta)}{r_{ij}}$$

(B.6)

The summation is now rapidly convergent with increasing $\underline{G}$ and r. The self interaction energy terms must be substracted.

Appendix C

Interfacial matching in cubic systems

1. Coherent structure

- Negative misfit ($a_1 < a_2$)

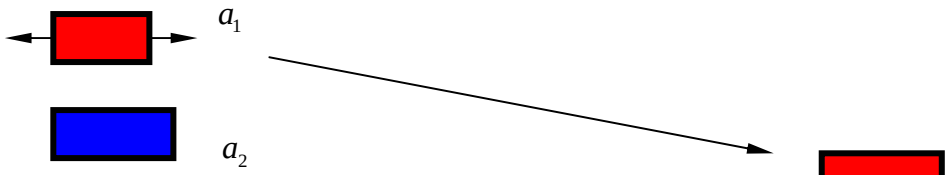

- Positive misfit ($a_1 > a_2$)

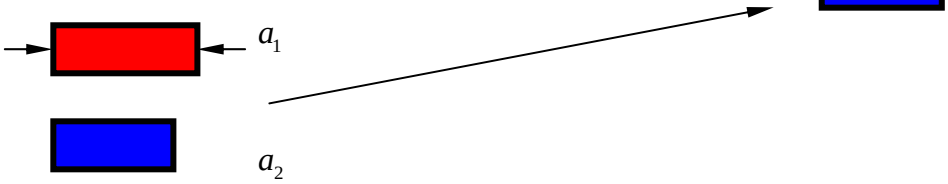

The misfit associated with these configurations, F, can be calculated following equation:

$$F = \frac{(a_1 - a_2)}{(a_1 + a_2)/2} \times 100, \qquad \textbf{(C.1)}$$

where a_1 and a_2 represent the bulk lattice parameters for the thin film and support.

To obtain coherence the thin film needs to be compressed, C, by:

$$C = \frac{(a_1 - a_2)}{a_1} \times 100 \qquad \textbf{(C.2)}$$

2. Incommensurate structure

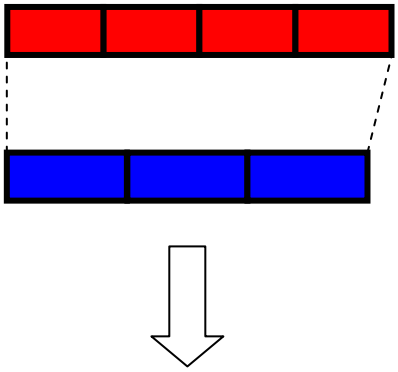

$$F = \frac{(4a_1 - 3a_2)}{(4a_1 + 3a_2)/2} \times 100 \qquad \textbf{(C.3)}$$

3. Commensurate structure

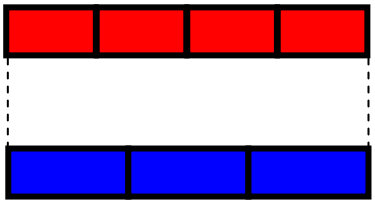

4. Near Coincidence Site Lattice (NCSL)

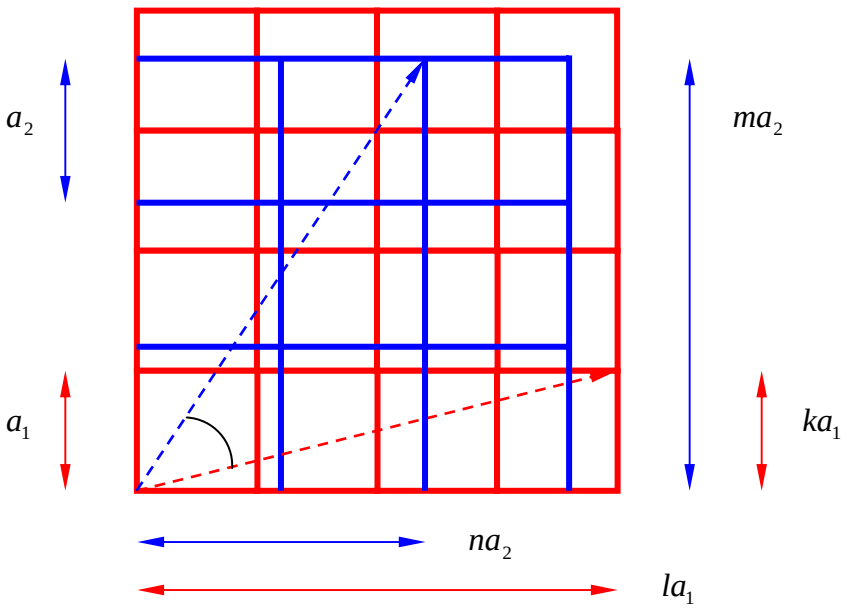

A two-dimensional coincidence site lattice between two materials with cubic symmetry can be realised by rotating one lattice with respect to the other about the axis normal to the interface. Exact coincidence occurs when:

$$\left(\frac{a_1}{a_2}\right)^2 = \frac{(m^2+n^2)}{(k^2+l^2)}, \qquad \textbf{(C.4)}$$

where k, l, m, n are integers.

The rotation angle required to bring the two crystals into exact coincidence is:

$$\theta = \tan^{-1}\left(\frac{n}{m}\right) \pm \tan^{-1}\left(\frac{l}{k}\right) \qquad \textbf{(C.5)}$$

The misfit, which must be accommodated by the expansion or contraction of the crystal is given by:

$$F = \frac{a_1\sqrt{(k^2+l^2)} + a_2\sqrt{(m^2+n^2)}}{\left[a_1\sqrt{(k^2+l^2)} + a_2\sqrt{(m^2+n^2)}\right]/2} \qquad \textbf{(C.6)}$$

Other configurations, which include matching in hexagonal systems and matching between various (hkl)/h'k'l') combinations can also be generated using NCSL (Sutton 1987 and Sayle T. X. T. 1993).

Appendix D

Surface type structures for cubic fluorite materials

Surfaces of inorganic materials, oxides in our case, can be classified into three types according to their atomic arrangement (Tasker 1979).

- **Type 1** surfaces can be described as a stack of planes comprising equal number of cations and anions. Therefore the net charge on each plane is 0 and there is no dipole moment normal to the surface (figure D.1a and b). This category includes fluorite (110) and (310) surfaces, rocksalt (100) and (110) surfaces and perovskite (100) surface (Sayle T. X. T. 1994a and Conesa 1995).
- **Type 2** surfaces, which include fluorite (111), comprise charged planes arranged symmetrically (O-Ce-O, three plane repeat unit, figure D.1c). The dipole moment perpendicular to the surface is zero because of the symmetrical stacking sequence.
- **Type 3** surfaces, such as fluorite (100), consist of alternating layers of cations and anions, which introduce a dipole moment perpendicular to the surface (figure D.1d). The dipole moment can be neutralized if defects are created on the surface (turning a type 3 surface in a type 2 surface, ½O-Ce-½O) (Vyas 1989). It was shown experimentally that a CeO_2(001) surface supported on $SrTiO_3$ is terminated with 0.5 monolayers of oxygen (Herman 1999a and 1999b). Noguera (2000) in his work summarizes polar oxide surfaces (rock-salt, spinel, corundum structures) and examine their stability focusing on surface atomic configuration.

The stability of ceria surfaces, increases in the order **type3 < type1 < type2**, **(100) < (310) < (110) < (111)** (Sayle T. X. T. 1994a). It was found also that for ceria-zirconia solid solutions (including pure zirconia), stability of the surfaces is **(310) < (110) < (111)** (Balducci 1998).

Considering their atomic arrangement these type of surfaces can have specific properties, e.g. catalytic properties. For example a perfect flat surface as (111) might have diminished catalytic properties in comparison

with a (310) surface, which has atomic steps on the surface (these steps can constitute active centres for the catalytic material). Also the (100) surface, which presents a dipole moment normal to the surface has the tendency to reconstruct in order to neutralize this dipole and therefore can constitute a more active surface for a catalyst.

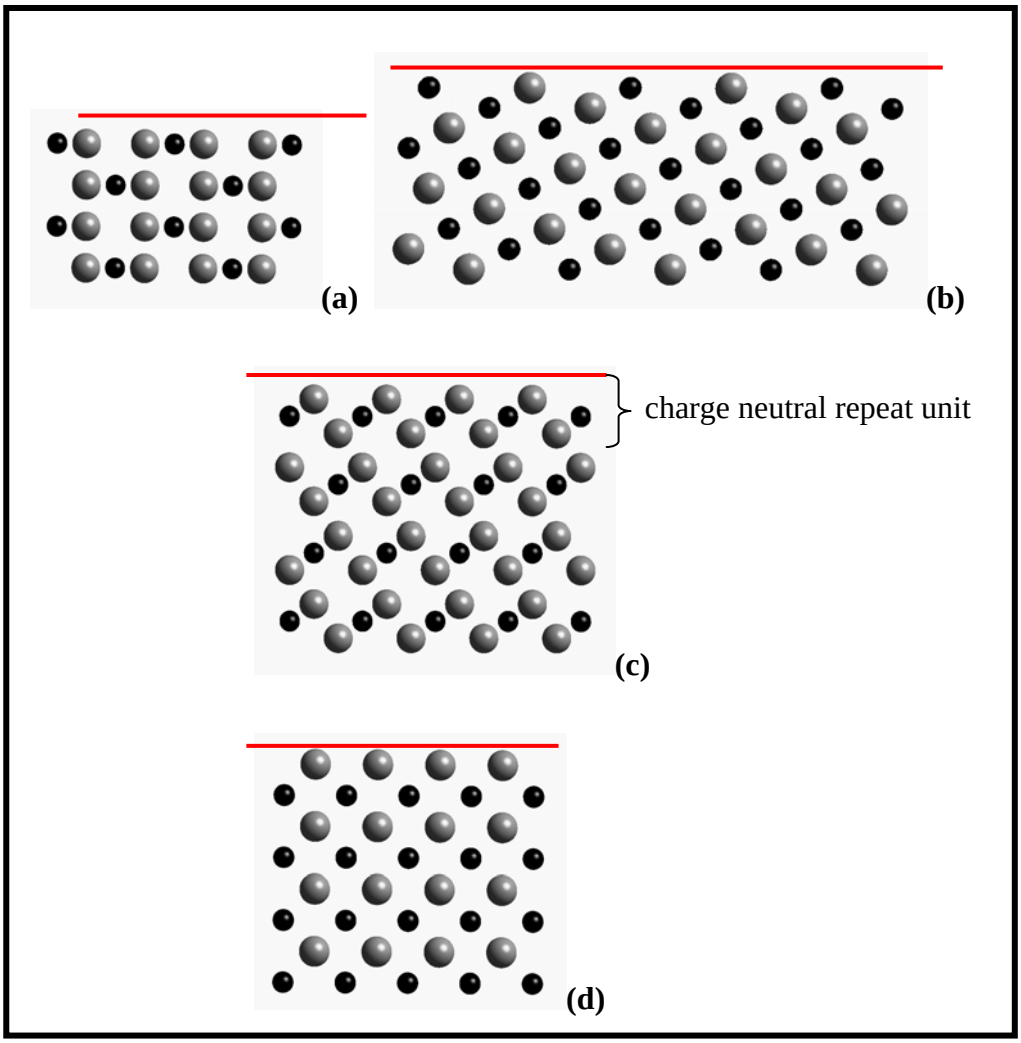

Fig. D.1. *Side view of four fluorite oxide surfaces: (a) (110); (b) (310); (c) (111) and (d) (100). Cations are represented with black spheres and oxygen anions with dark grey spheres. The red line indicates the surface.*

Appendix E

Crystallographic characteristics of materials with various structural types (Weast 1982, Bever 1986)

Material	Crystal system	Space group	Structure type	Lattice parameter
Mo	cubic	Im3m	body-centered cubic	a=3.1472
Pt	cubic	Fm3m	face-centered cubic	a=3.9231
Ag	cubic	Fm3m	face-centered cubic	a=4.0862
Si	cubic	Fd3m	diamond	a=5.4305
MgO	cubic	Fm3m	rock salt	a=4.2117
CaO	cubic	Fm3m	rock salt	a=4.8108
SrO	cubic	Fm3m	rock salt	a=5.1602
BaO	cubic	Fm3m	rock salt	a=5.5393
FeO	cubic	Fm3m	defect rock salt	a=4.3088
CeO_2	cubic	Fm3m	fluorite	a=5.411
TiO_2	tetragonal	P4/mnm	rutile	a=4.5937 c=2.9618
ZrO_2	monoclinic	$P2_1/c$	baddeleyite	a=5.1454 b=5.2075 c=5.3107
ZnO	hexagonal	$P6_3mc$	zincite	a=3.2495 c=5.2069
Al_2O_3	hexagonal	$R\bar{3}c$	corundum	a=4.7591 c=12.9894
$SrTiO_3$	cubic	Pm3m	tausonite	a=3.905

References

Adams, J. B., Wang, Z. and Li, Y., *Thin Solid Films*, 2000, **365**, 201-210.

Aguiar, R., Sánchez, F., Ferrater, C., Aguiló, M. and Varela, M., *Thin Solid Films*, 1998, **317**, 81-84.

Allan, N. L. and Mackrodt, W. C., *Advances in Solid-State Chemistry*, 1993, **3**, 221-270.

Allan, N. L., Barrera, G. D., Purton, J. A., Sims, C. E. and Taylor, M. B., *Physical Chemistry Chemical Physics*, 2000, **2**, 1099-1111.

Babelon, P., Dequiedt, A. S., MostefaSba, H., Bourgeois, S., Sibillot, P. and Sacilotti, M., *Thin Solid Films*, 1998, **322**, 63-67.

Bae, S. Y., Choi, H. S., Choi, S. Y. and Oh, Y. J., *Ceramics International*, 2000, **26**, 213-214.

Balducci, G., Kašpar, J., Fornasiero, P., Graziani, M., Islam, M. S., and Gale, J. D., *Journal of Physical Chemistry B*, 1997, **101**, 1750-1753.

Balducci, G., Kašpar, J., Fornasiero, P., Graziani, M. and Islam, M. S., *Journal of Physical Chemistry B*, 1998, **102**, 557-561.

Balducci, G., Islam, M. S., Kašpar, J., Fornasiero, P. and Graziani, M., *Chemistry of Materials*, 2000, **12**, 677-681.

Baudin, M., Wojcik, M. and Hermansson, K., *Surface Science*, 2000, **468**, 51-61.

Bäumer, M., Frank, M., Heeimeier, M., Kühnemuth, R., Stempel, S. and Freund, H. -J., *Surface Science*, 2000, **454-456**, 957-962.

Bever, M. B. ed., *'Encyclopaedia of Materials Science and Engineering'*, Pergamon Press, Oxford, 1986.

Born, M. and Huang, K., *'Dynamical theory of crystal lattice'*, Clarendon Press, Oxford, 1954.

Boulouz, M., Martin, L., Boulouz, A. and Boyer, A., *Materials Science and Engineering*, 1999, **B67**, 122-131.

Brazdeikis, A., Karlsson, U. O. and Flodström, A.S., *Thin Solid Films*, 1996, **281-282**, 57-59.

Brinkman, H. W., Briels, W. J. and Verweij, H., *Chemical Physics Letters*, 1995, **247**, 386-390.

Broadbelt, L. J. and Snurr, R. Q., *Applied Catalysis A*, 2000, **200**, 23-46.

Bush, T. S., Gale, J. D., Catlow, C. R. A. and Battle, P. D., *Journal of Materials Chemistry*, 1994, **4**, 831-837.

de Carolis, S., Pascual, J. L., Petterson, G. M., Baudin, M., Wójcik, M., Hermansson, K., Palmqvist, A. E. and Muhammed, M., *Journal of Physical Chemistry B*, 1999, **103**, 7627-7636.

Catlow, C. R. A. and Mackrodt, W. C., *'Computer simulation of solids'*, eds.

Catlow, C. R. A. and Mackrodt, W. C., *Lecture Notes in Physics*, 1982, **166**, 130.

Catlow, C. R. A., *'Computational techniques and simulation of crystal structures'* in *'Solid state chemistry techniques'*, eds. Cheetham, A. K. and Day, P., Clarendon Press, Oxford, 1987.

Catlow, C. R. A. and Price, G. D., *Nature*, 1990, **347**, 243.

Catlow, C. R. A., *Computational Materials Science*, 1994a, **2**, 6-18.

Catlow, C. R. A., Bell, R. G. and Gale, J. D., *Journal of Materials Chemistry*, 1994b, **4**, 781-792.

Catlow, C. R. A., Ackermann, L., Bell, R. G., Corà, F., Gay, D. H., Nygren, M. A., Pereira, J. C., Sastre, G., Slater, B. and Sinclair, P. E., *Faraday Discussions*, 1997a, **106**, 1-40.

Catlow, C. R. A., Ackermann, L., Bell, R. G., Gay, D. H., Holt, S., Lewis, D. W., Nygren, M. A., Sastre, G., Sayle, D. C. and Sinclair, P. E., *Journal of Molecular Catalysis A*, 1997b, **115**, 431-448.

Catlow, C. R. A., Bulatov, V. L. and Grimes, R. W., *Nuclear Instruments and Methods in Physics Research B*, 1997c, **122**, 301-310.

Cerius^2 3.0, Molecular Simulation, San Diego, 1997.

Cerrato, G., Bordiga, S., Barbera, S. and Morterra, C., *Applied Surface Science*, 1997a, **115**, 53-65.

Cerrato, G., Bordiga, S., Barbera, S. and Morterra, C., *Surface Science*, 1997b, **377-379**, 50-55.

Chambers, S. A., *Surface Science Reports*, 2000, **39**, 105-180.

Chang, C. L., Chern, G., Chean, Y. R. and Chen, C. L., *Applied Surface Science*, 2000, **161**, 448-451.

Chen, M., Luo, M. F., Zhou, R. X., Ding, Y. J. and Zheng X. M., *Indian Journal of Chemistry A*, 1999, **38**, 646-650.

Chern, G., *Surface Science*, 1997, **387**, 183-191.

Chern, G. and Cheng, C., *Journal of Vacuum Science and Technology*, 1999, **17**(4), 1097-1102.

Conesa, J. C., *Surface Science*, 1995, **339**, 337-352.

Cordatos, H., Ford, D. and Gorte, R. J., *Journal of Physical Chemistry*, 1996a, **100**, 18128-18132.

Cordatos, H., Bunluesin, T., Stubenrauch, J., Vohs, J. M. and Gorte, R. J., *Journal of Physical Chemistry*, 1996b, **100**, 785-789.

Dai, Z. R., Wang, Z. L., Chen, Y. R., Wu, H. Z. and Liu, W. X., *Philosophical Magazine A*, 1996, **72**, 415-430.

Dell'Agli, G., Ferone, C., Mascolo, G. and Pansini, M., *Solid State Ionics*, 2000, **127**, 223-230.

Dick, B. G. and Overhauser, A. W., *Physical Review*, 1958, **112**, 90-103.

Dmowski, W., Egami, T., Gorte, R. and Vohs, J., *Physica B*, 1996, **221**, 420-425.

Dmowski, W., Mamontov, E., Egami, T., Putna, S. and Gorte, R., *Physica B*, 1998, **248**, 95-100.

Domingos, H. S. and Bristowe, P. D., *Scripta Materialia*, 1999, **41**, 1347-1352.

Dong, L, Schnitker, J., Smith, R. W. and Srolovitz, D. J., *Journal of Applied Physics*, 1998, **83**, 217-227.

Dubourdieu, C., Kang, S. B., Li, Y. Q., Kulesha, G. and Gallois, B., *Thin Solid Films*, 1999, **339**, 165-173.

Dwivedi, A. and Cormack, A. N., *Journal of Solid State Chemistry*, 1989, **79**, 218-231.

Dwivedi, A. and Cormack, A. N., *Philosophical Magazine A*, 1990, **61**, 1-22.

Elidrisi, B., Addou, M., Regragui, M., Monty, C., Bougrine, A. and Kachouane, A., *Thin Solids Film*, 2000, **379**, 23-27.

Elliot, S., *'The physics and chemistry of solids'*, J. Wiley & Sons, Chichester, 1998.

Ernst, F., Rečnik, A., Langjahr, P. A., Nellist, P. D. and Rühle, M., *Acta Materialia*, 1999, **47**, 183-198.

Ewald, P. P., *Annalen der Physik*, 1921, **64**, 253-287.

Farrauto, R. J. and Heck, R. M., *Catalysis Today*, 1999, **51**, 351-360.

Ferrizz, R. M., Egami, T. and Vohs, J. M., *Surface Science*, 2000, **465**, 127-137.

Fisher, C. A. and Matsubara, H., 6th *International Symposium on Ceramic Materials and Components for Engines*, 1997, 832-837.

Fisher, C. A. J. and Matsubara, H., *Solid State Ionics*, 1998, **113-115**, 311-318.

Fisher, C. A. and Matsubara, H., *Computational Materials Science*, 1999a, **14**, 177-184.

Fisher, C. A. and Matsubara, H., *Journal of European Ceramic Society*, 1999b, **19**, 703-707.

Fornasiero, P., Kašpar, J., Sergo, V. and Graziani, M., *Journal of Catalysis*, 1999, **182**, 56-69.

Frank, F. C. and van der Merwe, J. H., *Proceddings of the Royal Society (London) A*, 1949, **198**, 205-225.

Gale, J. D., *Philosophical Magazine B*, 1996, **73**, 3-19.

Gao, P., Meng, L. J., dos Santos, M. P., Teixeira, V. and Andritschky, *Vacuum*, 2000, **56**, 143-148.

Gao, Y., Kim, Y. J., Chambers, S. A. and Bai, G., *Journal of Vacuum Science & Technology A*, 1997, **15**, 332-339.

Gao, Y., Herman, G. S., Thevuthasan, S., Peden, C. H. F. and Chambers S. A., *Journal of Vacuum Science & Technology A*, 1999, **17**, 961-969.

Garcia, G., Casado, J., Llibre, J., Cifre, J., Figueras, A., Galí, S. and Bassas, J., *Chemical Vapor Deposition*, 1997, **3**, 91-96.

Garcia, G., Figueras, A., Merino, R. I., Orera, V. M. and Llibre, J., *Thin Solid Films*, 2000, **370**, 173-178.

Garvie, R. C., *Journal of Physical Chemistry*, 1965, **69**, 1238-1243.

Garvie, R. C., *Journal of Physical Chemistry*, 1978, **82**, 218-224.

Gale, J. D., *Journal of Chemical Society, Faraday Transactions*, 1997, **93**, 629-637.

Gay, D. H. and Rohl, A. L., *Journal of Chemical Society, Faraday Transactions*, 1995, **91**, 925-936.

Giese, D. R., Lamelas, F. J., Owen, H. A., Plass, R. and Gajdardziska-Josifovska, M., *Surface Science*, 2000, **457**, 326-336.

Gnanarajan, S. and Savvides, N., *Thin Solid Films*, 1999, **350**, 124-129.

Golunski, S. E., Hatcher, H. A., Rajaram, R. R. and Truex, T. J., *Applied Catalysis B*, 1995, **5**, 367-376.

Gorbenko, O. Yu., Graboy, I. E., Kaul, A. R. and Zandbergen, H. W., *Journal of Magnetism and Magnetic Materials*, 2000, **211**, 97-104.

Gordon, R. G. and Kim, Y. S., *Journal of Chemical Physics*, 1972, **56**, 3122-3133.

Groppi, G., Cristiani, C., Lietti, L., Ramella, C., Valentini, M. and Forzatti, P., *Catalysis Today*, 1999, **50**, 399-412.

Hafner, J., *Acta Materialia*, 2000, **48**, 71-92.

Harding, J. H., *Reports on Progress in Physics*, 1990, **53**, 1403-1466.

Harding, J. H., Harris, D. J. and Parker, S. C., *Physical Review* B, 1999a, **60**, 2740-2746.

Harding, J. H., Harris, D. J. and Parker, S. C., *Surface Science*, 1999b, **422**, L183-L187.

Harris, D. J., Watson, G. W. and Parker, S. C., *American Mineralogist*, 1999, **84**, 138-143.

Hartmanova, M., Gmucova, K., Jergel, M., Thurzo, I., Kundracik, F. and Brunel, M., *Solid State Ionics*, 1999a, **119**, 85-90.

Hartmanova, M., Gmucova, K., Jergel, M., Thurzo, I., Kundracik, F. and Brunel, M., *Thin Solid Films*, 1999b, **345**, 330-337.

Hayashi, H., Sagawa, R., Inaba, H. and Kawamura, K., *Solid State Ionics*, 2000, **131**, 281-290.

Heifets, E. and Kotonim, E. A., *Thin Solid Films*, 2000, **358**, 1-5.

Herman, G. S., *Physical Review B*, 1999a, **59**, 14899-14902.

Herman, G. S., *Surface Science*, 1999b, **437**, 207-214.

Holzschuh, H. and Suhr, H., *Applied Physics Letters*, 1991, **59**, 470-472.

Imamura, S., Yamada, H and Utani, K., *Applied Catalysis A*, 2000, **192**, 221-226.

Inaba, H., Sagawa, R., Hayashi, H. and Kawamura, K., *Solid State Ionics*, 1999, **122**, 95-103.

Ishino, M., Yang, J., Makinara, K., Shi, J. and Hashimoto,M., *Journal of Vacuum Science and Technology A*, 2000, **18**, 2339-2343.

Islam, M. S., *Journal of Materials Chemistry*, 2000, **10**, 1027-1038.

Ito, M., Matsumoto, M. and Doi, M., *Fluid Phase Equilibria*, 1998, **144**, 395-401.

Jacobs, P. W. M. and Rycerz, Z. A., '*Molecular Dynamics Methods*' in '*Computer Modelling in Inorganic Crystallography*', ed. Catlow, C. R. A., Academic Press, London, 1997, 83-115.

Jacobsen, S. N., Helmersson, U., Erlandsson, R., Skarman, B. and Wallenberg, L. R., *Surface Science*, 1999a, **429**, 22-33.

Jacobsen, S. N., Madesen, L. D. and Helmersson, U., *Journal of Materials Research*, 1999b, **14**, 2385-2393.

James, M. A. and Hibma, T., *Surface Science*, 1999, **435**, 718-722.

Jensen, F., '*Introduction to Computational Chemistry*', J. Wiley and Sons, Chichester, 1999.

Jia, C. L., Siegert, M. and Urban, K., *Acta Materialia*, 2001, **49**, 2783-2789.

Jiménez, V. M., Espinós, J. P., GonzálesElipe, A. R., Caballero, A. and Yubero, F., *Journal de Physique IV*, 1999, **9**(P8 Pt2), 749-755.

Johnson, M. T., Michael, J. R., Gilliss, S. R. and Carter, C. B., *Philosophical Magazine A*, 1999, **79**, 2887-2898.

Jones, A. C., Leedham, T. J., Wright, P. J., Williams, D. J., Crosbie, M. J., Davies, H. O., Fleeting, K. A. and O'Brien, P., *Journal of European Ceramic Society*, 1999, **19**, 1431-1434.

Kado, T., *Surface Science*, 2000, **454-456**, 783-789.

Kanakaraju, S., Mohan, S. and Sood, A. K., *Thin Solid Films*, 1997, **305**, 191-195.

Karakasidis, T. E. and Evangelakis, G. A., *Surface Science*, 1999, **436**, 193-201.

Kašpar, F., Fornasiero, P. and Graziani, M., *Catalysis Today*, 1999, **50**, 285-298.

Khan, M. S., Islam, M. S. and Bates, D. R., *Journal of Materials Chemistry*, 1998, **8**(10), 2299-2307.

Kim, K. J., Moon, D. W., Lee, S. K. and Jung, K-H., *Thin Solid Films*, 2000, **360**, 118-121.

Kim, L., Kim, J., Jung, D., Park, C-Y., Yang, C-W. and Roh, Y., *Thin Solid Films*, 2000, **360**, 154-158.

Kim, Y. J., Gao, Y. and Chambers, S. A., *Surface Science*, 1997a, **371**, 358-370.

Kim, Y. J., Gao, Y. and Chambers, S. A., *Applied Surface Science*, 1997b, **120**, 250-260.

Kim, Y. J., Gao, Y., Herman, G. S., Thevuthasan, S., Jiang, W., McCready, D. E. and Chambers, S. A., *Journal of Vacuum Science & Technology A*, 1999, **17**, 926-935.

Kobayashi, H., Salahub, D. R. and Ito, T., *Catalysis Today*, 1995, **23**, 357-364.

Koinuma, H., Qiu, X. G., Tsuchiya, R., Kanda, N., Nishino, J., Ohtomo, A. and Kawasaki, M., *Applied Surface Science*, 1998, **127-129**, 403-409.

Konstantinov, K., Stambolova, I., Peshev, P., Darriet, B. and Vassilev, S., *International Journal of Inorganic Materials*, 2000, **2**, 277-280.

Koski, K., Holsa, J. and Juliet, P., *Surface and Coatings Technology*, 1999, **120-121**, 301-312.

Koster, A. J., Ziese, U., Verkleij, A. J., Janssen, A. H. and de Jong, K. P., *Journal of Physical Chemistry B*, 2000, **104**, 9368.

Kubo, M., Yamauchi, R., Vetrivel, R and Miyamoto, A., *Applied Surface Science*, 1994, **82/83**, 559-564.

Kubo, M., Miura, R., Yamauchi, R., Vetrivel, R. and Miyamoto, A., *Applied Surface Science*, 1995a, **89**, 131-139.

Kubo, M., Miura, R., Yamauchi, R., Katagiri, M., Vetrivel, R., Broclawik, E. and Miyamoto, A., *Japanese Journal of Applied Physics*, 1995b, **34**, 6873-6877.

Kubo, M., Stirling, A., Miura, R., Yamauchi, R. and Miyamoto, A., *Catalysis Today*, 1997a, **36**, 143-151.

Kubo, M., Oumi, Y., Miura, R., Stirling, A and Miyamoto, A., *AIChE Journal*, 1997b, **43**, 2765-2772.

Kubo, M., Oumi, Y., Miura, R., Fahmi, A., Stirling, A., Miyamoto, A., Kawasaki, M., Yoshimoto, M. and Koinuma, H., *Journal of Chemical Physics*, 1997c, **107**, 4416-4422.

Kubo, M., Oumi, Y., Miura, R., Stirling, A. Miyamoto, A., Kawasaki, M., Yoshimoto, M. and Koinuma, H., *Physical Review B*, 1997d, **56**, 13535-13542.

Kubo, M., Oumi, Y., Miura, R., Stirling, A., Miyamoto, A., Kawasaki, M., Yoshimoto, M. and Koinuma, H., *Journal of Chemical Physics*, 1998a, **109**, 8601-8606.

Kubo, M., Oumi, Y., Miura, R., Stirling, A., Miyamoto, A., Kawasaki, M., Yoshimoto, M. and Koinuma, H., *Journal of Chemical Physics*, 1998b, **109**, 9148-9154.

Kubo, M., PhD Thesis, Tonoku University, 1999.

Kubo, M., Oumi, Y., Takaba, H., Chatterjee, A., Miyamoto, A., Kawasaki, M., Yoshimoto, M. and Koinuma, H., *Physical Review B*, 2000, **61**, 16187-16192.

Lahaye, J., Boehm, S., Chambrion, PH. And Ehrburger, P., *Combustion and Flame*, 1996, **104**, 199-207.

Larsson, P-O. and Andersson, A., *Applied Catalysis B*, 2000, **24**, 175-192.

Leach, A. R., '*Molecular Modelling: Principles and Applications*', Addison Wesley Longman Ltd., Harlow, 1996.

Leach, A. R., '*Molecular Modelling: Principles and Applications*', Prentice Hall, London, 2001, second edition.

Lee, G. H., Yoshimoto, M. and Koinuma, H., *Applied Surface Science*, 1998, **127-129**, 393-397.

de Leeuw, N. H., Watson, G. W. and Parker, S. C., *Journal of Chemical Society, Faraday Transactions*, 1996, **92**, 2081-2091.

de Leeuw, N. H. and Parker, S. C., *Research on Chemical Intermediates*, 1999, **25**, 195-211.

Leoni, M., Jones, R. L. and Scardi, P., *Surface Coatings Technology*, 1998, **108-109**, 107-113.

Lewis, G. V., *Physica*, 1985, **131B**, 114-118.

Lewis, G. V. and Catlow, C. R. A., *Journal of Physics C*, 1985, **18**, 1149-1161.

Li, H. and Szpunar, J. A., in *'Grain Growth in Polycrystalline Materials III'*, eds. Weiland, H., Adams, B. L. and Rollett, A. D., 1998, 339-342.

Li, P., Chen, I. and Penner-Hahn, J. E., *Journal of American Ceramic Society*, 1994a, **77**, 118-128.

Li, P., Chen, I. and Penner-Hahn, J. E., *Journal of American Ceramic Society*, 1994b, **77**, 1281-1288.

Li, P., Chen, I. and Penner-Hahn, J. E., *Journal of American Ceramic Society*, 1994c, **77**, 1289-1295.

Li, T., Kildsig, D. O. and Park, K., *Journal of Controlled Release*, 1997, **48**, 57-66.

Liang, S., Chern, C. S., Shi, Z. Q., Lu, P., Lu, Y. and Kear, B. H., *Journal of Crystal Growth*, 1995, **151**, 359-364.

Lind, D. M., Berry, S. D., Chern, G., Mathias, H. and Testardi, L R., *Physical Review B*, 1992, **45**, 1838-1850.

Liu, Y, Zhong, B., Peng, S., Wang, Q., Hu, T., Xie, Y. N. and Ju, X., *Catalysis Today*, 1996, **30**, 177-181.

Luerßen, B., Günther, S., Marbach, H., Kiskinova, M., Janek, J. and Imbihl, R., *Chemical Physics Letters*, 2000, **316**, 331-335.

Luo, M. F., Zheng, X. M. and Zhong, Y. J., *Indian Journal of Chemistry A*, 1999, **38**, 703-707.

Machida, M., Uto, M., Kurogi, D., and Kijima, T., *Journal of Materials Chemistry*, 2001, **11**, 900-904.

Madkour, T. M. and Barakat, A. M., *Computational and Theoretical Polymer Science*, 1997, **7**, 35-46.

Maeda, T., Lee, G. H., Ohnishi, T., Kawasaki, M., Yoshimoto, M. and Koinuma, H., *Materials Science and Engineering*, 1996, **B41**, 134-137.

Maicaneanu, S. A., Sayle, D. C. and Watson, G. W., *Chemical Communications*, 2001a, 289-290.

Maicaneanu, S. A., Sayle, D. C. and Watson, G. W., *Journal of Physical Chemistry*, 2001b, in press.

Markaryan, G. L., Ikryannikova, L. N., Muravieva, G. P., Turakulova, A. O., Kostyuk, B. G., Lunina, E. V., Lunin, V. V., Zhilinskaya, E. and Aboukais, A., *Colloids and Surfaces A*, 1999, **151**, 435-447.

Masui, T., Ozaki, T., Machida, K. and Adachi, G., *Journal of Alloys and Compounds*, 2000, **303-304**, 49-55.

Matatov-Meytal, Y. I. and Sheintuch, M., *Industrial Engineering and Chemical Research*, 1998, **37**, 309-326.

Matsumoto, S., Ikeda, Y., Suzuki, H., Ogai, M. and Miyoshi, N., *Applied Catalysis B*, 2000, **25**, 115-124.

Méchin, L., Villegier, J-C., Rolland, G. and Laugier, F., *Physica C*, 1996, **269**, 124-130.

Mekhemer, G. A. H. and Ismail, H. M., *Colloids and Surfaces A*, 2000, **164**, 227-235.

Migita, S., Kasai, Y. and Sakai, S., *Journal of Low Temperature Physics*, 1996, **105**, 1337-1342.

Minervini, L., Zacate, M. O. and Grimes, R. W., *Solid State Ionics*, 1999, **116**, 339-349.

Minervini, L., Grimes, R. W., Kilner, J. A. and Sickafus, K. E., *Journal of Materials Chemistry*, 2000, **10**, 2349-2354.

Mogensen, M., Sammes, N. M. and Tompsett, G. A., *Solid State Ionics*, 2000, **129**, 63-94.

Morris, B. C., Flawell, W. R., Mackrodt, W. C. and Morris, M. A., *Journal of Materials Chemistry*, 1993, **3**, 1007-1013.

Møller, P. J., Komolov, S. A. Lazneva, E. F. and Egebjerg, T., *Applied Surface Science*, 1999, **142**, 210-214.

Musolino, V., Dal Corso, A. and Selloni, A., *Physical Review Letters*, 1999a, **83**, 2761-2764.

Musolino, V., Selloni, A. and Car, R., *Physical Review Letters*, 1999b, **83**, 3242-3245.

Müller, B., Nedelmann, L. P., Fischer, B., Brune, H., Barth, J. V., Kern, K., Erdos, D. and Wollschläger, J., *Surface Review and Letters*, 1998, **5**, 769-781.

Nachtigallová, D., Nachtigall, P., Sierka, M. and Sauer, J., *Physical Chemistry Chemical Physics*, 1999, **1**, 2019-2026.

Nakatsuji, T., *Applied Catalysis B*, 2000, **25**, 163-179.

Newsam, J. M. and Li, Y. S., *Catalysis Today*, 1995, **23**, 325-332.

Nishikawa, H., Kanai, M. and Kawai, T., *Journal of Crystal Growth*, 1997, **179**, 467-476.

Noguera, C., *Journal of Physics: Condensed Matter*, 2000, **12**, R367-R410.

Nörenberg, H. and Briggs, G. A. D., *Physical Review Letter*, 1997, **79**, 4222-4225.

Nörenberg, H. and Briggs, G. A. D., *Surface Science*, 1998, **402-404**, 734-737.

Nörenberg, H., Dinelli, F. and Briggs, G. A. D., *Surface Science*, 1999a, **436**, L635-L640.

Nörenberg, H. and Briggs, G. A. D., *Surface Science*, 1999b, **424**, L352-L355.

Nörenberg, H., Dinelli, F. and Briggs, G. A. D., *Surface Science*, 2000, **446**, L83-L88.

O'Connell, M. and Morris, M. A., *Catalysis Today*, 2000, **59**, 387-393.

Ohnishi, T., Yoshimoto, M., Lee, G. H., Maeda, T. and Koinuma, H., *Journal of Vacuum Science & Technology A*, 1997, **15**, 2469-2472.

Oliver, P. M., Watson, G. W. and Parker, S. C., *Physical Review B*, 1995, **52**, 5323-5329.

Oliver, P.M., Parker, S. C., Edgell, R. G. and Jones, F. H., *Journal of Chemical Society, Faraday Transactions*, 1996, **92**, 2049-2056.

Ottosson, M., Lu, J. and Carlsson, J.-O., *Journal of Crystal Growth*, 1995, **151**, 305-311.

Oumi, Y., Yamano, H., Kubo, M., Vetrivel, R. and Miyamoto, A., *Catalysis Today*, 1995, **23**, 417-423.

Ozawa, M., *Journal of Alloys and Compounds*, 1998, **275-277**, 886-890.

Oyama, N., Ohta, E., Takeda, K., Shiraishi, K. and Yamaguchi, H., *Surface Science*, 1999, **433-435**, 900-903.

Ozawa, M. and Loong, C.-K., *Catalysis Today*, 1999, **50**, 329-342.

Pan, M., Meng, G. Y., Xin, H. W., Chen, C. S., Peng, D. K. and Lin, Y. S., *Thin Solid Films*, 1998, **324**, 89-93.

Pantu, P., Kim, K. and Gavalas, G. R., *Applied Catalysis A*, 2000, **193**, 203-214.

Park, G.-S. and Yang, G.-M., *Thin Solid Films*, 2000, **365**, 7-11.

Parker, S. C., Oliver, P. M., de Leeuw, N. H., Titiloye, J. O. and Watson, G. W., *Phase Transitions*, 1997, **61**, 83-107.

Parker, S. C., Grant, A. W., Bondzie, V. A. and Campbell, C. T., *Surface Science*, 1999a, **441**, 10-20.

Parker, S. C., de Leeuw, N. and Redfern, S. E., *Faraday Discussions*, 1999b, **114**, 381-393.

Pasel, J., Speer, V., Albrecht, C., Richter, F. and Papp, H., *Applied Catalysis B*, 2000, **25**, 105-113.

Pfau, A. and Schierbaum, K. D., *Surface Science*, 1994, **321**, 71-80.

Phillpot, S. R., Keblinski, P., Wolf, D. and Cleri, F., *Interface Science*, 1999, **7**, 15-31.

Plass, R., Feller, J. and Gajdardziska-Josifovska, M., *Surface Science*, 1998, **414**, 26-37.

Polli, A. D., Wagner, T., Gemming, T. and Rühle, M., *Surface Science*, 2000, **448**, 279-289.

Putna, E. S., Vohs, J. M. and Gorte, R. J., *Journal of Physical Chemistry*, 1996, **100**, 17862-17865.

Putna, E. S., Vohs, J. M. and Gorte, R. J., *Catalysis Letters*, 1997, **45**, 143-147.

Putna, E. S., Bunluesin, T., Fan, X. L., Gorte, R. J., Vohs, J. M., Lakis, R. E. and Egami, T., *Catalysis Today*, 1999, **50**, 343-352.

Qiu, H. and Hashimoto, M., *Vacuum*, 2000, **59**, 411-416.

Rao, G. R., Kašpar, J., Meriani, S., di Monte, R. and Graziani, M., *Catalysis Letters*, 1994, **24**, 107-112.

Ramamoorthy, R., Sundararaman, D. and Ramasamy, S., *Solid State Ionics*, 1999, **123**, 271-278.

Rocchini, E., Trovarelli, A., Llorca, J., Grahan, G. W., Weber, W. H., Maciejewski, M. and Baiker, A., *Journal of Catalysis*, 2000, **194**, 461-478.

Rocher, A. and Snoeck, E., *Materials Science and Engineering*, 1999, **B67**, 62-69.

Rue, G. H., Yoo, D. H. and Kim, H. K., *Journal of the Korean Physical Society*, 1999, **35**, S1247-S1250.

Sahibzada, M., Steele, B. C. H., Zheng, K., Rudkin, R. A. and Metcalfe, I. S., *Catalysis Today*, 1997, **38**, 459-466.

Sayle, D. C., Catlow, C. R. A., Perrin, M.-A. and Nortier, P., *Journal of Physics and Chemistry of Solids*, 1995a, **56**, 799-805.

Sayle, D. C., Sayle, T. X. T., Parker, S. C., Harding, J. H. and Catlow, C. R. A., *Surface Science*, 1995b, **334**, 170-178.

Sayle, D. C., Catlow, C. R. A., Perrin, M. A. and Nortier, P., *Journal of Physical Chemistry*, 1996a, **100**, 8940-8945.

Sayle, D. C., Gay, D. H., Rohl, A. L., Catlow, C. R. A., Harding, J. H., Perrin, M. A. and Nortier, P., *Journal of Materials Chemistry*, 1996b, **6**, 653-660.

Sayle, D. C., Catlow, C. R. A. and Perrin, M. A., *Physical Review B*, 1997a, **56**, 15952-15961.

Sayle, D. C., Catlow, C. R. A., Perrin, M. A. and Nortier, P., *Journal of Materials Chemistry*, 1997b, **7**, 1971-1923.

Sayle, D. C., Catlow, C. R. A., Gale, J. D., Perrin, M. A and Nortier, P., *Journal of Physical Chemistry* A, 1997c, **101**, 3331-3337.

Sayle, D. C., *Journal of Materials Chemistry*, 1998a, **8**, 2025-2032.

Sayle, D. C., Catlow, C. R. A., Perrin, M. A. and Nortier, P., *Microporous and Mesoporous Materials*, 1998b, **20**, 259-267.

Sayle, D. C., *Journal of Materials Chemistry*, 1999a, **9**, 607-616.

Sayle, D. C., Maicaneanu, S. A., Slater, B. and Catlow, C. R. A., *Journal of Materials Chemistry*, 1999b, **9**, 2779-2787.

Sayle, D. C., *Journal of Materials Chemistry*, 1999c, **9**, 2961-2964.

Sayle, D. C., Catlow, C. R. A., Harding, J. H., Healy, M. J. F., Maicaneanu, S. A., Parker, S. C., Slater, B. and Watson, G. W, *Journal of Materials Chemistry*, 2000a, **10**, 1315-1324.

Sayle, D. C. and Watson, G. W., *Journal of Materials Chemistry*, 2000b, **10**, 2241-2243.

Sayle, D. C. and Watson, G. W., *Physical Chemistry Chemical Physics*, 2000c, **2**, 5491-5499.

Sayle, D. C. and Watson, G. W., *Surface Science*, 2001a, **473**, 97-107.

Sayle, D. C. and Watson, G. W., *Journal of Physical Chemistry*, 2001b, **105**, 5506-5514.

Sayle, D. C., Catlow, C. R. A., Dulamita, N., Healy, M. J. F., Maicaneanu, S. A. Slater, B. and Watson, G. W., *Molecular Simulation*, 2001c, in press.

Sayle, T. X. T., Parker, S. C. and Catlow, C. R. A., *Journal of Chemical Society, Chemical Communications*, 1992, **14**, 977-978.

Sayle, T. X. T., Catlow, C. R. A., Sayle, D. C., Parker, S. C. and Harding, J. H., *Philosophical Magazine A*, 1993, **68**, 565-573.

Sayle, T. X. T., Parker, S. C. and Catlow, C. R. A., *Surface Science*, 1994a, **316**, 329-336.

Sayle, T. X. T., Parker, S. C. and Catlow, C. R. A., *Journal of Physical Chemistry*, 1994b, **98**, 13625-13630.

Schnitker, J. and Srolovitz, D. J., *Modelling Simulation Materials Science*, 1998, **6**, 153-164.

Schwarz, J. A., Contescu, C. and Contescu, A., *Chemical Review*, 1995, **95**, 477-510.

Sebastian, I., Bertrans, T., Meinel, K. and Neddermeyer, H., *Faraday Discussions*, 1999, **114**, 129-140.

Shluger, A. L., Rohl, A. L. and Gay. D. H., *Physical Review B*, 1995a, **51**(19), 13631-13644.

Shluger, A. L., Rohl, A. L. and Gay. D. H., *Journal of Vacuum Science and Technology*, 1995b, **13**(3), 1190-1197.

Siokou, A. and Nix, R. M., *Journal of Physical Chemistry B*, 1999, **103**(33), 6984-6997.

Smith, W. and Forester, T. R., *The DL_POLY Molecular Simulation Package*, URL: http://www.dl.ac.uk/TCSC/Software/DL_POLY, 1999.

Somorjai, G. A., *'Introduction to surface chemistry and catalysis'*, J. Wiley & Sons Inc., New-York, 1994.

Sotiropoulou, D. and Ladas, S., *Surface Science*, 2000, **452**, 58-66.

Španková, M., Vávra, I., Gaži, Š., Machajdík, D., Chromik, Š., Fröhlich, K., Hellemans, L. and Beňačka, Š., *Journal of Crystal Growth*, 2000, **218**, 287-293.

Srinivasan, R., Davis, B. H., Rice, L. A. and de Angelis, R. J., *Journal of Materials Science*, 1992, **27**, 661-670.

Srinivisan, R., Hubbard, C. R., Cavin, O. B. and Davis, B. H., *Chemistry of Materials*, 1993, **5**, 27-31.

Stampe, P. A. and Kennedy, R. J., *Journal of Crystal Growth*, 1998, **191**, 478-482.

Štefanić, G., Music, S., Grzeta, B., Popovic, S. and Sekulic, A., *Journal of Physics and Chemistry of Solids*, 1998a, **59**, 879-885.

Štefanić, G., Music, S., Grzeta, B., Popovic, S. and Sekulic, A., *Croatica Chemica Acta*, 1998b, **71**, 789-806.

Štefanić, G., Popovic, S. and Music, S., *Materials Letters*, 1998c, 36, 240-244.

Stefanovich, E. V., Shluger, A. L. and Catlow, C. R. A., *Physical Review B*, 1994, **49**, 11560-11571.

Stoneham, A. M. and Harding, J. H., *Acta Materialia*, 1998, **46**, 2255-2261.

Sutton, A. P. and Balluffi, R. W., *Acta Metallurgica*, 1987, **35**, 2177-2201.

Suzuki, K., Kubo, M., Oumi, Y., Miura, R., Takaba, H., Fahmi, A., Chatterjee, A., Teraishi, K. and Miyamoto, A., *Applied Physics Letters*, 1998a, **73**, 1502-1504.

Svedberg, E. B., Jemander, T. S., Lin, N., Erlandsson, R., Hansson, G., Birch, J. and Sundgren, J. –E., *Surface Science*, 1999, **443**, 31-43.

Suzuki, K., Endou, A., Miura, R., Oumi, Y., Takaba, H., Kubo, M., Chatterjee, A., Fahmi, A. and Miyamoto, A., *Applied Surface Science*, 1998b, **130-132**, 545-548.

Suzuki, T. and Souda, R., *Surface Science*, 2000, **445**, 506-511.

Tamura, S., Ishida, T., Magara, H., Mihara, T., Tabata, O. and Tatsuta, T., *Thin Solid Films*, 1999, **344**, 142-144.

Tasker, P. W., *Journal of Physics C*, 1979, **12**, 4977-4984.

Telfer, G. B., Gale, J. D., Roberts, K. J., Wilde, P. J. and Meenan, P., *Acta Crystallographica Section A*, 1997, **53**, 415-420.

Terrible, D., Trovarelli, A., de Leintenburg, C., Primavera, A. and Dolcetti, G., *Catalysis Today*, 1999, **47**, 133-140.

Trovarelli, A., *Catalysis Review Science and Technology*, 1996, **38**, 439-520.

Trovarelli, A., de Leitenburg, C. and Dolcetti, G., *CHEMTECH*, 1997, **27**, 32-37.

Trovarelli, A., de Leitenburg, C., Boaro, M. and Dolcetti, G., *Catalysis Today*, 1999, **50**, 353-367.

Vallet-Regi, M., Conde, F., Nicolopoulos, S., Ragel, C. V. and Gonzáles-Calbet, J. M., *Materials Science Forum*, 1997, **235**, 291-296.

Van Vlack, L. H., '*Materials Science for Engineers*', Addison-Wesley Publishing Company, Reading, Massachusets, 1970, 105.

Vasco, E., Vasquez, L., Aguilo, M. and Zaldo, C., *Journal of Crystal Growth*, 2000, **209**, 883-889.

Vidal, H., Kašpar, J., Pijolat, M.,, Colon, G., Bernal, S., Cordón, A., Perrichon, V. and Fally, F., *Applied Catalysis B*, 2000, **27**, 49-43.

Vidmar, P., Fornasiero, P., Kašpar, J., Gubitosa, G. and Graziani, M., *Journal of Catalysis*, 1997, **171**, 160-168.

Vyas, S., Grimes, R. W., Gay, D. H. and Rohl, A. L., *Journal of Chemical Society, Faraday Transactions*, 1998, **94**, 427-434.

Wagner, T., Kirchheim, R. and Rühle, M., *Acta Metallurgica and Materialia*, 1992, **40**, S85-S93.

Wakiya, N., Yamada, T., Shinozaki, K. and Mizutani, N., *Thin Solids Films*, 2000, **371**, 211-217.

Waltenburg, H. N., and Moller, P. J., *Surface Science*, 1999, **439**, 139-145.

Wang, A., Belot, J. A., Marks, T. J., Markworth, P. R., Chang, R. P. H., Chudzik, M. P. and Kannewurf, C. R., *Physica C*, 1999, **320**, 154-160.

Wang, D., Guo, Y., Liang, K. and Tao, K., *Science in China A*, 1999, **42**, 80-86.

Wang, H. B., Xia, C. R., Meng, G. Y. and Peng, D. K., *Materials Letters*, 2000, **44**, 23-28.

Wang, J.-A., Chen, L-F. and Li, C-L., *Journal of Materials Science Letters*, 1998, **17**, 533-535.

Wang, L. and Clancy, P., *Surface Science*, 2001, **473**, 25-38.

Wang, J.-A., Chen, L-F. and Li, C-L., *Journal of Molecular Catalysis A*, 1999, **139**, 315-323.

Wang, R.-P., Zhou, Y. L., Pan, S. H., Zhang, H., Guo, X. X., Xiong, X. M., Lu, H. B., Zhen, Z. H. and Yang, G. Z., *Journal of Applied Physics*, 1998, **84**, 1994-1997.

Wang, S., Wang, W., Liu, Q., Zhang, M. and Qian, Y., *Solid State Ionics*, 2000, **133**, 211-215.

Wang, X., Olafsson, S., Sandström, P. and Helmersson, U., *Thin Solid Films*, 2000, **360**, 181-186.

Wang, Y., Sun, Y., Xu, Y. and Chen, S., *Spillover and Migration of Surface Species and Catalysis*, 1997, **112**, 143-150.

Wang, Z., Oda, S., Karlsteen, M., Södervall, U. and Willander, M., *Japanese Journal of Applied Physics*, 2000, **39**, 4164-4167.

Watari, N. and Ohnishi, S., *Catalysis Today*, 1995, **23**, 371-377.

Watson, G. W., PhD Thesis, University of Bath, 1994.

Watson, G. W., Kelsey, E. T., de Leeuw, N. H., Harris, D. J. and Parker, S. C., *Journal of Chemical Society, Faraday Transactions*, 1996, **92**, 433-438.

Watson, G. W., Tschaufeser, P., Wall, A., Jackson, R. A. and Parker, S. C., '*Lattice energy and Free Energy Minimisation Techniques*' in '*Computer Modelling in Inorganic Crystallography*', ed. Catlow, C. R. A., Academic Press, London, 1997, 57-81.

Watson, G. W., Kelsey, E. T. and Parker, S. C., *Philosophical Magazine* A, 1999, **79**, 527-536.

Watson, G. W., Oliver, P. M. and Parker, S. C., *Surface Science*, 2001, **474**, L185-L190.

Weast, R. C. and Astle, M. J. eds., *CRC Handbook of Chemistry and Physics*, 1982-1983, 63rd edition, page F-179, CRC Press Inc., Boca Raton, Florida.

Wedepohl, P. T., *Proceedings of the Physical Society London*, 1967, **92**, 79-93.

Wollschläger, J., *Defect and Diffusion Forum*, 1998, **164**, 37-56.

Wollschläger, J., Viernow, J., Tegenkamp, C., Erdös, D., Schröder, K. M. and Pfnür, H., *Applied Surface Science*, 1999, **142**, 129-134.

Wunderlich, W., Fujimoto, M. and Ohsato, H., *Thin Solid Films*, 2000, **375**, 9-14.

Xiong, X. M., Zhou, Y. L., Lu, H. B., Chen, Z. H. and Yang, G. Z., *Physica C*, 1998a, **298**, 178-184.

Xiong, X. M., Wang, R. P., Zhou, Y. L., Guo, X. X., Lu, H. B., Pan, S. H., Yang, G. Z., Liu, C. F., Wu, X., Zhang, X. P. and Zhou, L., *Journal of Vacuum Science & Technology A*, 1998b, **16**, 2501-2504.

Yamahara, K., Okazaki, K. and Kawamura, K., *Catalysis Today*, 1995, **23**, 397-402.

Yamamura, Y., Kawasaki, S. and Sakai, H., *Solid State Ionics*, 1999, **126**, 181-189.

Yokomochi, Y., Ohtsuka, H., Tabata, T., Okada, O., Yokoi, Y., Ishikawa, H., Yamaguchi, R., Matsui, H., Tachibana, A. and Yamabe, T., *Catalysis Today*, 1995, **23**, 431-437.

Zacate, M. O., Minervini, L., Bradfield, D. J., Grimes, R. W., and Sickafus, K. E., *Solid State Ionics*, 2000, **128**, 243-254.

Zafeiratos, S. and Kennou, S., *Surface Science*, 1999, **443**, 238-244.

Zamar, F., Trovarelli, A., de Leintenburg, C. and Dolcetti, G., *Chemical Communication*, 1995, 965-966.

Zandbergen, H. W., Connoly, E., Graboy, I. E., Svetchnikov, V. L. and Kaul, A. R., *Physica C*, 2000, **329**, 37-44.

Zhu, Y. X. and Hu, Y. H., *Journal of Rare Earths*, 1996, **14**, 81-87.

Zorn, M. E., Tompkins, D. T., Zeltner, W. A. and Anderson, M. A., *Applied Catalysis B*, 1999, **23**, 1-8.